Exploiting Degrees of Freedom in Active Nanophotonic Devices



June Sang Lee

Somerville College

University of Oxford

A thesis submitted for the degree of

Doctor of Philosophy

Trinity 2023

This thesis is dedicated to my parents.

Acknowledgements

Starting my DPhil amidst the onset of the COVID-19 pandemic, I have been through many ups and downs, experienced big changes in my life, and grown up not only as a researcher but as an individual. In retrospect, the past four years seem to have passed within a few nanoseconds. Nonetheless, when I reflect on each moment within this period, it unfolds as a full of invaluable time. This is truly because of everyone who has shared these moments with me and has provided unwavering support. Despite the fact that only my name appears on this thesis, the credit for this work is certainly not mine, but to all the contributions from each of them.

First and foremost, I would like to express my deepest gratitude to my supervisor, Professor Harish Bhaskaran. Harish, you have always exemplified to me the qualities of a great leader, advisor, and friend within our group. Thank you very much for all of your guidance and mentorship since day one. You have always been open-minded, supportive, and sometimes critical, but most importantly I always have felt that you had my back, which indeed encouraged me (even my pessimistic view on my research) to develop myself as a better researcher. I feel extremely fortunate to have lots of in-depth discussions and small talks with you all the time, both within and outside of the office. Thank you so much for everything.

Nick, although I did not expect my DPhil journey would have been so strongly bonded with you until the end of my first year, I feel extremely lucky that I could have spent most of my DPhil with you. Thank you very much for your excellent mentoring and support during every stage of my research, whether I succeeded or failed. You are humble on the outside, yet incredibly strong on the inside. You are not just a great friend, but also a fantastic mentor. You are an excellent collaborator as well as an exceptional scientist. You still pretend as if you did nothing despite sharing, teaching, and providing me with so

many invaluable things. I really feel grateful and indebted to you. Many thanks for everything.

Even now, Samarth, you are sitting right behind me, as you always have been since the beginning of our DPhil journey. I should say I was privileged to have begun my DPhil together with you. It is strange because we have never collaborated on the same project, yet I have always regarded you as my partner on every project in which I was involved. Perhaps it is because I have often relied on you academically or emotionally. Working alongside you has been an enjoyable experience that has taught me a lot about work ethics and professionalism, as well as your thoughtful mindset. Thank you very much.

I would also like to thank Mengyun for her endless support beyond our projects. Mengyun, I do appreciate your goodhearted minds and understanding. You never hesitated to lend a helping hand to me and others (which is never easy!). Thank you so much for your generous contribution. Of course, while no names are mentioned here, I am extremely thankful to all of my colleagues, previous and current members of our Advanced Nanoscale Engineering group, for their help and support, as well as all those enjoyable moments.

I would like to extend my gratitude to Paul and Radka at the cleanroom and colleagues at Bodle Technologies Ltd for all of their help with my projects. I also acknowledge the financial support from Oxford Ryniker Lloyd Graduate Scholarship as well as Somerville College and Department of Materials at Oxford.

Finally, I want to thank my friends and families, both within and outside of Oxford. I am especially grateful to my family, who have always been the most important people in my life. I am deeply grateful to my sister (Seo-Yeon) and brother-in-law (Cheol-Woo) for their never-ending support and love. Also, bidding farewell to my old friend, Jjong, and welcoming my new niece and nephew (Sang-Byn, Ha-Ryn, and Sang-Woon) to our family, had certainly marked my life during the DPhil period, and I cherish all these moments dearly. My heartfelt gratitude goes to my dear Minji, who has been not only supportive

but also inspirational in every aspect of my life. Lastly, I would like to name my parents here, Young-Mi Yang and Seung-Ki Lee, who truly deserve all the credit for this journey. Their unconditional love and support have been my pillars of strength. A final note of appreciation goes to my father (Seung-Ki Lee), whom I look up to as a scientist and a man.

June Sang Lee
Oxford, 2023

Abstract

The field of nanophotonics has witnessed remarkable progress, driven by the pressing need to expand device functionalities across multiple photonic degrees-of-freedom. Active nanophotonic devices further offer reconfigurable photonic capabilities across temporal scales, but the challenge of seamlessly bridging these dimensions to achieve multifaceted functionalities persists. This thesis tackles this challenge by leveraging multiple photonic bandwidths in compact active nanophotonic devices, thereby maximizing the device functionalities in photonic domains, spatial configurations, and temporal dynamics. To accomplish this, three distinct approaches are experimentally investigated, each harnessing a different property of light — such as polarization, phase and wavelength —across a range of platforms, such as electro-optic nanowires, metasurfaces, and integrated photonic circuits.

First, the thesis introduces the implementation of a polarization-sensitive electro-optic cell using hybridized-active-dielectric nanowires. By utilizing the $Ge_2Sb_2Te_5$ phase-change alloy as the active material, this cell exhibits a polarization-dependent electrical readout, demonstrating nonlinear switching behavior of a hybrid nanowire. Expanding on this concept, a multi-nanowire configuration harnesses polarization as a tunable vector, enabling polarization-selective (de)multiplexing and computing operations at an extremely compact scale of $\ll 5$ μm. As a result, this breakthrough significantly enhances computing density by several orders of magnitude compared to its electronic counterparts. These findings unlock new possibilities for realizing device reconfigurabilities in polarization-space and portend a new paradigm for a wide range of tunable nanophotonic devices.

The concept of active nanoresonators is further extended by assembling them in a periodic array and implementing an active metasurface. Low-loss, optically-sensitive materials,

such as Sb_2Se_3, are employed to selectively tune optical phase delays based on the geometry and material states of the nanoresonators. This phase-gradient metasurface acts as flat optics, manipulating the emerging wavefront to achieve lensing, steering, or holographic imaging of the optical beam. The active tunability of the material adds extra functionalities, enabling the realization of varifocal zoom lenses in the telecommunication range using a flat metasurface of Sb_2Se_3 nanopillars. The dynamic reversible switching of such low-loss active material is then investigated using optical or electrically-programmed thermal pulses, leveraging the capabilities of low-loss meta-optics.

In the final chapters of this thesis, the active nanophotonic functionalities are interfaced with integrated photonic circuits. Such a system features the first prototype of photonic spatio-spectral reconfiguration capable of wavelength-selectively addressing the optical states of a single photonic waveguide. By combining the concept of standing-waves in a microring resonator with active $Ge_2Sb_2Te_5$ nanoantennas, the spatial degrees-of-freedom of guided modes in waveguides are harnessed with active material reconfigurability. Multiple nanoantennas arranged at a compact spacing (~460 nm) realize a multi-spectral modulator, enabling parallel communication of wavelengths and independent modulation of individual nanoantennas at respective channels. Consequently, the optical storage density is observed to exponentially increase as the system gets cascaded, while holding potential for integration with additional electro-optical controllability. These findings present an alternative pathway for maximizing device functionalities along the wavelength dimension in integrated photonic circuits, enabling applications such as high-bandwidth communication and computing.

Contents

Abstract viii

List of Figures xiv

List of Abbreviations xx

1. Introduction 1

1.1 Motivation 1
1.2 Exploitation of photonic resonances in reconfiguring phase-change material 4
1.3 Objective and outlines 5
1.3.1 Objective 5
1.3.2 Outline 5
1.4 Key findings and new science 8
1.5 Statement of originality 9

2. Phase-change nanophotonics: A review 11

2.1 Phase-change material for nanophotonic applications 11
2.2 Switching mechanism of phase-change material 12
2.3 Optical properties of phase-change material 20
2.4 Out-of-plane nanophotonic resonances with phase-change material 24
2.4.1 Tunable dielectric nanoantennas 25
2.4.2 Active dielectric metasurfaces using phase-change material 29
2.5 Integrated photonic circuits with phase-change material 32
2.5.1 Phase-change non-volatile memory cells 33
2.5.2 In-memory neuromorphic computing 35
2.6 Chapter summary and perspective 38

3. Device fabrication and measurement setup for active nanophotonic platforms 42

3.1 Device fabrication of a phase-change nanophotonic system 42
3.1.1 Wafer preparation 42

3.1.2 Phase-change nanoresonators 43
3.1.3 Integrated nanophotonic circuits 45
3.1.4 Chip alignment and electrical integration 47
3.2 Custom-built measurement setup: Switching and probing 49
3.2.1 Free-space optical setup 49
3.2.2 Integrated all-photonic measurement 55
3.3 Chapter summary 59

4. Polarization-selective switching of hybridized-active-dielectric nanowires 61

4.1 Motivation: Polarization-selective reconfigurability in a single element 61
4.2 Hybridized-active-dielectric (HAD) nanowires 63
4.2.1 Device outline and operational principle: An electro-optic cell 63
4.2.2 Optical simulation 65
4.2.3 Thermal simulation 71
4.3 Electro-optical measurement of a hybrid nanowire 75
4.3.1 Intensity-dependent modulation 77
4.3.2 Polarization-dependent modulation of electric current 82
4.4 Multi-nanowire configuration 87
4.4.1 Polarization-selective response in a multi-nanowire system 87
4.4.2 Matrix-vector multiplication using polarization 97
4.5 Further exploitation of the hybridized-active-dielectric nanowire 103
4.6 Chapter summary, critical review and outlook 106
4.7 Acknowledgement and contribution 111

5. Active phase-gradient metasurfaces using low-loss phase-change material 113

5.1 Overview: Assembling an array of phase-selective nanostructures 114
5.2 Active low-loss metasurfaces using Sb_2Se_3 Mie resonators 115
5.2.1 Optical modelling of meta-atom 115
5.2.2 Low-loss, tunable metasurfaces using Sb_2Se_3 120
5.2.3 Tunable metalens 125
5.2.4 Dynamic hologram 133
5.3 Active switching of low-loss phase-change material 134
5.3.1 Optical switching of phase-change thin films 135

5.3.2 Electrically programmable metasurfaces using a micro-heater 144
5.4 Further exploitation of low-loss metasurfaces for multi-factor switching 152
5.5 Chapter summary 155
5.6 Acknowledgement and contribution 157

6. Spatio-spectral reconfiguration of coherent integrated nanophotonics 160

6.1 Overview: Exploiting spatial degrees of freedom in integrated photonics 161
6.2 Theoretical wave propagation analysis 163
6.2.1 Dielectric waveguides 163
6.2.2 Microring resonators 165
6.2.3 Coherent perfect absorption with standing-waves 168
6.3 Photonic spatio-spectral reconfiguration 173
6.4 Spatio-spectral reconfiguration in a microring resonator 177
6.4.1 Tunable GST nanoantenna on a microring resonator 177
6.4.2 Wavelength-selective reconfigurability 183
6.5 Expanding the number of modulation 192
6.6 Advantages of enhanced functionalities in the PSR system 196
6.7 Further exploitation of spatio-spectral photonics 202
6.8 Chapter summary 207
6.9 Acknowledgement and contribution 209

7. Conclusion and outlook 212

7.1 Polarization: Hybridized-active-dielectric nanowire 213
7.2 Phase: Active low-loss metasurface 213
7.3 Wavelength: Spatio-spectral reconfiguration in integrated photonics 214
7.4 Critical review and outlook 215

Publications 224

Bibliography 229

List of Figures

1.1 Nomenclature of nanophotonics with respect to multiple dimensions of functionalities .. 3
2.1 Schematics of melt-quenching process of PCMs. ... 13
2.2 Phase-transition dynamics of (A) nucleation-dominated GST and (B) growth-dominated AIST during pulse-irradiated crystallization process ... 14
2.3 Designs of indirect electrical switching using microheaters. ... 15
2.4 Demonstrations of electrical threshold switching. ... 17
2.5 Schematic demonstrations of optically switching PCMs ... 19
2.6 Refractive index of GST and its applications ... 21
2.7 Demonstration of low-loss PCM ... 23
2.8 Scattering behavior of dielectric Mie resonators ... 26
2.9 Tunable Mie resonators exploiting PCM ... 28
2.10 Phase-change metasurfaces for wavefront manipulation ... 31
2.11 Phase-change integrated photonic memories ... 33
2.12 Phase-change in-memory computing unit ... 36
2.13 Photonic tensor core ... 37
2.14 Exploiting optical degrees of freedom with the active tunability of PCMs ... 39
3.1 Fabrication flow chart of phase-change nanoresonators ... 43
3.2 Pattern layout for e-beam lithography of nanostructures ... 44
3.3 Optical microscope scan of an array of Sb_2Se_3 nanostructures (*left*) with and (*right*) without proximity effect correction technique ... 45
3.4 Fabrication of integrated photonic circuits. ... 46
3.5 Fabrication of active nanophotonic devices with alignment markers ... 47
3.6 Images of the fabricated sample ... 48
3.7 Schematic diagram of parts of custom-built optical microscope for optimizing (A) imaging and (B) illumination path ... 50
3.8 Optimization of condenser lens position in a custom-built microscope ... 52
3.9 Schematic diagram of custom-built microscope with red switching laser ... 53

3.10 Custom-built microscope with electrical microprobes mounted on a XYZ stage. 55
3.11 Static transmission measurement of integrated photonic circuits. 56
3.12 Pump-probe measurement of integrated photonic circuits using optical switches. 58
4.1 Schematic diagram of a HAD nanowire across two electrodes 63
4.2 Microscope images of a HAD nanowire 64
4.3 Polarization-dependent optical spectra of the HAD nanowire with the amorphous-GST66
4.4 Cross-sectional field profile of the HAD nanowire with an amorphous-GST layer 67
4.5 Polarization-dependent optical spectra of the HAD nanowire with the crystalline-GST 68
4.6 Cross-sectional field profile of the HAD nanowire with a crystalline-GST layer 68
4.7 Spectral responses of nanowires as a function of varying nanowire widths. 70
4.8 Spectral responses of nanowires as a function of varying polarization angles 71
4.9 Cross-sectional view of temperature profiles within HAD nanowires 74
4.10 Cross-sectional views of temperature profiles at different polarization angles 74
4.11 Calculated average temperature and normalized absorption of a HAD nanowire 75
4.12 Schematics of the electro-optic measurement setup of the HAD nanowire 76
4.13 Calibration of polarization modulation using half-wave plate (HWP) 77
4.14 Reversible switching of the HAD nanowire 78
4.15 Intensity-dependent multilevel operation of the HAD nanowire 80
4.16 Normalized 1D photocurrent profile and fitted curves along the scanning distance. 81
4.17 Time-trace measurements of polarization-selective electrical readouts for (**A**) crystallisation and (**B**) amorphization 83
4.18 Time-trace electrical readouts for polarization- and laser power-dependent switching 84
4.19 2D normalized intensity maps of observed readout contrasts as a function of polarization and laser power 85
4.20 Freely-accessible multilevels of the HAD nanowires 86
4.21 Microscope images of multi-nanowire configuration 88
4.22 Simultaneous time-traced electrical readout of multi-nanowire configuration 89
4.23 Multi-nanowire measurement during amorphization processes 90
4.24 Measurement of polarization-selective switching under misalignment conditions 92
4.25 Simulated absorbed-power distribution of nanowire for various nanowire widths 93
4.26 Reconfigurable polarization-selective demultiplexing 94
4.27 Reconfigurable polarization-selective demultiplexing with amorphization processes .. 95

4.28 Current reversing effect 96
4.29 Schematics of matrix-vector multiplication utilizing polarization as a tunable factor. . 98
4.30 Experimental results of matrix-vector multiplication employing polarization-selective weights 99
4.31 Calculated temperature profile and optical absorption of a nanowire with varying polarizations at low laser power 100
4.32 Normalized absorption spectra of nanowires with varying lengths (i.e. aspect ratio).. 102
4.33 Asymmetric photoconductance of the nanowire with varied position of illumination 104
4.34 Scanning-type hyperspectral imaging using multiple HAD nanowires 106
5.1 Sb_2Se_3 dielectric metasurfaces 116
5.2 Optical response of a a-Sb2Se3 nanopillar array 116
5.3 Mode overlap in the Sb_2Se_3 meta-atom 118
5.4 Mode overlap in the Sb_2Se_3 meta-atom with reduced thickness 119
5.5 Design of a single-focal Sb_2Se_3 metalens 121
5.6 Fabrication process of high aspect-ratio Sb_2Se_3 nanopillars. 122
5.7 Microscope images of Sb_2Se_3 dielectric metasurfaces 123
5.8 (**A**) Schematic diagram and (**B**) photo of metalens measurement setup 125
5.9 Simulated electric field of a single-focal, intensity-tunable Sb_2Se_3 metalens 127
5.10 Experiment measurement of a single-focal, intensity-tunable Sb_2Se_3 metalens 128
5.11 Improved mode overlap in the Sb_2Se_3 meta-atom with a dielectric cladding layer 129
5.12 Varifocal Sb_2Se_3 metalens 131
5.13 Dynamic holograms using low-loss PCM metasurfaces 134
5.14 Schematic illustration of out-of-plane optical switching of low-loss phase-change material using high-power laser pulses at visible wavelength. 135
5.15 Measurement of Sb_2S_3 thin film optical switching 137
5.16 Optical images of low-loss PCM thin film illuminated by visible laser pulses. 139
5.17 Dynamic reversible switching of various PCMs using single-shot pulses 140
5.18 Dynamic switching of Sb_2Se_3 on the microring resonator and MZI 143
5.19 Dynamic GeTe metasruface with electro-thermal pulses given by NiCr heater 146
5.20 Measurement of switching cycles in the GeTe thin film and metasurfaces 148
5.21 GeTe nanowire array 150
5.22 Dynamic GeTe meta-deflector 151

5.23 Multi-factor switching of low-loss resonators 153
5.24 Sb_2Se_3 polarization-encrypted nanowire pixels. 154
6.1 Schematic illustrations of two photonic systems, demonstrating (**A**) free-space photonic devices and (**B**) photonic integrated circuits 162
6.2 Schematic illustration of (**A**) 1D slab waveguides and (**B**) 2D waveguides, and (**C**) cross-sectional TE mode profile in 2D waveguides 164
6.3 Schematic illustrations of all-pass ring resonators 166
6.4 Schematics of two counter-propagating travelling waves and standing-waves 169
6.5 Comparison of conventional and standing-wave PICs. 174
6.6 Schematic illustrations of PSR 176
6.7 Simulated electric-field distribution of standing waves in a plain waveguide 177
6.8 PSR in a microring resonator. 178
6.9 Simulated absorption spectrum of GST nanoantennas in a microring resonator 180
6.10 Optical microscope image of a microring PSR system 181
6.11 Experimental demonstration of selective absorption of GST nanoantennas in a PSR system 182
6.12 Wavelength-selectively reversible system by optical pulses 183
6.13 Wavelength-selective active switching cycles of GST/Au nanoantennas with optical pulses at different wavelengths 184
6.14 Full-intensity spectra of the PSR system. 185
6.15 Exploring spectral selectivity through varying sizes and quantities of nanoantennas. 187
6.16 Multilevel wavelength-selective operation 188
6.17 Dynamic multi-spectral modulator in a single element 189
6.18 Measured spectra of a multi-spectral modulator 190
6.19 Wavelength-selective reversibility in the microring PSR system 191
6.20 Spatio-spectral relation in a plain waveguide with two couter-propagating waves 193
6.21 Multiple independent modulation in a single PSR system 195
6.22 Transmission spectra of a PSR microring resonator with a radius of 15 μm 196
6.23 Schematics of the enhanced optical storage density in the upscaled PSR system. 199
6.24 Schematic illustration of a PSR microring resonator with varying the optical phases of input arms 200
6.25 Demonstration of PSR microring resonator with optical phase delays 201

6.26 Photonic-crystal microcavities for spatio-spectral accessibility 203
6.27 Photonic crystal microcavities with two counter-propagating waves..... 205
6.28 Electrically-programmable PSR system 206
Table 4.1 101
Table 6.1 198

List of Abbreviations

AFM	Atomic Force Microscope
CPA	Coherent Perfect Absorption
CCD	Charge-Coupled Device
EBL	Electron-Beam Lithography
EDFA	Erbium-Doped Fiber Amplifier
EOM	Electro-Optical Modulator
FDTD	Finite-Difference Time-Domain
FEM	Finite Element Method
FWHM	Full-Width at Half Maximum
GST	Germanium Antimony Telluride ($Ge_2Sb_2Te_5$)
HAD	Hybridized-Active-Dielectric
HWP	Half-Wave Plate
IPA	Isopropyl Alcohol
LED	Light-Emitting Diode
MAC	Multiply-Accumulate Operation
MEMS	Micro-Electromechanical System
MIR	Mid Infrared
MVM	Matrix Vector Multiplication
MZI	Mach-Zehnder Interferometer

NIR	Near Infrared
NMP	N-Methylpyrrolidone
OAM	Orbital Angular Momentum
OM	Optical Microscope
PCM	Phase Change Material
PIC	Photonic Integrated Circuit
PMMA	Poly (methyl methacrylate): positive photoresist
PSR	Photonic Spatio-spectral Reconfiguration
RF	Radio-Frequency
RIE	Reaction Ion Etching
SAM	Spin Angular Momentum
SMU	Source Meter Unit
SEM	Scanning Electron Microscope
TE	Transverse Electric
TM	Transverse Magnetic

Chapter 1

Introduction

1.1 Motivation

The desire to scale down science and technology has long been a human interest, driving the emergence of quantum physics in the 1920s and the development of nanotechnology over the last few decades. Researchers have extensively studied the value of continued miniaturization of electronic devices, as defined by *Moore's law*, which predicts that the number of electronic transistors per given chip size will double every two years.[1] As a result of the reduction in transistor size, device density has significantly increased, and this has led to the maximization of device functionalities along the spatial dimension, thereby resulting in a myriad of achievements in nanotechnology. However, it has become increasingly challenging and unnecessary to overcome physical limits in scaling down, as the spatial resolution of silicon transistors ultimately reaches the sub-50 nm range.[2,3] Consequently, nanophotonic devices have experienced rapid growth due to the multifaceted properties of light that can extend the dimension of functionalities to their optical domains, such as polarization,[4] wavelength,[5] or angular momentum.[6] Although

nanophotonics offer high-bandwidth and high-speed capabilities, revolutionizing the field of optical communication,[7] the size of photonic devices still remains bulky, degrading the device densities. Such a tradeoff poses a crucial challenge for both the photonic and electronic communities.

One approach to addressing this challenge is the exploitation of active materials to further increase the functionalities in the time dimension for both photonic and electronic devices. This can be achieved by deterministically modulating the active material states, making the device functionality reconfigurable over a temporal scale rather than static. Phase-change materials (PCMs),[8,9] a type of active material capable of tuning the optical properties depending on its crystallographic state, have been widely studied as a functional material in active nanophotonic applications ranging from optical storage,[10] routing,[11] and neuromorphic computing[12] to dynamic displays[13] and holograms.[14] The key feature of exploiting extra photonic degrees-of-freedom from these phase-change nanophotonic devices, however, has remained elusive. These also have a large device footprint, which adheres to an unmet requirement and the critical difficulty of increasing the number of photonic functionalities at a constrained spatial scale. Hence, as illustrated in Figure 1.1, this thesis focuses on investigating the active functionalities over optical, spatial, and temporal dimensions by designing and experimentally demonstrating ultracompact active nanophotonic prototypes that capitalizes on multiple degrees-of-freedom. Such densely packed device functionalities offer a promising alternative to conventional *Moore's law* and open up new possibilities, especially for information storage and processing. Each prototype embodies a unique core functionality that leverages specific optical properties, such as polarization, phase, or wavelength.

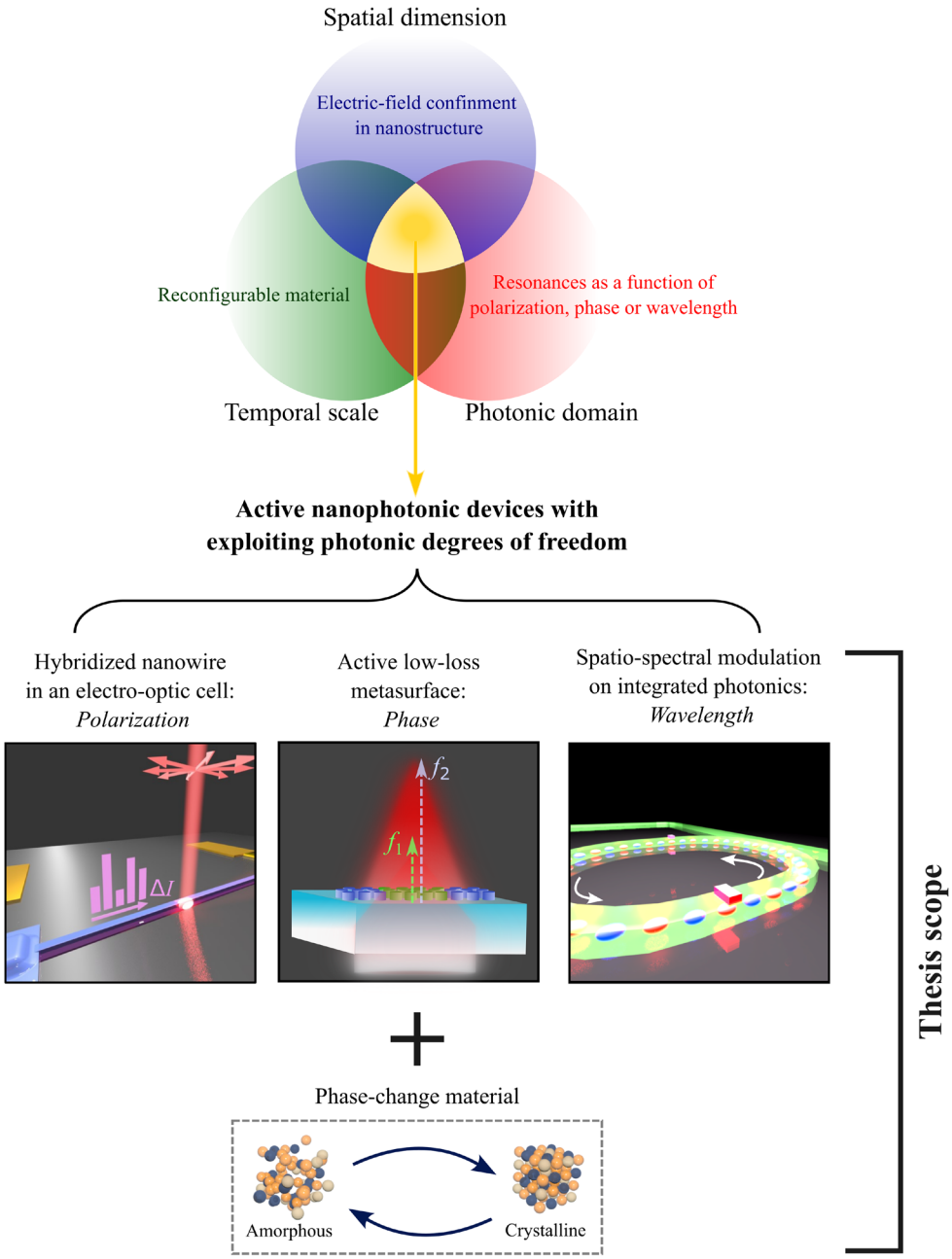


Figure 1.1 Nomenclature of nanophotonics with respect to multiple dimensions of functionalities. The spatial dimension of the device is determined by the electric-field confinement, while the photonic domains rely on the exploitation of optical properties such as polarization, phase, or wavelength. Temporal scale refers to the reconfigurability of materials. Active nanophotonics that combines and exploits multiple photonic degrees-of-freedom achieves multi-dimensional functionalities that span across these domains. These are achieved by three foundational photonic frameworks exploiting phase-change material with hybridized nanowires, metasurface or integrated photonics. Each system capitalizes on the advantages of photonic domains, such as polarization, phase and wavelength, respectively.

1.2 Exploitation of photonic resonances in reconfiguring phase-change material

PCM is widely regarded as a functional material due to its switching behavior between two or more stable crystalline phases. Such functionality is truly achieved during the phase-transition of the material and is further enhanced depending on the various phase-transition approaches.[9,10,14-16] However, most state-of-the-art phase-change nanophotonic devices have primarily focused on the change of the system resulting from switching the materials, rather than the transition itself. In other words, a wide range of phase-change resonators have demonstrated dynamic modulation of optical resonances by reconfiguring the PCM, but not dynamic switching behavior as a function of optical resonances. For instance, the polarization-dependence of one-dimensional (1D) phase-change structures has been exploited to tune the polarization state (i.e., optical resonances) by varying the states of PCMs.[17] However, there is an absence of investigation into tuning the material states with varying resonances (i.e., polarization). Despite the multifunctional features of resonances, the switching mechanism of PCM has relied on monotonic intensity modulation,[10] thus lacking the inherent functionality that arises from multifaceted optical properties. This work therefore directly combines the optical resonances into the reconfigurability of PCMs, achieving resonance-dependent phase-change switching and enhancing the selective functionalities of nanophotonic devices in polarization- (*Chapter 4*), phase- (*Chapter 5*), and wavelength-space (*Chapter 6*).

1.3 Objective and outlines

1.3.1 Objective

This thesis aims to demonstrate the concept of three foundational photonic prototypes, each of which possesses a distinct capability for phase-change nanophotonic devices in multi-dimensional optical space.

- **Polarization-selective system**: Polarization-selectively addressable nanowire for in-memory photonic computing with using polarization as a tunable factor.
- **Phase-gradient metasurface**: Lossless dielectric metasurface using an array of active nanoresonators to realize reconfigurable manipulation of wavefront propagation.
- **Wavelength-selective integrated photonic circuits**: A photonic waveguide with active nanoantennas that can wavelength-selectively reconfigure the optical states at a highly confined scale for parallelized photonic storage, routing or computing applications.

1.3.2 Outline

The content of this thesis is organized in the following way:

Chapter 2 reviews the fundamental properties and switching mechanisms of PCMs. The discussion on both lossy and low-loss types of PCMs is further included, followed by an overview of state-of-the-art phase-change nanophotonics in free-space and integrated photonic platforms.

Chapter 3 discusses the overall fabrication procedures and the custom-built optical measurement setups which are used to implement and test most of the nanophotonic devices in this thesis. The nanophotonic devices are broadly classified into two parts: Free-space photonic devices, such as nanowires or metasurfaces, and integrated photonic circuits. Each section is described separately to describe distinct experimental methodologies for each platform.

Chapter 4 presents the first prototype of polarization-selective reconfigurabilities within hybridized-active-dielectric (HAD) nanowires. The operational principle of polarization-selective switching from hybrid GST/Si nanowires is discussed, along with optical and thermal simulation analysis. Full experimental demonstration of polarization-selective switching in single and multi-nanowire system is shown, along with suggestions for the use of such systems in polarization-selective in-memory computing. Quantitative evaluation of computing density is included to demonstrate the dramatically enhanced functionalities at an ultracompact scale via polarization-space. The potential of such a concept and HAD structure beyond computing applications is further demonstrated, thereby showing the first-ever presentation of using polarization with active tunability.

Chapter 5 describes active phase-change metasurfaces that extend the idea of single active nanostructure to an array of phase-change nanoelements. By designing individual nanoelements to exhibit distinct optical phase shifts, the concept of dynamic wavefront manipulation using active phase-gradient metasurfaces is demonstrated. Importantly, the investigation of metasurfaces is carried out along with a search for a new class of low-loss

PCM (Sb_2Se_3 or GeTe), thereby opening up a new pathway for enhancing optical functionalities without sacrificing efficiency. To verify these concepts, the experimental demonstration of low-loss tunable metalens is described, followed by an extensive investigation on dynamic switching capabilities of low-loss PCMs.

Chapter 6 discusses achieving wavelength-selective reconfigurabilities in integrated photonic chips. The main idea of this chapter is to transfer the new functionalities of exploring multiple degrees-of-freedom in *Chapter 4-5* into an integrated photonic platform for better scalability. To achieve this, the first model of exploiting spatial degrees-of-freedom in in-plane mode propagation with reconfigurable materials is demonstrated by using the concepts of standing-waves and coherent perfect absorption. Both experimental and simulation analyses on spatio-spectral relations implement the non-volatile wavelength-selective system by combining phase-change nanoantennas onto a standing-wave microring resonator. Further analysis of extending such spatio-spectral degrees-of-freedom in integrated photonics is provided, which raises interesting implications for maximizing computing parallelism as well as high-resolution detection or imaging.

Chapter 7 summarizes the main achievements and experimental findings in this thesis and the contributions to the field of active nanophotonics and reconfigurable materials. Furthermore, the perspectives on active multi-dimensional nanophotonic systems are included.

1.4 Key findings and new science

This thesis investigates the following hypotheses which identify the gap between active nanodevices and multi-dimensional photonic functionalities:

- First-ever demonstration of polarization-selective reconfigurabilities with hybridized-active-dielectric (HAD) nanowires that can be generalized to a wide range of active and non-linear materials.
- Experimental implementation of polarization-selectively addressable and electrically-readable matrix-vector multiplication units that surpasses the computing density of electronic counterparts by several orders of magnitude.
- First experimental demonstration of low-loss active material (Sb_2Se_3) for varifocal flat-lenses.
- Large-area electrical switching and free-space optical switching of low-loss PCM (GeTe and Sb_2Se_3) for active metasurfaces.
- First prototype of spatio-spectral reconfiguration that utilizes the concept of active coherent perfect absorption of phase-change nanoantennas.
- Wavelength-selective modulation over multiple channels on a single photonic element.
- Demonstration of utilizing spatial degrees-of-freedom in integrated photonics and the enhancement of modulation and multiplexing densities by several orders compared to other integrated multiplexers.

Furthermore, the author of the thesis has contributed to the design and demonstration of the following tools:

- Design, simulation and manufacturing of hybridized-active-dielectric nanowires.
- Optical pump-probe microscope setup with additional electrical micro-probes that can carry out spatial and spectral imaging, and electrical measurement while the optical and electrical programming can be done simultaneously.
- Free-space optical measurement setup of a varifocal meta-lens.
- Integrated pump-probe measurement setup for standing-wave transmission in a microring resonator.

1.5 Statement of originality

This thesis is the original work of the author and represents all the work and findings completed by the author throughout the course of his DPhil. The only exception to this is the fabrication of NiCr microheaters detailed in *Chapter 5*, which was performed by collaborators. However, it should be noted that this collaboration does not detract from the originality of the primary work and is intended solely to expedite experimental progress by leveraging existing expertise in the field. Any contributions made by collaborators have been appropriately acknowledged.

Chapter 2

Phase-change nanophotonics: A review

This chapter reviews the fundamentals and development of phase-change materials in the field of active nanophotonics and optoelectronics. It covers various optical platforms, from free-space optics including Mie resonators and metasurfaces to integrated photonic circuits, to encompass the state-of-the-art advances in phase-change nanophotonics.

2.1 Phase-change material for nanophotonic applications

By definition, phase-change materials (PCMs) are active materials that exhibit dynamic transitions in their crystalline structures due to time-dependent heat exchange processes.[9] These transitions result in two distinct stable states of material, allowing for active tunabilities in electrical, thermal, mechanical, or optical properties. Developed by *A. Waterman* in 1920s,[18] PCMs were initially in the form of salt hydrates undergoing a solid-to-liquid transition, while the focus has since shifted to phase-change chalcogenides, which offer non-volatile and high-contrast reconfigurabilities in electrical conductivity between their crystalline phases. Hence, over the past few decades, extensive research has

been conducted on phase-change chalcogenides as promising functional materials, spearheaded by the proliferation of rewritable optical or electronic technologies such as optical data storage[19,20] (eg, blu-ray disc) or phase-change random access memories (PC-RAM).[21] On the other hand, the field of phase-change nanophotonics has emerged, driven by breakthroughs in nanophotonic platforms such as flat optics and integrated photonic circuits. By transferring the reconfigurable functionalities of PCM onto photonic domains of sub-microns-sized structure, the field of phase-change nanophotonics has achieved a diverse range of functionalities, enabling the realization of dynamic metasurface[11] or active integrated photonic circuit.[22] Both metasurface and integrated nanophotonics incorporating PCMs have unlocked a wide array of photonic or optoelectronic applications, ranging from dynamic displays,[13,23] holograms,[24] switches,[25] solar absorber[26] to integrated photonic storage,[10,27] computing,[5] detection[28] and more.[11,29]

2.2 Switching mechanism of phase-change material

Phase-change chalcogenide is glassy material that contains at least one of following elements, such as Antimony (Sb), Germanium (Ge), Selenium (Se), Sulfur (S), or Tellurium (Te), and forms a compound with various ratios of stoichiometry. One of the most prototypical PCMs in nanophotonic platforms is Te-based alloys,[30,31] including Ge-Sb-Te (GST) or Ag-In-Sb-Te (AIST) which show stable switching dynamics as well as large electrical and optical contrast. These contrasts are attributed to formation of the so-called ‘metavalent’,[32,33] also known as resonant bonding,[34,35] in partially crystalline states and covalent bonding in amorphous states. In the case of GST, such a distinct bonding

nature is enabled in GST by the umbrella-flip of Ge atoms between tetrahedral and octahedral coordination.[36,37]

Phase-transition dynamics

The reversible phase transition in PCM is enabled by melt-quenching methods,[9] which involve two different time-dependent thermal excitation pulses, as shown in Figure 2.1. These energy pulses can be delivered through thermal, electrical or optical means and result in rapid amorphization and crystallization kinetics in PCMs. By heating the material above the glass transition temperature (T_g) using a long excitation pulse, a partially crystalline state can be formed (*SET*). Conversely, annealing the PCM above its melting point (T_m) and then rapidly cooling it at a rate exceeding 10^9 Ks^{-1} leads to the PCM returning to a disordered amorphous state (*RESET*). Mostly, the amorphous state demonstrates high electrical resistance and a low optical constant, while the crystalline state exhibits low electrical resistance and a high optical constant. These processes, in general, occur in the order of nanosecond time scales.

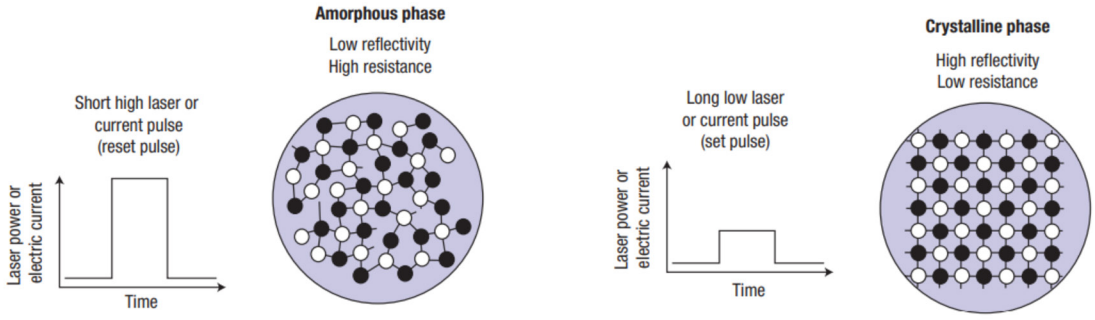


Figure 2.1 Schematics of melt-quenching process of PCMs. Melt quenching process requires a high-intensity energy pulse with rapidly cooling rate higher than 10^9 Ks^{-1} to form a state of disorder (amorphous). To crystallize it back, a long-duration energy pulse is needed that heat the material above the crystallization temperature. Adapted with permission from Ref. [9].

The mechanisms of these phase transitions can be broadly classified into two types, both of which involve melt-quenching processes as stated above. These two types are known as nucleation-dominated dynamics and growth-dominated dynamics, which are dictated by the composition of the phase change material (PCM). For instance, GST is a nucleation-dominated PCM, while AIST is a growth-dominated PCM,[30] as depicted in Figure 2.2. In the case of nucleation-dominated GST, small islands of crystalline nuclei are formed randomly during crystallization, and these nuclei continue to grow until they merge completely, resulting in complete crystallization. On the other hand, growth-dominated AIST involves the formation of only few nuclei during the nucleation stage, which subsequently grow until the entire material transforms into one crystal. This growth-dominated process is observed to be relatively slower compared to the nucleation-dominated mechanism. Nevertheless, both nucleation- and growth-dominated PCMs *SET* and *RESET* their material states in response to appropriate heat stimuli.

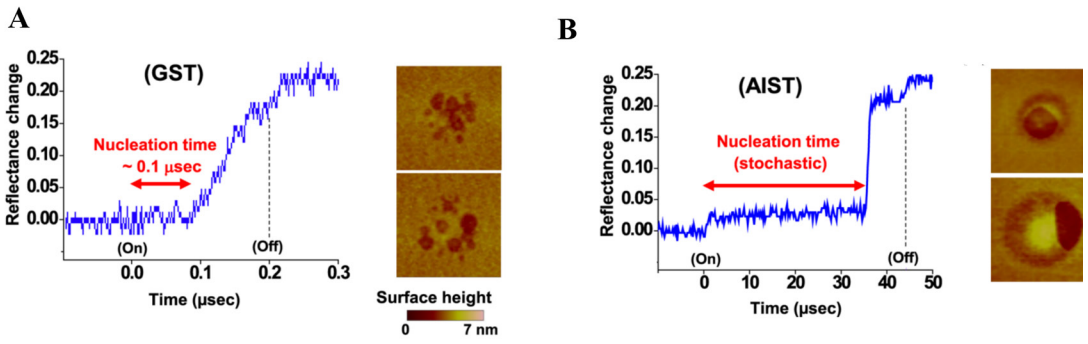


Figure 2.2 Phase-transition dynamics of (**A**) nucleation-dominated GST and (**B**) growth-dominated AIST during the pulse-irradiated crystallization process. Adapted with permission from Ref. [30].

Thermal switching using heaters

While the crystallization process can be achieved through a simple annealing method using a hot plate, achieving reversible switching necessitates precise control of thermal pulses at a resolution of tens of nanoseconds. This can be accomplished using an indirect microheater, which permits electrical modulation of pulse parameters to facilitate the *SET* and *RESET* processes. Figure 2.3 illustrates that the entire active region of the microheater is heated through Ohmic heating, and the transient temperature during each process is elevated above T_g or T_m to facilitate the reversible processes of phase-change thin film,[38] nanostrip[39] and metasurfaces.[40] The utilization of a microheater is particularly advantageous in nanophotonic applications because of its ability to switch a large volume of PCMs. This large volume of switching directly translates to significant improvement in modulation depth within the optical domain, which is beneficial for integrated photonic

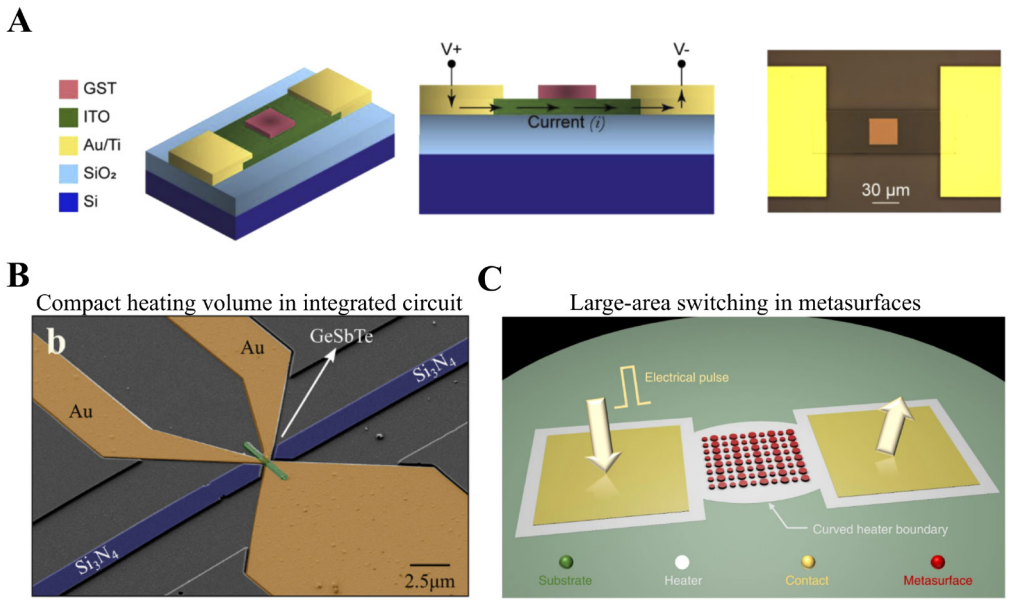


Figure 2.3 Designs of indirect electrical switching using microheaters. (**A**) GST thin film is switched by electrically-driven ITO microheaters. Metallic (Au or Pt) heaters are used to switch (**B**) the confined volume of GST strip or (**C**) a large area of GSST metasurface. Adapted with permission from Ref. [38-40].

circuits.[39] Moreover, the capability for large-area switching is promising for applications such as displays or holograms that employ thin-film or metasurface technologies. However, a tradeoff exists between switching area and reversibility, because the uniformity of heat dissipation and temperature profile degrades when using larger micro-heaters. As a result, the state-of-the-art microheaters used for large area metasurface switching impose a limitation on the number of reversible cycles, keeping it below 50-70 times.[40,41]

Direct electrical switching

Analogous to the Ohmic heating employed for indirect microheaters, pulse-modulated Joule heating can take place directly within the PCM channel in the electrical domain. Figure 2.4 presents a typical I/V curve that PCM between two electrodes,[9] generally forming a mushroom cell,[42] undergoes electrical threshold switching. Initially, when the material is in the amorphous state, applying a small voltage leads to a high linear resistance. However, surpassing a certain threshold voltage triggers a resistance switch due to the resistive heating over T_g. Subsequently, the resistance decreases by several orders of magnitude, leading to the formation of a conductive path and an increase in current. This surge in conductivity results Joule heating, which dissipates the heat throughout the conduction channel. The switching volume is determined by that of conductive filament formed by threshold switching, which is therefore highly confined to below sub-100 nm for high-endurance operations up to 10^9 cycles.[43]

Moreover, the restrained volume of electrical switching has facilitated the development of high-resolution and reconfigurable displays by leveraging the capabilities of raster

scanning nanoscale tips in a conductive atomic force microscopy (C-AFM) setup.[13] In this case, the PCM layer is embedded between the conductive bottom substrate (e.g., Pt) and top passivation layer (e.g., indium tin oxide (ITO)). Joule heating is possible with contact-mode C-AFM functioning by applying voltage between two conducting layers. Through the precise localization of electrical pulses using nanoscale conductive tips and finely scanning their positions, a pixelated threshold switching procedure has been achieved on a sub-micron scale.

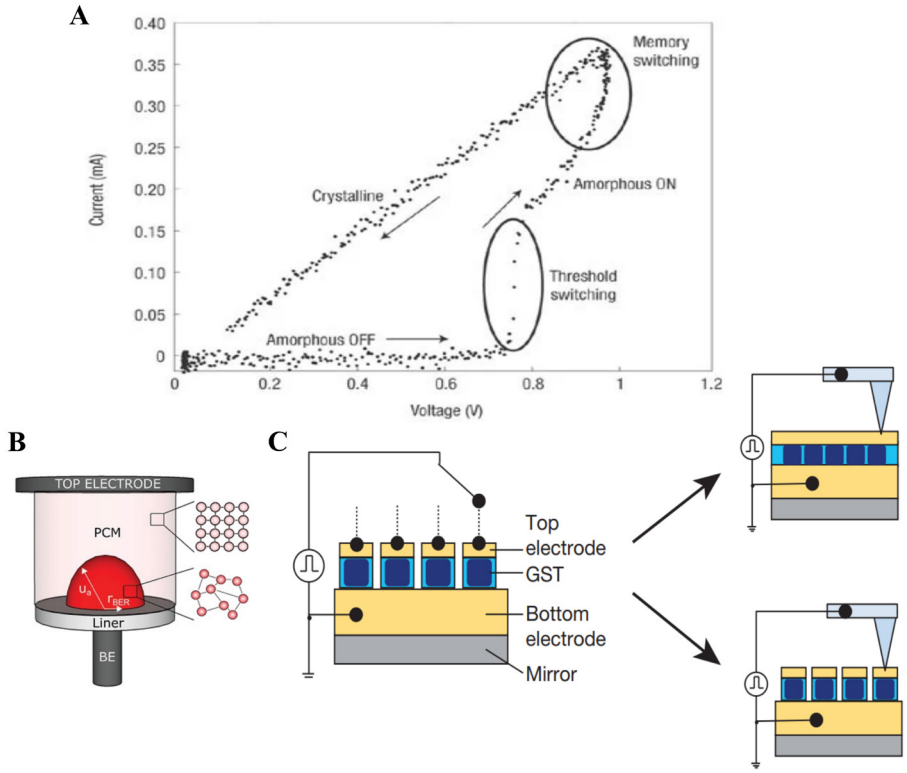


Figure 2.4 Demonstrations of electrical threshold switching. (**A**) I/V characteristic curve of GST during crystallization of a threshold switching that exploits GST as a conductive channel in (**B**) a mushroom cell and (**C**) pixelated forms using C-AFM tips. Adapted with permission from Ref [9], [42] and [13].

Optical switching via electromagnetic heat transfer

Similar to how electrical pulses induce Joule heating, optical pulses cause electromagnetic heating in the laser illumination region. As light gets attenuated by the material with its

imaginary part of the dielectric constant, the optically absorbed energy is dissipated as heat.[44] Such heat dissipation, whose peak temperature and cooling rates are modulated by optical pulse parameters, can be generated by a free-space optical beam and reversibly switch PCMs. This technique has proven to be reliable and has reached a high level of maturity in the development of rewritable optical discs such as CDs or DVDs (Figure 2.5A),[9] where the state of the material is stored using free-space illumination via a high numerical-aperture (*NA*) objective lens. The size of the switching volume is typically restricted by optical diffraction-limit, and it determines the optical storage density. Therefore, efforts have been made to shift the operating wavelength to shorter wavelengths or design geometrical resonant structures that confine the electric field tightly within the PCM cavity. These structures often take the form of metal-dielectric-metal Fabry-Perot cavities, with the PCM acting as the dielectric.[14] This design not only enhances the optical absorption to facilitate phase transitions but also minimizes the switching volume to improve storage densities. As a result, the application of such an approach has been extended to plasmonic[45] and Mie-resonant antennas,[46] and metasurfaces[11] for beam steering,[47] lensing,[48] perfect absorption,[49] and holographic[50] elements. Additionally, by integrating free-space lasers with high-resolution raster scanning stages, pixelated optical switching approaches have been developed (Figure 2.5B).[14]

Optical switching is also achieved in integrated photonic circuits, where the optical beam is injected through guided-mode light in a dielectric waveguide (Figure 2.5C).[22] By placing a thin layer of PCM onto the dielectric waveguide and sending optical pulses through the waveguide,[10] the evanescently-coupled light induces electromagnetic heating

within the PCM layer, enabling all-optical integrated phase-change tunability. This technique has proven to be robust, leading to the realization of large-scale phase-change integrated photonic circuits, which will be discussed in detail in *Chapter 2.3.2*. Although the size of most switching volumes is typically in the tens of microns, coupling the PCM with plasmonic nanogaps can significantly reduce the size to below 100 nm scale.

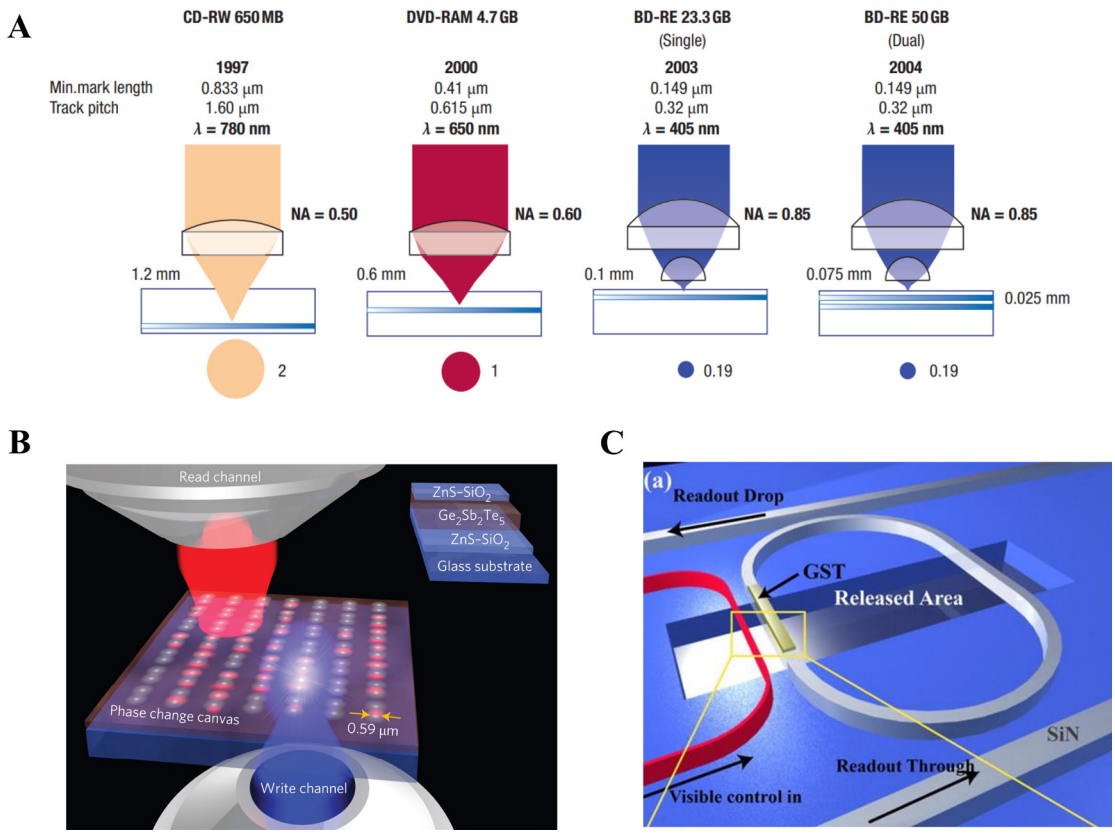


Figure 2.5 Schematic demonstrations of optically switching PCMs. (**A**) Optically rewritable discs (CD or DVDs). (**B**) Optically rewritable and readable phase-change metasurface using a raster scanning free-space laser. (**C**) All-optical integrated photonic circuits with PCM depositing onto a dielectric waveguide. Adapted with permission from Ref. [9], [14] and [22].

Femtosecond switching

The switching mechanism of PCM is still a topic of debate, particularly in the femtosecond regime, where melt-quenching is no longer applicable. Unlike electromagnetic heating,

the utilization of trained femtosecond laser pulses offers alternative pathways for switching PCMs through the destabilization of resonant bonds, without the need to reach T_m.[51,52] Therefore, the femtosecond-switching method is a non-thermal phase-transition approach that allows a homogeneous deviation from equilibrium carrier distribution, hence lattice destabilization in advance of thermal relaxation.[53] This process was also experimentally demonstrated by observing amorphization processes without any melting process, which correlates to the femtosecond laser pulse having a shorter time duration than thermal diffusion.[54] While the mechanism of photo-assisted resonant bond dissociation remains a subject of debate, sub-nanosecond switching operations offer an ultrafast reconfigurable system that holds potential benefits for various active or non-linear nanophotonic systems.

2.3 Optical properties of phase-change material

Lossy phase-change chalcogenides, $Ge_2Sb_2Te_5$ (GST)

GST is recognized as the prototypical PCM for nanophotonic applications due to the large electrical (Figure 2.4A)[9] and optical contrast (Figure 2.6A)[22] between its two stable nonvolatile states; amorphous and face-centered cubit (FCC) crystalline phases. In particular, within the telecommunication range (1500 – 1600 nm), GST exhibits a significant contrast in both the real (n) and imaginary (k) parts of the refractive index, favoring the applications of optical communication or programming. It is worth noting that the GST is found to be lossy, especially in its crystalline state ($k \sim 1$), which is however useful for amplitude modulated memory or computing applications (Figure 2.6B).[55] Despite the high material loss experienced by both states of GST in the visible

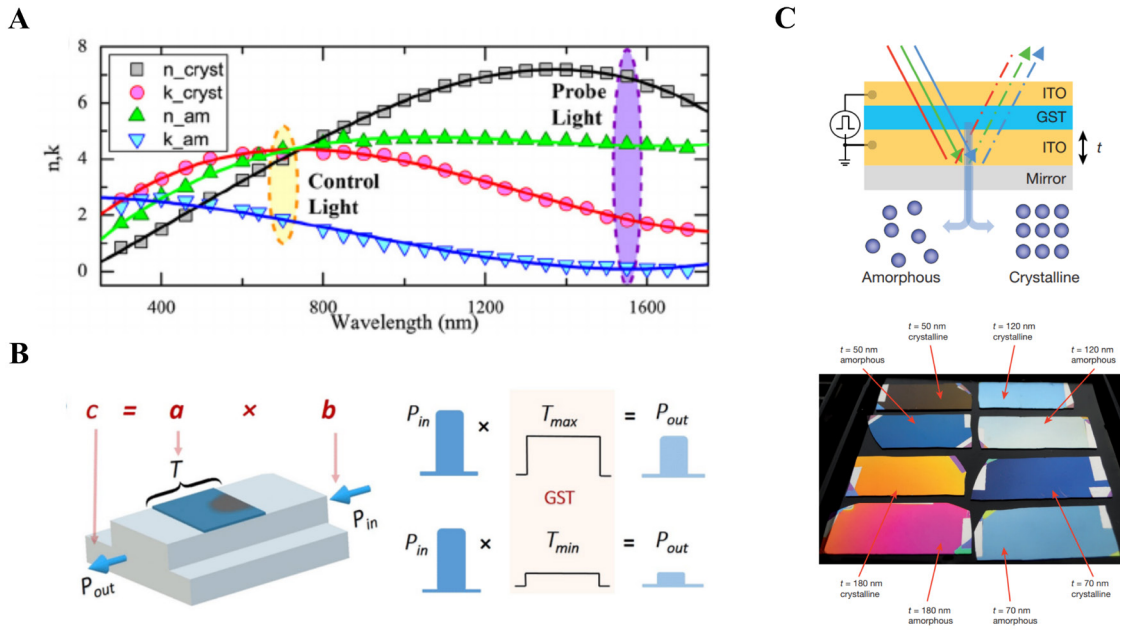


Figure 2.6 (**A**) Refractive index (n, k) of GST in amorphous and crystalline states, highlighting the significant difference in k within the telecommunication range (1500 – 1600 nm). (**B**) Schematic illustration showcasing the use of loss-tunable PCM for amplitude modulation or computing operations. (**C**) Stacked hybrid layers of PCM-dielectric, utilized to induce spectral shifts for display applications. Adapted with permission from Ref. [22], [55] and [13].

wavelength range, the integration of a thin layer of GST within hybrid dielectric stacks offers the ability to achieve tunable spectral responses without significantly degrading efficiency (Figure 2.6C).[13] As a result, a tunable display can be accomplished. The high material loss facilitates the incorporation of an ultrathin layer of GST (~7 nm), thereby enabling the development of a power-efficient and reconfigurable framework. Importantly, the GST exhibits dual electrical-optical functionality, meaning that the state of material simultaneously affects both electrical conductivity and optical constant. Consequently, optoelectronic 'mixed-mode' tunability between the electrical and optical domains can be achieved using a C-AFM tip[13] or a plasmonically-enhanced nanogap structure.[15] However, increasing the thickness of GST renders the entire system opaque, particularly in the

visible wavelength range, which makes it unsuitable for achieving highly efficient displays or measurfaces.

Low-loss phase-change materials

To mitigate unwanted insertion loss, researchers have explored a new class of PCMs that exhibit high optical contrast (Δn) and negligible loss (k). These materials, known as low-loss PCMs, include materials such as Sb_2S_3,[56,57] Sb_2Se_3,[58,59] $GeSe_3$,[60] or GSST.[40,48,61] As illustrated in Figure 2.7A,[59] Sb_2Se_3 or Sb_2S_3 display a real refractive index comparable to Si ($n \sim 3.8$), but with a significant contrast ($\Delta n \sim 1$) in the telecommunication range (1500 - 1600 nm) where the loss approaches zero. This suggests the potential of low-loss PCMs as a next-generation replacement for Si in integrated photonics, as demonstrated by the development of low-loss on-chip phase shifters (Figure 2.7C).[58] By precisely controlling the real part of optical constant only, the optical path length of nanophotonic system can be modulated, thus obtaining the tunable functionality of optical trimming, routing, or spectral shifting. This facilitates the realization of energy-efficient programmable photonic circuits with zero static energy and insertion loss. Furthermore, the low-loss tunability of these materials unlocks opportunities for highly efficient dynamic displays and metasurfaces (Figure 2.7B).[40] Not only do they exhibit minimal loss, but their high dielectric constant also allows for the confinement of visible to near-infrared (NIR) light within nanostructures, opening up new possibilities for active metasurfaces,[48] including metalenses, beam steerers, or metaholograms. While some research on active displays has been conducted on utilizing low-loss PCMs for color pixels, achieving a full RGB color space is hindered by non-trivial loss in short wavelengths.[60] As a result, low-loss phase-

change metasurfaces predominantly operate in the NIR[40,58] or mid-infrared (MIR)[48] wavelengths.

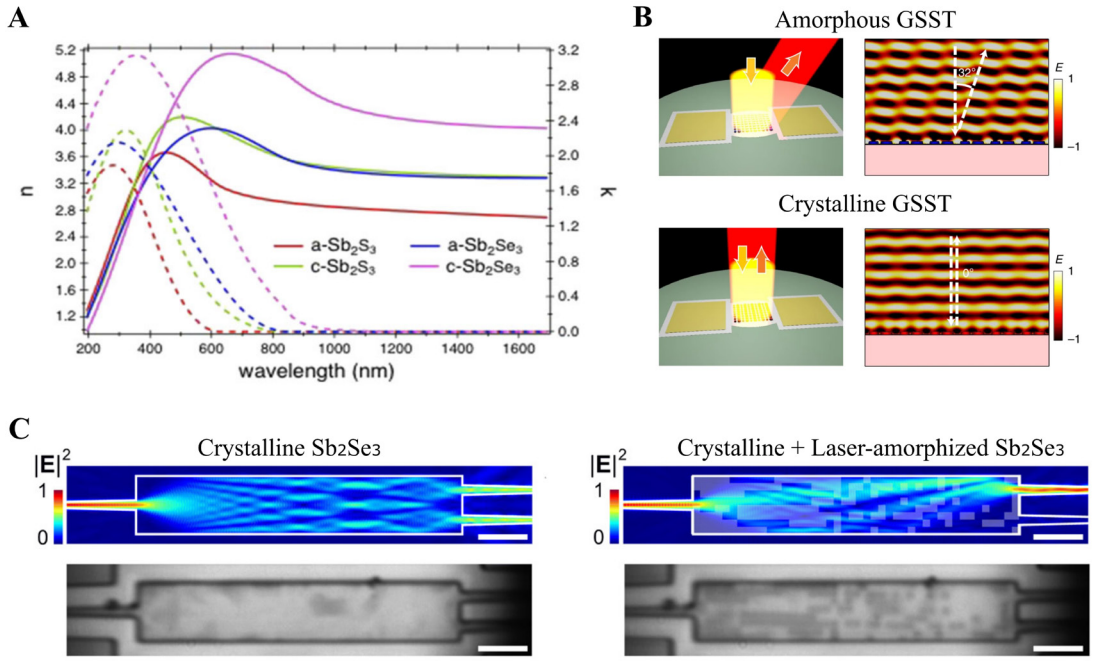


Figure 2.7 Demonstration of low-loss PCM. (**A**) Refractive index of Sb_2S_3 and Sb_2Se_3. Tunable optical contrast (Δn) with minimal loss (k) is observed in NIR wavelength. (**B**) Dynamic metasruface beam-steerer with using low-loss GSST on microheaters. (**C**) Reconfigurable Si multimode interferometer (MMI) with Sb_2Se_3 layer to tune the optical phase and routing. Sb_2Se_3 is switched by free-space laser in visible wavelength. Operating wavelength for **B-C** is NIR. Adapted with permission from Ref. [59], [40] and [58].

The low optical loss in these materials is attributed to their wide bandgap, which reduces free carrier absorption (FCA) in the NIR-MIR region. For instance, GSST achieves low loss through isoelectronic substitution of Te with lighter atoms like Se, effectively increasing the bandgap and minimizing FCA.[61] However, the reduction in the number of free carriers comes at the cost of a concurrent decrease in electrical conductivity, impeding direct electrical switching. Similarly, in the optical domain, the low-loss nature reduces absorption and hinders optical reconfigurability in a lossless spectral window. Therefore,

the reconfigurability of low-loss PCMs is achieved through indirect heating using micro-heaters[62] or by utilizing light with a wavelength higher than the bandgap of material. In the case of Sb_2Se_3 and Sb_2S_3, a visible red laser was employed to optically switch the material.[57] This is regarded as a crucial challenge of all-photonic low-loss phase-change systems that both absorptive and non-absorptive light need to be applied to achieve a fully reconfigurable system.

2.4 Out-of-plane nanophotonic resonances with phase-change material

Alongside significant progress in exploring various optical properties and expanding the functionalities of PCMs at the material level, there have been endeavors to integrate these functionalities into suitable nanophotonic resonant structures. These nanophotonic resonances enhance light-matter interaction within the PCM architectures, which therefore maximizes the reconfigurable optical responses.[16] In most cases, the PCM acts as a dielectric component within the resonator system, enabling strong confinement and oscillation of the electric-field while encountering distinct optical properties corresponding to the material states of the PCMs. As an illustrative example, Fabry-Perot type resonances can be realized through a reflector-PCM system. In this configuration, the cavity resonance is primarily affected by the thickness of the PCM layer, which acts as a tunable dielectric.[14,63] Despite the simplicity of configuration, such designs are highly effective in inducing tunable out-of-plane (i.e. free-space propagation) photonic modes, realizing reconfigurable bandpass filter[64] or displays.[13]

To further intensify the light-PCM interaction and resonance functionalities,

subwavelength-sized nanostructures of the PCM are explored. This enables the attainment of a more confined electric field or extinction cross-section through plasmonic,[47] photonic[46] or phonon-polariton[65] resonances. While PCM is widely used as high-index dielectrics in metal-dielectric plasmonic configurations, some metallic PCMs, such as In_3SbTe_2, can behave as tunable plasmonic metal themselves.[66] On the other hand, the PCM can be embedded within an all-dielectric system to minimize metallic losses,[67] taking advantage of Mie resonances that occur when the size of nanostructures is commensurate with subwavelength. These photonic resonances can be generated and reconfigured by hybrid PCM-dielectrics or high-index, low-loss PCMs using different geometries such as nanowires,[68] nanopillars,[60] or nanodisks.[69] The review of Mie photonic resonances, their application in PCMs, and the arrangement of multiple phase-change Mie resonators into an array to form a metasurface are explored in the following sections.

2.4.1 Tunable dielectric nanoantennas

Dielectric Mie resonances

The comprehensive nature of Mie theory[70,71] allows for its application to a wide range of materials, including dielectrics, metals, semiconductors, and magnetic materials, covering a broad spectrum of frequencies and sizes. In fact, an early illustration of Mie theory was the observation of changes in the color of colloidal solutions containing gold nanoparticles, which were attributed to variations in their size distribution.[72] Accordingly, Figure 2.8A *(left)* shows the strong scattering resonances of both metallic and dielectric nanospheres as a function of the size parameter (q), where q is defined as $q = 2\pi R/\lambda$, with R representing the sphere's radius.[73] While metallic nanospheres exhibit electric-dipole or quadrupole

responses induced by surface plasmon resonance (SPR), their magnetic behavior is negligible as the field within the sphere diminishes. On the other hand, it is remarkable that non-magnetic dielectric nanospheres generate a magnetic dipole through a circulating electric field that induces a magnetic moment at the center.[74] Such coexistence of strong

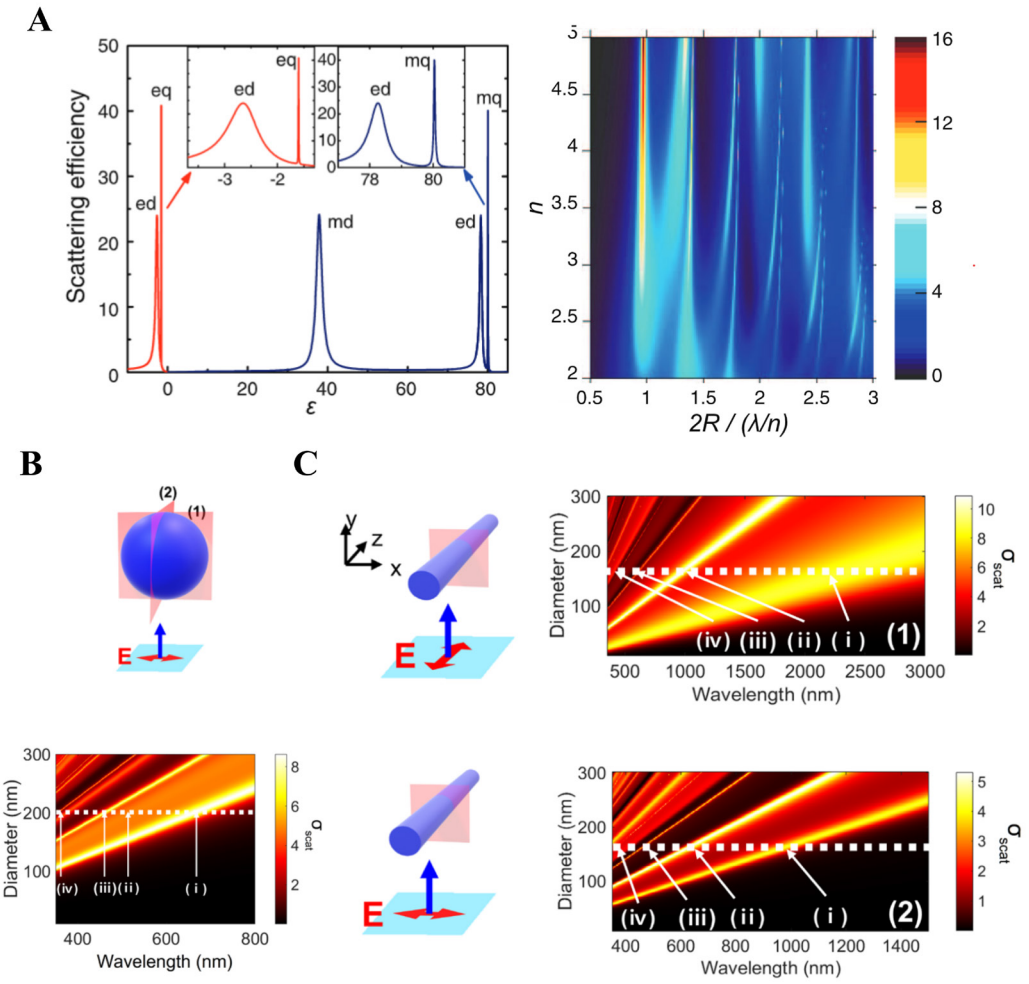


Figure 2.8 Scattering behavior of dielectric Mie resonators. (**A**) (*left*) Scattering efficiency as a function of dielectric permittivity (for a lossless particle with q = 0.5) for plasmonic materials (ε < 0) and dielectric materials (ε > 0). ed, eq, md and mq refer to electric-dipole, electric-quadrupole and magnetic dipole, and magnetic quadrupole, respectively. (*right*) Scattering efficiency of a lossless dielectric particle (color scale shown on the right) as a function of refractive index n and size parameter ($2R/(\lambda/n)$). Scattering cross sections of (**B**) sphere and (**C**) infinite cylinder with varying diameters. For cylinder, both incident parallel and perpendicular polarizations to the cylinder axis are considered. The permittivity of a sphere and a cylinder is 10 and 20, respectively. Adapted with permission from Ref. [73] and [75].

electric and magnetic responses, along with their interferences, introduces entirely new capabilities for manipulating the electromagnetic properties of light. Additionally, the low loss and high permittivity nature of dielectric materials make them a more favorable choice compared to metals.

As illustrated in Figure 2.8A (*right*), the resonance of lossless dielectric sphere relies on its refractive index (n) and all multipole responses become more pronounced as high-index ($n > 2$) further increases. Also, the spectral positions are dictated by the relative ratio of effective wavelength (λ/n) to the size ($2R$) of the nanosphere. This fundamental rule enables the possibility of passive tunability of spectral peaks by adjusting the size of the nanosphere. The scattering cross-sections of both nanosphere and nanocylinder exhibit a strong dependence on their respective diameters (Figure 2.8B-C), while these two fundamental analytical models, namely the sphere and infinite cylinder, have been widely utilized to elucidate the optical characteristics exhibited by a broad range of nanostructures.[75] It is important to highlight that unlike spheres, cylinders with diameters significantly smaller than the wavelength exhibit polarization-selective responses, where the electric-dipole resonance from the perpendicular response becomes negligible.[76] This polarization-selectivity, when combined with the reconfigurability of PCMs, will be extensively discussed in *Chapter 4*.

Tunable Mie resonances using PCMs

Figure 2.8A raises the interesting implications that active tunability of refractive index (n) in dielectric resonators can overcome the limitations of passive manipulation of Mie resonances. By replacing passive dielectrics with low-loss, high-index PCMs[40] or in

hybridized-dielectric form,[77] tunable Mie resonances can be achieved. Notably, PCM-based Mie resonances also attain multipolar contributions, as illustrated in Figure 2.9A, showcasing electric and magnetic dipoles within GSST nanowires that can be tuned by their crystalline states.[68] Similar forms of resonance are observed across an extensive range of geometries, such as nanodisk, nanopillar, or nanowires, and PCMs, including GST,[67] Sb_2S_3,[78] Sb_2Se_3,[79] Ge_2Se_3,[60] or GeTe.[80]

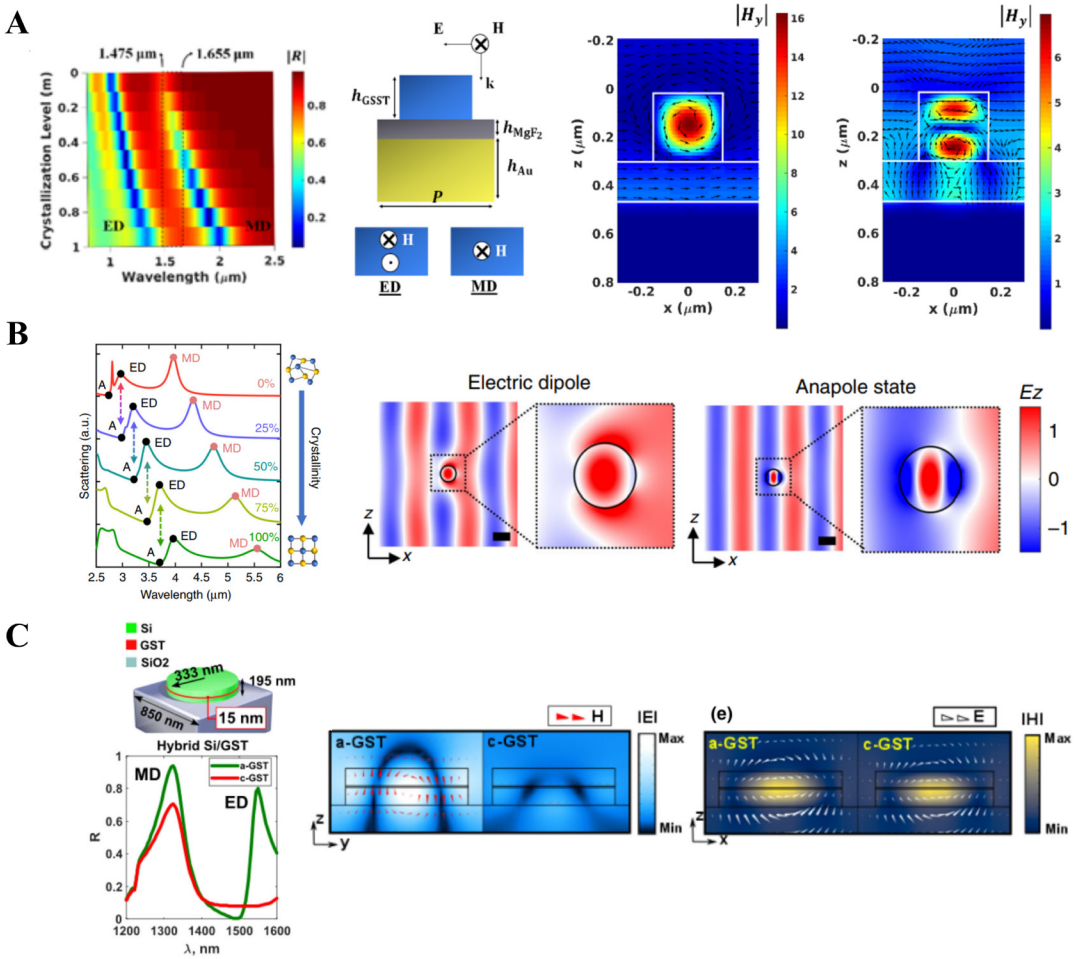


Figure 2.9 Tunable Mie resonators exploiting PCM. (**A**) Reflection and magnetic-field response of GSST nanowire that exhibits tunable electric- and magnetic-dipoles in NIR wavelengths. (**B**) Switchable scattering behavior of GST nanosphere featuring electric-dipole and anapole dark states with varying crystallinity of materials. (**C**) (*left*) Hybrid Si-GST nanodisk that exhibits mode-selective attenuation during crystallization of GST. (*middle*) Electric- and (*right*) magnetic-dipoles of amorphous and crystalline GST are illustrated. Adapted with permission from Ref. [68], [46] and [67].

Interestingly, the exploration of multipolar contributions to electromagnetic properties, unique to dielectrics rather than metals, provides new insights into fundamental physics and enables novel functionalities. In Figure 2.9B, the tunable optical mode shifts of the GST nanosphere are depicted between electric-dipole (i.e. bright) and anapole (i.e. dark) states.[46] The anapole mode refers to the superposition of co-located electric and toroidal (i.e. poloidal current on a torus of circulating magnetic field),[69] resulting in dark states due to the destructive interference of such dipoles. The dynamic control of index change in the GST sphere induces broadband mode shifting and scattering contrast. Likewise, the utilization of an array of all-dielectric Ge/GST nanodisks was shown to result in enhanced transmission and reduced reflection by achieving scattering cancellation between electric and magnetic dipoles,[81] a mechanism known as the Kerker condition.[82] Furthermore, selective modulation on multipolar modes is demonstrated using hybrid configurations of lossless dielectrics and lossy PCMs (Figure 2.9C).[67] By embedding GST into a Si nanodisk, the crystallized GST selectively attenuates electric-dipoles while leaving magnetic-dipoles almost unaffected. This underlines the potential of exploiting lossy PCMs in appropriate hybridized forms to tune dielectric Mie resonances.[77,81]

2.4.2 Active dielectric metasurfaces using phase-change material

The assembly of these switchable PCM resonators into a periodic array enables the implementation of a phase-change metasurface,[11] offering programmable manipulation of the wavefront in free-space applications. Such system facilitates the active control over various optical properties including amplitude,[49] phase,[24] polarization,[17] and frequency[47] of imprinting light.[16] For modulation of light amplitude, a metal-PCM system is

commonly employed to regulate the excitation of surface plasmon polaritons (SPPs) at the interfaces between the metal and PCM.[17,41,47,83] Figure 2.10A illustrates the demonstration of tunable perfect absorption in a GST-Ag system, where the Ag substrate functions as both a back reflector and a heater for switching the GSTs.[49] In the crystalline state of GST, near unity absorption is achieved due to enhanced dissipation inside the plasmonic cavity and destructive interference between the non-resonant reflection of Ag and the resonant scattering of GST nanoantennas. The tunable absorption can be utilized not only for amplitude modulation but also for multispectral thermal imaging at MIR wavelengths. A gap-plasmonic structure with a low-loss GST filling the dielectric gap exhibits near-perfect absorption (>90%) in the MIR range (2-5 μm) and demonstrates redshifts of up to 700 nm upon crystallization of GSTs (Figure 2.10B).[47] This tunable MIR absorption can be employed as tunable thermal imaging pixels, effectively detecting and distinguishing objects based on their thermal emission of blackbody radiation. Similarly, various designs of tunable perfect absorbers or thermal imaging were demonstrated in phase-change metasurfaces.[83-85]

The active control of optical phase is a crucial aspect of flat optics for effectively manipulating wavefront propagation through the interference between individual nanoantennas. However, plasmonic metasurfaces are not ideal for optical phase shifters due to their inherent losses. In contrast, low-loss PCMs are preferred for such applications as they allow for optical phase shifts without insertion loss, thereby enabling the realization of reconfigurable Huygens' metasurfaces.[86] Huygens' principle postulates that each point on a wavefront can be regarded as a tiny source of secondary waves,[87] under the critical assumption that these sources radiate exclusively in the forward direction.

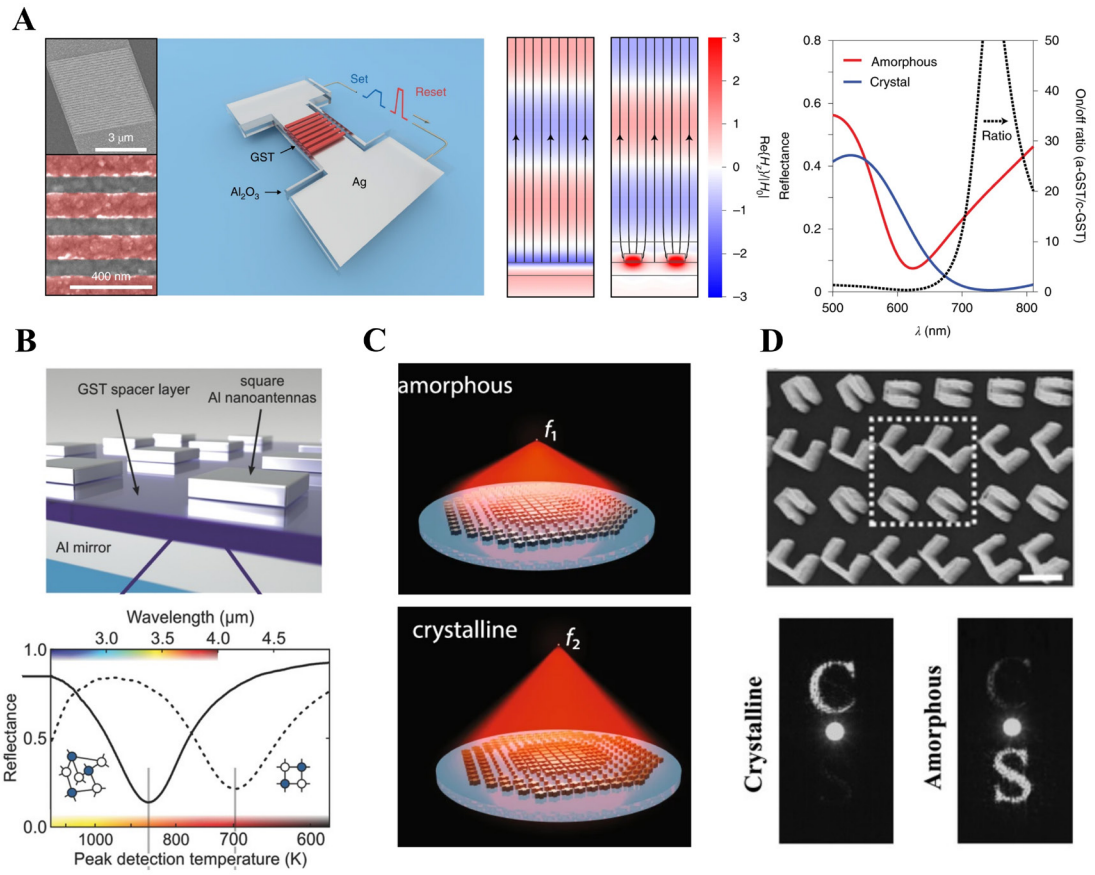


Figure 2.10 Phase-change metasurfaces for amplitude modulation and wavefront manipulation. (**A**) An assembly of GST nanowires on Ag cavity, inducing near-perfect absorption during crystallization. (*middle*) The scattered field for bare Ag substrate exhibits an out-of-phase field profile compared to the one with GST nanowires. (**B**) Al-GST-Al gap-plasmonic cavity shows tunable near-perfect absorption based on the crystallinity of GSTs, with potential applications in multi-spectral tunable thermal imaging. (**C**) Schematic representation of a low-loss GSST varifocal lens, allowing non-volatile switching of the focal point with minimal insertion loss. (**D**) Tunable meta-hologram with using U-shaped GST nanoantennas. Adapted with permission from Ref. [49], [47], [48] and [24].

Unidirectional scattering can be achieved using dielectric Mie resonators that exhibit mode overlap between electric and magnetic dipoles.[88] By adjusting the size of these dielectric resonators, the optical phase can be controlled. Through meticulous manipulation of the optical phase of each Huygens meta-atom (unit cell of the metasurface) within the range of 0 to 2π, the metasurface can accumulate position-dependent phase delays, thereby facilitating the manipulation of emerging wavefronts with high

transmission efficiency. This phase gradient profile can be tailored by varying the crystalline states of the resonators, enabling the realization of reconfigurable flat optics, encompassing dynamic metalenses (Figure 2.10C),[48,89] holograms (Figure 2.10D),[24] and beam steering.[40]

Additionally, the polarization and optical angular momentum of incoming light can be modulated in a non-volatile manner using plasmonic metasurfaces comprising Au nanoantennas on GST thin films.[17] Overall, it is important to emphasize that the reconfigurability of PCMs introduces additional degrees-of-freedom, expanding the tunability of optical properties in existing metasurface platforms that traditionally exhibit passive tunability based on spatial or spectral variations.

2.5 Integrated photonic circuits with phase-change material

While PCMs have been utilized in various nanophotonic systems that employ free-space illumination, many of these implementations impose limitations on integration capability, system scalability, and cascadability in upscaled systems. This becomes particularly challenging for applications such as advanced optical storage and multi-layered computing. Consequently, there has been a quest for new platforms that can effectively combine photonics and PCMs, leading to the development of phase-change integrated photonics. The proliferation of photonic interconnects and optoelectronic components on photonic integrated circuits (PICs), combined with the recent advancements in PCMs, has propelled significant advancements in programmable integrated photonics.[90]

2.5.1 Phase-change non-volatile memory cells

Since the first exploitation of PCM in integrated photonics through the analysis of a suspended SiN waveguide with deposited GST,[22] subsequent experimental efforts have been made to integrate GST thin films on dielectric waveguides for optical switches. A significant breakthrough was achieved by *C. Rios* in 2015,[10] wherein on-chip multilevel programming of a micron-sized patch of GST was successfully accomplished, representing a critical milestone in the development of all-optical phase-change integrated circuits (Figure 2.11A). The underlying concept is based on that in-plane mode within a dielectric waveguide experiences lossy GST attenuation through evanescent coupling. The tunable crystalline state of GST and the disparity between probe and pump wavelengths allow for real-time, non-volatile modulation of the phase and amplitude of guided mode transmission. This switching capability was then combined with other advanced integrated

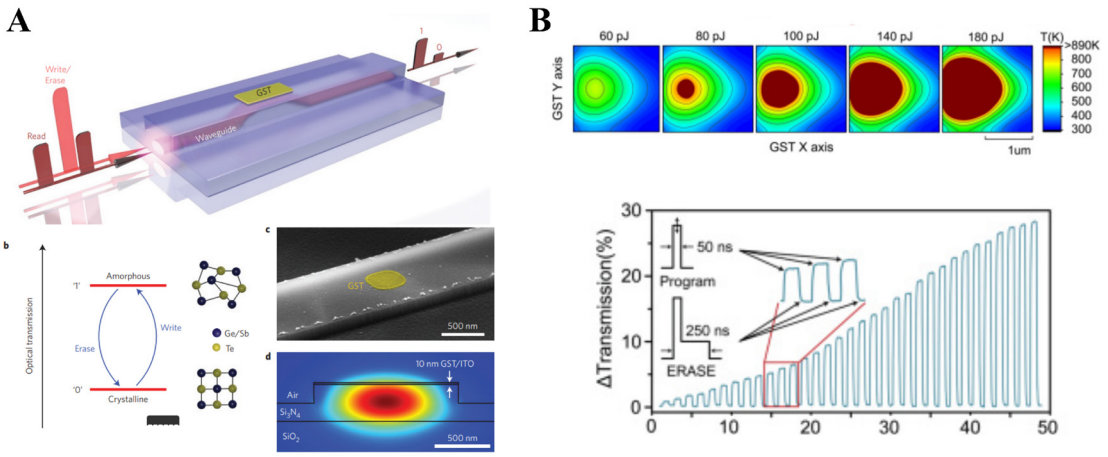


Figure 2.11 Phase-change integrated photonic memories. (**A**) A micro-strip of GST deposited on a SiN waveguide enables evanescent coupling between GST and the guided modes, resulting in distinct transmission attenuation based on the crystalline states of the GST. The device utilizes different wavelengths of pump and probe beams for simultaneous programming and optical response monitoring. (**B**) Reliable multilevel switching is achieved for up to 5-bit photonic memories using precisely controlled a single, double-step pulse, where pulse width modulation allows precise control of the fraction of GST switching. Adapted from Ref. [10] and [27].

photonic components like Mach–Zehnder interferometer (MZIs),[91] crossings,[92] or microring resonators[93,94] to attain improved modulation depth or addressable resonant characteristics. It is important to highlight that the rapid, high-contrast, non-volatile, and compact reconfigurability of PCMs makes them appealing when compared to other volatile methods such as electro-,[95,96] thermo-,[97] magneto-,[98] or mechano-optical[99] tuning schemes, which necessitate static energy, long retention time, or bulky device integration. The attainment of reliable multilevel operation in PCMs plays a crucial role in the realization of high-density multinary photonic memories with high fidelity, which has therefore led to the investigation of underlying mechanisms of optical phase-switching in PCMs on a waveguide. The physical origin of multiple intermediate states in PCMs is attributed to the fractional volume of the switched crystalline region relative to the initial amorphous states.[10,15,27,55,100] Such volume of the switched domains varies as a function of the pulse parameters such as laser power or pulse duration. However, the areal distribution between the amorphous and crystalline regions continuously varies the local attenuation coefficient during pulse operation, limiting the reproducibility of phase-switching processes. In order to enhance stability and increase the number of addressable multilevels, additional optimization was carried out by manipulating the pulse conditions, which involved modifying the pulse shape or adjusting the number of pulses. As a result, a remarkable 5-bit photonic memory (34 programmable levels) was achieved using a single, double-step optical pulse within a rapid timeframe of 250 ns (Figure 2.11B).[27] This achievement naturally opens up the potential of on-chip computing by providing addressable device states with a high density of information.

2.5.2 In-memory neuromorphic computing

The ability to control the weighting coefficients of non-volatile PCM cells opens up interesting possibilities for achieving on-chip in-memory computing in the optical domain. This architectural approach resolves the Von Neumann bottleneck, which is a limitation in classic computers that require the separation of memory and central processing units.[101] Figure 2.12A illustrates a fundamental in-memory computing unit,[55] where the output transmission (*c*) is obtained by multiplying the intensity of a low-power continuous-wave (CW) probe laser (*b*) with the fraction of crystallized GST (*a*). This allows for simultaneous realization of non-volatile data storage and scalar multiplication between the optical input and the material state in a single cell. The material state is programmed by high-power optical pump pulses at different wavelengths. Then, more complex tasks, such as matrix-vector multiplications, can be performed (Figure 2.12A, *bottom*) by assembling multiple of these scalar multiplication units. Each in-memory unit (i.e. individual GST cell) is programmed with distinct pump pulses, and the outputs are combined using a beam splitter. These multiply-accumulate (MAC) operations serve as essential building blocks for various artificial learning and neuromorphic computing applications.[102] Furthermore, these integrated PCM in-memory units can operate in parallel across multiple wavelengths, significantly enhancing computing density.[5] The cascadability of devices further allow performing a variety of neuromorphic or arithmetic processing, such as logic-gate operation[103] or addition/subtraction.[92] The computing operation can also be achieved through alternative methods such as electronically-programmable indirect heaters (Figure 2.12B)[104] or plasmonically-enhanced mixed-mode (electrical-optical) architectures (Figure 2.12C).[15]

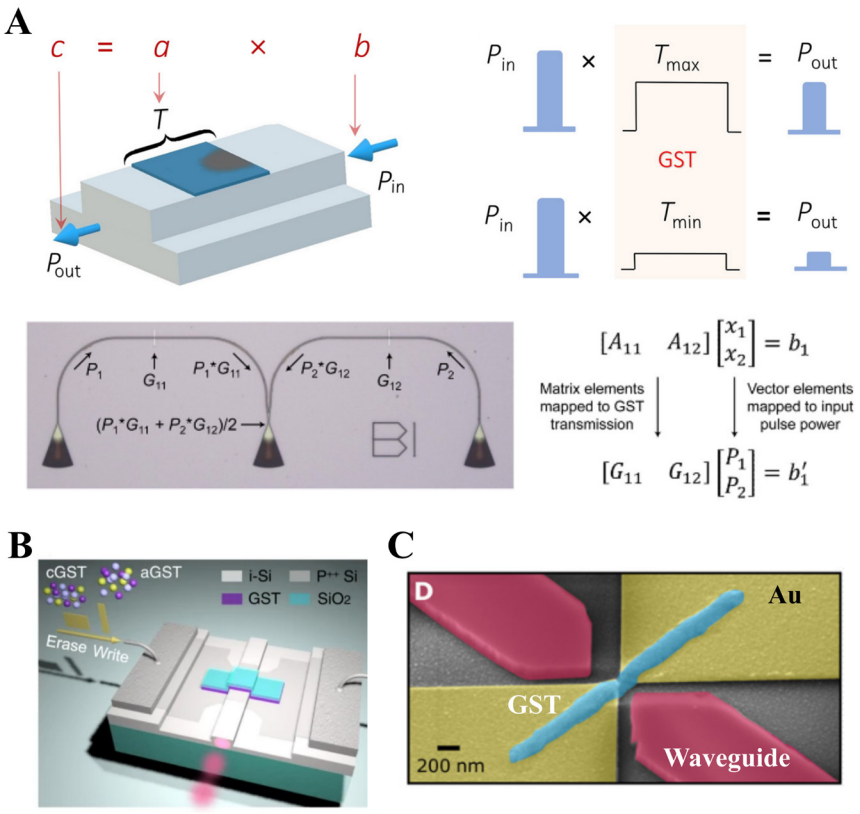


Figure 2.12 Phase-change in-memory computing unit. (**A**) All-optical in-memory computing device using GST-based nanophotonic memory cell. The low energy probe power (P_{in}, *b*) propagates through the waveguide, attenuated by the fraction of crystalline region (*T*, *a*). The crystallization is achieved by a high-power pump pulse (P_{out}, *c*). Scalar multiplication is carried out at each GST cell and matrix-vector multiplication is performed by combining the output pulses of two multiplication units using a waveguide splitter. (**B**) Microheaters or (**C**) plasmonically-enhanced nanogap enable the realization of an in-memory dot product engine using electrically programmable memory cells. Adapted with permission from Ref. [55], [104] and [15].

Significant progress has also been made in upscaling in-memory computing and MAC operations from the individual device level to chip-scale convolutional processing. Figure 2.13 illustrates the realization of all-photonic crossbar architectures,[5] inspired by electronic memristive arrays.[105] This was facilitated by the implementation of directional couplers to carry the computed information between networks and the exploitation of PCMs to program the matrix elements. Notably, the convolutional processing has been performed in a parallel fashion across multiple wavelength channels through the

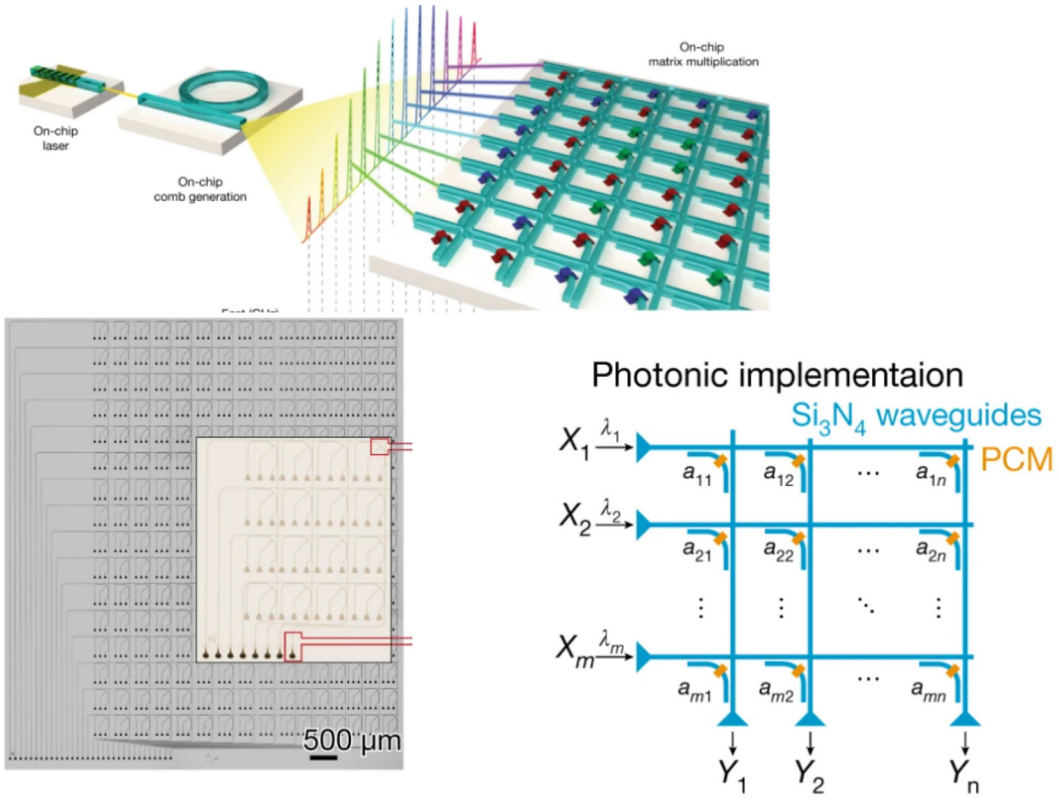


Figure 2.13 Photonic tensor core. Photonic convolutional processing is performed via parallel matrix-vector multiplications, where a vector is encoded in wavelength-multiplexed amplitude of frequency comb and matrix elements are programmed by the state of GSTs. Directional couplers at each junction ensures equal spitting of the carrier light across all matrix cells. Adapted with permission from Ref. [5].

employment of wavelength-division multiplexing (WDM), which in turn significantly increased the compute density (measured in trillions of operations per second - TOPS), surpassing those of other state-of-the-art tensor cores. Thus, this photonic-PCM-matrix exhibits promising feasibility and potential for the development of fast, efficient, and scalable all-optical computing hardware. This hardware can be seamlessly integrated at the wafer-scale level through complementary metal-oxide-semiconductor (CMOS) technology. Along with photonic convolutional processing in all-optical matrices, different types of neuromorphic systems have been constructed, such as neurosynaptic

networks based on all-optical spiking synapses[93,106] or backpropagation-free associate learning.[107] These systems combine the threshold-switching behavior of PCMs with intriguing photonic features of optical couplers or resonators. The training of these networks is carried out by the synaptic pulses, enabling the execution of complex computing tasks at high speeds and low energy.

2.6 Chapter summary and perspective

This chapter is intended to provide a comprehensive overview, spanning from fundamental concepts to state-of-the-art developments, in the field of phase-change nanophotonics across various photonic platforms such as nanoresonators, metasurfaces and photonic integrated circuits. Additionally, the progress in seeking out new material, particularly low-loss PCMs, has been discussed. Despite the proliferation of PCM nanophotonic platforms and its functional applications, the fundamental question of whether photonic degrees-of-freedom are effectively exploited by active tunability of PCMs remains unanswered.

Although the capability to increase the number of addressable states in PCM devices revolutionized the field of active nanophotonics in applications of optical storage, communication, and computing, efforts to expand these reconfigurabilities to diverse optical domains has been elusive. Recent demonstrations have showcased the exploitation of wavelength,[10] phase[108] or circular polarization[109] as tunable factors to program device states (Figure 2.14). However, most designs still necessitate the use of bulky photonic or electronic components in integrated photonics, or lack an intuitive principle for harnessing

the optical degrees-of-freedom in free-space photonics, thereby limiting their potential range of application.

It is true that exploiting photonic bandwidth has proven to be of immense significance, as evidenced by the great impact of wavelength-multiplexed photonic tensor core (see Figure 2.13) in portending a new paradigm in tunable photonic devices. Whilst such multiplexing approaches are now widely employed to expand the communication capacity, their use to enhance the programming functionality has not seen the same uptake.

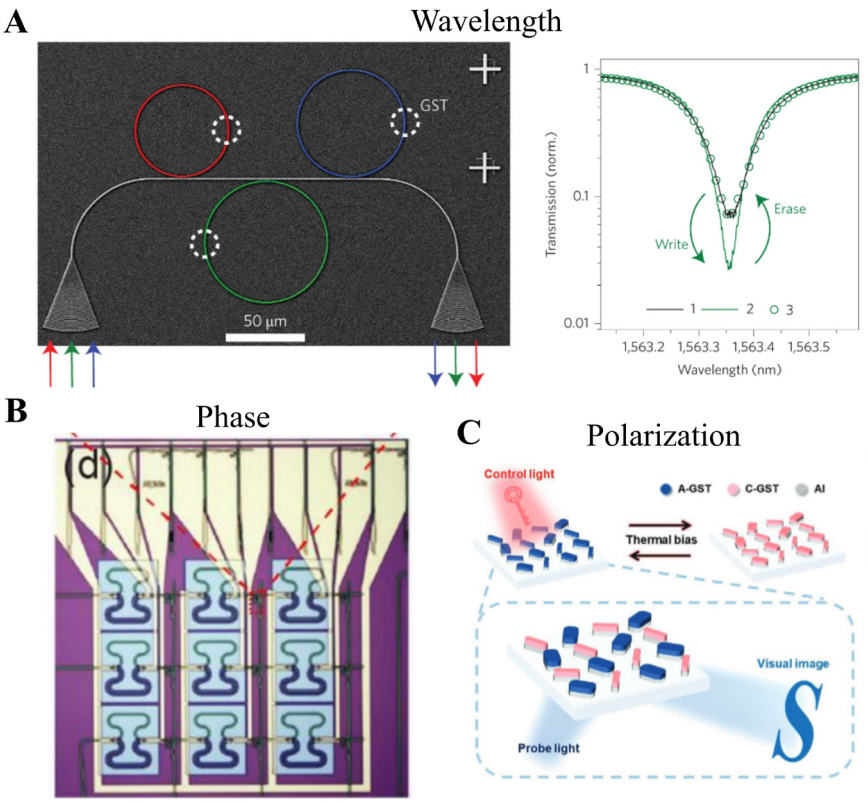


Figure 2.14 Exploiting optical degrees of freedom with the active tunability of PCMs. (**A**) Wavelength-selectively addressable photonic memory cells using GST on multiple micro-ring resonators with different radii. Distinct resonant positions are selected to program the GST over the wavelength domain (**B**) Electrically programmable thermal phase shifters are utilized to modulate the splitting ratio of MZI branches and reconfigure the states of GST phase-selectively. (**C**) Circular polarized light is sent to the Au-GST metasurface, which partially crystallizes the metasurface so that information can be encrypted in a polarization-selective manner. Adapted with permission from Ref. [10], [108], and [109].

In the light of a rapidly widening search for reconfigurable photonics and new active materials, an important conclusion can be drawn here: the realization of a conceptual and practical framework that interfaces the benefits of photonic bandwidths with the reconfigurability of active material it is a crucial challenge, an unmet need, and of timely significance in the PCM community. Therefore, it is critical to develop a core functionality that not only achieves the above-mentioned capabilities, but can also be generalized and applied to other active materials or systems, which make up the motivation of this thesis.

Chapter 3

Device fabrication and measurement setup for active nanophotonic platforms

This chapter describes an overview of fabrication procedures and experimental setups used to perform optical and electrical measurements of phase-change nanoelements on both free-space and integrated photonic platforms. Detailed fabrication or measurement techniques for each project are further outlined in detail in *Chapters 4-6*.

3.1 Device fabrication of a phase-change nanophotonic system

3.1.1 Wafer preparation

All wafers were subject to a standard cleaning process in acetone and isopropyl alcohol (IPA) with ultrasonic agitation in advance of fabrication. The wafers were dried by nitrogen gas, heated on a hotplate at 100 °C for 1 minute to remove any remaining moisture, and further treated with low-power oxygen plasma to enhance the adhesion for spin-coating the e-beam resist or depositing the phase-change layer.

3.1.2 Phase-change nanoresonators

A variety of phase-change nanostructures are presented in this thesis, including nanowires (i.e. 1D nanoresonators) or nanodisks. As shown in Figure 3.1, all these structures were fabricated by firstly defining the features with e-beam lithography (EBL, JEOL JBX-5500) and then carrying out the lift-off in N-Methyl-2-pyrrolidone (NMP) followed by the deposition of phase-change materials via RF-sputtering (Nordiko® or AJA). The dimension of nanostructure is usually 100 – 500 nm (Figure 3.2), necessitating the use of a high-resolution mode (mode 4, high-focusing lens) with a low beam current (100 pA). These patterns were written on a single layer of positive resist AR-P 6200 (CSAR 62) which is spin-coated on top of the substrate and subsequently baked at 150 °C. EBL was performed at a dose of 180 μCcm^{-1}, followed up by the development process in AR 600-546, methyl isobutyl ketone (MIBK), and IPA for 30, 15, and 15 seconds, respectively. It is worth noting that the proximity effect correction technique was employed for a dense

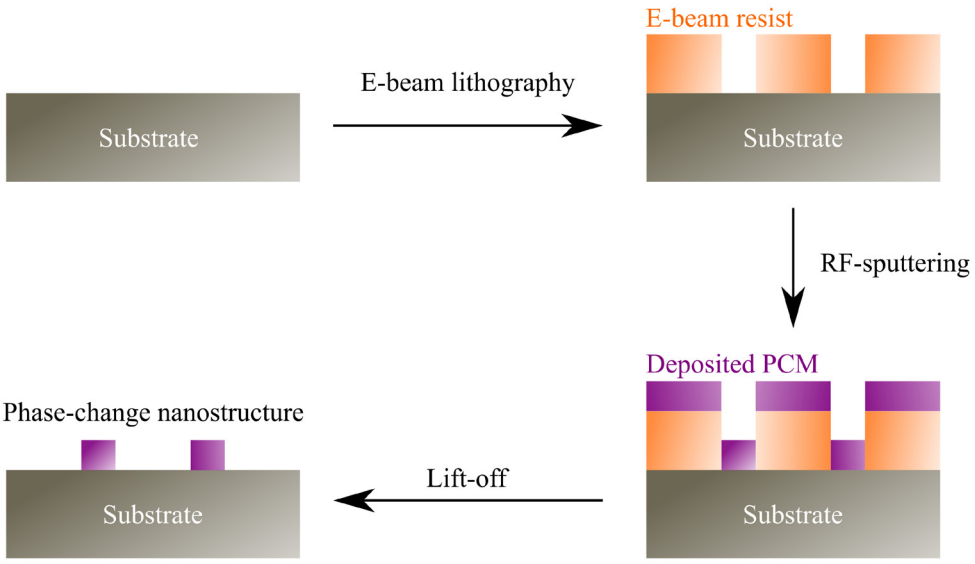


Figure 3.1 Fabrication flow chart of phase-change nanoresonators. A plain substrate is subject to e-beam lithography, sputtering and lift-off processes.

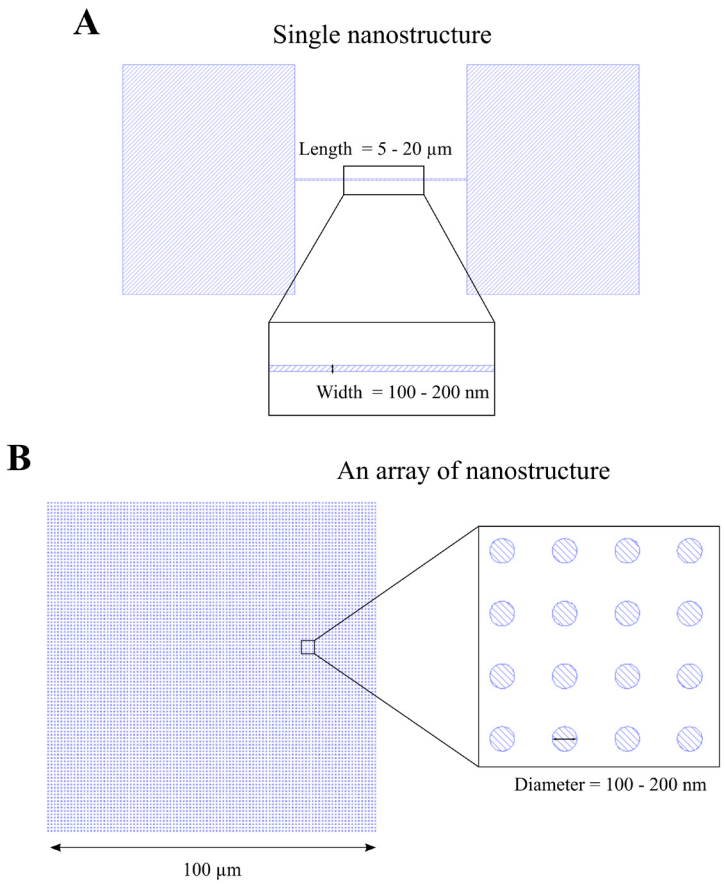


Figure 3.2 Pattern layout for e-beam lithography of (**A**) a nanowire and (**B**) an array of nanodisks.

array of nanostructures, such as metasurfaces to avoid any overexposure issue. The electron dosage of each feature was modified by applying the exposure dose distribution function, which is often a basic Gaussian function, to the base dose of the process. Such effects were carried out by Beamer software, and the metasurface with proximity effect correction exhibits enhanced pattern fidelity and high-resolution patterning (Figure 3.3). In addition, a double layer of poly(methyl-methacrylate) (PMMA) resists (495K A6 and 950K A3) was utilized to facilitate the lift-off process for the high-thickness nanostructure, with the soft-bake temperature and exposure dose raised to 180 °C and 630 μCcm^{-1}, respectively. In this case, the development was carried out in a 1:3 mixture of MIBK and

IPA for 1 minute before being rinsed with IPA. The deposition thickness of the phase-change layer was usually 50 – 250 nm with a ~10 nm of passivation layer, such as indium tin oxide (ITO) or SiO_2, while the sequential deposition of GST/Si layers (15/65 nm) was required for hybridized-active-dielectric nanowires, which will be mainly discussed in *Chapter 4*.

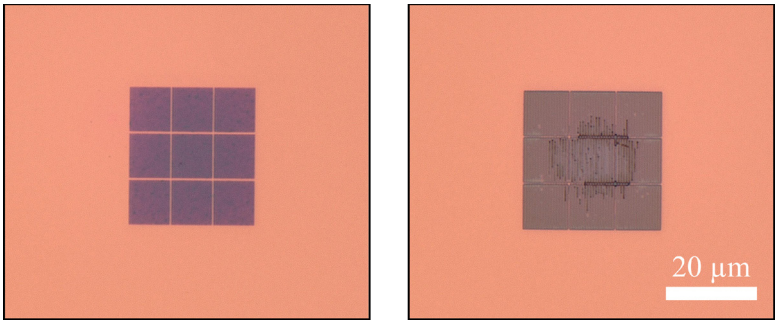


Figure 3.3 Optical microscope scan of an array of Sb_2Se_3 nanostructures (*left*) with and (*right*) without proximity effect correction technique. Sb_2Se_3 nanoresonator has a width of (*left*) ~200 nm and (*right*) ~350 nm with an interspacing separation of 300 nm.

3.1.3 Integrated nanophotonic circuits

The silicon-on-insulator (SOI) wafers with a top layer of 220 nm Si on a 3.3 µm isolation layer of SiO_2 were used for the integrated nanophotonic devices. As demonstrated in Figure 3.4A, phase-change nanophotonic circuits primarily involve the fabrication of Braggs-grating couplers and optical waveguides to enable in-plane mode coupling and propagation. To define the features of such photonic elements, a first run of EBL was performed with a positive tone resist (CSAR 62) as mentioned in *Chapter 3.1.2*, but with a slightly reduced exposure dosage of 160 μCcm^{-1}. Apodised design of grating couplers were used to minimize backscattering and unwanted interferences (Figure 3.4 B-C). The patterned substrate was then processed by reaction ion etching (RIE, Oxford Instruments) under the following conditions in the mixture gas of CHF_3 (50 sccm) and SF_6 (15 sccm)

with an RF power of 100 W. Devices were etched for 50 seconds at a depth of 110 nm, which corresponds to half of the thickness of top Si layer. The remaining resist was sequentially rinsed away by acetone and IPA. The partially-etched Si waveguides (i.e. thickness of 110 nm) with a width of 500 nm support the fundamental transverse-electric (TE) propagating mode, as demonstrated by the simulated cross-sectional view of the electric-field distribution within a Si waveguide (Figure 3.4D). Building on this waveguide design, more complex integrated components such as microring resonators and multimode interferometers (MMIs) were implemented in *Chapter 6*. In general, the phase-change layer was placed onto the Si waveguide by sequential processes of the second EBL to open the window, RF-sputtering of phase-change material, and lift-off. The fabrication of additional layers requires fine alignment during EBL processes, which is discussed in the following section (*Chapter 3.1.4*).

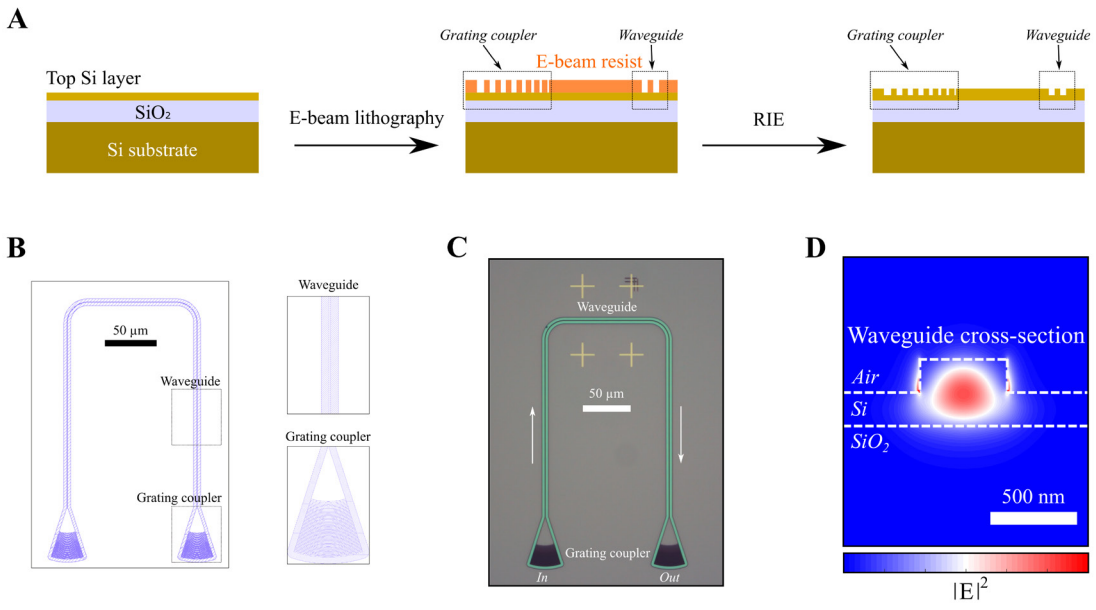


Figure 3.4 (**A**) Fabrication flow chart of integrated photonic circuits. Photonic elements such as grating couplers or dielectric waveguides are defined by e-beam lithography and RIE etching processes. (**B**) Pattern layout of a plain waveguide with input and output grating couplers (**C**) Optical microscope image of partially-etched Si waveguide with grating couplers. (**D**) Simulated cross-sectional view of the electric-field profile of a partially-etched Si waveguide.

3.1.4 Chip alignment and electrical integration

The alignment of e-beam lithography is an important step in overlaying different layers of patterns and transferring the phase-change nanostructure onto nanophotonic platforms. This alignment ensures the accurate placement of phase-change nanowires or metasurfaces within electro-optic cells or nanoantennas within integrated photonic circuits. To achieve this, the metallization of alignment reference markers was required, which involved the lift-off process followed by sequential processes of EBL and thermal evaporation of the Cr adhesion layer and Au layer with thicknesses of 5 and 75 nm, respectively. In this case, the feature sizes in the micron scale allowed for the use of low resolution-mode EBL (*mode 2*) with a beam current of 10 nA, enabling a much faster process than high resolution-mode EBL (*mode 4*, 100 pA) by a factor of 100. Furthermore, these metallized patterns not only served as alignment markers but also as electrodes in

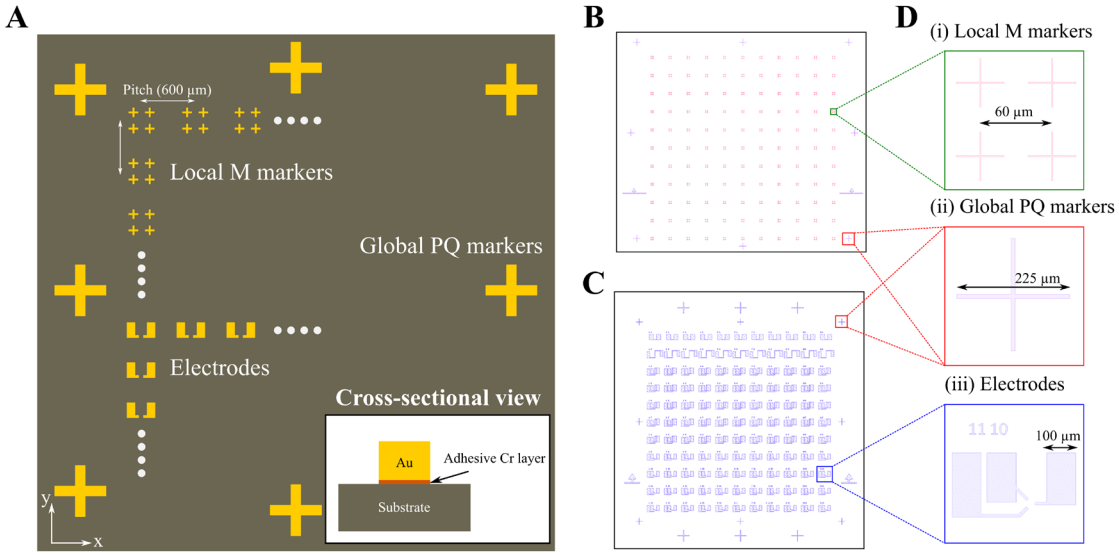


Figure 3.5 (**A**) A standard layout of Au alignment markers and electrodes. Inset shows the schematic cross-sections of alignment markers or electrodes. GDS pattern layouts are shown for (**B**) local markers and (**C**) electrodes, while global markers are included in both layouts. An enlarged layout for each element is shown in (**D**).

electro-optic cells, eliminating the need for additional EBL processes for the electrical integration of the phase-change nanophotonic system.

There were two types of alignment markers, namely global PQ markers located at the boundary of the entire chip and local M markers positioned within the boundary of each device (Figure 3.5). The PQ markers facilitated coarse alignment, which was sufficient for defining phase-change nanostructures that do not require highly precise alignment, such as positioning nanowires between two micron-sized electrodes. On the other hand, the M markers ensured high-precision alignment for geometrically complex or highly-sensitive nanostructures, such as 100 nm-sized nanoantennas at the center of microring

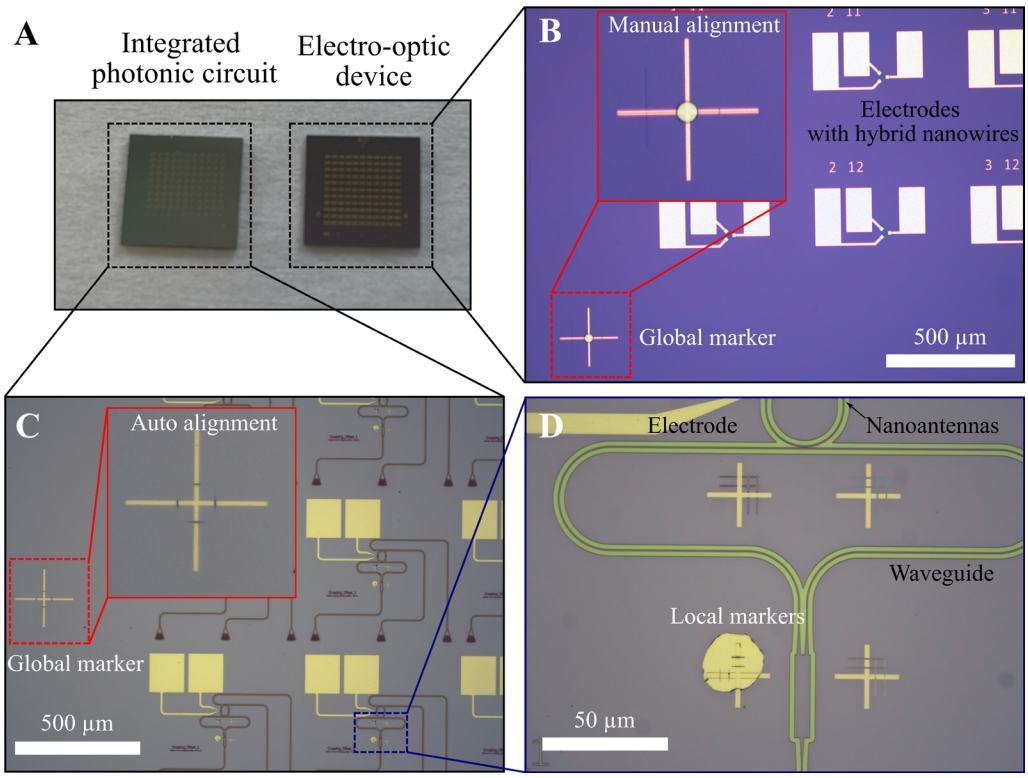


Figure 3.6 Images of the fabricated sample. (**A**) A photo and (**B-D**) OM images of integrated photonic circuits and electro-optic device. (**B**) Hybrid nanowires are placed between Au electrodes by manual alignment with global markers. (**C**) Global PQ and (**D**) local M markers are used to finely place the nanostructure on the waveguide.

waveguides. The interspacing distance between local markers (i.e. the boundary size of each device) was 600 µm for both x and y directions. Optical microscope (OM) images of fully fabricated devices, including the hybrid electro-optic cell and integrated photonic circuits, demonstrate the use of alignment markers and electrodes (Figure 3.6). The trace of e-beam scanning was clearly visible in both global and local alignment markers, where hybrid nanowires were aligned onto electrodes using PQ markers, while phase-change nanoantennas were aligned onto integrated photonic elements using local M markers. Some slight misalignment of nanowires can be observed due to the lower alignment precision; however, in most cases, the coarse alignment was sufficient for positioning the nanowire between electrodes that are larger than 100 µm in size.

3.2 Custom-built measurement setup: Switching and probing

3.2.1 Free-space optical setup

To enable optical access to the microns- or submicrons-sized phase-change structure in free-space, a customized optical microscope was constructed. The measurements were performed using an optical cage system with a diameter of 25 mm. Optical illumination was mainly provided by a broadband light-emitting diode (LED, Thorlab) for the purpose of general imaging. However, red laser diodes (Vortran Stradus, 639 nm) or infrared lasers (Santec TSL 550 or Keysight) were utilized for optical switching or reading of phase-change devices. The electrical probe system was also built to allow electrical reading and switching of the devices.

Optical imaging in the microscope

The first step towards building the optical microscope was to establish the main optical path based on Kohler illumination,[110] which ensures uniform illumination in the bright field of view, particularly in high numerical-aperture (*NA*) lens systems. This technique involves focusing the incoming light on the rear focal plane of the imaging lens, minimizing the unwanted image of the illumination source.[111]

The imaging path was firstly optimized in prior to adjusting the illumination path. As shown in Figure 3.7A, the main imaging path consisted of an infinity-corrected objective lens (20X, 0.28 *NA,* Mitutoyo) and a plano-convex tube lens with a focal length of 180 mm. The image plane was detected using a charge-coupled device (CCD) camera

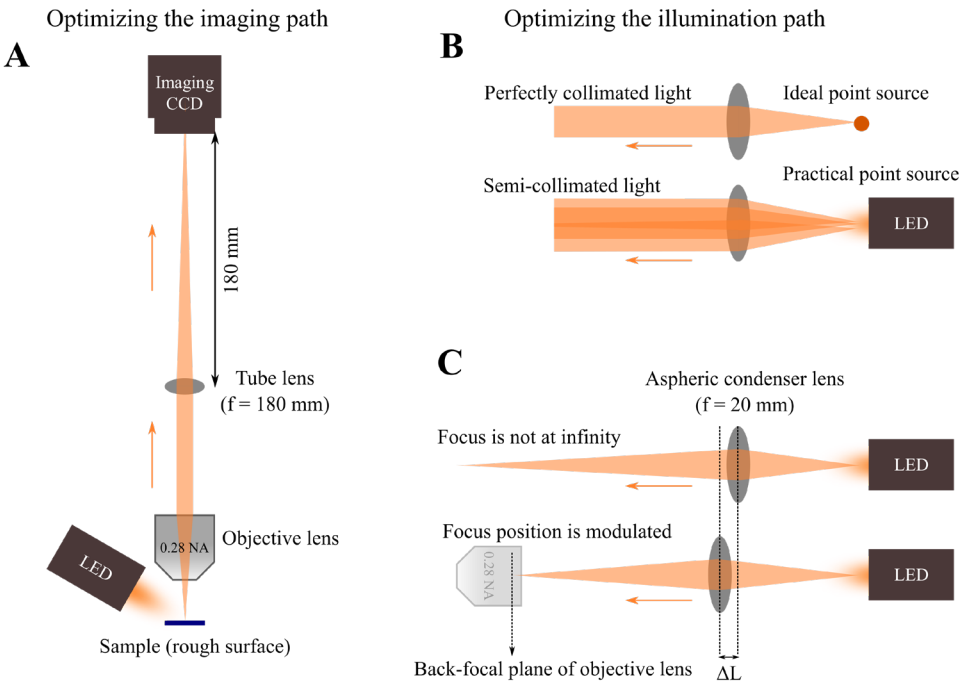


Figure 3.7 Schematic diagram of parts of custom-built optical microscope for optimizing (**A**) imaging and (**B**) illumination paths. (**A**) The LED is illuminated at an arbitrary angle to the sample with a rough surface to facilitate the scattering while position of objective lens is adjusted to its working distance. (**B**) The imperfect illumination point source induces semi-collimated light propagating through the optical lens and (**C**) the position of such a condenser lens can be fine-tuned to focus at the back focal plane of the objective lens.

(Thorlab). To achieve focus, the LED was illuminated at a specific angle onto a sample with a rough surface, such as the backside of a Si wafer, allowing for sufficient backscattering in the object plane to be detected by the objective lens. By fixing the position of the tube lens precisely 180 mm away from the imaging CCD camera, the distance between the objective lens and the sample surface was adjusted to its working distance until the sample was in focus. This optimization of the optical imaging path assumed that each scattering event on the sample surface as a secondary point source of light.

Then, an aspheric condenser lens with a focal length of 20 mm was employed to establish the Kohler illumination path. In practical cases, the LED illumination was considered an imperfect point source, resulting in imperfect collimation of light after propagating through a lens. This causes the image plane of the illumination source to be located at a finite distance rather than at infinity and can be further modulated by adjusting the position of the lens away from the object plane (Figure 3.7C). Using this concept, the aspheric condenser lens was used to focus the illumination onto a rear focal plane of objective lens, ensuring even illumination on the sample. The focal point of the illumination source (D_2) was highly sensitive to the position of the aspheric condenser lens (D_1, Figure 3.8A). When D_1 corresponds to its focal length (20 mm), D_2 was observed to be nearly infinite, while it was significantly reduced to 400 mm by slightly shifting D_1 to 21 mm. Such relations allowed for fine tuning of the position of aspheric condenser lens ($D_1 = 22 – 23.5$ mm) within a cage system with the LED mounted on it. Figure 3.8B demonstrates the optimized setup with even illumination onto the sample, while utilizing 50:50 beam splitters to guide the illumination path and an XY linear translation stage (Thorlab) to

control the sample position. An additional beam splitter divides the imaging path into two parts: one for imaging the sample with the CCD camera and the other for measuring spectral responses with a fiber-coupled spectrometer (OceanInsight). A fiber collimator was connected to couple the free-space light into the optical fiber. The actual setup, as shown in Figure 3.8C, corresponds to the schematic diagram in Figure 3.8B, with the addition of an extra illumination path for the laser. Similarly, the transmission-mode optical microscope was constructed in a horizontal pathway for the purpose of measuring the infrared metalens, which will be discussed in *Chapter 5*.

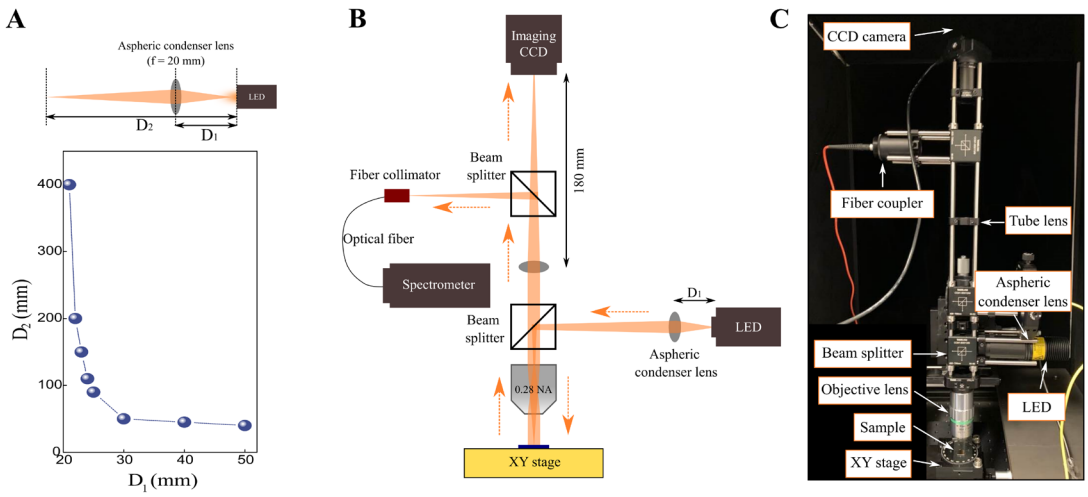


Figure 3.8 (A) (*top*) Schematic diagram and (*bottom*) the measured results to demonstrate the change in distance between object and image plane (D_2) as a function of distance between lens and object plane (D_1). (**B**) Schematic diagram and (**C**) photo of a custom-built optical microscope.

Optical switching of phase-change material using a visible laser

For optical switching of phase-change materials, high-power optical pulse excitation is required. In this setup, a red laser diode (Vortran Stradus, 639 nm) was employed, with a maximum input power of 150 mW. As shown in Figure 3.9, the fiber-coupled red laser, which is linearly polarized, was mounted onto a microscope cage system using a fiber

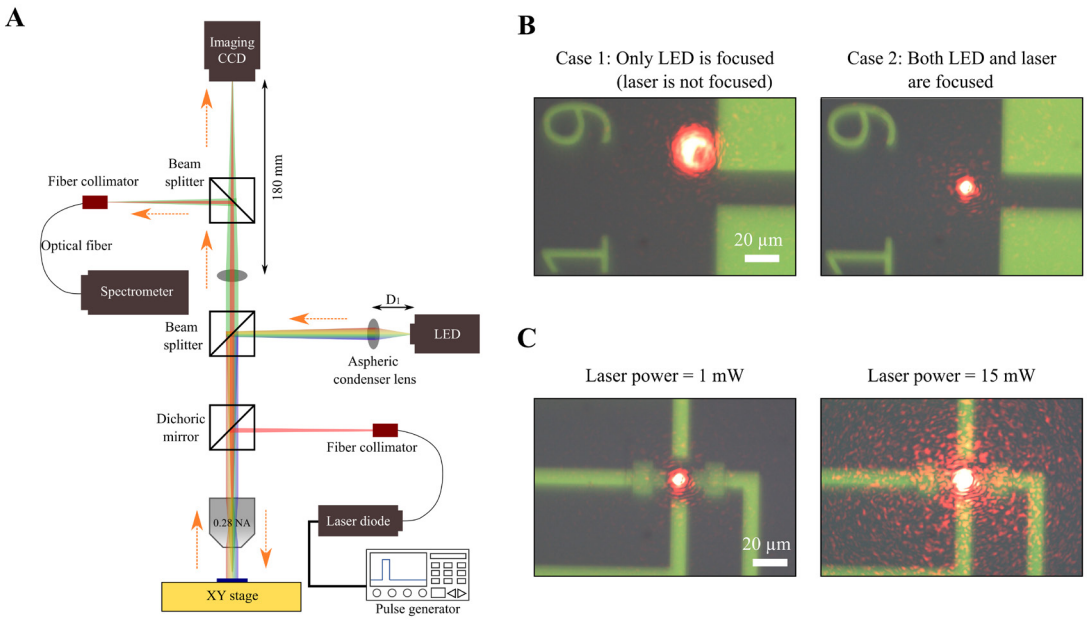


Figure 3.9 (A) Schematic diagram of custom-built microscope with a red switching laser. Laser is modulated by pulse generator and illuminated onto the sample via a short pass dichroic mirror (600 nm). OM images of the electro-optic cell with a focused red laser to show (**B**) (*left*) the ideal case and (*right*) the failure of simultaneous focus of the laser and nanowire array and (**C**) the size of the laser spot with varying laser power.

coupler (Thorlab, FC/APC connector). Two-axis rotational adjustment (Thorlab, KAD11F) allowed for the tilting angles of illumination to be adjusted, fine-tuning the focus and lateral position of the laser on the sample.

To maximize the laser power on the sample, a short-pass (600 nm) dichroic mirror was used. This mirror transmits all the laser light (638 nm) onto the sample without sacrificing 3 dB of power loss, as would be the case with a 50:50 beam splitter. Only a fraction of LED light below the wavelength of 600 nm was transmitted through the mirror, resulting in optical imaging in green color. The collimated red laser was focused directly onto the sample by the objective lens, and the size of the focal spot can vary depending on the laser power (Figure 3.9C) or the working distance between the sample and the objective lens. The misalignment of Kohler illumination or a mismatch between the position of the lens

and its focal length can sometimes result in an unclear observation of both the laser spot focus and the sample (Figure 3.9B). Ideally, the laser spot size was kept below 5 μm under laser illumination with an input power of less than 5 mW, ensuring that the focused laser illumination has sufficient power for switching the phase-change material.

To generate laser pulses ranging from nanoseconds to seconds, a 100 MHz electrical pulse generator (TG5011) was used. The Vortran laser diode, in digital modulation mode, supports a bandwidth of up to 200 MHz under the operating input voltage of 2 V. The rise/fall time of the pulse was set to the minimum value, which is approximately 25 ns. The detailed pulse condition for switching different types of phase-change material is further discussed in *Chapter 4 – 6*.

Electrical integration and measurement

By combining the electrical integration with the custom-built optical microscope, optoelectronic measurements become possible. This integration is particularly advantageous for phase-change devices, as it allows for simultaneous reading and programming of the electrical and optical states of the phase-change material.

To generate electrical signals within the device, microprobes were coupled to the electrical pads on the chip. The XYZ micro-positioners (Signatone) enabled precise positioning of the probes, as depicted in Figure 3.10. These probes were then connected to source meter units (SMUs) that can deliver current or voltage to the device and simultaneously measure the corresponding current or voltage, respectively. For the electrical measurements of phase-change materials, a dual-channel SMU (Keithley 2614B) was employed. This SMU is capable of sourcing and measuring two independent signals with a common ground. To

prevent excessive current flow during crystallization and reduce the potential drop across the phase-change element, current limiting resistors were included in series with the phase-change elements. In certain cases, direct-current (DC) electrical signals were directly supplied by a pulse generator (TG5011) to generate electrical pulses on the microheater. This was done to switch low-loss phase-change materials, which will be discussed further in *Chapter 5*.

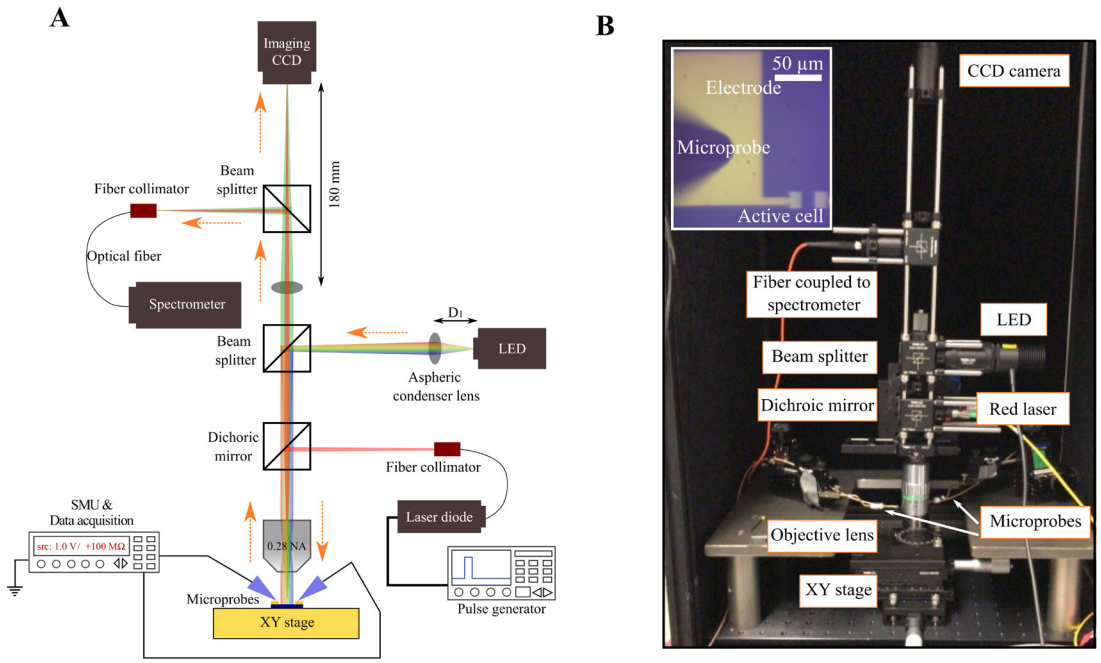


Figure 3.10 (A) Schematic diagram and (**B**) photo of a custom-built microscope with electrical microprobes mounted on an XYZ stage. Electrical signals are generated and measured by SMUs. Inset shows OM image of electrodes in a chip with the microprobe in contact.

3.2.2 Integrated all-photonic measurement

In order to test integrated phase-change nanophotonic circuits, it is essential to build an integrated all-photonic setup that differs significantly from the previous free-space optical setup. In this integrated setup, most optical components were fiber-coupled, except for the fiber array used to couple light in and out of the chip. There were two main types of

measurements: static transmission measurement for passive characterization of transmission and the pump-probe setup utilizing optical switches to actively control and monitor the dynamic behavior of the phase-change material integrated into the photonic circuits.

Static transmission measurement

As illustrated in Figure 3.11, the wavelength-tunable continuous-wave (CW) laser (Santec, TSL-550) in the telecommunication wavelength range (1500 – 1600 nm) was employed to measure the transmission state of the device. To achieve optimal coupling transmission into the Bragg grating couplers on the chip, the laser was first polarized (Thorlabs, FPC032) and then coupled into the couplers through a micro-spaced fiber-array. The spacing between the fiber-array channels matched that of the grating couplers on the chip (127 or 250 μm). Precise alignment between the fiber array and the chip was ensured using a 3-axis piezoelectric-modulated stage (Physik Instrumente) and a microscope with a varifocal lens (Navitar). The optimized transmission from the output grating couplers was

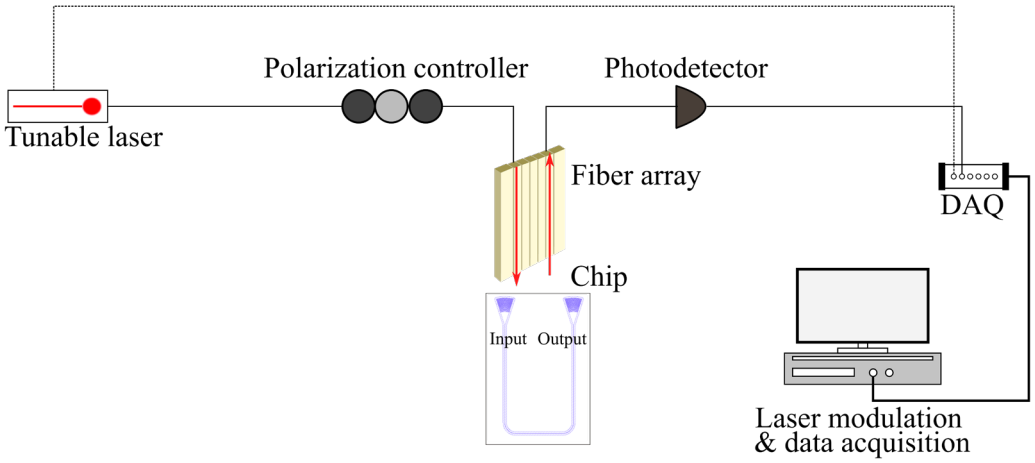


Figure 3.11 Schematic diagram of static transmission measurement of integrated photonic circuits.

collected by the fiber-array and directed to a 200 KHz low-noise photoreceiver (New Focus, Model 2011). The output signal from the photoreceiver was then sent to the data acquisition (DAQ, National Instruments) unit. For spectrum measurement, the fast wavelength sweep mode of tunable laser with 0.5 nm wavelength precision was employed. The laser, piezoelectric stage, and DAQ were controlled by a custom-built LabView program.

Pump-probe setup using an optical switch

The pump-probe experiment in this work utilized a single tunable laser source along with rack optical switches (Gezhi) to route each probe and pump line separately, as demonstrated in Figure 3.12. It differs from conventional pump-probe setups in that it allows for the specific case of programming and measuring standing-waves in coherent nanophotonic circuits (*Chapter 6*), whereas conventional pump-probe setups typically employ multiple laser sources with different wavelengths guiding into the chip through multiple grating couplers for pump and probe pathways, respectively.

At first, the CW laser was divided into two lines with a ratio of 1:9. The probe line was connected to sequential polarizers and one of the channels in the optical switch. On the other hand, the pump line was initially polarized and then transformed into pulses using an electro-optical modulator (EOM, Lucent Technologies) controlled by an electrical pulse generator (AFG3102C, Tektronix). The EOM modifies the CW laser into customized pulse shapes and lengths according to the modulation in the pulse generator. The resulting pulse was then amplified by an erbium-doped fiber amplifier (EDFA, HPP-PMFA-21-10 from Pritel) to increase the transmitted power using controllable gain. The

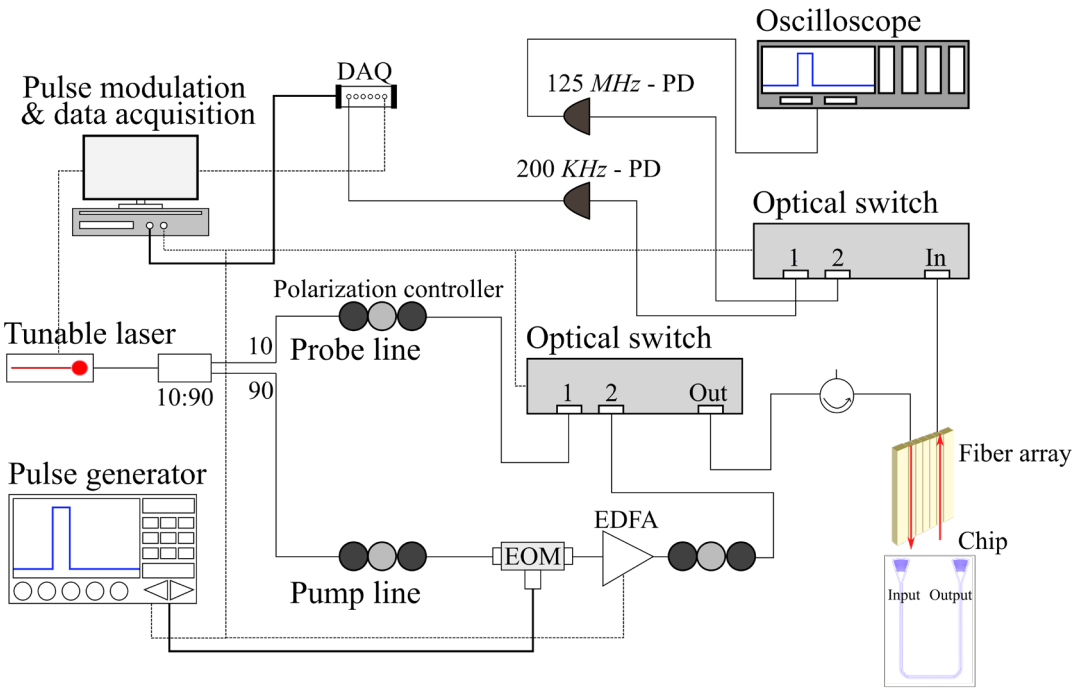


Figure 3.12 Schematic diagram of pump-probe measurement of integrated photonic circuits using optical switches.

amplified pulse from the EDFA was polarized to optimize coupling with the grating coupler and is connected to the other channel of the optical switch. The output of the optical switch was coupled into the input grating coupler of the device, and the setup ensured that back-reflections were avoided by incorporating an optical circulator. The output signal of the chip was collected by the other channel of the fiber array and sequentially transmitted to the second optical switch. The probe and pump lines were separated, allowing the CW probe laser to be directed to a 200 KHz photoreceiver (New Focus, Model 2011), while the high-power pulse was directed to a 125 MHz photoreceiver (New Focus, Model 1811) connected to a 4 GHz oscilloscope (Telktronix, TDS7404B). A custom-built LabView program controlled the laser, piezoelectric stage, optical switches, pulse generators, and data acquisition (DAQ) system. The control of the input

and output optical switches was synchronized to ensure that the probe and pump lines were completely decoupled with a delay time of 1 ms.

3.3 Chapter summary

This chapter has presented the overall fabrication procedures as well as the optical setups and instrumentation employed for multiple phase-change photonic devices, which were largely divided into two systems; free-space optics and integrated photonic systems. Although the description of the main branch of fabrication methodology and measurement setup has been provided herein, these configurations are utilized in the upcoming chapters with additional modifications in order to demonstrate the operation of various photonic device types.

Chapter 4

Polarization-selective switching of hybridized-active-dielectric nanowires

This chapter showcases the active nanophotonic system that capitalizes on polarization as a tunable parameter to maximize the device functionalities. The chapter demonstrates the polarization-selective non-volatile reconfigurability using hybridized-active-dielectric (HAD) nanowires. The motivation and operational principle of HAD nanowires are described in *Section 4.1* and *4.2*, which includes optical and thermal simulation analysis. *Section 4.3* covers the most of electro-optic measurements of HAD nanowires. Furthermore, the polarization-selective matrix-vector multiplication is demonstrated through a multi-HAD-nanowire configuration in *Section 4.4*. The potential applications of the HAD system are discussed in *Section 4.5*, followed by a summary in *Section 4.6*.

4.1 Motivation: Polarization-selective reconfigurability in a single element

As discussed in *Chapter 2.2* and *2.5.1*, the current optical switching mechanism of phase-

change material (PCM) relies on intensity-dependent laser annealing and lacks any polarization-selectivity, primarily due to the elusive nature of tunable and polarization-selective nanostructures. Polarization is considered a powerful multiplexing parameter that can significantly enhance information capacity through orthogonal polarizations. Yet, the advantageous potential of polarization-multiplexing remains untapped in active nanophotonic systems. By combining polarization-selectivity with active material tunability, a wide range of unexplored device functionalities can be achieved, including polarization-selective switches, routing, and computing. To enable this, a polarization-selective photonic resonator (Figure 2.8C) is needed to confine light at the resonant polarization angle,[76] allowing the targeted polarization to interact with the active material and serve as the switching mechanism, realizing so-called polarization-selective laser annealing. This can be realized by combining a thin tunable absorber, such as lossy PCM, with a polarization-selective dielectric resonator, forming a hybridized-active-dielectric (HAD) system. As a result, the device functionality can be enhanced through polarization-space, interfacing photonic degrees-of-freedom with active reconfigurabilities, which is the primary motivation for this thesis.

The concept of HAD nanowires presented in this work introduces the first prototype of single-element polarization-selective reconfigurability, recognizing the significance of polarization as a multiplexing parameter. Polarization encompasses various types, such as linear, elliptical, or circular polarization, and can be further extended to angular momentum concepts by incorporating varying phase or polarization profiles of the electric-field to enable orbital or spin angular momentum.[112,113] Therefore, although this work focuses on achieving linear-polarization-selective tunability using HAD nanowires,

the concept can be expanded to include chirality-selective or angular-momentum-selective structures. Furthermore, the configuration can be extended to other active materials hybridized with dielectrics that exhibit active tunability and satisfy resonance conditions, making it applicable to various applications including photonic memories and computing.

4.2 Hybridized-active-dielectric (HAD) nanowires

4.2.1 Device outline and operational principle: An electro-optic cell

Figure 4.1 illustrates the schematics and operational principles of the electro-optic system utilizing the HAD nanowire. A free-space optical pump was utilized to control the crystalline state of the HAD nanowire. The nanowire, measuring 15 μm in length and 180 nm in width, consists of a combined thickness of 80 nm, with a bottom layer of 15 nm of

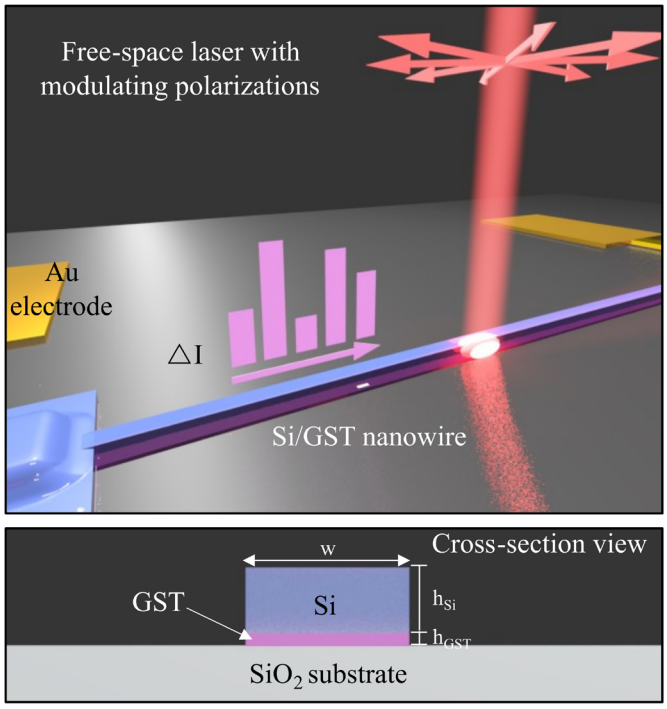


Figure 4.1 Schematic diagram of a HAD nanowire across two electrodes. The nanowire, with a width of approximately 180 nm, consists of a GST layer (15 nm) on top of a Si layer (65 nm). The nanowire is illuminated by polarized laser light at a wavelength of 638 nm, while the electrical current (ΔI) is monitored.

GST and a top layer of 65 nm of Si. Metal electrodes (Cr/Au) were connected to the nanowire, enabling the measurement of electric current through the GST while it was illuminated by the laser. The whole electro-optic cell was fabricated on 525 µm-Si wafers with a 330 nm-SiO_2 layer. The optoelectronic tunability of GST permits mixed-mode operation, meaning that the switching in one domain affects the state in the other domain. In this case, the optical switching of GST resulted in a change in electrical conductance by converting its state from the amorphous (*low* optical absorption, *high* electrical resistance) to the crystalline (*high* optical absorption, *low* electrical resistance) phase. During the electrical measurement, the power and polarization of the laser were adjusted while maintaining a fixed wavelength of 638 nm, which was optimized for achieving the dielectric resonances of hybrid nanowires (described in *Chapter 4.2.2*). Optical

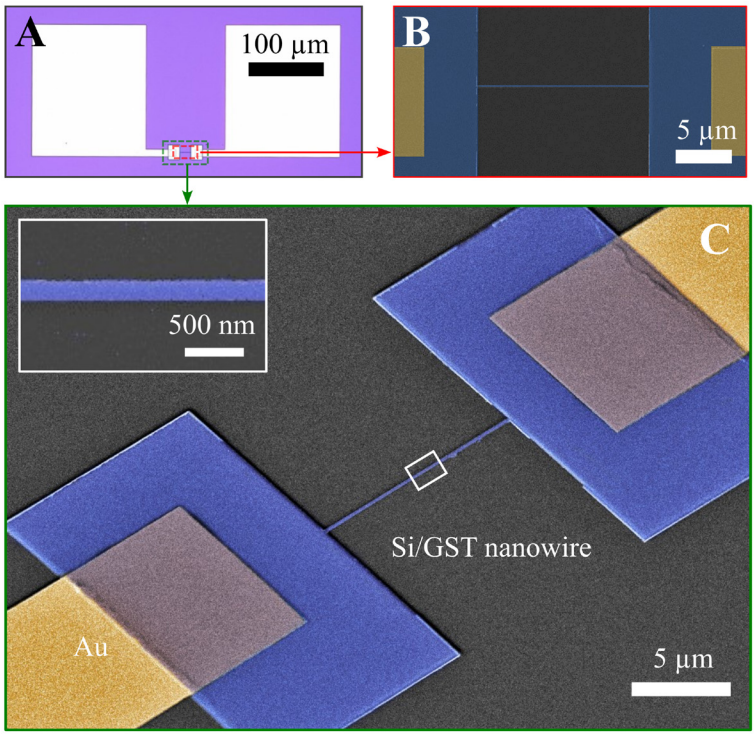


Figure 4.2 Microscope images of a HAD nanowire. (**A**) OM and (**B-C**) false-colored SEM images of the device. (**B**) Top-view and (**C**) angled-view of SEM images are displayed. Inset shows an enlarged view of a nanowire. Scale bars are (**A**) 100 µm and (**B-C**) 5 µm.

microscope (OM) and scanning electron microscope (SEM) scans of the device are shown in Figure 4.2. Overall, the HAD nanowire-based electro-optic system demonstrates polarization-selective optical reconfigurability and electrical accessibility. The choice of Si and GST materials was driven by the requirement to implement high-index, low-loss resonators (Si) in close proximity to a thin switchable absorber (GST). The incoming free-space electromagnetic waves are coupled to the high-index dielectric nanowires to induce polarization-dependent photonic resonances. The position and intensity of the absorption peaks are influenced by the geometry and polarization of nanowires. When a thin layer of high-loss material (GST) is introduced beneath the dielectric cavity, most of the coupled multipole field is asymmetrically absorbed by the lossy layer, while the dielectric resonance is preserved. This hybrid configuration requires a top dielectric layer of sufficient thickness to effectively confine the electric field within the nanowire, while the bottom lossy layer should be thin enough to avoid compromising the resonance in the top layer. Additionally, the thickness of the bottom layer needs to be adequate to induce a significant change in current upon optical pulse excitation.

4.2.2 Optical simulation

Numerical simulations were conducted using Lumerical Finite-Difference Time-Domain (FDTD) software to verify the operational principle of polarization-selective absorption in the HAD nanowire by calculating absorption/reflection spectra, electric field distribution, and absorbed power distribution in hybrid nanowires. A 2D model was employed based on the cross-sections of hybrid nanowire (Si/GST) on a SiO_2/Si substrate (Figure 4.1) under illumination of a plane-wave source. A 3D model was also employed

for Figure 4.32 to describe the optical responses as a function of nanowire lengths. The dielectric function of GST and Si in the nanowires was determined through ellipsometry measurements on thin films prepared by RF-sputtering. The dielectric functions of SiO_2 and Si in the substrates were obtained from Palik.[114] A perfectly matched layer (PML) was used for as an absorbing boundary condition along the optical propagation direction, with large periodic boundary condition applied in the lateral directions to calculate the optical response of a single hybrid nanowire. It is important to highlight that in practice, incident light is focused on the nanowire through a low 0.28 *NA* lens. However, as similarly described in the other work on a dielectric Mie nanowire,[115] the optical response of hybrid nanowire is expected to stay consistent for incident light at different angular distributions (i.e. Gaussian beam with different *NA*).

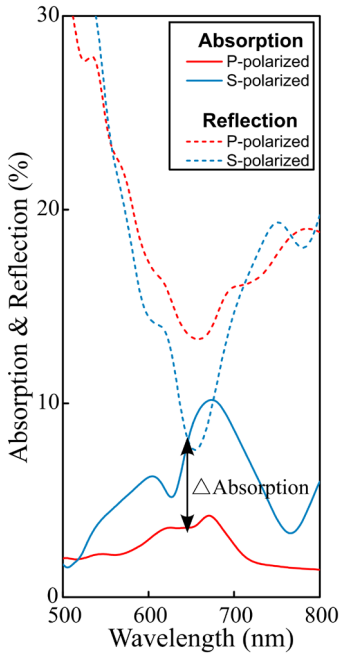


Figure 4.3 Polarization-dependent optical spectra of the HAD nanowire with an amorphous-GST layer. Calculated absorption and reflection spectra of a hybrid nanowire when illuminated with s-polarized (*blue*) and p-polarized (*red*) light. Only the absorption of the GST layer is considered, revealing a distinct contrast at 638 nm.

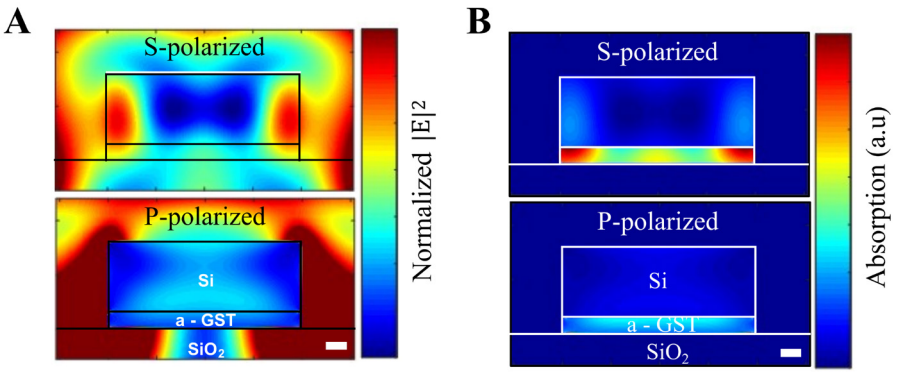


Figure 4.4 Cross-sectional field profile of the HAD nanowire with an amorphous-GST layer. FDTD simulations of (**A**) electric-field distribution and (**B**) absorbed power distribution are calculated under s-polarized (*top*) and p-polarized (*bottom*) illumination at 638 nm. Scale bar, 20 nm. a.u., arbitrary units.

Figure 4.3 – 4.4 illustrates that the absorption within the GST layer is modulated by the polarization-selective dielectric resonances of the Si cavity. By calculating the reflection/absorption spectra of the HAD nanowire under two orthogonal polarizations (Figure 4.3), it is evident that around 638 nm, the absorption peaks and corresponding reflection dips are more prominent when the incident electric field aligns with a long axis of the nanowire (s-polarized) compared to when it is perpendicular (p-polarized). Under s-polarized illumination, the Si layer acts as a dielectric resonator, allowing for strong mode localization. These higher-order mode excitations were exclusively observed with s-polarized light, while negligible electric field confinement occurs under p-polarized illumination due to the vanishing response of electric/magnetic multipoles perpendicular to the long axis of nanowire. This polarization-selective coupling leads to polarization-dependent absorption within the bottom lossy GST layer, as depicted in Figure 4.4B. Remarkably, this selective electric field confinement in Si and absorptive coupling in GST was observed in both the amorphous and crystalline states (Figure 4.5 – 4.6) of GST, suggesting the capability of HAD nanowire for reversible polarization-selective switching.

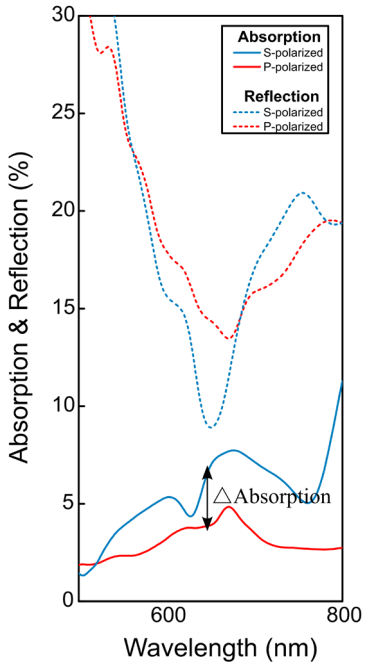


Figure 4.5 Polarization-dependent optical spectra of the HAD nanowire with a crystalline-GST layer. Calculated absorption and reflection spectra of a hybrid nanowire when illuminated with s-polarized (*blue*) and p-polarized (*red*) light. Only the absorption of the GST layer is considered, revealing a distinct contrast at 638 nm.

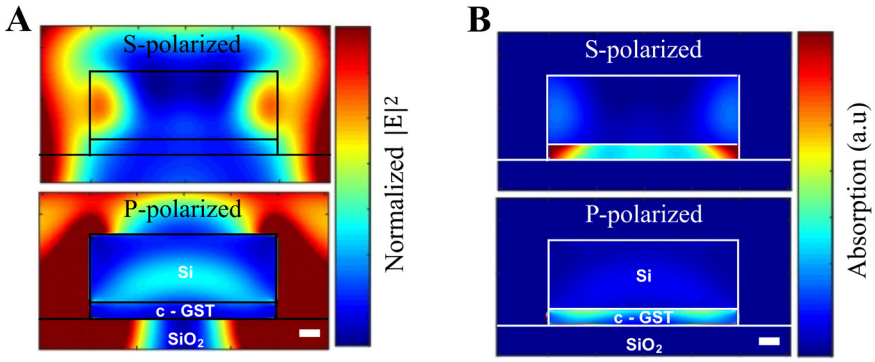


Figure 4.6 Cross-sectional field profile of the HAD nanowire with a crystalline-GST layer. FDTD simulations of (**A**) electric-field distribution and (**B**) absorbed power distribution are calculated under s-polarized (*top*) and p-polarized (*bottom*) illumination at 638 nm. Scale bar, 20 nm. a.u., arbitrary units.

It is important to highlight that the hybrid nanowire system tends to excite higher-order resonances, while the fundamental mode is generated in longer wavelengths (~1.2 μm). This is primarily due to the systemic limitation imposed by the wavelength of the high-

power laser in the setup, which was confined to 638 nm. This can be further improved by changing the excitation wavelength or replacing the dielectrics with higher index materials. Additionally, although a SiO_2/Si substrate was used in this device, opting for a glass substrate is preferred which can help mitigate the generation of complex resonance modes caused by the additional interference effect within SiO_2 layer. These aspects are recognized as the limitation of the system, demanding for further improvements to enhance efficiency and selectivity in switching.

To investigate the effect of nanowire width on the system, an extended analysis of reflection and absorption for different types of nanowires (bare Si, Si/aGST, and Si/cGST) is presented, with variations in nanowire widths and incident polarization angles (Figure 4.7 – 4.8). The simulation included an excessively large boundary condition (≥ 2 μm) to ensure no mode overlap between adjacent elements and to explore the spectral responses of individual nanowires. A hybridized form of dielectric resonances is produced, coupled with thin-film interactions at a 330 nm-thick SiO_2 layer on the substrates. Increasing the s-polarized nanowire widths resulted in red-shifted reflection dips, indicating confinement of multipolar excitations within the nanowire. Such wavelength-dependency can be improved and exploited as an additional tunable parameter by tightening the electric-field confinement via metal capping[115,116] or optimizing the resonances to the fundamental mode. The stationary reflection dip at 600 nm, regardless of nanowire widths, corresponds to Fabry-Perot resonances from the SiO_2 thin film. These reflection dips are primarily translated into absorption peaks in all three scenarios. For polarization-dependent reflection/absorption changes, hybrid nanowires with 180 nm widths exhibit spectral properties close to the resonant wavelength. Under s-polarized illumination, reflection

decreases and absorption increases as the incident polarization angle approaches 90°, indicating dominant dielectric excitations. Since the electro-optic devices operate at a wavelength of 638 nm within the higher-order mode resonances of the nanowires (630-660 nm), polarization-sensitive absorption is observed, enabling polarization-sensitive resonant switching.

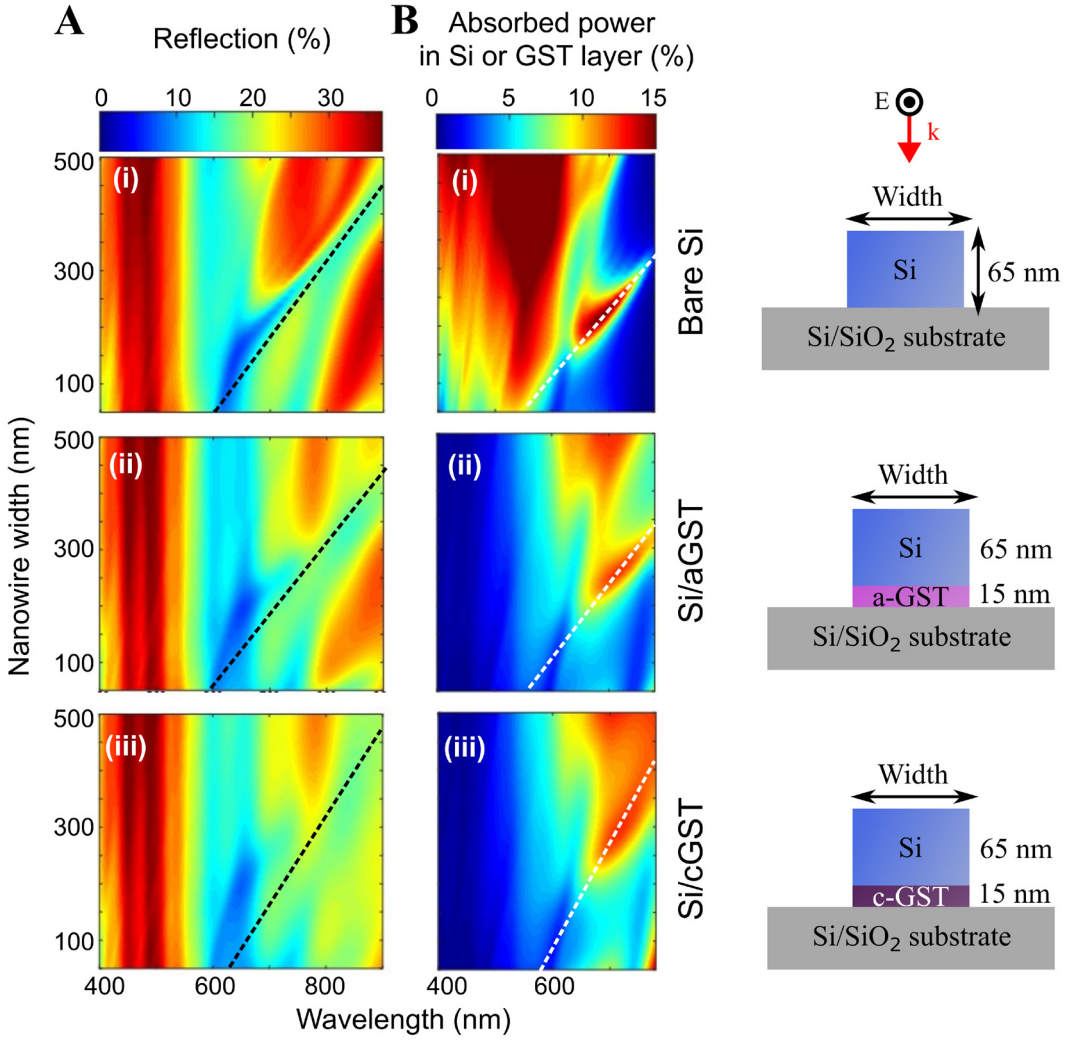


Figure 4.7 Spectral responses of nanowires as a function of varying nanowire widths. (**A**) Calculated maps of reflection spectra and (**B**) absorption spectra as the nanowire widths are varied. The calculations are performed for three configurations: bare Si (i, *top*), Si/aGST (ii, *middle*), and Si/cGST (iii, *bottom*), under s-polarized illumination. The dotted lines represent the hybridized dielectric resonances of the nanowires. For absorption, only the Si or GST layer is considered in each calculation: (i) bare Si, (ii) Si/aGST, and (iii) Si/cGST, respectively.

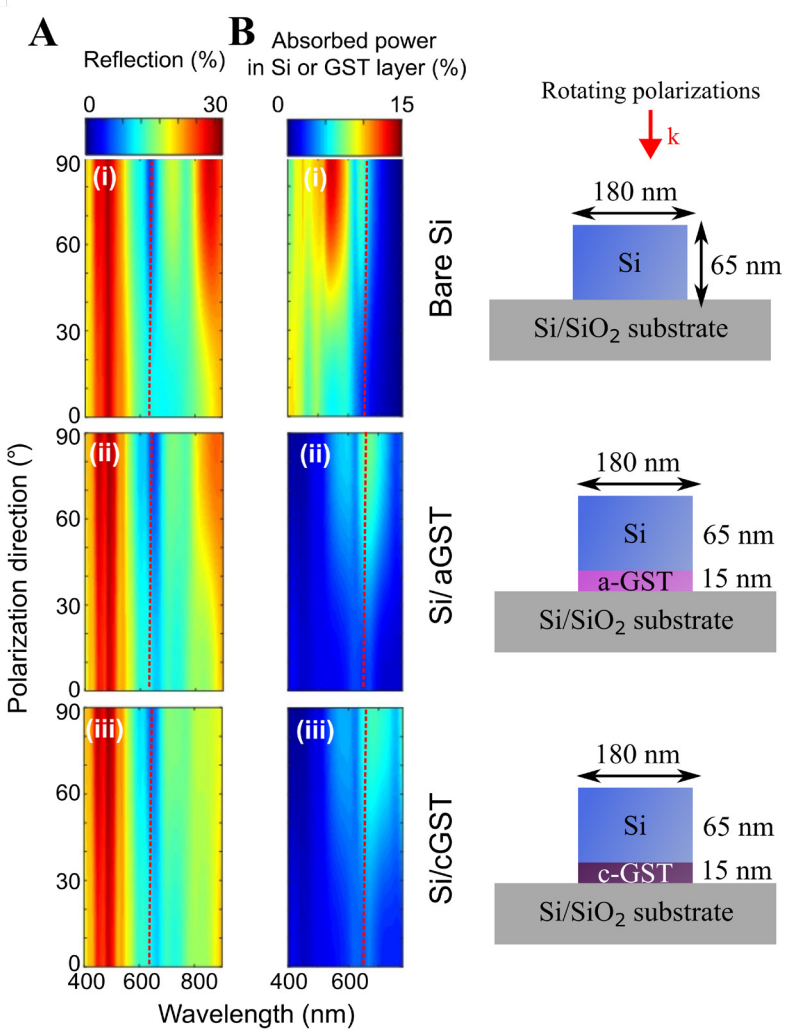


Figure 4.8 Spectral responses of nanowires as a function of varying polarization angles of illumination. (**A**) Calculated maps of reflection spectra and (**B**) absorption spectra as the polarization angles are varied from 0° (p-polarized) to 90° (s-polarized), for nanowires with a width of 180 nm. The calculations are performed for three configurations: bare Si (i, *top*), Si/aGST (ii, *middle*), and Si/cGST (iii, *bottom*). The red dotted lines represent the laser line at 638 nm. For absorption, only the Si or GST layer is considered in each calculation: (i) bare Si, (ii) Si/aGST, and (iii) Si/cGST, respectively.

4.2.3 Thermal simulation

In order to validate the dynamic switching behavior and investigate the transient thermal response, 2D Finite Element Method (FEM) thermal simulations were conducted using COMSOL Multiphysics. These simulations aimed to explore the electromagnetic heating

of hybrid nanowires when subjected to plane-wave illumination, with variations in polarization directions, laser powers, or pulse duration. In the electromagnetic heat transfer model, the absorbed light in a lossy medium converts electromagnetic field intensity into heat through Joule heating. As a result, the magnitude of heat source (Q) can be expressed as follows:[117]

$$Q = \frac{1}{2} Re(\boldsymbol{J} \cdot \boldsymbol{E}) \tag{4. 1}$$

,where $\boldsymbol{J}$ and $\boldsymbol{E}$ represent the electric current density vector and electric field vector respectively. The induced heat which distributes to the whole volume in a time-dependent manner can be calculated in FEM simulations by coupling of two following equations: Maxwell's equation *(4. 2)* and the heat conduction equation *(4. 3)*.[118]

$$\nabla^2 \boldsymbol{E} - {k_0}^2 \varepsilon_r \boldsymbol{E} = 0 \tag{4. 2}$$

$$\rho C_p \frac{dT}{dt} - \nabla \cdot (\varkappa \nabla \mathrm{T}) = Q \tag{4. 3}$$

Here, in the Maxwell equation, k_0 and ε_r denote the wavenumber and relative permittivity of the material respectively. In the heat conduction equation, ρ, C_p, $\varkappa$, and T represent the mass density, heat capacity, thermal conductivity, and temperature of the medium respectively. The heat capacity, thermal conductivity, and density of GST were derived from the experimental results of previous studies.[119,120] Size-dependent thermal properties was neglected due to the observation that the thermal conductivity of GST shows negligible changes until the length of GST (i.e. heat transport direction) decreases to smaller than ~5 nm, according to the quantitative analysis of molecular dynamics within the GST.[121] The dissipation of heat, primarily originating from the highly absorbed regions of the GST, facilitates the uniform spreading of temperature rise across the cross-sections

during phase-switching operations, as illustrated in Figure 4.9 – 4.10. In these figures, only the temperature profiles of the nanowire and substrate are taken into account to provide a clearer illustration of the heat dynamics within the phase-change layer. However, it is important to note that convective heat flux (q_0) to free space was also included in the simulation, which can be described as $q_0 = h(T_{ext} - T)$ with heat transfer coefficient of h (=5 W/m^{2}K) and external air temperature T_{ext} (= 25 °C).

For the amorphization process, high laser power (32 mW) was simulated with a short duration (80 ns), whereas for crystallization, lower power (9 mW) was used with a longer duration (1 µs). In Figure 4.9A and 4.9C, where the pulse duration is significantly shorter than the required switching time (i.e., 5 ns), the cross-sectional temperature profiles resemble the absorption profile of the GST depicted in Figure 4.4B. However, beyond the required switching time (1 µs and 80 ns) in Figure 4.9B and 4.9D, the temperature distribution becomes uniform across the GST cross-section, surpassing the switching temperatures (493 and 900 K, respectively). Moreover, the variation in input polarization angles (Figure 4.10) resulted in a sinusoidal-like increase in average temperature, which was aligned with the corresponding trend in optical absorption (Figure 4.11). It was observed that, in both crystallization and amorphization processes, the temperature of the GST could be raised above its glass transition temperature (T_g; ~493 K) and melting point (T_m; ~900 K) when subjected to s-polarized pulses (i.e., 90°), whereas p-polarized illumination (i.e., 0°) failed to induce the switching of crystalline states.

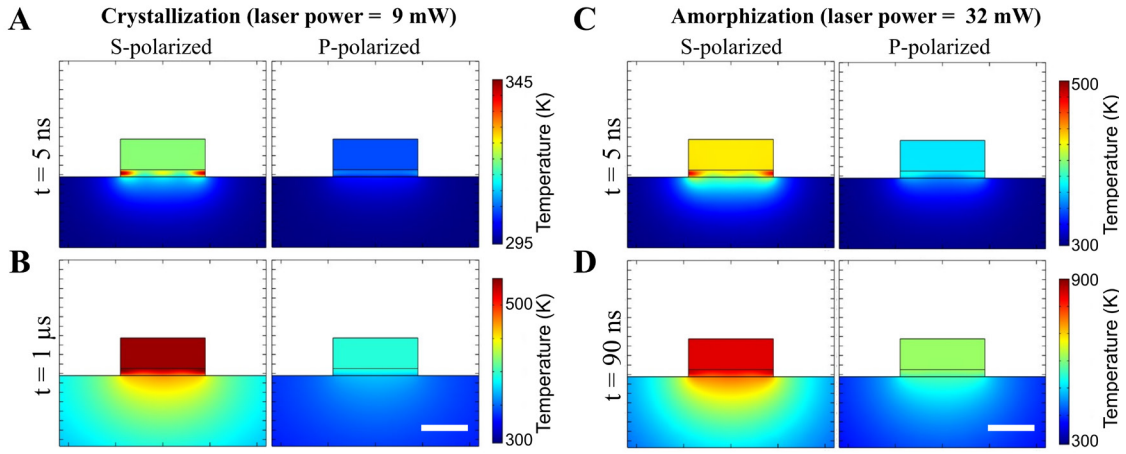


Figure 4.10 Cross-sectional view of temperature profiles within HAD nanowires. The temperature profiles depict (**A-B**) crystallization processes and (**C-D**) amorphization processes, with laser power (pulse durations) of 9 mW (1 µs) and 32 mW (80 ns), respectively. The left panels represent S-polarized nanowires, while the right panels represent P-polarized nanowires. The top panels illustrate the temperature profile after 5 ns of pulse illumination, while the bottom panels depict the temperature profile immediately after the corresponding pulse durations (i.e., 1 µs for crystallization and 80 ns for amorphization). Scale bar is 100 nm.

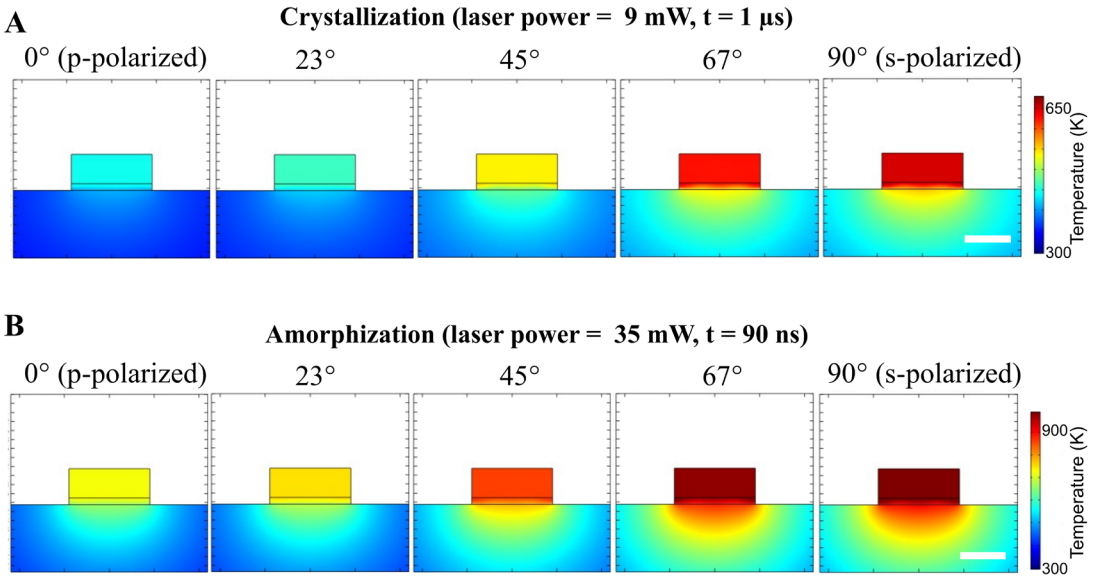


Figure 4.9 Cross-sectional views of temperature profiles at different polarization angles. The laser power (pulse duration) used is 9 mW (1 µs) for the crystallization process (**A**) and 35 mW (80 ns) for the amorphization process (**B**). Scale bar is 100 nm.

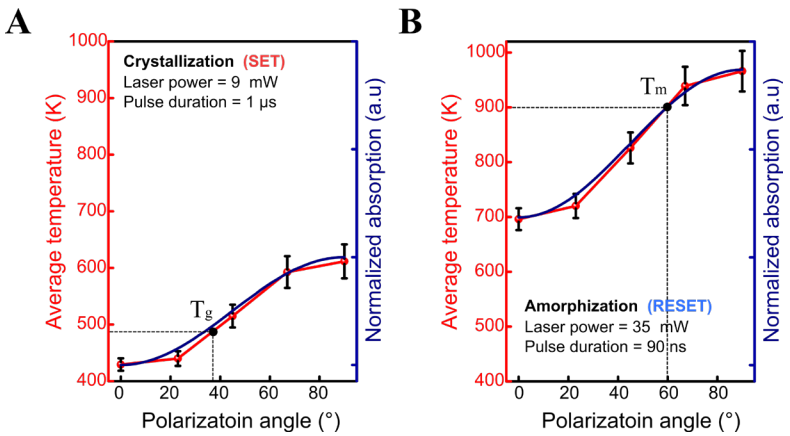


Figure 4.11 Calculated average temperature and normalized absorption within the GST of a HAD nanowire, plotted as a function of polarization for (**A**) crystallization and (**B**) amorphization processes. T_g and T_m refer to the glass transition temperature and melting point of GST, respectively.

4.3 Electro-optical measurement of a hybrid nanowire

The switching characteristics of the devices, based on the calculated pulse parameters in *Chapter 4.2.3*, were experimentally evaluated through the electrical monitoring of the conductance state of an initially crystalline nanowire. A direct-current (DC) source voltage of 1 ± 0.4 V was applied across the nanowire, and the current passing through its terminals was measured using a source meter unit. Simultaneously, nanosecond optical pulses at 638 nm were applied through a 0.28 *NA* objective (Figure 4.12), while rotating the polarization angles from s- to p-polarized states. To ensure the complete crystallization of the GST, the device was preheated on a hot-plate (200 °C) for 5 minutes before the measurements. The experimental setup, as depicted in Figure 3.10, was slightly modified by incorporating a half-wave plate (HWP) to adjust the polarization directions of the illumination on the sample. In order to achieve reliable switching processes, the laser light was slightly defocused to achieve a more uniform power distribution and minimize any damage at the center of the laser spots. The final optical powers were measured and

calibrated by rotating the HWP, ensuring consistent power levels as the polarization was varied (Figure 4.13). Taking into account a slight misalignment of the focused spot, a ±1.5 mW fluctuation in laser power was accounted for. The laser power was measured using an optical power meter (Thorlabs, PM100D) in the same experimental setup. Using this setup, the experimental measurement of intensity-dependent modulation is discussed first in *Chapter 4.3.1*, followed by polarization-selective switching in *Chapter 4.3.2*.

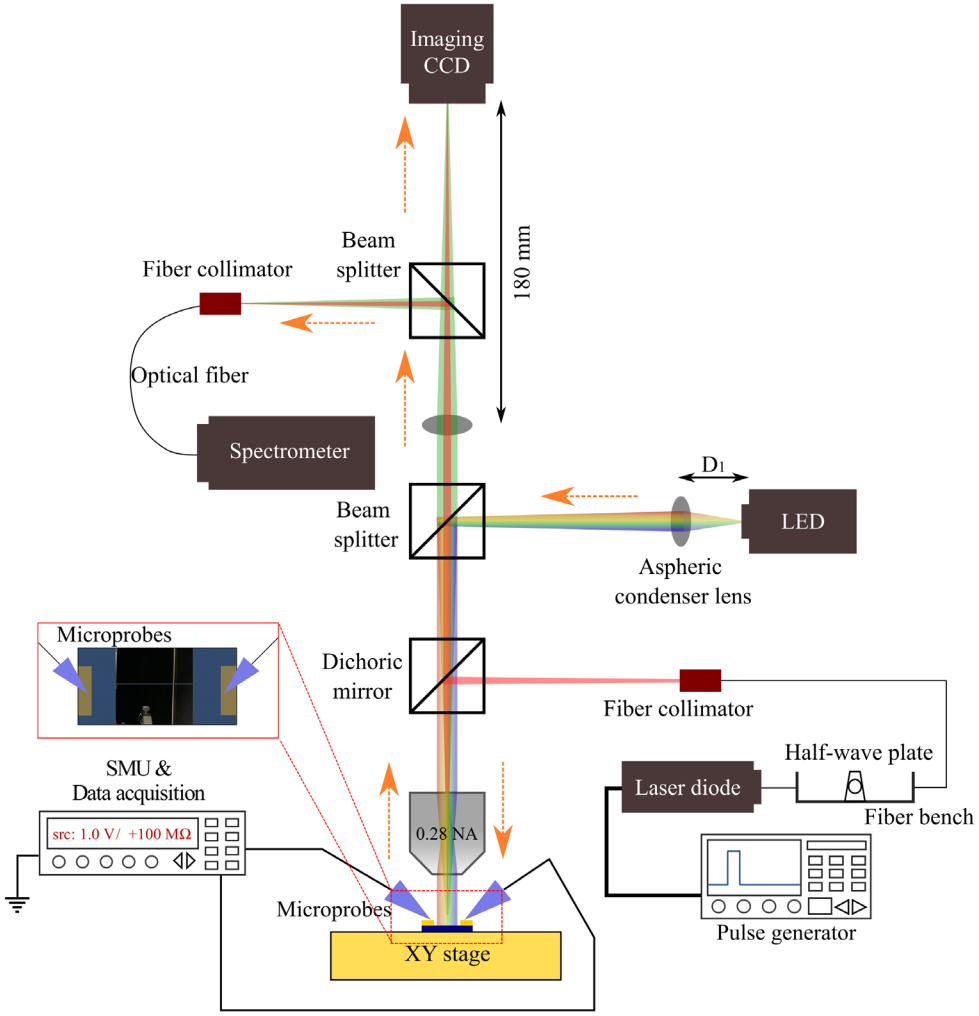


Figure 4.12 Schematics of the electro-optic measurement setup of the HAD nanowire. Electrical current across nanowires is monitored, while the incident polarization of pulsed laser is varied using half-wave plate (HWP).

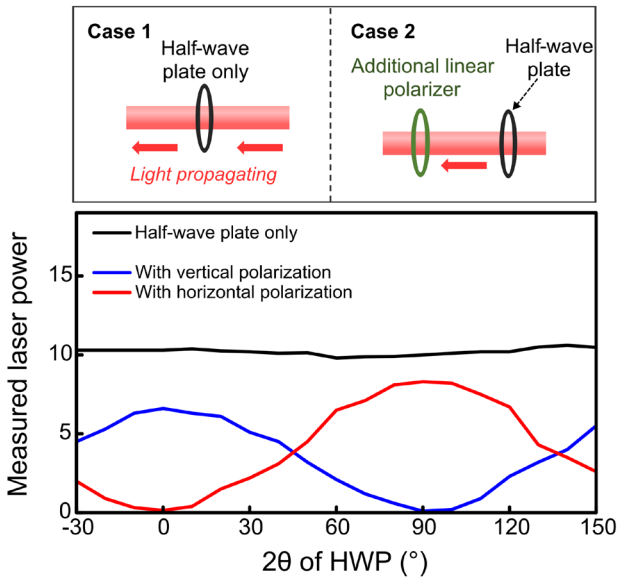


Figure 4.13 Calibration of polarization modulation using half-wave plate (HWP). Measured laser power as the angle ($\boldsymbol{\theta}$) of the HWP is rotated. The schematics illustrate the configuration of optical components used for each measurement. The black line represents the power measurement with only the HWP inserted. The red and blue lines correspond to the power measurement with an additional linear polarizer at 0° (*blue*, vertical) and 90° (*red*, horizontal) angles, respectively.

4.3.1 Intensity-dependent modulation

Binary reversible switching

The reversible cyclability of the device was tested by applying optical pulses with the polarization angle fixed at 90° (i.e. s-polarized). The nanowire was initially heated on a hot-plate to fully crystallize it, followed by the reversible cycles of *RESET* (amorphization) and *SET* (crystallization) processes. A single pulse with a high amplitude of 35 mW for 80 ns was used to *RESET* the nanowire, while a pulse with a lower amplitude (9 mW) for a longer period (1 µs) was required to *SET* the nanowire (Figure 4.14A). The results of ten reversible cycles are demonstrated in the time-trace electrical measurement (Figure 4.14B), showing a high contrast output (>1700%) without degradation in the current readouts (≤ 5%). Once the pulse was applied, the state remained switched, signifying its non-volatile

feature. The high modulation contrast of electrical readout is ascribed to the significant change in conductivity of the GST nanowire, ranging from tens of KΩ (crystalline) to a few MΩ (amorphous). This contrast can be retained as long as the width of nanowire remains confined below the optical switching area induced by focused laser spot. The readout noise is mainly attributed to a thermal fluctuation in the setup or internal background noise from the SMU. This can be further improved by several approaches, such as the implementation of vibration-isolation system for reducing the drift or the use of wire bonding for the electrical interconnections to minimize the mechanical vibration of electrical probes.

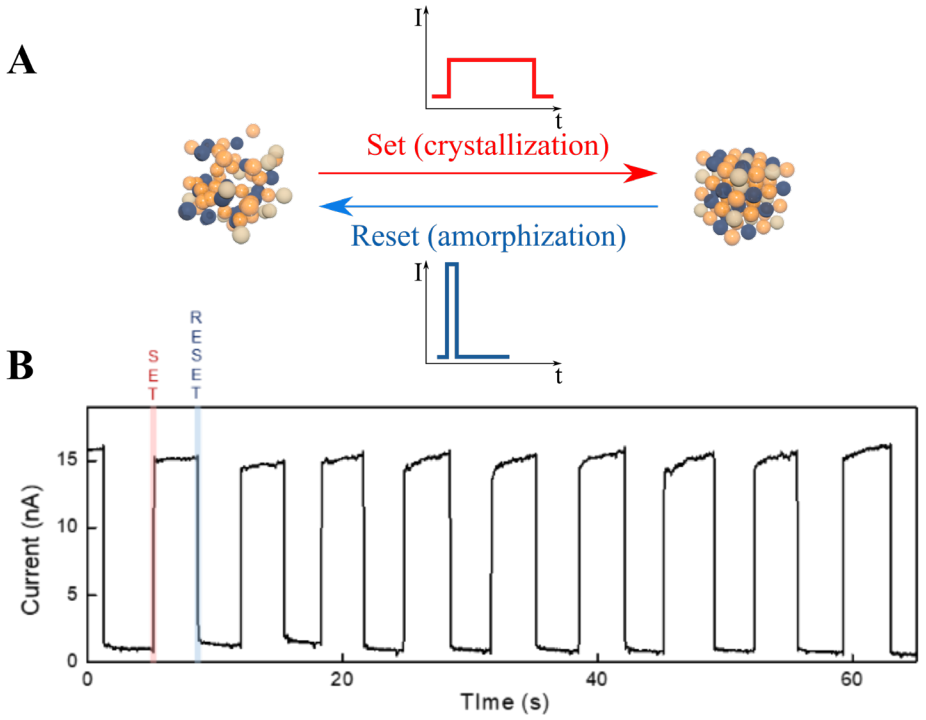


Figure 4.14 Reversible switching of the HAD nanowire. (**A**) Schematic representation of the reversible switching process of the GST under different pulse conditions. Crystallization (*SET*) requires a low-power pulse with a longer duration, while amorphization (*RESET*) requires a high-power pulse with a shorter duration. (**B**) Time-trace electrical readout measurement. The *SET* process involves an optical pulse of 9 mW at 1 µs, while the *RESET* process involves an optical pulse of 35 mW at 80 ns, both at a fixed polarization angle of 90° (s-polarized).

As described in *Chapter 2.2*, the non-volatile switching of GST is achieved through a melt-quenching process between amorphous and polycrystalline states, facilitated by optical pulses that induce temporal electromagnetic heating. To enhance the reproducibility of switching, the initial conditioning step involves isothermally annealing the GST layer and switching it to crystalline states in advance of inducing laser-annealed transitions. The timescale of these optical pulses shows a good agreement with previous studies,[9,10] where the amorphization typically occurs with pulses shorter than 100 ns with a fast cooling rate ($> 10^9$ Ks^{-1}) while the crystallization takes longer than few hundreds of nanoseconds. This non-volatile process of the GST has been proven for high endurance of ~10^9 or ~10^{12} switching cycles for photonic and electronic devices,[43] respectively, and without any drift in the optically switched states for at least 24 hours.[27] Furthermore, it is important to note that the change of volume expansion or shrinkage within the GST layer is observed to be negligible (< 5%), in contrast to other phase-change chalcogenides such as $GeSe_3$.[122] Although some tensile stress can be generated by rapid localized heating, causing a slight change in bond length of GST layer, this change does not significantly affect the conductivity of GST. Therefore, there is expected to be no fundamental material limitation to prevent the achievement of high cyclability and endurance in the device.

Intensity-dependent multilevel switching

The ability to tune the conductance of the nanowire between multiple levels was investigated by applying intensity-modulated pulses. The repeatable, distinct multilevels were achieved by tuning the laser power (Figure 4.15A) or pulse duration (Figure 4.15B). These multilevel states exhibited a linear relationship with the intensity parameters for

both the *SET* and *RESET* processes. For *SET* processes, the laser powers were adjusted in the range of 5 to 10 mW, labelled as P_{C1} to P_{C8}, while for *RESET* processes, the powers were varied from 34 to 38 mW, indicated as P_{A1} to P_{A10}. These non-volatile multilevels

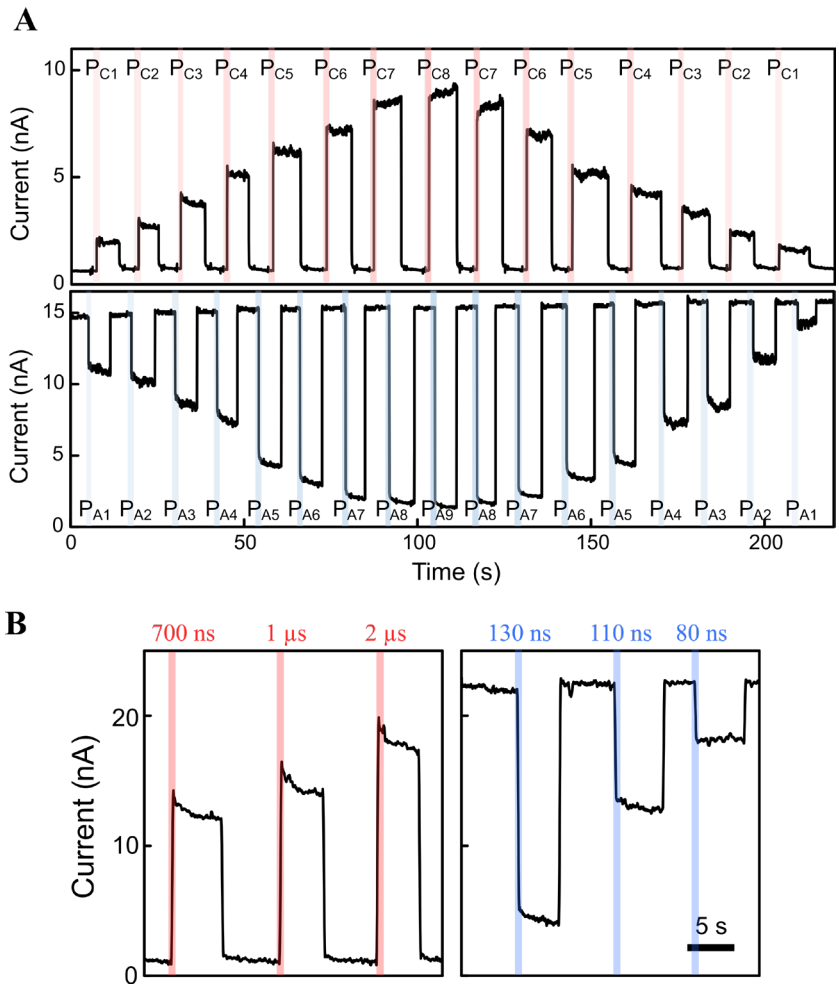


Figure 4.15 Intensity-dependent multilevel operation of the HAD nanowire. (**A**) Laser power-dependent multilevel (*top*) Electrical readouts for crystallization processes at various optical pulse powers ranging from 5 (P_{C1}) to 10 (P_{C8}) mW, with a fixed pulse duration of 1 µs. (*bottom*) Electrical readouts for amorphization processes at various optical pulse powers ranging from 26 (P_{A1}) to 37 (P_{A9}) mW, with a fixed pulse duration of 80 ns. Identical initialization pulses (*RESET* for (*top*), *SET* for (*bottom*)) are applied after each programming pulse. (**B**) Pulse duration-dependent multilevel. The power is 11 *mW* (*left*, *SET*) and 25 mW (*right*, *RESET*), with the pulse lengths changing. The polarization angle of all optical pulses described here is fixed at 90° (s-polarized). Initialization pulses (*RESET* for (*left*), *SET* for (*right*)) are applied after each programming pulse.

can be restored to their original states by sending initialization *RESET* pulses for Figure 4.15A (*top*) and 4.15B (*left*) or *SET* pulses for Figure 4.15A (*bottom*) and 4.15B (*right*). The slight volatile behavior observed in the readout after each programming pulse is attributed to the thermal drift in the setup.

The underlying mechanism behind the multilevel operation in phase-change materials can be attributed to the fractional volume of the material that undergoes a phase transition between different crystalline phases, as explained in the referenced literature.[10,15,27,55,100] The volume of the switched domains is influenced by pulse parameters such as laser power or pulse duration. This volume corresponds to the region that reaches temperatures higher than the glass transition temperature (~495 K) or the melting point (~900 K) of the GST. In the case of the HAD nanowire, the switching area primarily depends on the light-nanowire interaction volume, which varies with laser power. To validate this,

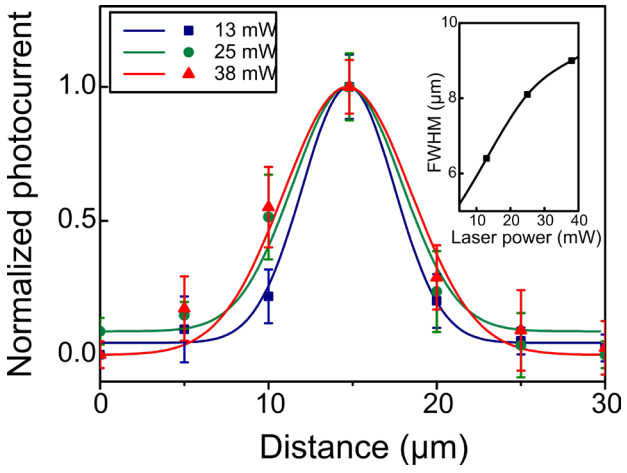


Figure 4.16 Normalized 1D photocurrent profile and Gaussian fitted curves along the scanning distance under different continuous wave (CW) laser powers. The full-width-half-maxima (FWHM) of each curve is measured as 6.4 μm (blue), 8.1 μm (green), and 9.1 μm (red), approximately representing the laser-nanowire interaction sizes. Inset images illustrate the polynomial-fitted trend of the nanowire cross-sections interacting with laser illumination as a function of laser power. The actual switching area can be slightly smaller than the measured spot sizes, depending on the duration of laser pulses.

photoconductance measurements were conducted along the long axis of a nanowire under different laser power illuminations (Figure 4.16). Although the stage movement resolution was not very high (~5 µm), an increasing trend in the full-width-half-maxima (FWHM) of the photoconduction point-spread-function was observed as the laser power increased from 13 to 38 mW. The polynomial-fitted trend provides an estimation of the interacting volume of nanowire under the focused illumination with different laser power. This feature indicates that the interaction area of nanowire with laser illumination remained smaller than 5 µm for laser powers below 9 -10 mW. This also proves that the laser-nanowire interaction area increases as a function of laser power, and such a trend is also in good agreement with the results of intensity-dependent multilevels in Figure 4.15.

4.3.2 Polarization-dependent modulation of electric current

Polarization-selective binary switching

Time-trace electrical measurements were demonstrated in Figure 4.17 for optical pulses at two polarizations (0° and 90°). For this experiment, the parameters for pulse duration and laser power were deducted from the *SET* and *RESET* pulses in Figure 4.14. Only s-polarized pulses switched the state of HAD nanowires and resulted in a reversible, non-volatile change in conductivity, while p-polarized illumination induced negligible changes. The magnitude of change in electrical current (ΔI) under s-polarized pulses was several orders of magnitude larger than that for p-polarized pulses, highlighting the ability to selectively modulate the electrical characteristics of nanowires based on the polarization of incident light pulses.

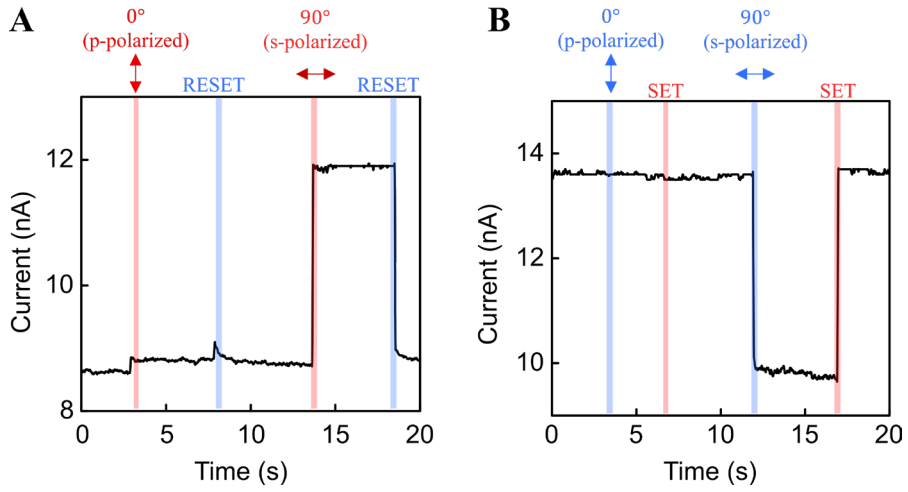


Figure 4.17 Time-trace measurements of polarization-selective electrical readouts for (**A**) crystallisation and (**B**) amorphization using p-polarized (0°) and s-polarized (90°) pulses.

Polarization-dependent multilevel operation

The ability to tune nanowire conductance between multiple levels using a combination of light intensity modulation and polarization selection was investigated. Figure 4.18 shows the results of sending five pulses (0° to 90°) at four distinct powers (12 to 7 mW) and a constant pulse duration (1 µs). At 12 mW, the change in conductance was minimal at 0° polarization and increased significantly as the polarization approached 90°. This switching threshold behavior was consistent across all tested laser powers. At 12 mW, the current exhibits a rapid increase starting at 23° polarization and saturates at 45° polarization. Decreasing the laser power shifted the threshold to higher polarization angles. A similar switching behavior was observed during the amorphization (*RESET*) process, with the threshold polarization shifting from 0° to 45° as the *RESET* laser power is reduced from 38 to 28 mW with a constant pulse duration of 80 ns. Additionally, it was observed that the saturating polarizations increased with decreasing power. This polarization control allows for reaching intermediate levels, providing an additional degree of control in

achieving predetermined conductance states.

Figure 4.19 presents a map of the normalized magnitude of readout current changes (|ΔI|) as a function of incident power and polarizations. The change in readout current saturated in the top left corner when either laser power or polarization was above the threshold. Below saturation, the reached conductance state varied depending on both laser power (x-

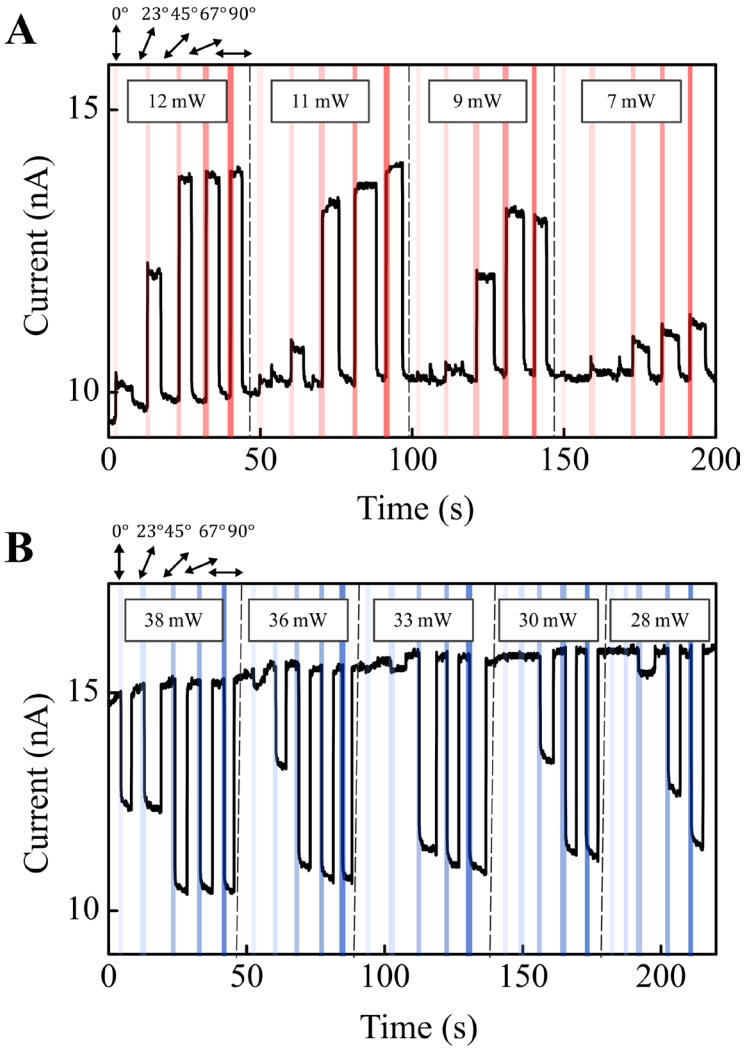


Figure 4.18 Time-trace electrical readouts for (**A**) crystallization and (**B**) amorphization processes at each division as a function of polarizations ranging from 0° to 90° (colored vertical lines). The laser power varies between 12 and 7 *mW* (**A**) (crystallization, *red* lines) and 38 and 28 *mW* (**B**) (amorphization, *blue* lines). The pulse duration for crystallization and amorphization was 1 µs and 80 ns, respectively.

axis) and polarization (y-axis). While the modulation of nanowire state shows a linear relationship with laser power as demonstrated in *Chapter 4.3.1*, the polarization-dependent switching leads to more abrupt changes in the readout. This behavior is attributed to the formation of a conducting path, which relies on a polarization-selective temperature rise above the threshold, as opposed to a linearly-increasing switching area as a function of laser intensity. These linear and non-linear intensity trends of electrical readout as a function of laser power and polarization, respectively, offer intriguing implications for multi-nanowire design in *Chapter 4.4*.

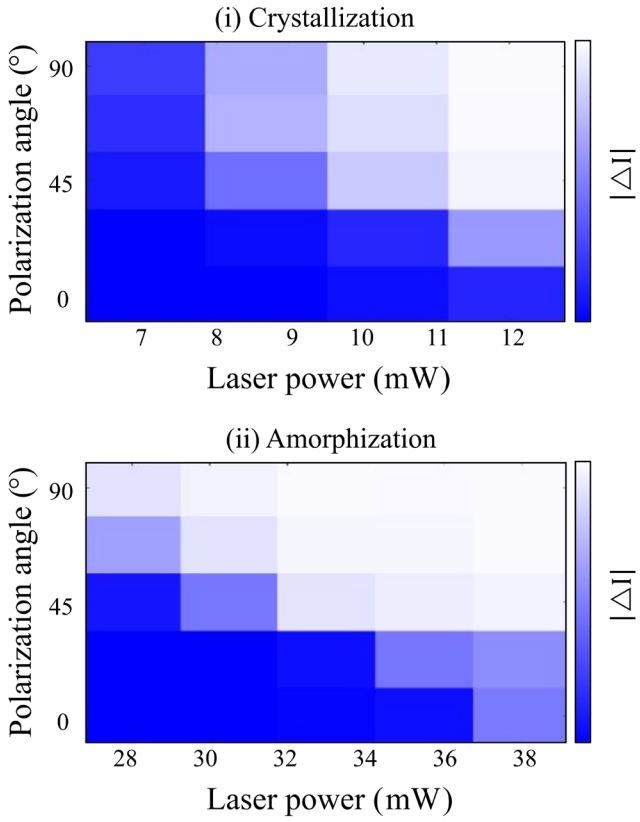


Figure 4.19 2D normalized intensity maps of observed readout contrasts as a function of polarization and laser power. The electrical readout data was extracted from Figure 4.18.

Freely accessible multilevel memories

In Figure 4.20A, stepwise changes in current readouts were observed when three consecutive polarization-controlled *SET* and *RESET* pulses (0°, 45°, and 90°) were applied at fixed powers of 7.5 and 30 mW, respectively. The switching thresholds were located around 45° polarization. The readout of the system depends on the solid state of the nanowires, which modulates their resistivity. This state was programmed using laser pulses and remains nonvolatile until the subsequent pulse. By increasing the fixed laser

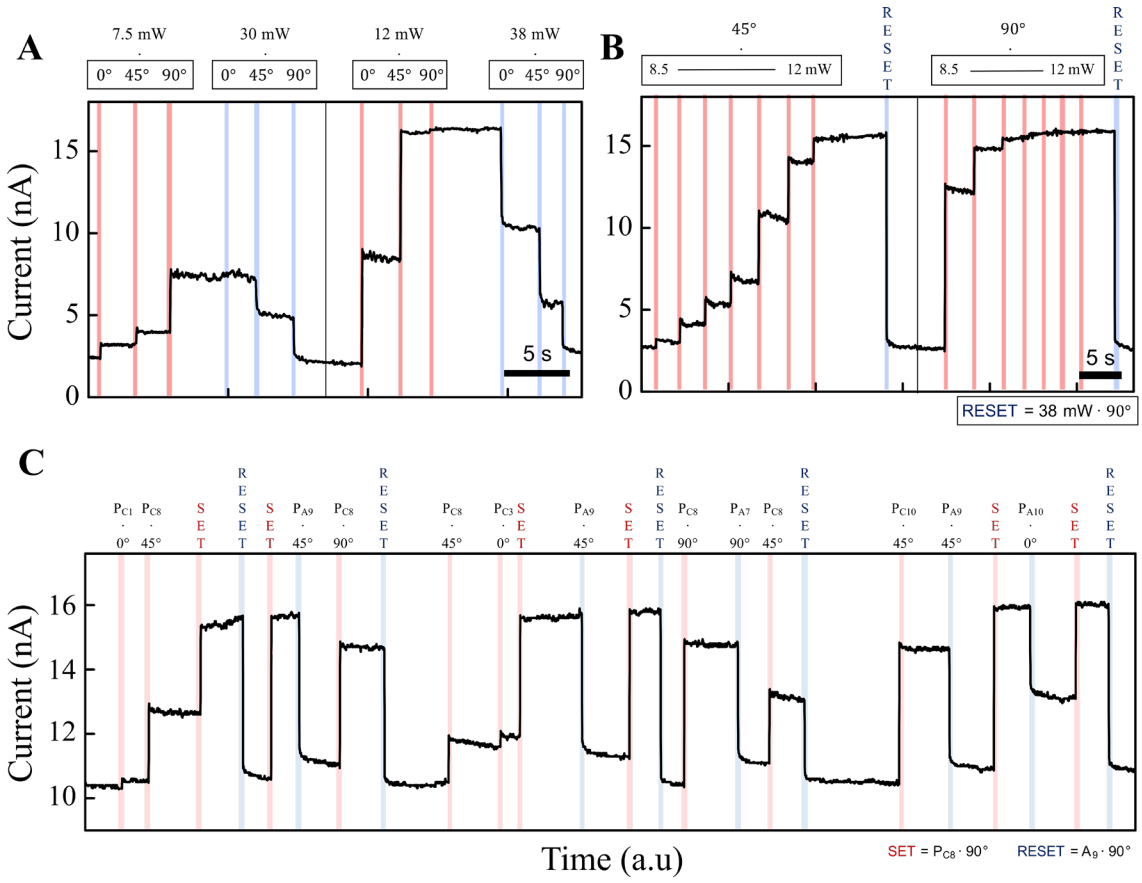


Figure 4.20 Freely-accessible multilevels of the HAD nanowires dependent on polarization and laser power. Time-trace electrical readouts with (**A**) varying polarization at fixed power, (**B**) ramping power at different polarizations, or (**C**) randomly programmed pulses. (**A**) The polarizations range from 0° to 90°, while the laser powers vary for crystallization (*red*) and amorphization (*blue*): 7.5 and 12 mW, and 30 and 38 mW, respectively. (**B**) The polarizations are set at 45° and 90°, while the laser power increases from 8.5 to 12 mW. (**C**) Each notation corresponds to a specific laser power for crystallization, ranging from P_{C1} (5 mW) to P_{C8} (10 mW).

power for both *SET* and *RESET* processes, the threshold polarizations were shifted to 0°. This polarization-controlled operation constitutes a nonlinear system where the selection of thresholds by polarization results in high-contrast multilevel outputs.

In contrast, linearly accessible levels were observed when the laser power was modulated (8.5 to 12 mW) at a fixed polarization, as shown in Figure 4.20B. At 45° polarization, the current readout gradually increased with each pulse and saturated at 12 mW. When the polarization was set to 90° (s-polarized), a power of 9.5 mW was sufficient to saturate the readout. The saturation current level remained unchanged at different polarizations, but varied with different laser powers. This highlights that the saturation levels are determined by the total switched area of the GST layer, which depends on the incident laser power. These results demonstrate a strategy for tailoring the threshold and saturation of nonvolatile readouts through polarization and power, respectively. By leveraging these properties, the accessibility of polarization- and power-dependent multilevels in any random order can be achieved (Figure 4.20C). The observed discrepancies between the absolute values of the multilevel states can be further improved by optimizing the alignment and focusing of the laser.

4.4 Multi-nanowire configuration

4.4.1 Polarization-selective response in a multi-nanowire system

The non-linear readout change as a function of polarizations provides an intriguing possibility of achieving simultaneous multichannel measurement by exploiting polarization as a selector of the HAD nanowire. A key advantage of multichannel

configurations is the ability to acquire multiple selective outputs from a single input of polarized light. A multichannel device was fabricated, consisting of two nanowires aligned orthogonally to each other, denoted as +45° for *nanowire A* and -45° for *nanowire B* (Figure 4.21). Both nanowires were biased at a constant voltage (~1 V) with the third *nanowire C* kept at ground, and the intersection of the nanowires was illuminated by a laser. By applying polarization-controlled optical input, the crystalline phase of each nanowire can be selectively switched while simultaneously monitoring the electrical current.

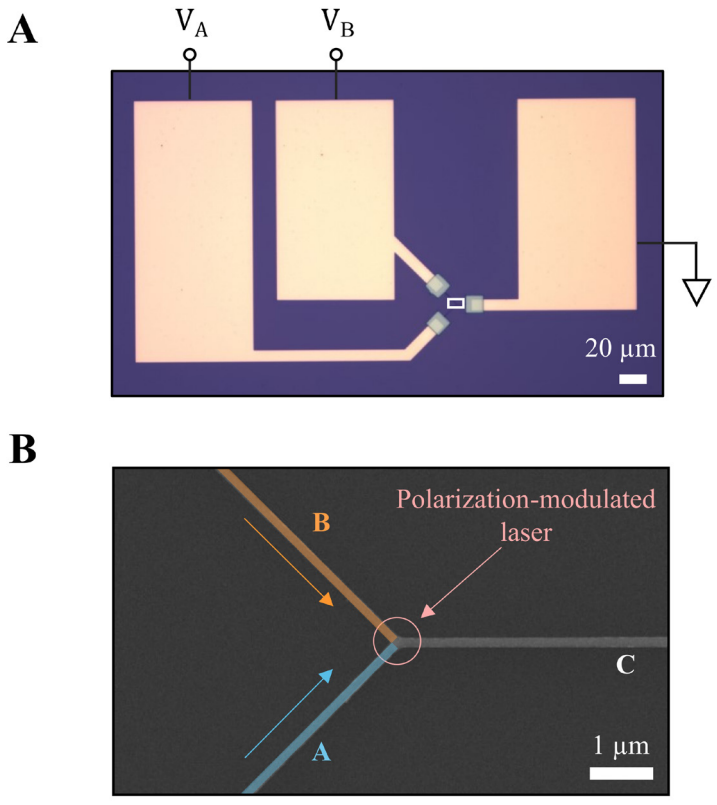


Figure 4.21 Microscope images of multi-nanowire configuration. (**A**) OM and (**B**) SEM images of multi-nanowires measurement. The nanowires A and B are positioned orthogonally and intersect at the junction, denoted as +45° and −45°, respectively. Each nanowire is independently biased as V_A and V_B. The intersection is illuminated by a focused laser. The scale bars represent 20 *µm* and 1 *µm* for (**A**) and (**B**), respectively.

Case 1: Imperfect laser alignment and power setting

The polarization-selective electrical readouts, depicted in Figure 4.22, were observed as the device received +45° and -45°-polarized pulses with a decrease in laser power from P_{C9} (~ 11 mW) to P_{C4} (~ 6 mW). When +45°-polarized light was pulsed, a distinct contrast in current readouts between *nanowire A* (s-polarized) and *nanowire B* (p-polarized) was observed. This observation clearly indicates that *nanowire A* experienced a larger area of laser-crystallized GST compared to *nanowire B*. Similar results were obtained when the light was polarized at -45°, where *nanowire B* exhibited s-polarization and a larger current variation. The absolute current levels decreased as the laser power (i.e., switching area) was reduced, while the polarization-dependent behaviors of the respective nanowires were preserved.

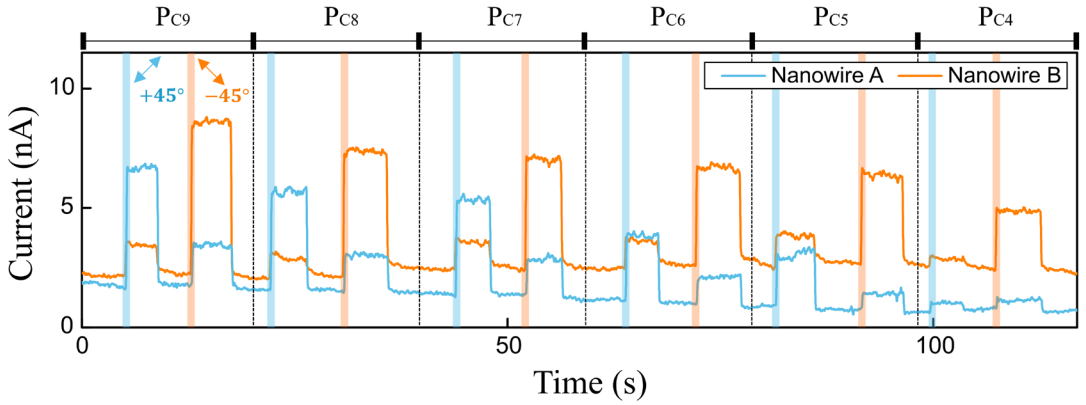


Figure 4.22 Simultaneous time-traced electrical readout of multi-nanowire configuration. The readouts are demonstrated when (*cyan*) the +45° polarized pulse and (*orange*) the −45° polarized pulse are illuminated for crystallization. The measurements are performed at varying laser powers, ranging from P_{C9} (11 mW) to P_{C4} (6 mW). The readouts are initialized using a high-power amorphization pulse.

Throughout the measurement, nontrivial currents were still observed from p-polarized nanowires, primarily due to the unwanted switching in shared intersection area (~ 200 nm wide), or imperfect laser alignment that resulted in a higher intensity change in adjacent

nanowires (p-polarized nanowire or *nanowire C*). However, for instance, at 11 mW laser power, the readout of the p-polarized element constituted only <34% of the dominant s-polarization, thus contributing weakly to the system.

The polarization-selective behavior was also evident during the amorphization (*RESET*) processes as the laser power of the *RESET* pulse decreased from P_{A9} (~35 mW) to P_{A4} (~28 mW) as shown in Figure 4.23. In this process, a device was illuminated with an excessively long pulse (~1 s) of continuous wave (CW) laser to achieve complete crystallization of a previously amorphized domain. Figure 4.23B illustrates the reversible electrical readouts obtained by using nanosecond pulses for amorphization and a one-second-long CW laser for crystallization. Volatile changes in photoconductance were also

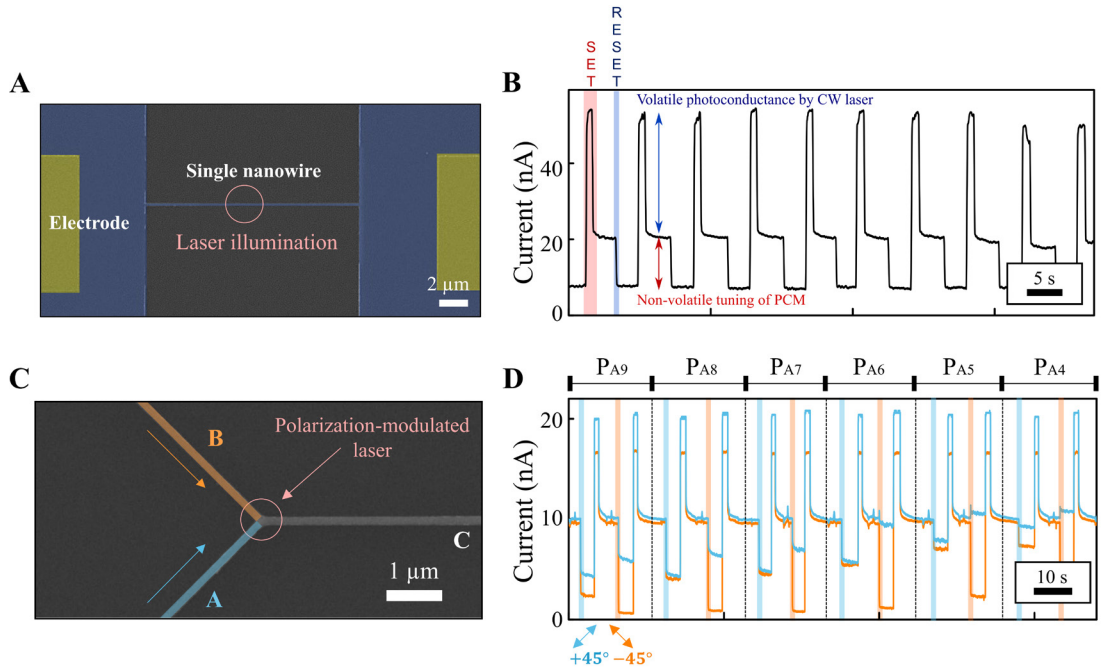


Figure 4.23 Multi-nanowire measurement during amorphization processes. (**A**) OM image and (**B**) the time-trace electrical readouts of device cyclability when the CW laser is illuminated for 1 second to *SET* the device, and a nanosecond pulse to *RESET* it back. (**C**) SEM image and (**D**) simultaneous time-traced measurement of electrical readouts from each nanowire when (*cyan*) the +45° polarized pulse and (*orange*) the −45° polarized pulse are illuminated for crystallization. The measurements are performed at varying laser powers, ranging from P_{A9} (35 mW) to P_{A4} (28 mW). The readouts are initialized using one-second-long CW illumination.

observed during the CW laser illumination. While the volatile changes exhibited consistency when induced by polarized pulses, the non-volatile phase change demonstrated polarization-selectivity (Figure 4.23C-D), as anticipated. Although some discrepancies were observed in absolute current intensities between the two nanowires, the device consistently exhibited good and repeatable contrast in readouts for both s- and p-polarized illumination scenarios. However, the contrast was not significantly noticeable at 35 mW laser power since the p-polarized pulse was already capable of surpassing the switching threshold. Nevertheless, the reduction in laser power (~29 mW) resulted in an increase in the threshold polarization angles, leading to more distinguishable current contrasts. At low laser power, the switching threshold became sufficiently large to amorphize s-polarized nanowires but was not sufficient to ensure full amorphization of the intersected area between the two nanowires.

The consistency of polarization-selective switching is hindered primarily by two factors: the spatial misalignment of the focused laser with the operational nanowires and the excessive laser power required to switch the intersection area (~200 nm) or *nanowire C*. *Nanowire C* serves as the output channel, responsible for summing up the electric current from the other operational nanowires (*nanowire A* and *B*). To ensure the suppression of undesired switching and observe changes solely in the conductivities of *nanowire A* and *B*, it is crucial to maintain a constant state of *nanowire C* during operation. To verify this, a switching experiment was conducted to deliberately control the misalignment (Figure 4.24). Shifting the laser position closer to *nanowire C* (Figure 4.24C, *top*) resulted in nonselective changes in electrical readouts, regardless of the polarization of the incoming light. Conversely, moving the laser towards *nanowire B* (Figure 4.24C, *bottom*) led to a

nonselective change in readouts under the +45°-polarized pulse, while pronounced polarization selectivity was observed under the -45°-polarized pulse. These observations indicate inconsistent polarization selectivity due to laser misalignment. Despite using a manual translation stage with limited resolution, the limitations imposed by misalignment can be overcome by precisely controlling the sample or laser position using a high-resolution piezoelectric stage. Although misalignment is considered a limitation in this work, the fine control of laser position holds promise for providing additional functionality in the future, as demonstrated by previous reports on silicon nanowire-based electro-optic logic gates achieved through laser position control.[123]

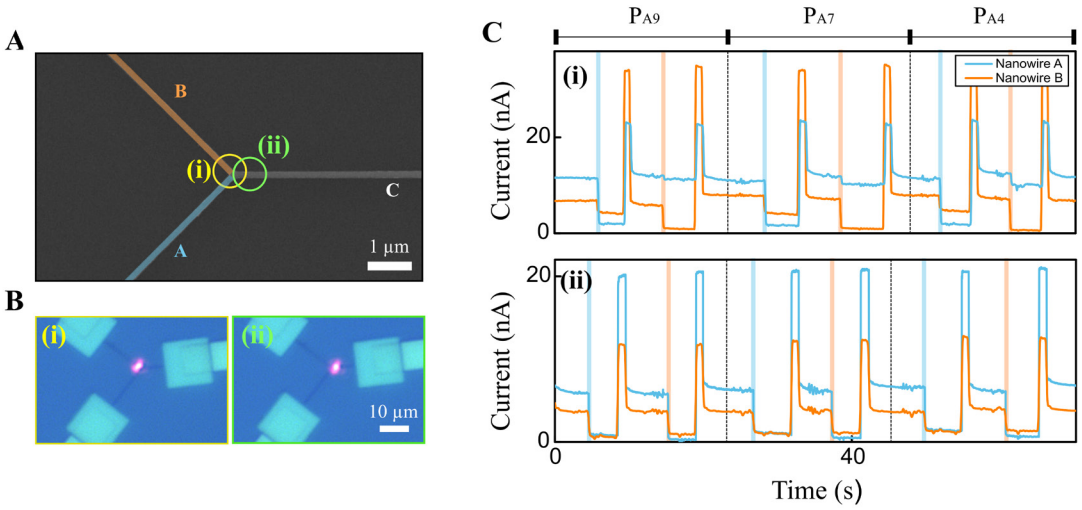


Figure 4.24 Measurement of polarization-selective switching under misalignment conditions. (**A**) SEM and (**B**) OM images of multi-nanowire configuration deliberately positioned in a misaligned location relative to the center of intersection. (**C**) Simultaneous time-traced measurement of electrical readouts from each nanowire under two different misaligned positions, denoted as (*i*) and (*ii*), when illuminated with +45° polarized pulse (*cyan*) and −45° polarized pulse (*orange*). The measurements are performed at varying laser powers, ranging from P_{A9} (35 mW) to P_{A4} (28 mW). The readouts are initialized using one-second-long CW illumination.

Alternatively, the absorption of *nanowire C* can be further minimized by reducing its width, as demonstrated in Figure 4.25. Notably, the 90 nm-wide nanowire (*nanowire C*)

exhibits lower absorption compared to the 180 nm-wide nanowires (*nanowire A* and *B*). As a result, *nanowire A* and *B* can be selectively switched by s- and p-polarized pulses of incoming light, while *nanowire C*, aligned at 45° to the input polarization angles, remains unaffected. However, a narrower width of *nanowire C* may lead to higher resistivity; therefore, the resistivity of *nanowire C* should always be lower than that of *nanowire A* and *B*. This can be achieved by utilizing metallic materials, such as Al or Au, for *nanowire C*.

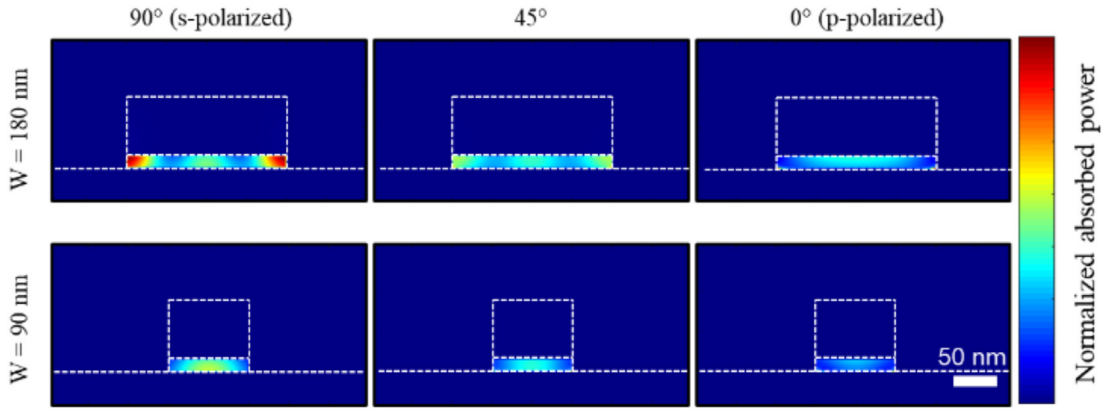


Figure 4.25 Simulated absorbed-power distribution for various nanowire widths. The top image depicts a nanowire width of 180 nm, while the bottom image shows a nanowire width of 90 nm. The incident polarizations are set to (*left*) 90°, (*middle*) 45°, and (*right*) 0°. Scale bar is 50 nm.

Case 2: Reconfigurable polarization-selective demultiplexing

In order to maximize polarization selectivity, the laser power of optical pulses was reduced to enable reconfigurable polarization-selective demultiplexing (Figure 4.26), rather than relying on practically-demanding approaches such as optimizing the geometry or material of *nanowire C*, as stated earlier.

Figure 4.26B-C demonstrates that the conductance levels or weights of each nanowire are determined by utilizing different low laser powers ranging from 5 to 7 mW with

increments of approximately 0.6 mW. When a +45° polarized pulse (7 mW) was applied to the system, *nanowire A* (s-polarized) underwent selective crystallization, while *nanowire B* (p-polarized) remained unaffected (Figure 4.26B (*left*)). Similarly, a −45° polarized pulse (5.6 mW) exclusively switched *nanowire B*, while *nanowire A* remained unaffected (Figure 4.26B (*right*)). As a result, only s-polarized nanowires responded to

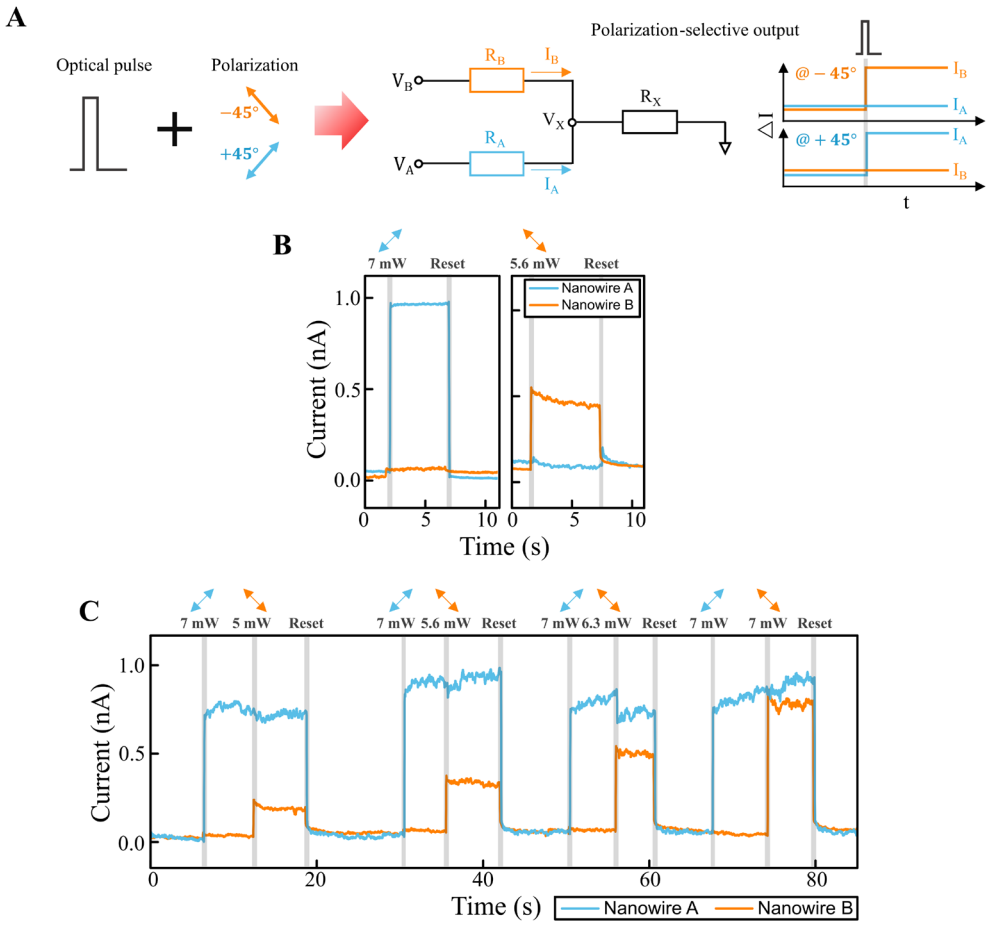


Figure 4.26 Reconfigurable polarization-selective demultiplexing. (**A**) Schematic illustrating polarization-selective demultiplexing, with optical pulses of +45° and −45° polarizations resulting in selective responses in resistances R_A and R_B, and corresponding currents I_A and I_B. Simultaneous time-traced measurement of normalized electrical readouts from multiple channels is shown for (**B**, *left*) the +45° polarized pulse (7 mW) and (**B**, *right*) the −45° polarized pulse (5.6 mW). The readouts are initialized by a high-power amorphization pulse. (**C**) Reconfigurable and polarization-selective demultiplexing, where +45° polarized pulses (*cyan arrows*) of the same laser power (7 mW) are applied, followed by −45° polarized pulses (*orange arrows*) with reconfigurable laser powers (ranging from 5 to 7 mW) to *SET* multiple weighting coefficients.

the input pulses, making the system more robust for polarization-selective threshold operation. The reconfigurability of polarization demultiplexing was then verified by independently encoding distinct weighting coefficients to both nanowires simultaneously (Figure 4.26C). Initially, *nanowire A* was selectively crystallized using a +45° polarized pulse (7 mW; *cyan arrows*). Subsequently, a −45° polarized pulse with a smaller laser power (5 mW; *orange arrows*) was employed to switch *nanowire B* to a specific intermediate state. Thus, polarization was utilized to independently control each nanowire. By increasing the laser powers of −45° polarized pulses, it became possible to selectively define five distinct levels of *nanowire B* without affecting *nanowire A*, thereby allowing for more precise modulation of polarization-selective states. This process exhibits robustness, as *nanowire A* consistently reached the same current level without influencing *nanowire B* when +45° polarized pulses of the same laser power were applied in a similar manner. Such reconfigurable polarization-demultiplexing functionality was also demonstrated during amorphization processes by varying the laser power from 34 to 35.2 mW (Figure 4.27).

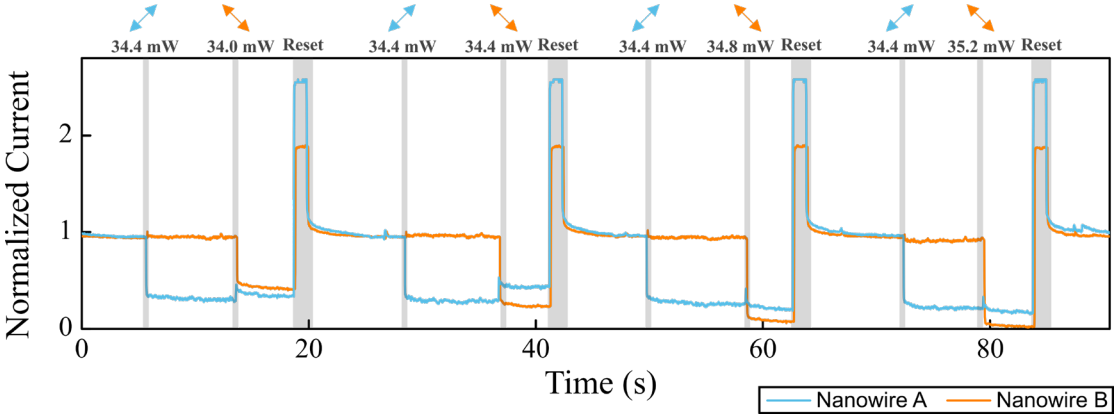


Figure 4.27 Reconfigurable and polarization-selective demultiplexing with amorphization processes, where +45° polarized pulses (*cyan arrows*) of the same laser power (34.4 mW) are applied, followed by −45° polarized pulses (*orange arrows*) with reconfigurable laser powers (ranging from 34 to 35.2 mW) to set multiple weighting coefficients. The readouts are initialized by a long crystallization pulse.

Nontrivial current-reversing effect was also observed in some cases of amorphization process (Figure 4.28). For instance, the polarization-selective amorphization of *nanowire B* induced not just reduction of current in *nanowire B*, but also a slight increment of current in *nanowire A*. This is due to the fact that the shared potential at V_x correlates the current in *nanowire A* (I_A) with the change in resistance in *nanowire B* (R_B), particularly when the resistance exceeds the range. This effect was also seen when the potential of the voltage source (V_B) was abruptly reduced from 1 to 0.5 V, causing a greater proportion of the current from V_A to flow to R_x. This constraint, however, can be overcome by drastically lowering load resistance R_x, such as by metallizing *nanowire C* with Al or Au.

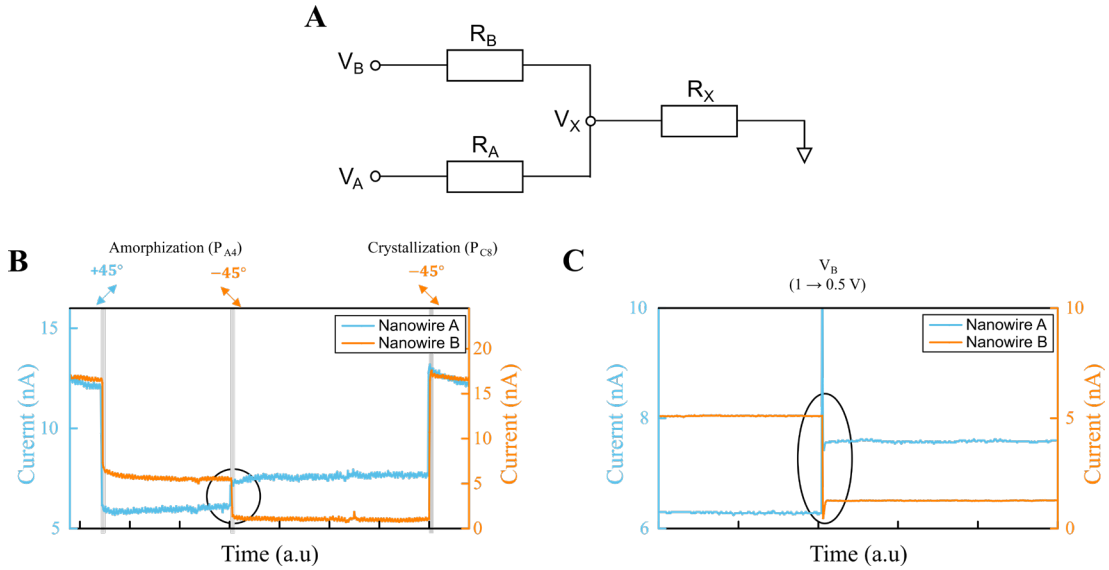


Figure 4.28 Current reversing effect. (**A**) Equivalent electric circuit of multi-nanowire configuration. Current reversing effect (**B**) when -45°-polarized amorphization pulse increases R_B significantly or (**C**) by decreasing the source voltage V_B from 1 to 0.5 V.

However, it should be noted that such design, as evident from the aforementioned results, enables active access to micron-scale polarization-division multilevels with decoupled parameters, whereas current state-of-the-art metasurface-based polarization-division

(de)multiplexing operates in a passive or volatile manner.[124-126] These results reveal not only reconfigurable encoding of up to five nonvolatile multilevels, but also operation at extremely limited scales with active switching areas as small as 5 μm. The interaction area of the focusing laser determines the device footprint, and employing a higher *NA* objective lens can, in theory, improve the spatial resolution, which is ultimately restricted only by the optical diffraction limit. The diffraction limit of focusing laser on this setup is found to be ~ 1.1 μm, while the actual switching area can be slightly larger than this limit due to the imperfect laser alignment or nontrivial heat dissipation along the nanowire.

4.4.2 Matrix-vector multiplication using polarization

The ability to program multilevel states/weights in phase-change materials, such as the GST layer in the HAD nanowires, has been previously utilized in works for providing fast and efficient arithmetic, neuromorphic, and in-memory computing processing.[5,10,92,93] Similar operations can also be carried out using HAD nanowire devices, with the additional benefit of tunability/selection demonstrated by the distinct polarization sensitivity showcased above. Hence, the in-memory matrix-vector-multiplication (MVM)[55] with exploiting polarization as a tunable vector are demonstrated in Figure 4.29. In this case, the sum of the inputs to *nanowires A* and *B*, modulated by their relative weighting, determines the electrical output of the total current (I_T) through *nanowire C*. Each nanowire is subjected to scalar multiplication between the electrical input (V_A or V_B) and the conductivity of the respective nanowire, which serves as synaptic weights (w_A or w_B). These relations can be described in the following equation as,

$$I_T = [V_A \quad V_B] \begin{bmatrix} w_A \\ w_B \end{bmatrix} \tag{4. 4}$$

w_A and w_B are determined by the polarization-selectivity function $f(\emptyset)$ as below

$$w_A = f(\emptyset_1) \tag{4. 5}$$

$$w_B = f(\emptyset_2) \tag{4. 6}$$

,where $\emptyset$ is polarization angle of each optical pulse.

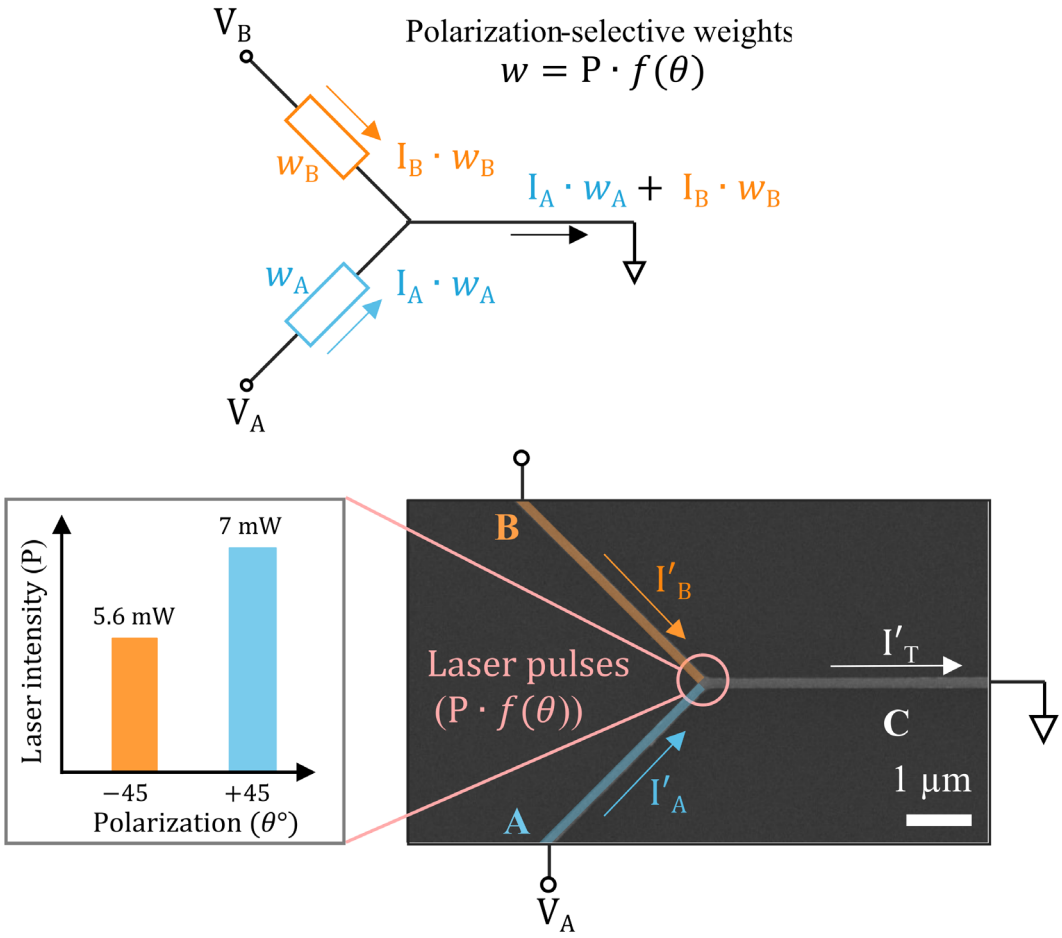


Figure 4.29 Schematic illustration of matrix-vector multiplication utilizing polarization as a tunable factor. Each nanowire undergoes scalar multiplication between the electrical inputs (V_A and V_B) and synaptic weights (w_A and w_B), resulting in output products (~I_A and ~I_B). The total output (I_T) is the sum of these products. The synaptic weights correspond to the conductance parameter of each nanowire (1/R), while the load resistance (R_x) is assumed to be much smaller than the resistances of *nanowires A* and *B* (R_A and R_B). The weights depend on the laser power (P) at specific polarizations (θ). In this demonstration, laser powers of 5.6 mW and 7 mW are used as examples for −45° and +45° polarizations, respectively.

Thus, the multiplication was performed electro-optically, and the addition of two inputs was simultaneously carried out in the electrical domain. Figure 4.30A depicts a single run of matrix-vector multiplication to demonstrate the principle. The nanowires were selectively weighed using polarization, and the resulting output current I'_T was measured by varying the currents at each nanowire. Due to the polarization-selectivity, only s-polarized light can update the synaptic weights of corresponding nanowires, thereby enabling polarization-selective scalar multiplication. As shown in Figure 4.30B, deterministic weight updates enable the execution of cascaded MAC operations, where the subsequent weight updates sequentially lead to new outputs I''_T and I'''_T. These operations can be repeated until either the entire active region of the nanowire becomes crystallized, or a *RESET* pulse is applied.

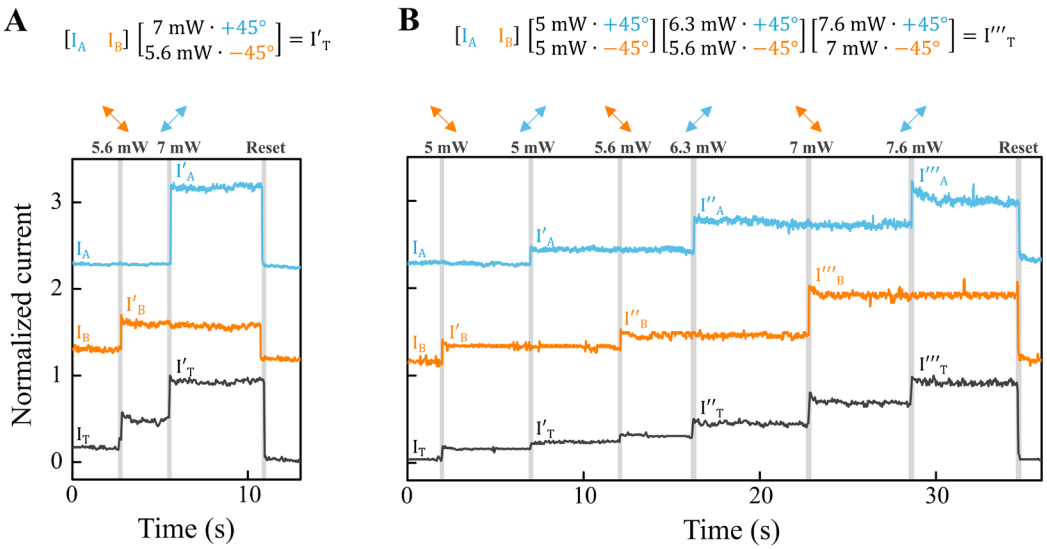


Figure 4.30 Experimental results of matrix-vector multiplication employing polarization-selective weights. (**A**) Single run and (**B**) multiple runs of matrix-vector multiplication operations. The *cyan* and *orange* curves indicate the current flowing through *nanowires A* (I_A) and *B* (I_B), respectively. The *black* curves represent the total current (I_T) flowing through the third nanowire, as shown in Figure 4.29.

It is worth noting that this work achieved the execution of multiple MVM or multiply-accumulate (MAC) operations on a micron-sized element by utilizing a free-space laser. Such compact MAC operation was enabled by selectively choosing elements based on polarization-specific and confined resonances in nanowires. Therefore, the functionality density was found to be greatly increased because of the tight and highly selective confinement, and this can be further enhanced by integrating additional nanowires under the same illumination area. As depicted in Figure 4.31, by decreasing the input laser power below ~6.5 mW, the threshold polarization angle to crystallize the nanowire was above 45°. The incoming light at 45°-polarization cannot switch the nanowire and this allows more nanowires to be embedded at different orientations in a single device.

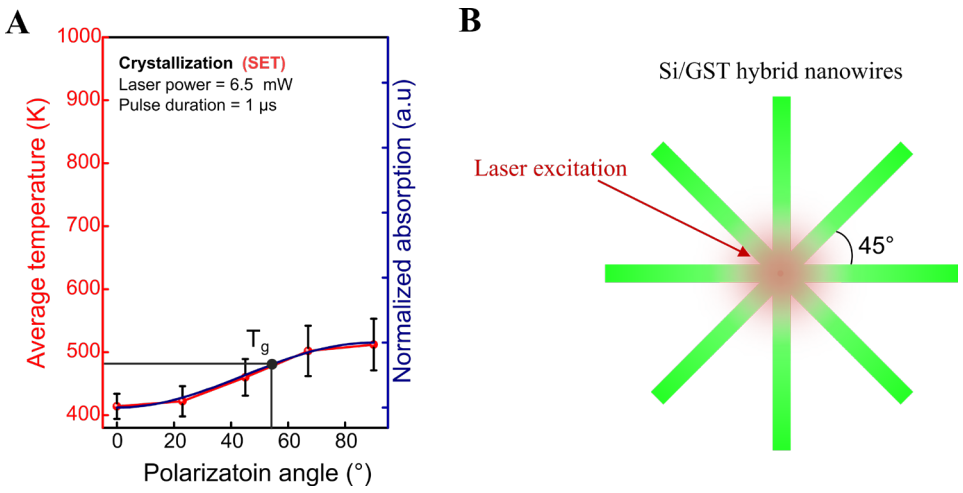


Figure 4.31 Calculated temperature profile and optical absorption of a nanowire based on the polarization angles at low laser power. (**A**) Average temperature and normalized absorption within the GST of a hybrid nanowire as a function of polarization angles during crystallization (6.5 mW). T_g represents the glass transition temperature of GST. (**B**) Schematic diagram of compact multi-polarization-addressable nanowires with 45° angle separation.

In order to quantitatively evaluate the potential of the multi-HAD-nanowire-system for ultrahigh-density and parallel modulation, the compute density between this device and current electronic and photonic architecture is demonstrated in Table 4.1. The compute

density analysis utilizes TOPS (trillions of operations per second)/area, a widely recognized figure-of-merit, as referenced.[5] The estimation of the clock speed in this scenario is based on the switching speed of the crystallization process, while the computing area is defined as the size of either a laser spot or a configuration featuring multiple nanowires. It was found that this system exhibits a significantly higher compute density compared to electronics,[127,128] surpassing it by several orders of magnitude. Moreover, the compute density of the HAD nanowire is comparable to that of photonic in-memory computing utilizing wavelength-division multiplexing. Additionally, the clock speed of the HAD-nanowire system can be improved by performing multiplication operations with dynamically changing volatile inputs like biasing voltage or electro-optically driven photoconductance ($>$GHz).[129] Notably, this system also offers the

	Multiplexing parameter	Clock speed	Number of operations per time step	Footprint of a MAC unit	Selectively tunable synaptic weights	Compute density (TOPS/mm^2)
This work (practical)	Polarization	1 MHz[a]	2	~21 × 25 µm[c] ~5 × 5 µm[d]	Yes	0.004 0.08
This work (theoretical)	Polarization	1 MHz[a]	4[b]	~500 × 500 nm[e]	Yes	16
Nature (2021)	Wavelength	12 or 18 GHz	16	~285 × 354 µm (SiN)[f] ~30 × 30 µm (SOI)[g]	No	1.2 (SiN) 162 (SOI)
Haswell E5-2699 v3	-	2.3 GHz	1	-	-	0.0039
Google TPU (ASIC)	-	700 MHz	1	-	-	0.28
Nvidia Tesla P40 (GPU)	-	1.3 GHz	1	-	-	0.1

Table 4.1 Quantitative comparison of computing density with current electrical and optical devices. [a)]Switching speed of a crystallization process. [b)]Number of polarizations that can be used in a single computing unit (from FDTD calculation in Figure 4.31). [c)]Size of multiple-nanowire configuration. [d)]Size of a laser spot at the laser power of 5 mW. [e)]Minimum required nanowire size for activating polarization-selective switching (based on FDTD calculation, see Figure 4.32).[f, g)]Size of each computing unit for silicon nitride (SiN) and silicon-on-insulator (SOI) platforms. Note: The active region or photonic tensor core area is considered for this system, and the convolutional photonic architecture from the reference (Ref. [5]) is evaluated separately. Ref. [5] and [127].

additional functionality of selectively tuning synaptic weights. The compute density is greatly affected by the size of device footprints, and substantial improvements can be achieved by incorporating more nanowires (Figure 4.31) or reducing the size of computing units (Figure 4.32). Figure 4.32 illustrates the calculation of nanowire absorption considering varying aspect ratios of nanowire lengths to widths. It was observed that polarization-selective absorption remained intact at a nanowire length (aspect ratio) of 500 nm (2.7:1), presenting an opportunity to scale down the electro-optic device and increase device densities. However, achieving simultaneous illumination on multiple computing units and ensuring their cascadability within a large-scale system will require further design optimization. Also, this Table 4.1 does not take into account the programming energy consumption, which has been found to be less efficient compared to other electro-optical modulators such as lithium niobate[96] or silicon carbide.[95] This is due to unwanted back reflection in the HAD nanowire (Figure 4.3), leading to an imperfect absorption within the GST layer. The work described herein primarily focused on the selective

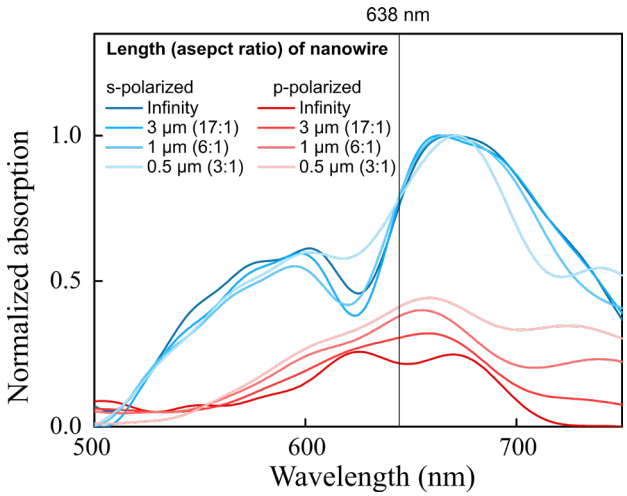


Figure 4.32 Normalized absorption spectra of nanowires with varying lengths (i.e. aspect ratio) for both s- and p-polarizations.

absorption properties as a function of incoming polarization, rather than the magnitude of absolute absorption itself. Therefore, the programming energy could potentially be reduced by improving the confinement of the electric field within the nanowire, utilizing techniques such as leveraging the fundamental mode or introducing an additional capping layer to enhance the electric field confinement, as discussed in *Chapter 4.2.2*. Despite the current suboptimal programming energy efficiency, it is important to highlight that the system operates in a non-volatile manner and features zero static power consumption. This allows the PCM-incorporated HAD nanowire to operate as an energy-efficient optical switch, particularly suitable for some in-memory computing[55] and convolutional processor[5] applications.

4.5 Further exploitation of the hybridized-active-dielectric nanowire

The potential functionalities of the HAD nanowire extend beyond computing. For instance, the combination of nanowire geometry and active tunability opens up intriguing possibilities for its use as a nanowire photodetector. Furthermore, the concept of the HAD configuration can be readily generalized to other active or dielectric materials that implement hybrid structures with functional dielectrics, enabling the realization of unique functionalities in spectral imaging. The examples below demonstrate these concepts.

Polarization-dependent photoconductor

By adjusting the spatial position of the CW laser light, asymmetric photoconductance can be detected and modulated. Figure 4.33 shows how the polarity of the change in

photoconductance is affected by the position of the focused laser illumination. The magnitude of photoconductance is directly proportional to the biasing voltage, laser power, and polarization angles, while the polarity of photoconductance is determined by the spatial location of the illumination along the nanowire axis. These features can be attributed to the formation of a thermo-voltage induced by an asymmetric temperature gradient resulting from laser annealing processes.[130] The observed features may also be

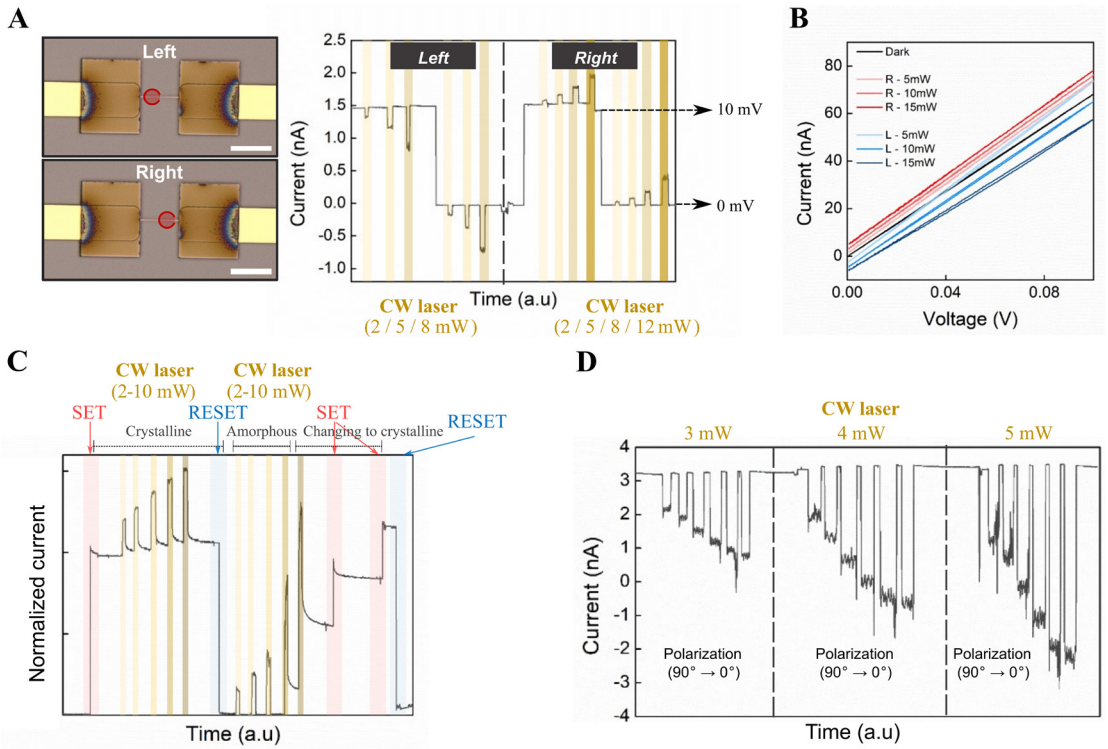


Figure 4.33 Asymmetric photoconductance of HAD nanowire with varied position of illumination. (**A**) (*left*) OM image, (*right*) time-traced electrical readout and (**B**) I-V curves of HAD nanowire depending on the position of laser illumination. Electrical readout increases (decreases) as the CW laser is illuminated on the right (*left*) of the long-axis of the nanowire. (**C**) Time-traced electrical readout of HAD nanowire, with *SET* and *RESET* laser pulses applied to crystallize and amorphize the device, respectively. CW laser illumination with varying power results in photoconductance. Note that the non-volatile phase-change was observed during high-power CW laser illumination as well. The *SET* (*RESET*) process involves an optical pulse of 9 (35) mW at 1 (0.08) μs. (**D**) Polarization and power-dependent photoconductance. Polarization is rotated from 90° (s-polarized) to 0° (p-polarized). The duration of each illumination is 1 s.

attributed to the photogating effect, a phenomenon that has been demonstrated in semiconductor nanowire photodetectors.[131,132]

Moreover, both volatile and non-volatile changes in the readout can be measured by illuminating the CW laser in different positions or by switching the nanowire using nanosecond pulses (Figure 4.33C). The volatility of these changes also depends on the polarization angles and CW laser power (Figure 4.33D), which raises interesting possibilities for employing this system as a polarization- or position-dependent electro-optical comparator. This was enabled by leveraging the spatial degrees-of-freedom through raster scanning the focused laser spot for free-space illumination.[123] The concept of exploiting spatial degrees-of-freedom has been further explored in integrated photonics, which will be discussed in *Chapter 6*.

Hyperspectral imaging using HAD nanowires with low-loss PCM

Forming low-loss dielectrics (eg, Si) with high index and sufficient thickness to support dielectric resonances, as well as a thin lossy layer (eg, GST) beneath to asymmetrically couple most of the light, is a prerequisite for satisfying the resonance and reconfigurability requirements of HAD nanowire. Instead of using static dielectrics and lossy PCMs, by incorporating low-loss PCM as tunable dielectric resonators and a lossy photoabsorber as a bottom detector, a novel scanning spectrometer structure can be realized (see Figure 4.34). By tuning the geometry or crystalline state of low-loss PCM (eg, Sb_2Se_3) the spectral absorption peak is accordingly shifted and detected by the thin absorber (eg, Ge). By gradually switching PCM via free-space laser annealing or integrated microheaters, a number of absorption peaks can be measured, thereby enabling scanning-type

hyperspectral imaging at spatially confined scales. Photoabsorber can be replaced with other thin photoconductors, such as 2D materials (eg MoS_2, $MoTe_2$).[133,134] A variety of unique functions can be unlocked by rearranging the structure and components of the HAD nanowire into various dielectrics, PCMs, or non-linear materials.

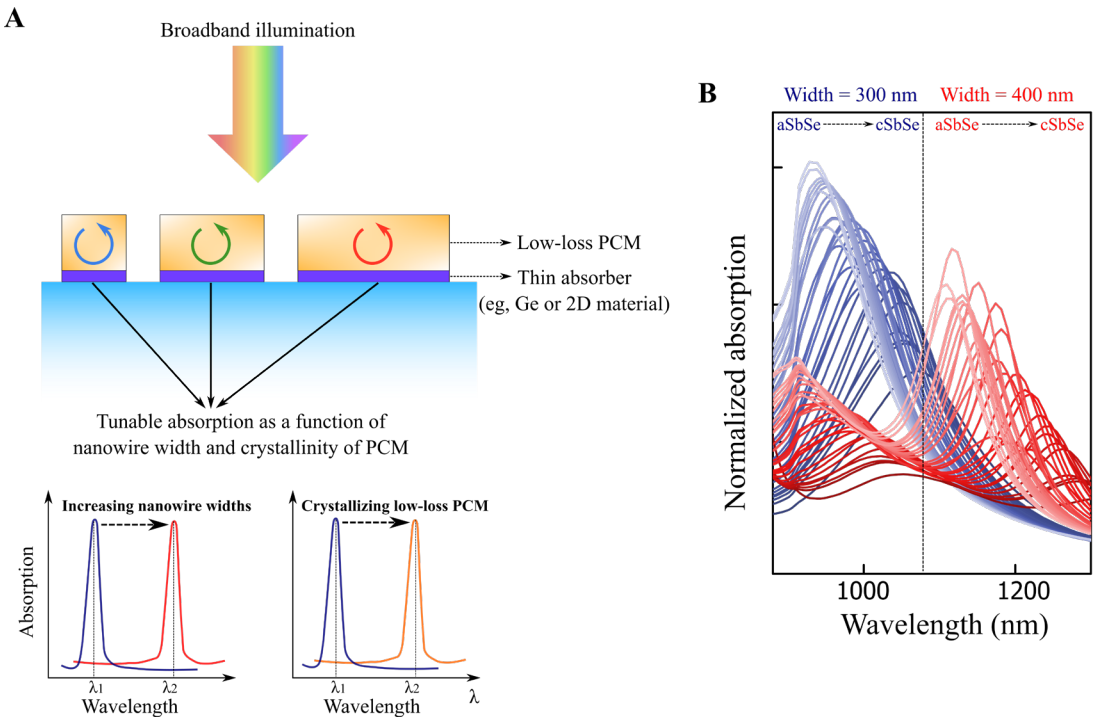


Figure 4.34 (**A**) Schematics of scanning-type hyperspectral imaging using multiple HAD nanowires in different widths and crystalline states. The dielectric resonance of low-loss PCM (Sb_2Se_3) results in the tunable absorption in the thin static absorber (eg, Ge). The absorption peak is redshifted by increasing the refractive index of low-loss PCM by crystallization or expanding the nanowire widths, respectively. (**B**) Calculated absorption spectra with the nanowire widths of 300 (*blue*) and 400 nm (*red*), as a function of change in crystalline states changing from amorphous (aSbSe) to crystalline (cSbSe). Thickness of Sb_2Se_3 and Ge are 130 and 10 nm, respectively.

4.6 Chapter summary, critical review and outlook

This chapter presents the first proof of concept for polarization-selective switching in a HAD nanowire, thereby expanding the dimension of functionalities into polarization

space. By employing this approach, this work achieved reconfigurable and non-volatile polarization-division (de)multiplexing of electrical conductivity. Furthermore, the combination of electrical coupling and polarization decoupling enabled the operation of MVM (Matrix-Vector-Multiplication) with the input polarization as a tunable vector element. These findings introduce a new tunable approach to phase-change photonic society, enabling a wide range of applications that leverage the diverse properties of light. This concept possesses many interesting attributes that can be extended to a larger framework, including:

- The tunability can extend beyond linearly polarized light to achieve tunable optoelectronics/photonics with vortex beams, utilizing adjustable factors such as orbital angular momentum or optical chirality. The tunability specific to orbital angular momentum (OAM)[6] is particularly potent due to its multiplexing capabilities.
- The electrical-accessibility of the HAD nanowire makes it suitable for various electro-optic devices or computing applications. Although parallel information processing occurs in the optical domain, the dual functionality of PCM in both the electrical and optical domains enables the reading and manipulation of device states in the electrical domain. This facilitates the so-called mixed-mode operation, which further enhances its benefits with nanowire optoelectronic devices.
- The HAD configuration can be expanded to include other combinations of active and non-linear materials. Specifically, the use of low-loss PCM and non-linear

absorbers such as 2D materials can leverage a range of interesting tunable functionalities.

Limitations

While this work serves as the first proof-of-concept exploiting polarization as a non-volatile tunable parameter for device reconfigurability, this system faces with certain technological limitations that require further enhancement, as outlined below:

1. **Orthogonality of polarization-multiplexing**

In the multi-nanowire measurements (*Chapter 4.4*), the experimental polarization-selective switching was achieved by applying pulses of two orthogonal polarizations with a specific time interval. This interval was necessitated due to the practical constraint of simultaneously exciting multiple polarizations using lasers, as well as to effectively showcase the concept of polarization-selective switching by applying each pulse individually. While two orthogonal nanowires (e.g., s- and p-polarized nanowires) inherently possess fully decoupled optical states, selecting any other combination of two or more nanowires (as shown in Figure 4.31) could result in undesired interference when subjected to coherent light with non-orthogonal polarizations (e.g., 0° and 45°). This challenge can be mitigated by introducing slight temporal or spectral differences between input pulses to reduce coherence. However, this approach may compromise operation speed or bandwidth. In an ideal case, orthogonal light properties such as orbital angular momentum (OAM)[6] can be used to address this issue.

2. Operation speed of phase-change material

PCM offers the advantage of non-volatility and substantial optical/electrical contrast within a compact volume, making it superior to the established polarization-modulated technologies like liquid-crystal devices[135] which often require larger switching volumes for optical contrast and are mainly limited to volatile tunability. However, the processing speed of phase-change operations is primarily constrained by the crystallization process, operating within the MHz range. This limitation could be problematic for some computing applications, particularly those involving frequent weight updates during processing. While the use of femtosecond pulses can significantly increase the PCM switching speed (*Chapter 2.2*), this approach requires further investigation to validate its physical mechanisms and establish robust multilevel programming operations.

On the other hand, alternative high-speed switching methods can be integrated into HAD systems. For instance, materials with epsilon-near-zero (ENZ) properties[136] or 2D materials[137] could be readily combined with dielectrics supporting polarization-selective resonance, enabling faster switching than GHz rates. However, such designs would need to engineer optical absorption capable of triggering the device reconfiguration. It is worth noting that these technologies typically exhibit volatile tunability, potentially leading to higher energy consumption compared to non-volatile techniques. Alternatively, non-volatile approaches like photoferroelectric switches[138] could be employed at the expense of modulation speed.

Therefore, various alternative switching methods can replace PCMs within HAD configuration, taking into account the merits and drawbacks of these tunable methods

in relation to specific applications. For example, in applications such as spectrometry, imaging, or spiking networks, volatile tunability is preferable, aligning with the choice of high-speed switching methods. As a result, the versatility of incorporating alternative switching methodologies into HAD systems can be viewed as an advantage rather than a limitation, offering the opportunity to harness diverse modulation approaches to their maximum advantage.

3. Scalability

One major limitation of the HAD nanowire system is its scalability. Currently, the scale of such functionality is constrained by the size of free-space illumination. While using free-space light to leverage spatial degrees-of-freedom is advantageous, it is still limited by the cascading capability of multiple free-space lasers. This can be ultimately overcome by employing fast raster scanning[139] or utilizing LED arrays[140] with individual control of each unit. Alternatively, polarization selectivity can be incorporated into scalable integrated photonic circuits using polarization converters (transverse-electric to transverse-magnetic modes)[141] and polarization-selective plasmonic nanogaps.[15] However, further study on integrated photonics is needed to enlarge the field-of-view of in-plane mode propagation (*Chapter 6*) and embed multiple polarization functionalities in waveguide modes. Another approach to upscale the functionality is to closely assemble multiple nanowires or nanoresonators in an array smaller than the illumination area, resulting in a subwavelength metasurface. This platform can unlock new functionalities, not only in the polarization domain but also in multiple photonic or spatial domains, as discussed in the next chapter (*Chapter 5*).

4.7 Acknowledgement and contribution

The concept of polarization-selective switching has been conceived by the author. All design, simulation, fabrication, and measurement were performed by the author. Device characterization was accomplished with the contribution of Nikolas Farmakidis. The work presented in this chapter has been published in the following article:

- J. S. Lee, N. Farmakidis, C. D. Wright, H. Bhaskaran, "Polarization-selective reconfigurability in hybridized-active-dielectric nanowires", *Science Advances,* **8 (24)**, eabn9459 (2022)

Also, this work has been presented at many international conferences, including *2022 MRS Fall Meeting*, *IEEE Nano 2022*, *EPCOS 2022*, *2023 MRS Spring Meeting* and press-releases, including *News in University of Oxford*, *Physics World,* and *Electro Optics*.

Chapter 5

Active phase-gradient metasurfaces using low-loss phase-change material

This chapter extends the functionality of active nanophotonic system from a single element to metasurfaces. Active metasurfaces are demonstrated using low-loss phase-change materials (PCMs) such as Sb_2Se_3, Sb_2S_3, Ge_2Se_3, or GeTe. Instead of polarization being used as a tunable factor in *Chapter 4*, the optical phase delay is exploited as an individual tunable component to implement metasurface, enabling wavefront manipulation. First, the design, simulation, and experimental results of the Sb_2Se_3 metalens are introduced (*Section 5.2*), followed by the results of active reversible switching of low-loss materials (*Section 5.3*). *Section 5.2* includes the demonstration of both single-focal and varifocal metalenses. *Section 5.3* covers the optical and electrical methods employed for dynamically switching low-loss phase-change material. *Section 5.4* shows the potential applications with additional functionalities, concluding with a summary in *Section 5.5*.

5.1 Overview: Assembling an array of phase-selective nanostructures

In *Chapter 4*, the device density was maximized through the incorporation of multiple photonic functionalities into a single nanostructure utilizing polarization-space. Although scaling up the number of elements is expected to proportionally enhance device functionality, the pivotal breakthrough lies in the arrangement of these nanoscale structures within a subwavelength periodic array. This approach unlocks a plethora of unique and unprecedented functionalities, aptly referred to as metasurfaces.

Metasurfaces serve as a potent platform for wavefront manipulation, leveraging the interference of adjacent wavelets with disparate optical phases.[87] In a similar case to the achievement of polarization-selectivity through the resonances of hybridized-dielectric nanowires discussed in *Chapter 4*, the relative phase delay of scattering resonance is dictated by tunable nanoresonators that can be modulated by size and material of the structure. Therefore, the assembly of phase-selective nanoresonator enables the position-dependent phase shifts, giving rise to phase-gradient metasurfaces. Due to scattering interferences between neighboring nanoresonators, such a metasurface allows manipulation of the emerging wavefront, paving the way for novel applications in adaptive optics[128,142] such as lenses, beam steering, and holograms. It is truly remarkable that these applications operate within ultrathin dimensions, commonly known as flat optics. A notable example is the flat lens (i.e. metalens),[143] which shows equivalent or even superior performance compared to traditional glass lenses, while being 100,000 times thinner in thickness. However, despite their advantages, flat optics are not without limitations, particularly in terms of their static properties, which prohibits post-fabrication modulation

of their functionalities. Thus, the use of PCMs to realize reconfigurable and phase-selective resonators marks a significant advancement in the pursuit of tunable metasurfaces.[11] In this case, optical scattering serves as the output response, thus favoring the utilization of low-loss phase-change materials to mitigate Ohmic loss.

5.2 Active low-loss metasurfaces using Sb_2Se_3 Mie resonators

Commencing with the work initiated by Zheludev *et al* in 2016,[14] the exploration of PCM-based metasurfaces has witnessed remarkable advancements. While many designs have employed GST as the tunable material for metasurface, the high insertion loss observed in the crystalline state of GST degrades device efficiency, thus limiting their overall performance and applicability. Consequently, extensive research has been carried out to discover low-loss alternatives for lossy phase-change chalcogenides.[57,62] A recent development involves GSST,[61] which exhibits exceptional broadband transparency and reconfigurable metalens was successfully realized;[48] however, their operating wavelength was limited to the mid-infrared (MIR) range (5.2 μm) due to small changes in real part of the refractive index (Δn) or non-trivial losses (k) below a wavelength of ~4 μm. Therefore, the experimental demonstration of a tunable all-dielectric metalens in the near-infrared (NIR) range remains elusive thus far.

5.2.1 Optical modelling of meta-atom

A dielectric metamaterial consists of an array of dielectric meta-atom, in this case Sb_2Se_3 nanopillars, which can support electromagnetic Mie resonances within their cavity (Figure 5.1A). Sb_2Se_3, which has recently emerged as a low-loss PCM in various photonic

applications,[58,60] exhibits exceptionally low optical loss ($k \sim 0$), alongside high optical index ($n > 3.5$) and index contrast ($\Delta n \sim 1$) within NIR wavelengths (1100 – 1600 nm). These high index-contrast, low-loss characteristics render it highly suitable for tunable meta-atoms. The plot of refractive indices for amorphous and crystalline states of Sb_2Se_3 (Figure 5.1B) was experimentally acquired by carrying out ellipsometry measurement (J.

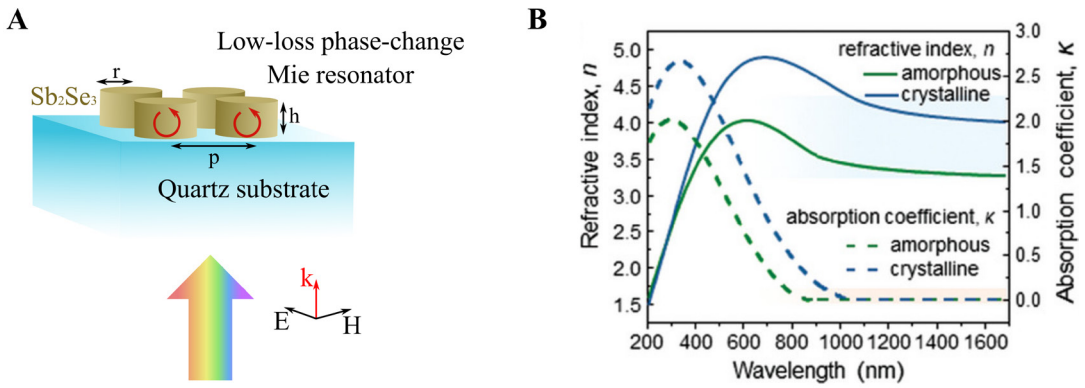


Figure 5.1 Sb_2Se_3 dielectric metasurfaces. (**A**) Schematic diagram of a Sb_2Se_3 nanopillar array on quartz substrate. (**B**) Measured refractive indices of the amorphous and crystalline states of Sb_2Se_3 thin film.

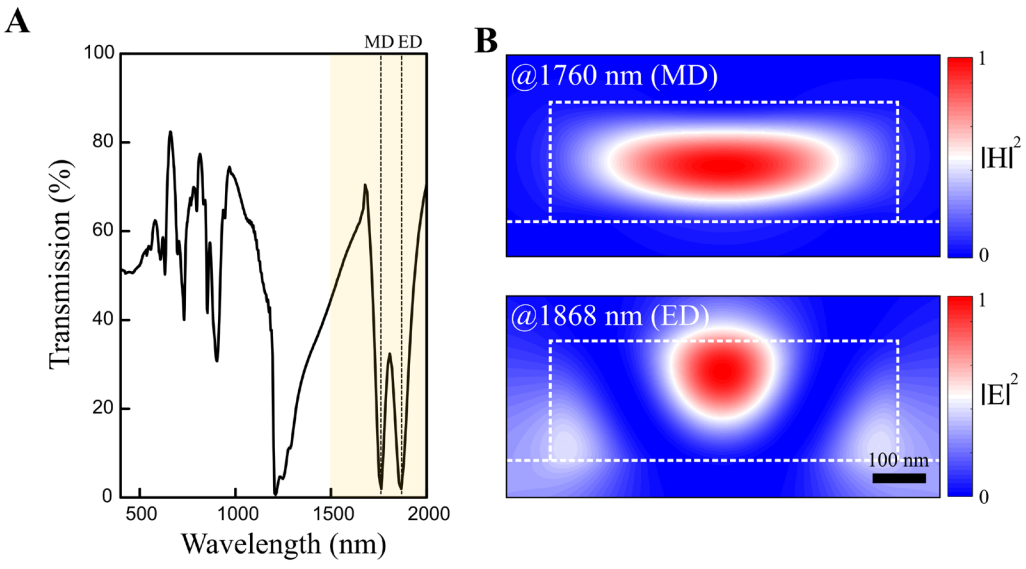


Figure 5.2 Optical response of a a-Sb_2Se_3 nanopillar array. (**A**) Transmission spectrum of an a-Sb_2Se_3 nanopillar array with the following parameters. p = 900 nm, r = 300 nm, h = 278 nm. Two spectral dips represent magnetic- and electric-dipoles, respectively. (**B**) Cross-sectional view of (*top*) magnetic and (*bottom*) electric-dipole modes in a nanopillar cavity at each spectral resonance. Scale bar is 100 nm.

A. Woollam) on a 250 nm-thick Sb_2Se_3 thin film and fitting the measured data with the Cody-Lorentz oscillator model.

Using this optical constant, the transmission spectrum of amorphous-Sb_2Se_3 (a-Sb_2Se_3) nanopillar array was simulated (Figure 5.2A). The nanopillars had fixed dimensions, with a radius (r) of 300 nm and a thickness (h) of 225 nm. The array maintained a fixed period (p) of 3 times the radius (i.e., 900 nm). It was evident that visible-NIR light generates complex multipolar resonant modes and experiences some attenuation due to non-trivial material loss, while NIR light above the wavelength of 1500 nm passes through the Sb_2Se_3 metasurfaces nearly undisturbed, except for spectral dips caused by electric- or magnetic-dipole resonances, as shown in Figure 5.2B. The presence of a strongly confined electromagnetic-nearfield within the nanopillar volume also indicates field enhancement from individual Mie resonators that are decoupled from adjacent elements.

The positions of these spectral dips (i.e. each dipole moment) vary depending on the size of nanopillars, as demonstrated in Figure 5.3A which displays a transmission spectral map as a function of nanopillar radii (100 – 400 nm). At a wavelength of 1550 nm and a nanopillar radius of 326 nm, there was observed to be a spectral overlap between electric and magnetic dipoles. This spatial and spectral overlap is significant because it allows constructive and destructive interference of the scattered field for both forward and backward propagation when the electric and magnetic dipole moments share the same wavelength, strength, and phase (as described in *Chapter 2.4.1*), as recognized by the Kerker condition.[82] This mode overlap enables achieving high transmission with 2π phase shifts around the resonant wavelength (λ - 1550 nm), which is twice the maximum phase delay that each resonance can exhibit (i.e., π) (Figure 5.3B). Such spectral mode overlap

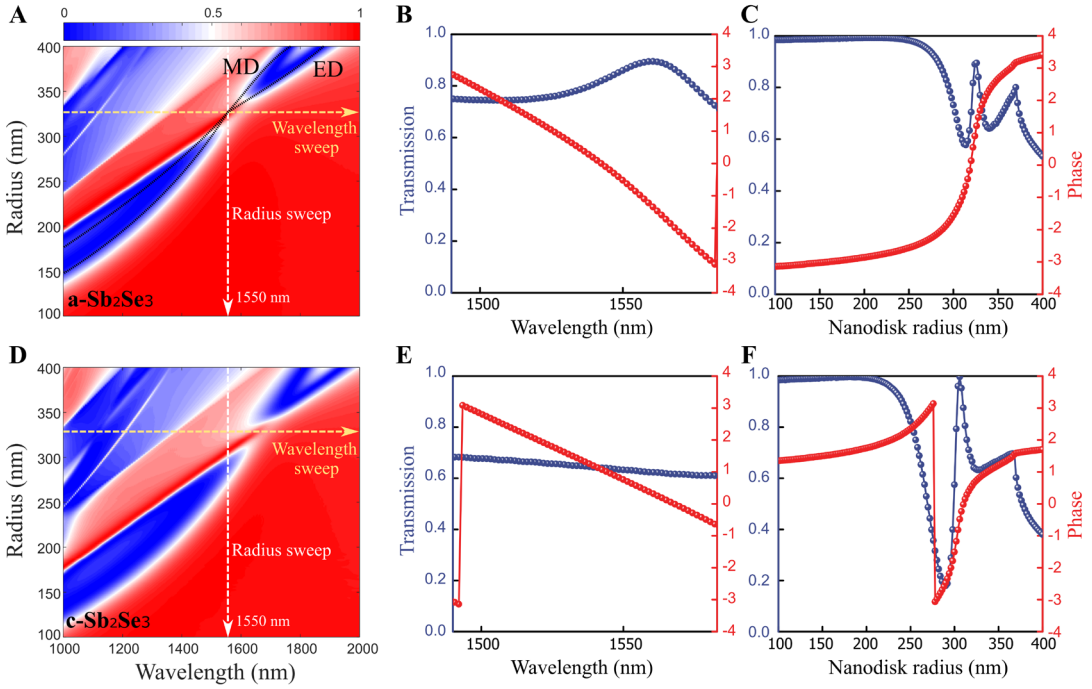


Figure 5.3 Mode overlap in the Sb_2Se_3 meta-atom. (**A, D**) Calculated transmission response of Sb_2Se_3 nanopillar array as a function of wavelength and its radius (r). The period of an array is $3r$. Spectral overlap between electric- and magnetic-dipoles is observed at the wavelength of 1550 nm for a-Sb_2Se_3. Transmission and phase response is demonstrated with (**B**, **E**) varying wavelengths (1490 – 1580 nm) at a fixed nanopillar radius of 326 nm and (**C**, **F**) with varying nanopillar radii (100 – 400 nm) at a target wavelength (1550 nm). *Top* (**A-C**) and *bottom* (**D-F**) rows demonstrate the results for amorphous- and crystalline-Sb_2Se_3 nanopillars, respectively.

can be tailored by adjusting the diameter of nanopillars (d = 100 – 400 nm), which in turn obtains a large optical phase modulation with an average transmission higher than 87% (Figure 5.3C). This relationship between phase and nanopillar diameter serves as an important guideline for designing Huygen's metasurfaces, and the accessibility to 2π phase shift is required to provide full control of the wavefront, realizing high-*NA* metalens.

Alternatively, phase modulation can be achieved by modifying the material properties, such as the crystallinity of PCM, instead of manipulating the geometrical parameters. A similar approach has been made in Ge-GST-Ge hybrid system, by tuning the crystallinity of GST.[81] However, this necessitates precise switching of material states, which will be

further discussed in *Chapter 5.3*.

Upon crystallization of the Sb_2Se_3, these spectral mode overlaps experience a significant redshift, thereby losing support for electric- and magnetic-dipole resonances at a wavelength of 1550 nm and resulting in an insufficient or random phase shift (Figure 5.3D-F). Hence, the capability of wavefront manipulation becomes inactive in the crystalline states. However, by reducing the thickness of the nanopillar to 235 nm, spectral mode overlap can be achieved in the crystalline states at a wavelength of 1500 nm (Figure 5.4). In this case, the desired transmission and phase profile (2π shift) are attained in crystalline states, but not in amorphous states. These switchable characteristics of the

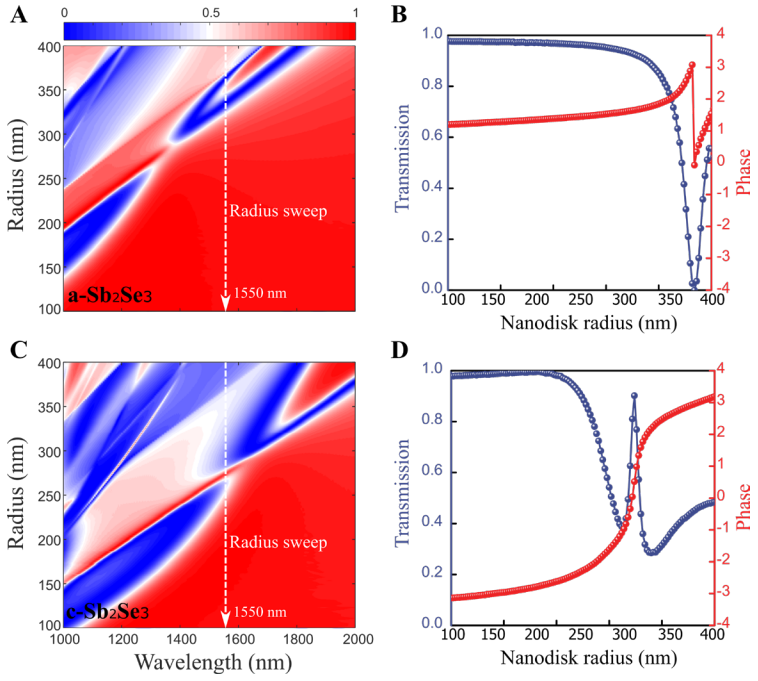


Figure 5.4 Mode overlap in the Sb_2Se_3 meta-atom with reduced thickness. (**A, C**) Calculated transmission response of a 235 nm-thick Sb_2Se_3 nanopillar array as a function of wavelength and its radius (r). The period of an array is $3r$. Spectral overlap between electric- and magnetic-dipoles is observed at the wavelength of 1550 nm for c-Sb_2Se_3. (**B, D**) Transmission and phase response are demonstrated with varying nanopillar radii (100 – 400 nm) at a target wavelength (1550 nm). *Top* (**A-B**) and *bottom* (**C-D**) rows demonstrate the results for amorphous- and crystalline-Sb_2Se_3 nanopillars, respectively.

optical phase profile of the meta-atom, based on varying crystallographic phases of Sb_2Se_3, can be applied to reconfigurable phase-gradient metasurfaces, as discussed in the following section.

5.2.2 Low-loss, tunable metasurfaces using Sb_2Se_3

Design and modelling

According to Huygen's principle that each point on a wavefront is considered as a secondary source of outgoing waves,[87] the metalens is designed based on the hyperbolic function of phase profiles with treating each spatial location as a unit-cell of a meta-atom (Figure 5.5A). In order to make the size of unit-cell constant for design simplicity, the period of the meta-atom unit cell (i.e. *p*) was fixed at 1020 nm. This design also achieved full 2π phase coverage with varying nanopillar radii (Figure 5.5B-C) with compromising some reduction in transmission intensity at redshifted resonance (1580 nm). The decrease in transmission intensity can be attributed to the degradation and spectral broadening of dipole modes, particularly noticeable in nanopillars with larger radii and tighter interspacing. This can be further improved by several approaches, which will be discussed later.

At the surface between two different mediums (Figure 5.5D), the continuous phase discontinuities ($\frac{d\varphi}{dx}$) lead to the modified Snell's law of refraction as following

$$k_2(sin\theta_2) = \frac{d\varphi}{dx} - k_1 \sin(\theta_1) \qquad (5.\ 1)$$

where k refers to the wavevector ($\frac{2\pi n}{\lambda}$) in the travelling medium of refractive index *n*, and $\frac{d\varphi}{dx}$ refers to the nonzero local phase gradient. θ_1 and θ_2 describe the incident and refracted

angles. For on-axis illumination of the lens (θ_1=0), k relation is mainly described by the phase gradient ($\frac{d\varphi}{dx}$), and such a phase gradient of a metalens is determined by the differentiation of the phase distribution of a nanopillar array separated by subwavelength distance. This subwavelength spacing allows for the assumption of continuous phase discontinuities. As a consequence, the phase profile for a 1D hyperbolic lens with a focal length of f can be represented as below.[144]

$$\varphi(x) = -\frac{2\pi}{\lambda}(\sqrt{x^2 + f^2} - f) \qquad (5.\ 2)$$

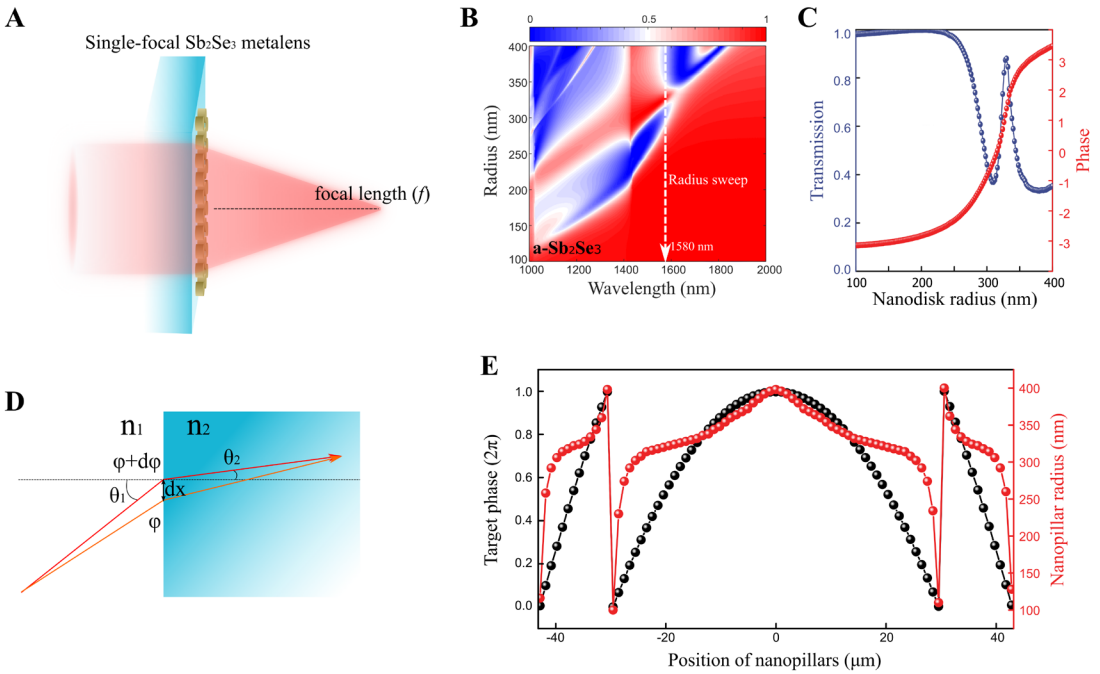


Figure 5.5 Design of a single-focal Sb_2Se_3 metalens. (**A**) Schematic diagram of a Sb_2Se_3 metalens with a focal length (*f*). An array of differently-sized Sb_2Se_3 nanopillar focuses the wavefront into a focal point. (**B**) Transmission response of *a*-Sb_2Se_3 nanopillars as a function of wavelength and radius at the fixed period of unit cell (*p* = 1020 nm). (**C**) Transmission and phase response as a function of nanopillar radii at 1580 *nm*, deducted from **B**. (**D**) Schematics used to derive the modified Snell's law from Fermat's principle, that is given by the phase discontinuities at the interface between two media (n_1 and n_2). φ and $\varphi+d\varphi$ represent phase shifts arisen by each light path (*orange* and r*ed* line) at the interface. (**E**) Hyperbolic phase profile and corresponding nanopillar radii along the lateral position for implementation of metalens with a focal length of 120 μm.

Accordingly, the phase profile for a 2D hyperbolic lens is described by:

$$\varphi(x,y) - \varphi(o) = -\frac{2\pi}{\lambda}(\sqrt{x^2+y^2+f^2} - f) \qquad (5.\ 3)$$

where o is the center of metalens. The calculated phase distribution and corresponding nanopillar radii at the designated positions are shown in Figure 5.5E for a single focal length (f) of 120 μm. Similar methodologies are employed for the implementation of varifocal metalens. However, a distinct phase distribution is required for the demonstration of dynamic holograms, which will be discussed in *Chapter 5.2.4*.

Fabrication of high aspect-ratio Sb_2Se_3 nanopillars

The fabrication of Sb_2Se_3 nanopillars presents a challenge due to the requirement of high aspect ratios of heights (> 250 nm) to diameters (~ 200 nm). When depositing a thick layer of Sb_2Se_3, the lift-off process becomes especially challenging. This leads to a failure of lift-off when using a thin layer of e-beam resist (~300 nm) due to conformal sidewall deposition onto the developed patterns, or poor lithography resolution when using a thick layer of resist (>800 nm). To overcome these challenges, an alternative approach is

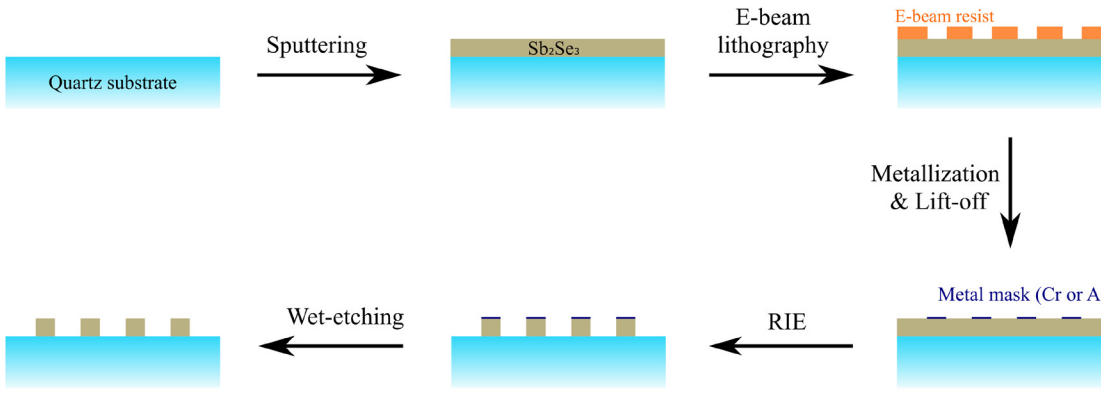


Figure 5.6 Fabrication process of high aspect-ratio Sb_2Se_3 nanopillars.

proposed in this work. Instead of the typical lift-off methods described in *Chapter 3.1.2*, the fabrication process involves creating a metal hard disk followed by a directional reactive ion etching (RIE) process, as illustrated in Figure 5.6.

Firstly, thick Sb_2Se_3 layer (h = 278 nm) was deposited on a quartz-coated glass substrate via RF-sputtering technique. Then, similar to the process shown in Figure 3.1, e-beam lithography was carried out using a positive-tone resist (CSAR) with a dosage of 180 μCcm^{-1}. However, in this case, a conductive polymer (ESPACER 300Z) was additionally coated onto the soft-baked resist to mitigate any charging effect from the e-beam exposure onto the glass substrate. After e-beam writing, the patterned substrate was rinsed in DI water for 1 minute, and then subjected to development process in AR 600-546, MIBK,

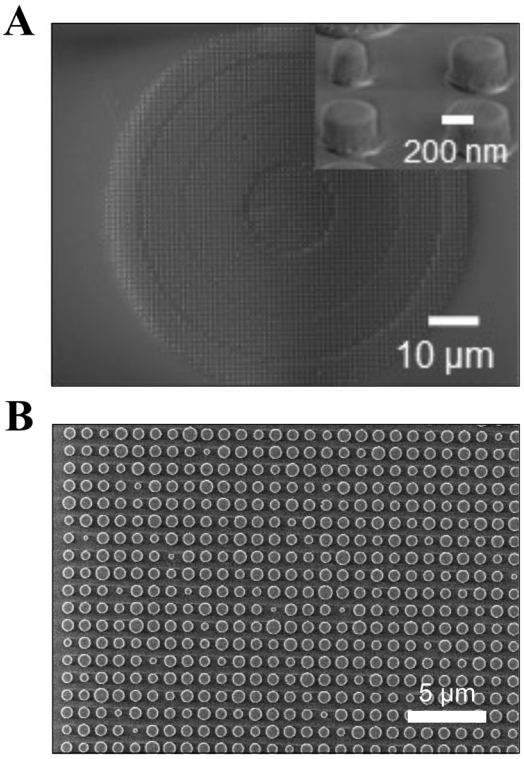


Figure 5.7 Microscope images of Sb_2Se_3 dielectric metasurfaces. (**A-B**) SEM scans of Sb_2Se_3 nanopillars with a height of 278 nm. A thin metal layer (~ 10 nm) is remained on top of the Sb_2Se_3 nanopillar in **A**, serving as a protective layer for the metalens experiment, while it has been etched away in **B** for the hologram experiment.

and IPA. The fully developed device was metallized with a thin layer (~ 5-10 nm) of Cr or Al by e-beam (Plassys) or thermal (Edwards 306) evaporator. A subsequent lift-off process in NMP was employed, with the thin metal layer serving as a hard mask for deep etching processes. These etching processes utilized RIE with a mixture gas of CHF_3 (44 sccm) and O_2 (6 sccm) with an RF power of 250 W. Any remaining residue was thoroughly rinsed with heated NMP, acetone, and IPA. Finally, the thin metal layer was removed by immersing the sample in a metal etchant for 5 minutes, followed by rinsing with IPA. For the metalens experiment, the Cr hard mask was retained as a protective capping layer. Images of the Sb_2Se_3 nanopillars with and without the metal hard mask layer are presented in Figure 5.7. The sample was heated on a hot-plate at 220 °C for 5 minutes for crystallization, while it was annealed at 270 °C for 30 minutes for the device of varifocal lens to ensure their full crystallization.

Measurement set-up

The customized optical measurement setup for active metalens is displayed in Figure 5.8. The tunable NIR laser (Keysight, N7711A) was used as a laser source that transmits through the transparent Sb_2Se_3 measurface sample, and the scattered light is collected by a 0.28-*NA* objective lens, and ultimately sent to a digital CCD camera (Cam IR, Scintacor) through a tube lens. The movement of sample was precisely modulated by piezo-motorized scanning stage (Physik Instrument) in all XYZ axis. The sample was initially imaged by LED and CCD camera (Thorlab) in visible wavelengths in advance of the NIR metalens experiment. A 2D image map was acquired at each position along the propagation axis (z-axis), with a step size of 200 nm. To determine the focusing efficiency,

the acquired image was arbitrarily normalized using the maximum light intensity from both states of Sb_2Se_3 or the transmission of the bare glass substrate.

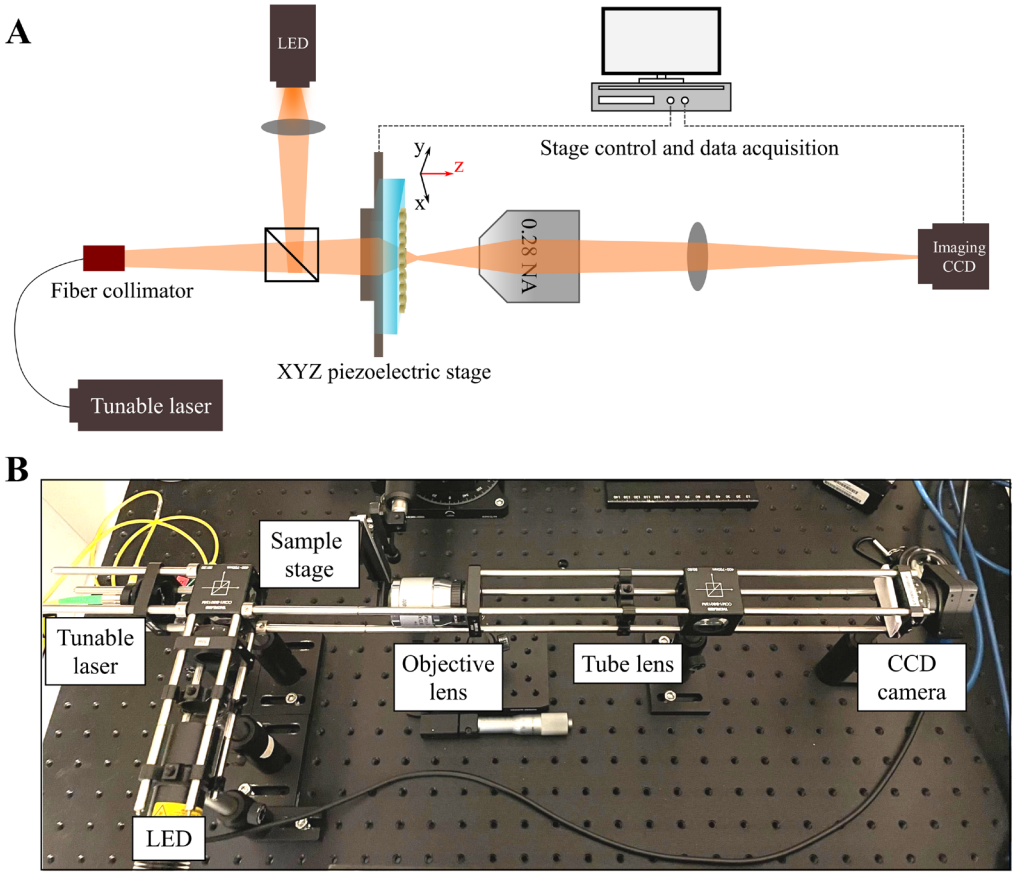


Figure 5.8 (**A**) Schematic diagram and (**B**) photo of the measurement setup for the metalens experiment.

5.2.3 Tunable metalens

Intensity-tunable single-focal metalens

A tunable single-focal metalens consisting of periodically arranged Sb_2Se_3 nanopillars (p = 1.02 μm) was designed to focus light with a focal length of 120 μm when the Sb_2Se_3 was in the amorphous state, but did not focus light in the crystalline state, as described in the previous chapter.

Figure 5.9A-B demonstrates the 2D electric-field distribution across the amorphous and crystalline Sb_2Se_3 metalens with a full size (i.e. diameter) of 70 μm. It was observed to exhibit a tightly confined electric-field at a focal spot that is 116.63 μm away from the metalens. Although some aberration effects caused a broadening of the focal spot, this can be improved by optimizing the phase distributions or increasing the feature sizes (i.e., *NA*) of the metalens. The calculated full-width at half-maximum (FWHM) was 3.09 μm, which approximated the theoretical diffraction limit ($\lambda/2NA$). The focusing efficiency was determined to be 27.09%, which is defined as the ratio of the light intensity concentrated at the focal spot (within a radius three times the FWHM) to the transmitted power through the bare glass substrate.[48,145] However, when the material was changed to a crystalline state, the focus was lost due to the mismatch of optical phase modulation. These simulations indicate that such near-IR meta-lens can be focused *on* (amorphous) and *off* (crystalline) at a target focal plane in response to the crystalline states of the Sb_2Se_3. The 1D normalized electric-field intensity profile (Figure 5.9C) shows the contrast of focusing intensity upon different crystalline phases of Sb_2Se_3, indicating the high modulation $\Delta I/I_0$ of 90.98% at the focal point, where I_0 is the focusing light intensity when the Sb_2Se_3 is in amorphous state. Partial crystallization of Sb_2Se_3 (e.g., 50% crystallinity) further allows fine tuning of the focusing intensity. The estimated partial crystallinity of PCM is obtained by the effective medium theory from the literature.[46,146,147] By using the Lorentz-Lorenz relation, the optical constants of Sb_2Se_3 in intermediate states can be expressed as follows:

$$\frac{\varepsilon_{I^{PCM}}(\lambda, C) - 1}{\varepsilon_{I^{PCM}}(\lambda, C) + 2} = C \times \frac{\varepsilon_{C^{PCM}}(\lambda) - 1}{\varepsilon_{C^{PCM}}(\lambda) + 2} + (1 - C) \times \frac{\varepsilon_{A^{PCM}}(\lambda) - 1}{\varepsilon_{A^{PCM}}(\lambda) + 2} \qquad (5.\ 4)$$

where C $(0 \leq C \leq 1)$ describes the relative crystallinity between fully amorphous and crystalline states and $\varepsilon_{C^{PCM}}$, $\varepsilon_{A^{PCM}}$ and $\varepsilon_{I^{PCM}}$ refers to the dielectric permittivities of crystalline, amorphous, and intermediate crystalline states of PCM, respectively.

The intensity modulation of the metalens based on the crystallinity of Sb_2Se_3 was not a result of material absorption loss, but rather originated from the engineering of optical phase profiles. Additionally, a tunable metalens capable of focusing light in the crystalline state of Sb_2Se_3, but losing its focusing ability in the amorphous state, could be achieved by using thinner nanopillars with a height of 235 nm, as the mode overlap was observed

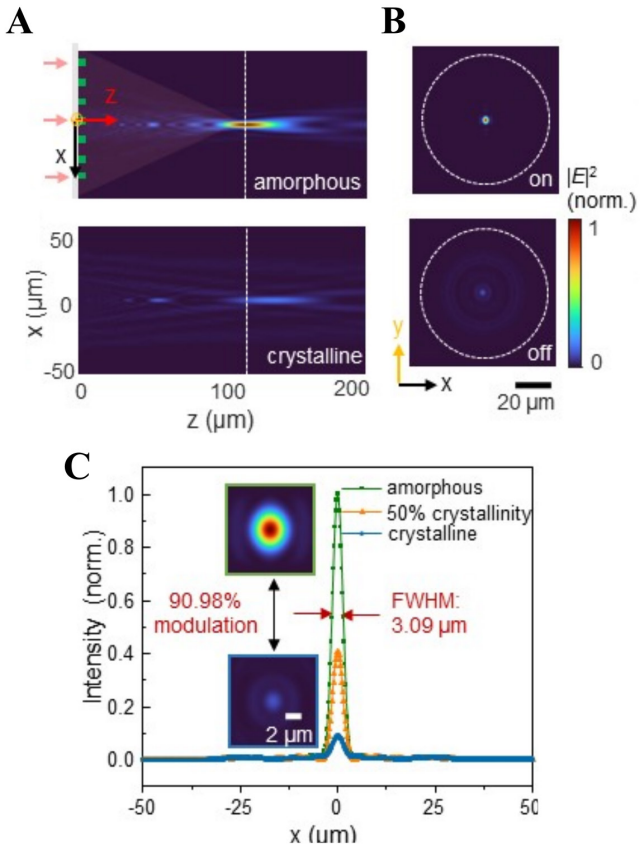


Figure 5.9 Simulated electric field of a single-focal, intensity-tunable Sb_2Se_3 metalens. (**A**) Simulated electric field distribution along the z-axis (direction of light propagation) and (**B**) at the focal plane. The white dotted line outlines the metalens dimensions. (**C**) 1D simulated electric-field profile of metalens with different crystallinities along the x-axis at the focal point. (**A-B**) *top* and *bottom* rows show the results when Sb_2Se_3 is in amorphous and crystalline states, respectively.

in the *c*-Sb_2Se_3 nanopillars (Figure 5.4). Hence, the high refractive index and negligible loss of Sb_2Se_3 enable excellent intensity-tunable lens performance for both amorphous and crystalline states of Sb_2Se_3. The transmission map was then experimentally visualized by finely scanning the piezoelectric stage in z-direction and acquiring 2D images with a CCD camera (Figure 5.10). The measured results show a good agreement with the calculated ones, indicating a focusing efficiency of 23.0% and a FWHM of 2.46 μm at a focal spot with focal length (*f*) of 115.2 μm in amorphous states. After the metalens was

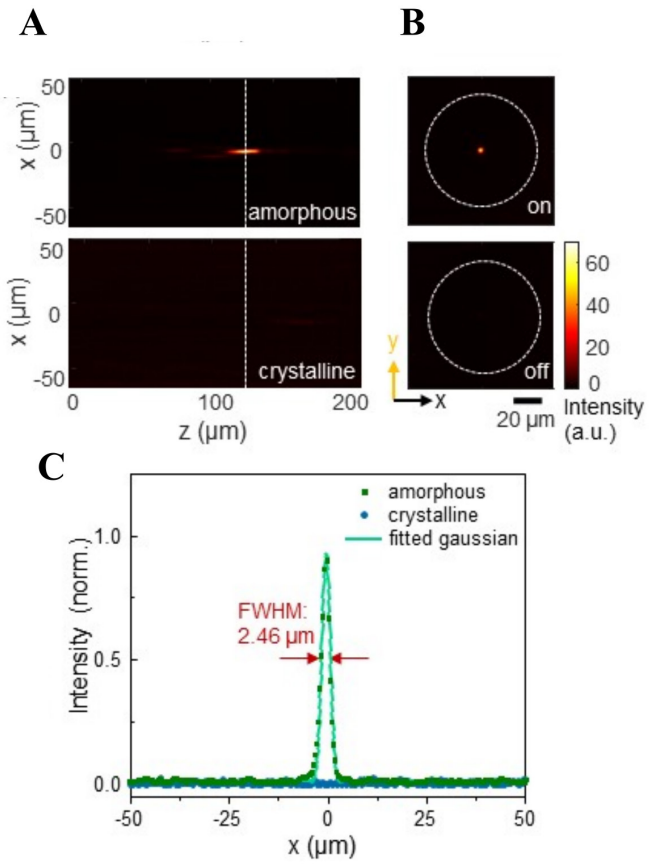


Figure 5.10 Experiment measurement of a single-focal, intensity-tunable Sb_2Se_3 metalens. (**A**) Measured light intensity along the z-axis (direction of light propagation) and (**B**) at the focal plane. The white dotted line outlines the metalens dimensions. (**C**) Measured light intensity distributions along the x-axis at the focal plane, normalized to the maximum intensity during focusing. (**A-B**) *top* and *bottom* rows show the results when Sb_2Se_3 is in amorphous and crystalline states, respectively.

heated on a hotplate and crystallized, it exhibits negligible focusing at the same focal point ($\Delta I/I_0$ = 94.8%).

The focusing efficiency, however, was found to be degraded compared to the ideal Huygen's metasurface. This is attributed to non-trivial backscattering due to imperfect spatial and spectral mode overlap, particularly for those wide nanopillars (r > 350 nm) with a fixed period (p = 1050 nm) that can experience interelement coupling between neighboring nanopillars.[148] Such limitation can be addressed by either further optimizing geometries of nanopillar[149] or replacing the surrounding medium with an appropriate dielectric environment, such as a transparent polymer with a refractive index of 1.4.[86,145] Such adjustments enhance field confinement, modulate the spectral width of the resonances, thereby mode resolving the issue of mode mismatch and enhancing the destructive interference of back-reflection. Accordingly, Figure 5.11 illustrates the achievement of full phase coverage and near-unity transmission intensity (>96.2%) by

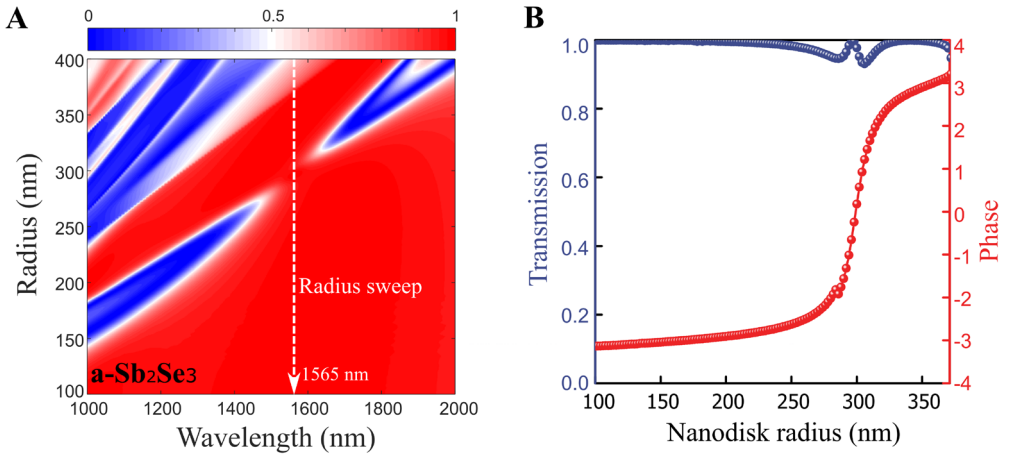


Figure 5.11 Improved mode overlap in the Sb_2Se_3 meta-atom with a dielectric cladding layer. (**A**) Calculated transmission response of Sb_2Se_3 nanopillar array with a dielectric capping layer with a thickness of 500 nm and its index (n) of 1.44 as a function of wavelength and its radius (r). The period of an array is 3r. Spectral overlap between electric- and magnetic-dipoles is observed at the wavelength of 1565 nm. (**B**) Transmission and phase response at a resonant wavelength (1565 nm) with a varying nanopillar radius from 100 to 370 nm. 2π phase shift is achieved with an average transmission of 96.2%.

using a dielectric medium (n = 1.44) on Sb_2Se_3 nanopillars. Furthermore, additional numerical optimization and design techniques, such as local periodization or global optimization, can minimize electromagnetic coupling between adjacent nanopillars and improve the focusing efficiency of a Huygens' metalens.[148]

Varifocal metalens

The use of low-loss Sb_2Se_3 material was then exploited to tune the focal length upon its crystalline phases, realizing active varifocal metalens. The layout and schematics of metalens are illustrated in Figure 5.12A-B, that consists of two regions (denoted in *green* and *blue* colors). Each region supports distinct phase profiles at different crystalline states, the inner region (*region* 1) possesses a focal length of 50 μm (f_1) in the amorphous state, while it does not focus light in the crystalline state. Conversely, the outer region (*region* 2) focuses light at 120 μm (f_2) in the crystalline state, but not in the amorphous state. Therefore, this design superimposes two spatially-decoupled, intensity-tunable lenses with different focal lengths and operating crystalline states (i.e., material states of Sb_2Se_3 that enable light focusing).

Figure 5.12 showcases the demonstration of a single tunable metalens that can vary its focal length from 50 μm (f_1) to 120 μm (f_2). The simulated electric-field distribution along the propagation axis reveals light focusing at 52.6 μm (f_1) when the material is in the amorphous state, and at 110.2 μm (f_2) when Sb_2Se_3 is in the crystalline state. The calculated focusing efficiencies demonstrate similarity, measuring at 7.58% for f_1 and 9.39% for f_2, which suggests that both material states exhibit low-loss characteristics. The FWHM at each focal plane was 2.11 μm and 2.40 μm, respectively. Additionally, there

was a modulation of focusing intensity amounting to 72.55% (at f_1) and 61.96% (at f_2) when the Sb_2Se_3 nanopillars underwent crystallization.

The decrease in focusing efficiency and modulation range for the varifocal metalens, compared to the single-focal metalens, is attributed to the shared-aperture layout. To enhance performance, it is suggested to implement improvements that enable binary switching of metasurfaces between arbitrary phase profiles with a more efficient design methodology, instead of nanopillars, to select optimal meta-atom geometries.[48] Also, the experimental results agree qualitatively with the calculation, demonstrating crystalline-

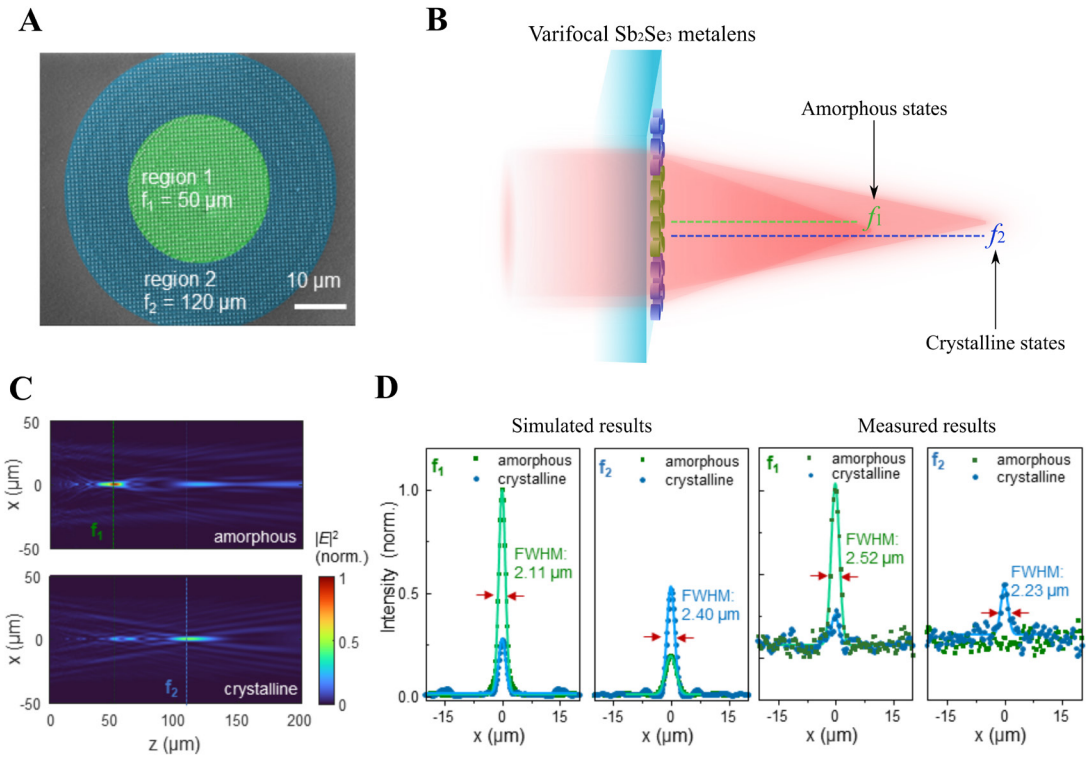


Figure 5.12 Varifocal Sb_2Se_3 metalens. (**A**) False-colored SEM scan of the fabricated varifocal metalens and (**B**) the schematic diagram, showcasing *region 1* (total lens radius R < 17.5 μm) focusing light at a focal length of f_1 when Sb_2Se_3 is in the amorphous state, and *region 2* (17.5 μm < R < 35 μm) focusing light at a focal length of f_2 when it is in the crystalline state. (**C**) Simulated electric-field distribution along the propagation axis for the (*top*) amorphous and (*bottom*) crystalline states of Sb_2Se_3. The focal plane distances are 52.6 μm for f_1 and z = 110.2 μm for f_2. (**D**) (*left*) Simulated and (*right*) measured light intensity at each focal planes for the amorphous state (*green*) and crystalline state (*blue*) of Sb_2Se_3. Measured data was normalized to the maximum intensity when light is focused at the first focal point f_1.

states-selective focusing behavior at focal length of 41 μm for f_1 (amorphous) and 123 μm for f_2 (crystalline) with comparable focusing efficiency (5.74% and 2.97%, respectively) and FWHM (2.52 μm and 2.23 μm, respectively).

An important aspect of this varifocal metalens is that it operates as a standalone component with an ultrathin profile, eliminating the need for integrating additional bulky devices or lossy materials. For example, varifocal metalenses that incorporate mechanical actuation rely on MEMS techniques,[150] electro-optic cell,[151] or stretchable substrates,[152] which involve cumbersome physical movements and pose challenges in minimizing the system footprint. Liquid crystal[153] or geometrical phase-dependent metasurfaces[154] can enhance the compactness of tunable metalenses, but they rely on manipulating light polarization to adjust the focal planes, introducing unwanted polarization-sensitive focusing, particularly undesirable in imaging applications.

In contrast, the varifocal metalens incorporating Sb_2Se_3 nanopillars achieves polarization-insensitive focusing and offers focal length tunability from 41 to 123 μm within compact dimensions. The use of Sb_2Se_3, which exhibits refractive index tuning with negligible static loss, ensures that the focusing efficiency remains comparable for both material states without experiencing absorption losses. This is a notable achievement considering that common phase-change chalcogenides like GSTs typically exhibit significantly higher losses in their crystalline state.

However, it is important to acknowledge that the experimental focusing efficiency of the varifocal lens was observed to be lower than that of state-of-the-art dielectric metalenses.[48,155] This performance degradation was attributed to two main factors: (1) design-related issues including suboptimal meta-atom shape or uneven spacing between

meta-atoms, and (2) practical challenges resulting in additional optical losses due to the presence of a thin Cr hard mask or backscattering from a rough surface. Although these issues could potentially be improved by various methods mentioned above, such as structural optimization or the incorporation of a dielectric medium, the focus of this work centered on establishing the first proof-of-concept experimental validation of an active dielectric metalens using low-loss PCMs.

5.2.4 Dynamic hologram

By further manipulating the phase profiles of meta-atoms, a wide range of wavefront shaping possibilities can be achieved using flat optical elements, such as holograms. Similar to metalenses, each building block of a metasurface allows for local control of phase and amplitude of light. The overall phase distribution of the unit cells can be determined through iterative algorithms such as the Gerchberg-Saxton algorithm.[156,157] Figure 5.13 illustrates the generation of a phase mask for a metasurface through iterative forward and backward diffraction propagations between the electric fields in the hologram plane (u) and the imaging plane (U). The iteration starts with a random phase profile and continues with the optimization of hologram phases (φ) based on the target image amplitude (U_0). This eventually leads to the generation of the reconstructed image (U).

To implement each unit cell corresponding to a single pixel of the hologram phase, a 1-to-1 mapping method was employed using the full phase coverage profile of Sb_2Se_3 nanopillars, as described in Figure 5.3. Figure 5.13C demonstrates the successful fabrication of a metasurface hologram consisting of Sb_2Se_3 nanopillars, capable of producing high-resolution holographic imaging of the reconstructed image, such as the

example of the University of Oxford logo. While only simulation results are presented here, this approach can be readily applied to experimental measurements of metasurface holograms, offering a high degree of freedom in reconstructing the transverse profile of light with complex amplitude information.

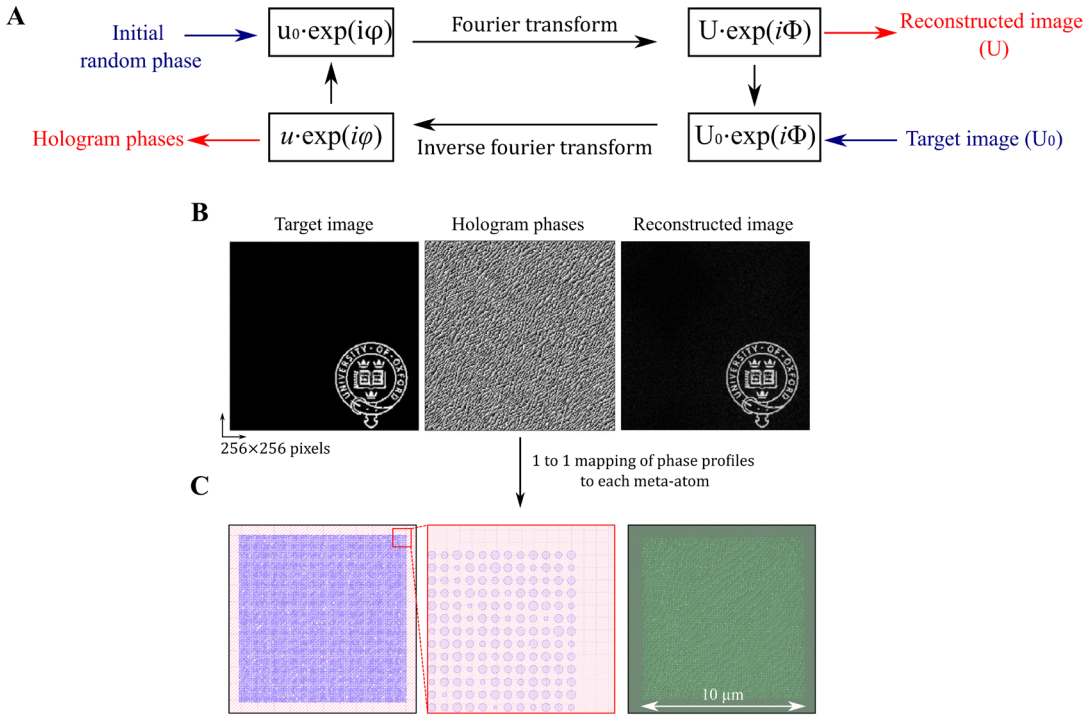


Figure 5.13 Dynamic hologram using low-loss PCM metasurfaces (**A**) Gerchberg-Saxton algorithm method to implement hologram phase profiles. Initial random phase is applied to the system, and the iterative process of Fourier and inverse Fourier transform with the target amplitude ($\boldsymbol{U_0}$) ultimately induces the hologram phases (φ). (**B**) Simulated results of 256^2 pixels showing target image, the implemented hologram phases, and the reconstructed image. (**C**) A lithography pattern design of Sb_2Se_3 nanopillars and OM image of the fabricated Sb_2Se_3 nanopillar arrays for low-loss metasurface hologram.

5.3 Active switching of low-loss phase-change material

In the previous chapters, active metasurfaces were showcased; however, their tunability was non-reversible and relied on hot-plate heating, which could only crystallize the as-

deposited amorphous state of Sb_2Se_3. To fully leverage the advantages of active metasurfaces, achieving active reconfigurability of the devices is crucial. Nevertheless, achieving active switching of low-loss PCMs presents an additional challenge, primarily due to their low absorption, which limits heating above the melting point of materials. Furthermore, demonstrating reliable switching of such materials on a large-area metasurface has proven to be an even more formidable challenge. In this chapter, different methodologies for switching low-loss PCMs are presented, involving the use of visible lasers or micro heaters. These approaches aim to overcome the limitations associated with active switching of PCMs and open up possibilities for their implementation in practical large-area metasurfaces.

5.3.1 Optical switching of phase-change thin films

As depicted in Figure 5.1 and supported by existing literature, low-loss phase change materials like Sb_2Se_3, Sb_2S_3, or $GeSe_3$ still exhibit noticeable absorption at red wavelengths (>600 nm). While this optical absorption can degrade scattering efficiency

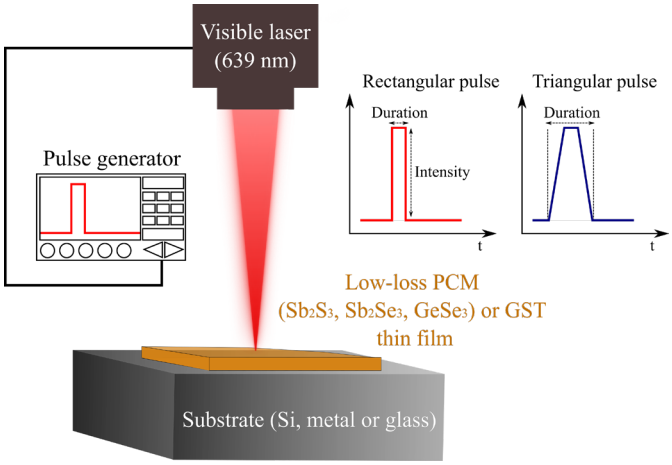


Figure 5.14 Schematic illustration of out-of-plane optical switching of low-loss phase-change material using high-power laser pulses at visible wavelength.

in visible wavelengths, it also provides an opportunity for optically switching the material using a visible laser. Figure 5.14 illustrates the experimental setup where a high-power, pulsed visible red laser (639 nm) is directly illuminated onto various types of phase-change surfaces via free-space optics (as the setup is shown in Figure 3.9). The specific pulse conditions vary depending on the materials, as different cooling rates are required for effective switching, and the choice of substrates influences heat dissipation. Additionally, the shape of the pulses, such as rectangular or triangular, yields different outcomes. This section focuses on demonstrating the capability of optical switching across different materials and substrates, highlighting the importance of dynamic switching, particularly for low-loss materials that have not yet been extensively explored in terms of reversibility.

Power-dependent crystallization

Firstly, the optical switching of low-loss material Sb_2S_3 was tested, by applying 1-second-long pulses with varying laser power (11 – 23 mW) onto the as-deposited Sb_2S_3/SiO_2 (30/10 nm) thin film on a Si substrate (Figure 5.15). By utilizing the absorption near the Urbach tail of Sb_2S_3, the illuminated area could be selectively switched through electromagnetic heating, resulting in a localized change to a blue color. Higher laser power led to increased saturation of blue tones, indicating a transition to a more crystalline state. This switching could be performed independently at specific points or continuously while scanning the surface. Raster scanning with low-power laser illumination (Figure 5.15A, *bottom*) exhibited trajectories of laser excitation with slightly darker color changes due to overlapping exposure during scanning. Raman spectroscopy measurements confirmed

these changes, revealing an increased peak intensity at 300 cm^{-1} corresponding to Sb-S crystalline bonding.[57] The Raman spectrum was measured at distinct laser-switched regions with different laser power settings, suggesting that the crystallinity of the Sb_2S_3 surface could be controlled by adjusting the laser power. However, the presence of an

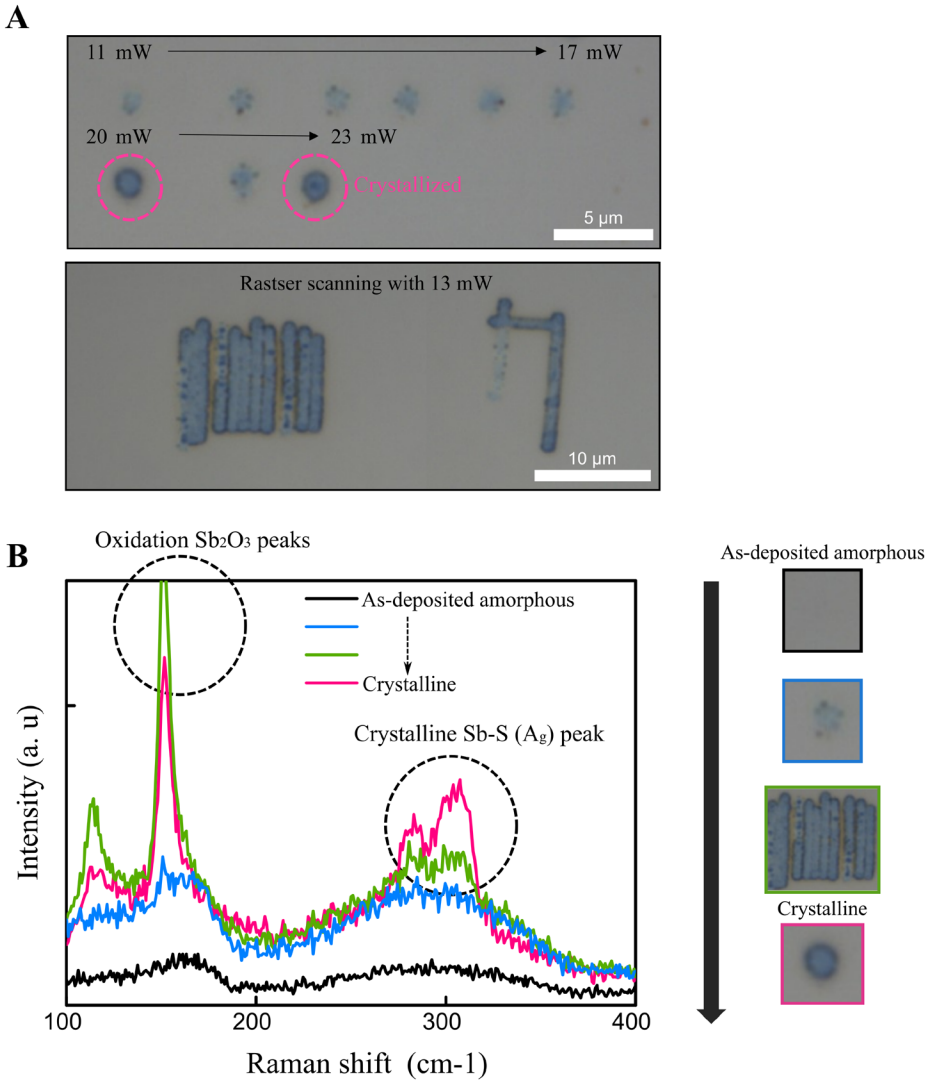


Figure 5.15 Measurement of Sb_2S_3 thin film optical switching. (**A**) Optical microscope images of Sb_2S_3 thin film on Si with a 10 nm SiO_2 passivation layer on top, where Sb_2S_3 undergoes optical crystallization by focused laser pulses. (*top*) Laser pulses with a duration of 1 s is sent with varying power from 11 to 23 mW, or (*bottom*) laser was continuously illuminated during scanning the surface. (**B**) Raman spectra of optically-switched Sb_2S_3 from as-deposited amorphous to crystalline states. Each spectrum was obtained from the different location of laser-switched area with various laser power settings.

increased oxidation or defect peak indicated the potential for sample degradation or ablation with high-power lasers. This degradation can be further enhanced by replacing the capping layer with ZnS-SiO_2 which prevents sulfur migration.[57]

The degree of optical switching was not solely dependent on laser power but also on the number of pulses or pulse duration,[27] which linearly increased the applied heat energy to the sample. Figure 5.16A-B demonstrated that both Sb_2S_3 and $GeSe_3$ exhibited an energy threshold where the sample began to ablate beyond crystallization. This ablation was related to rapid cooling rates resulting from high-intensity pulses, which caused the exposed region to rupture via delamination, ablation, or void creation. Slower materials like Sb_2S_3, Sb_2Se_3, or $GeSe_3$ exhibited more noticeable ablation compared to faster phase-change chalcogenides such as GST, which undergo both amorphization and crystallization within microseconds (Figure 5.16C). Ablation issues arising from rapid cooling rates could be mitigated by manipulating the pulse shape, such as using a triangular pulse with a slower decay. The triangular-pulse approach made the switching behavior more robust, ensuring reliable optical switching during raster scanning. Figure 5.16D depicted two squares (100×100 μm^2) of crystallization that showed uniform switching over a large area using raster scanning with triangular pulses. Crystallization of the as-deposited $GeSe_3$ surface could be successfully achieved with a laser power of 22 mW, but higher laser power caused irreversible damage.

Trapezoidal-pulse operations were also conducted on Sb_2Se_3 surfaces, which exhibited more successful switching behavior. A trapezoidal pulse was generated by arbitrarily adjusting the rise and fall edges of a rectangular pulse, typically with equal time intervals (1/3 s for crystallization, 700/3 ns for amorphization) for the rise, plateau, and fall phases.

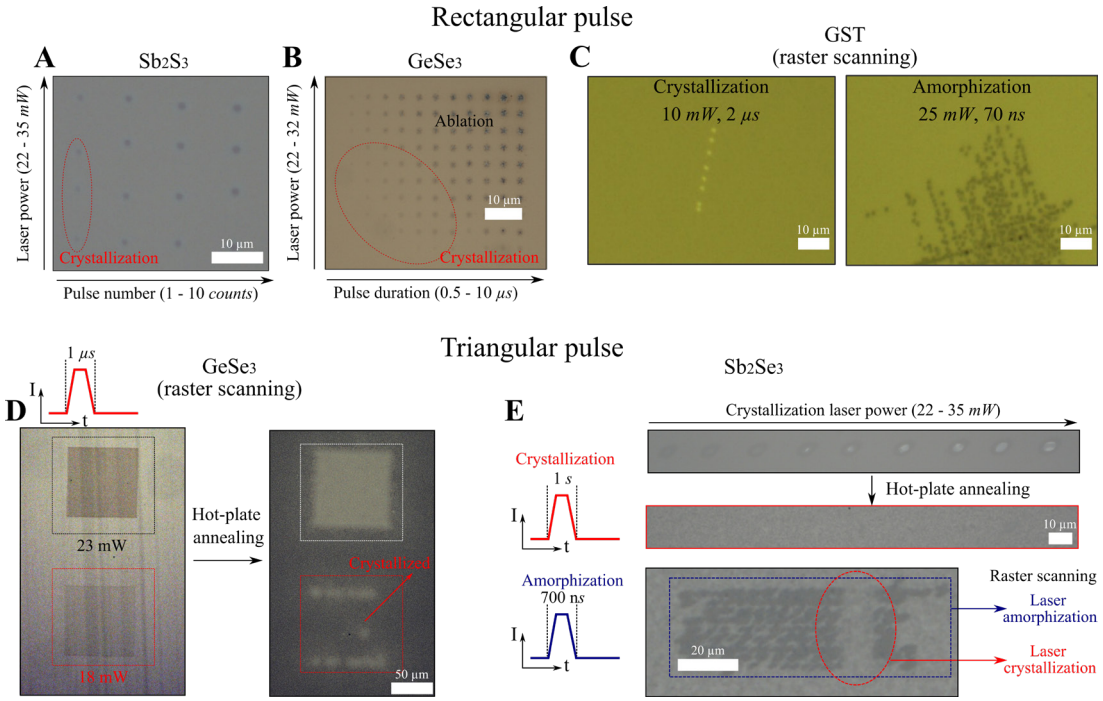


Figure 5.16 Optical images of low-loss PCM thin film illuminated by visible laser pulses. (**A-B**) Sb_2S_3 or $GeSe_3$ thin film with its thickness of 30 or 50 nm, respectively, are optically switched by a single rectangular pulse with varying laser power or pulse number/duration**.** (**C**) 20 nm-thick GST film is optically (*left*) crystallized from as-deposited amorphous states or (*right*) amorphized from hot-plate annealed states during scanning the surface. (**D-E**) Raster scanning of trapezoidal pulses onto (**D**) $GeSe_3$ and (**E**) Sb_2Se_3 with different laser power, and subsequent hot-plane annealing. (**E**, *bottom*) Reversible laser switching of Sb_2Se_3 with trapezoidal pulses. Note that the contrast of the image was tuned to clarify the color change.

A higher thickness (180 nm) of the material and its lower glass transition temperature (220 °C) also helped induce higher switching contrast and more reliable results. Triangular pulses with most laser powers crystallized the materials, as confirmed by the disappearance of laser spots after heating the entire chip on a hot-plate. This operation reliably resulted in dynamic reversible switching, as shown in Figure 5.16E, where the first amorphization triangular pulse switched the first rectangle to darker colors and then completely reverted it to a crystalline state with crystallization pulses. Multiple trials confirmed Sb_2Se_3 as one of the most robust low-loss PCMs, demonstrating relatively reliable switching performance.

Dynamic switching behavior

To further validate this, various types of PCMs were tested for their dynamic optical switching behavior in Figure 5.17. Despite the relatively low image resolution of the video snapshot, the reversible switching behavior of lossy GST and low-loss PCMs like Sb_2S_3 and Sb_2Se_3 could be clearly observed upon applying appropriate *SET* and *RESET* pulses. The green tone color resulted from the insertion of a short-pass dichroic mirror (< 600 nm) in the optical beam path. Generally, using slightly more lossy materials and greater

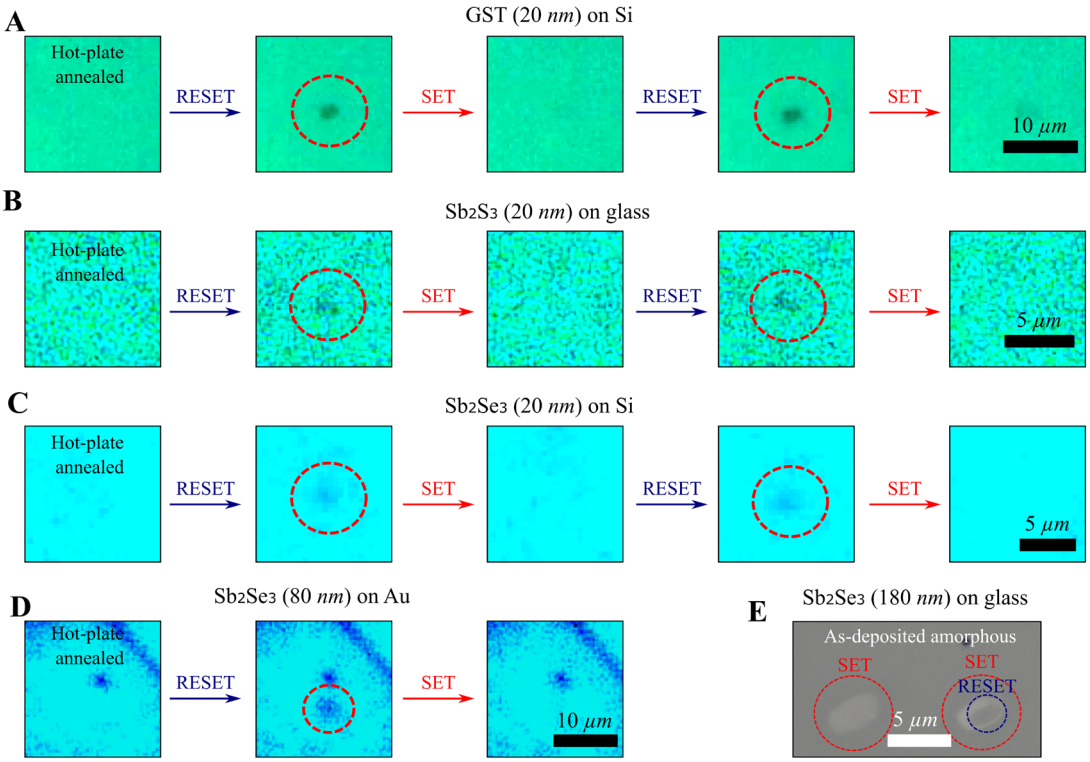


Figure 5.17 Dynamic reversible switching of various PCMs using single-shot pulses. Video snapshots of reversible switching for (**A**) GST on a Si substrate, (**B**) Sb_2S_3 on a glass substrate, (**C**) Sb_2Se_3 on a Si substrate and (**D**) Sb_2Se_3 on a Au substrate. *SET* and *RESET* processes refer to crystallization and amorphization operations, respectively. Pulse conditions are as followings: and the details of pulse conditions are as follows: **A**, *SET*: 2.5 mW, 1 μs / *RESET*: 12 mW, 80 ns. **B**, *SET*: 0.5 mW, 1 s / *RESET*: 4 mW, 600 ns. **C**, *SET*: 10 mW, 500 ms / *RESET*: 21 mW, 500 ns. **D**, *SET*: 15 *mW*, 1 s / *RESET*: 20 mW, 500 ns. (**E**) OM image showing single-shot crystallization and subsequent single-shot amorphization of Sb_2Se_3 on a glass substrate.

thickness provided better contrast, while employing a heat-insulating substrate (e.g., glass) facilitated low-energy switching due to reduced heat dissipation into the surrounding environment. Sb_2Se_3 consistently exhibited reliable dynamic switching responses across different substrates. It also demonstrated reversible switching, starting from the as deposited amorphous states. In many cases, it is preferable to first heat the PCM on a hot plate to ensure complete full crystallization, which facilitates reversible switching due to the increased absorption in crystalline states. However, a single-shot reversible switching test was performed on as-deposited amorphous Sb_2Se_3, indicating full reversibility of the material from any arbitrary state (Figure 5.17E). This also suggests the advantages of bypassing the hot-plate annealing processes that significantly increases the surface roughness of most of low-loss PCMs whose nucleation sites can be damaged during annealing.[57] The spot sizes of switching area by focused laser pulses were found to be ~5 and ~3 μm during crystallization (1.5 mW, 1 s) and amorphization (15 mW, 500 ns) operations, respectively. The energy required to switch power can vary depending on the alignment of the focused spot on the sample surface. Accordingly, the size of switching area varies with laser power, pulse duration or types of substrates, leading to distinct heat dissipation (i.e. temperature gradient) across the phase-change layer.

From this series of dynamic switching experiments, it is worth emphasizing that optical switching is reversible as long as the material effectively absorbs light at the laser wavelength (e.g., 638 nm). The laser conditions for optically-induced switching were affected not only by the imaginary part of the refractive index of material but also by the type of substrate, which affects heat conduction rate. Additionally, the spot size of each switching event could be controlled by adjusting the *NA* of the objective lens. In this work,

a single type of objective lens (0.28 *NA*) was utilized, resulting in spot size of a few microns. Considering all these factors, it becomes evident that various types of low-loss PCMs can be reversibly switched in the optical domain. Furthermore, by combining the optimized laser-switching procedures with raster-scanning techniques, the potential for large-area (eg, metasurface) switching is realized. Similar to optically reconfigurable metasurfaces that utilize optical *write* and *read* pulses in GST metasurfaces,[14] this visible-laser switching technique can facilitate the development of reconfigurable low-loss active metasurfaces. In this case, visible lasers can be used for *writing*, while infrared light can be employed for *reading* out the response, in a wavelength-selective manner.

Out-of-plane optical switching onto integrated photonic resonators

The capability to optically switch these low-loss PCMs was further exploited for potential integration into photonic circuits, presenting the integrated low-loss phase shifters.[62] These phase shifters play a crucial role in various photonic applications such as routing and computing,[158] which has therefore led to recent advancements in developing transparent PCMs on integrated photonic circuits. However, achieving reversible switching in such low-loss phase-shifting photonic circuits has proven to be challenging. To address this, a method utilizing out-of-plane pulses in the visible wavelength was employed to program the in-plane-mode phase shifter in the NIR range. In doing so, this further allowed for a quantitative evaluation of phase switching in low-loss PCMs by incorporating highly sensitive photonic resonators like micro-ring resonators or Mach-Zehnder interferometers (MZIs).

In this experiment, the out-of-plane light at NIR wavelengths was directed towards the integrated photonic resonators and collected by coupling it in and out of guided-mode propagation within a dielectric waveguide, using input and output grating couplers (Figure 5.18). By depositing small patches of Sb_2Se_3 onto the waveguide, the effective refractive index of the in-plane mode could be controlled based on the tunable dielectric constants of Sb_2Se_3. This index manipulation enabled tuning of the spectral resonance in microring

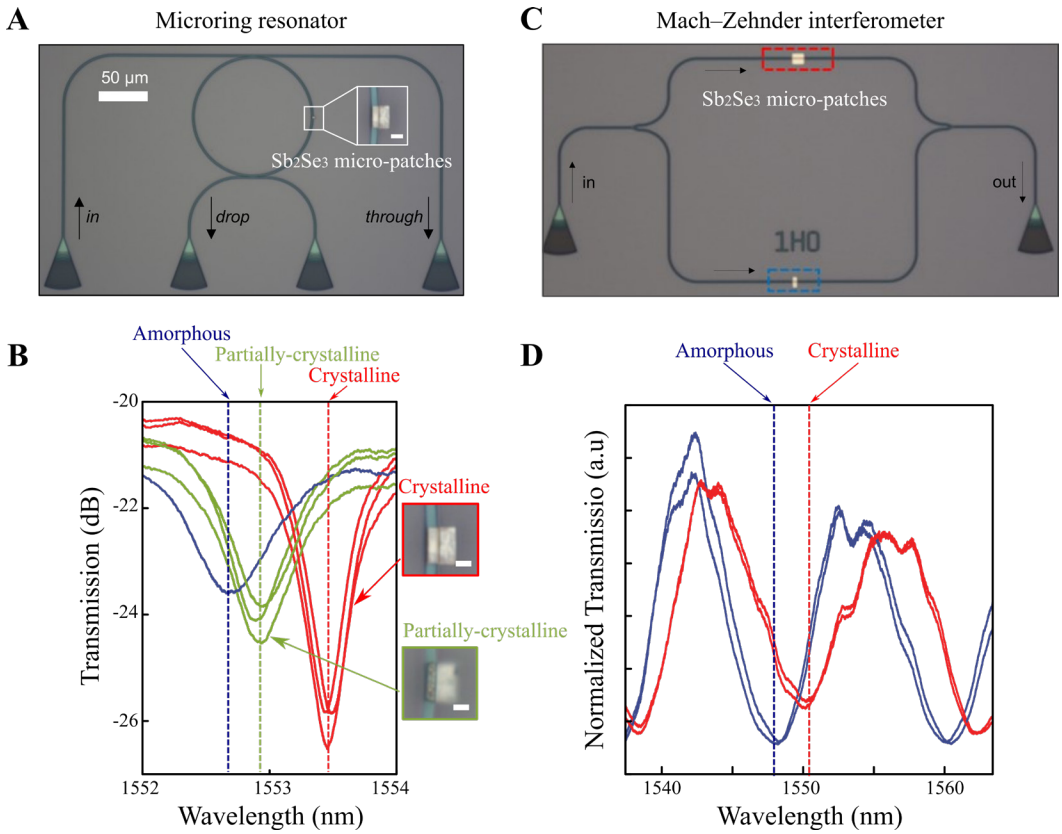


Figure 5.18 Dynamic switching of Sb_2Se_3 on the microring resonator and MZI. (**A**) OM image of a microring resonator with a Sb_2Se_3 layer deposited. (**B**) Transmission measurement of ring resonators with evanescently coupled Sb_2Se_3 at the through port while switching their phase state by the out-of-plane laser from crystalline (*red*) to partially-amorphous (*green*) and amorphous (*blue*) phases and back. Inset images are optical microscope scans of Sb_2Se_3 layers on ring resonators for each crystalline phases. Scale bar is 2 μm. (**C**) OM image of a MZI with a Sb_2Se_3 layer deposited. (**D**) Transmission measurement of MZI with Sb_2Se_3 layer that is reversibly switched by the out-of-plane laser. Optical pulse parameters for crystallization and amorphization are 3 mW with 500 ms, 20 mW with 500 ns, respectively.

resonators or MZIs, affecting their output responses. Further details regarding the operations and benefits of phase-change integrated photonic circuits will be discussed in *Chapter 6*.

Optical programming of low-loss PCM was achieved by illuminating the device with out-of-plane visible laser pulses through raster scanning. Prior to optical switching, the device was heated on a hot plate to ensure complete crystallization of the Sb_2Se_3. During scanning the surface and subjecting the Sb_2Se_3 layer to a series of amorphization pulses, a clear blueshift of the resonance in both the microring resonator was observed (Figure 5.18B). This resulted in a slightly darker color for the Sb_2Se_3 on the waveguide. The process was reversible, and partial crystallization was also achieved by modulating the exposure coverage through raster scanning. Some reduction in the quality factor was also detected, primarily attributed to the damage caused by high-power rectangular amorphization pulses. Optimization of pulse parameters, such as utilizing of triangular pulses, can help mitigate this issue. Similarly, reversible optical switching was observed in the interference patterns of the MZIs, demonstrating a blueshift during amorphization and a redshift during crystallization. In summary, the use of visible optical switching in low-loss materials allowed for the dynamic alteration of the propagating optical phase within integrated photonic circuits, while maintaining minimal insertion loss.

5.3.2 Electrically programmable GeTe metasurfaces using a micro-heater

Enabling fast and large-area switching is a crucial requirement for the realization of enlarged, active metasurfaces. However, the previous method of phase-switching using lasers had limitations in terms of the active area coverage, as it was constrained to the size

of the focused laser illumination. Consequently, raster scanning of the laser was necessary for achieving large-area switching, which in turn restricted the speed of operation. To overcome this limitation, it is advantageous to shift the switching stimuli from the optical domain to the electrical domain, allowing for electrical addressing of the PCM elements. Nevertheless, direct electrical switching of the PCM is hindered by the filamentation effect. This effect restricts the switching to a confined volume, where a thin wire of PCM that initially crystallizes becomes a pathway for electrical current with significantly higher conductivity compared to the surrounding amorphous matrix.[100] Hence, uniform crystallization of the entire PCM volume becomes difficult.[40,41] Furthermore, low-loss PCMs exhibit electrically-resistive characteristics in both crystalline phases, exacerbating the difficulty of establishing an electrical channel and reconfiguring the material. Therefore, achieving switching homogeneity across large areas of low-loss PCMs becomes even more demanding.

To address this challenge, this work proposes the implementation of electrically programmable microheaters that induce indirect heating through an electrothermal approach. Figure 5.19 illustrates the use of NiCr semi-transparent microheaters with metal contacts. The size of the microheater is 50×50 μm², which is sufficiently large to accommodate an array of sub-micron-sized meta-atoms. GeTe was selected as the low-loss material for this purpose, exhibiting lossy behavior in the visible-NIR region, while transitioning to a more transparent state in the telecommunication range (1500 – 1600 nm). In addition to this, GeTe demonstrates faster crystallization kinetics and a lower melting temperature (121 °C) compared to other low-loss materials like Sb_2Se_3 or Sb_2S_3, and these properties can be further controlled by adjusting the stoichiometric proportion of Te

content.[159] The control of melting point is found to be significant for achieving high-endurance cycling.[160] In this work, GeTe is presented in two different forms: thin films and an array of nanowires with varying thicknesses (h = 30, 110 nm) and nanowire widths (100 – 900 nm).

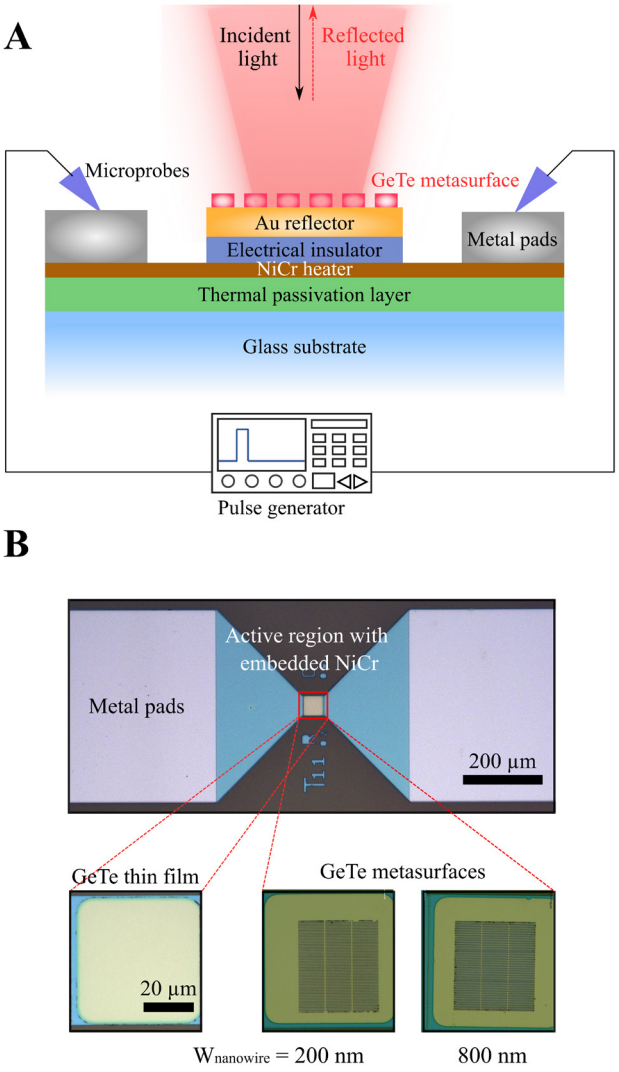


Figure 5.19 Dynamic GeTe metasruface with electro-thermal pulses given by NiCr heater. (**A**) Schematic diagrams showing an electro-optical setup that measures the reflection of GeTe metasurface during the application of electrically-programmed thermal pulses. (**B**) OM images of micro heaters with GeTe thin film or metasurfaces. The metasurface consists of GeTe nanowires.

Dynamic switching of a large-area GeTe layer using electro-thermal pulses

The dynamic reflection responses of the GeTe surface were measured using a visible light source (400 – 700 nm), while electro-thermal pulses of varying pulse widths and amplitudes were generated using a pulse generator (i.e., applying a potential difference across two metal pads). In Figure 5.20A, OM images depict the Ge thin film in its as-deposited state, followed by electro-thermal crystallization (*SET*) via a rectangular pulse with an amplitude of 1.1V and a duration of 2.1 µs, and subsequent full crystallization through hot-plate annealing. The brightness of the film color increased as GeTe underwent crystallization, which was confirmed by the reflection measurement shown in Figure 5.20B. The reflection at a wavelength of 532 nm was continuously monitored, while a series of *SET* and *RESET* electro-thermal pulses were sent to the GeTe thin film. The processes were carried out either from the as-deposited amorphous state or the hot-plate annealed crystalline state. Amorphization (*RESET*) was achieved using pulses with an amplitude of 4.1V and a duration of 500 ns. The modulation contrast ($\Delta I/I_{base}$) was found to be ≤5%, with an overall decay observed when switching was started from the as-deposited phase. This feature could be attributed to a vacancy ordering mechanism and the formation of unstable crystalline domains. To improve the contrast and reliability of the devices, a thermal annealing step was required before reversible switching, as demonstrated by a conditioning treatment in other PCM cells.[161]

The reversible switching was also measured in GeTe nanowire metasurfaces with a thickness of 110 nm and widths of 300 nm, as shown in Figure 5.20C, exhibiting consistent reversible switching over 100 and 530 cycles. Due to the extended measurement time, some drift in the reflection measurement was observed, which could be attributed

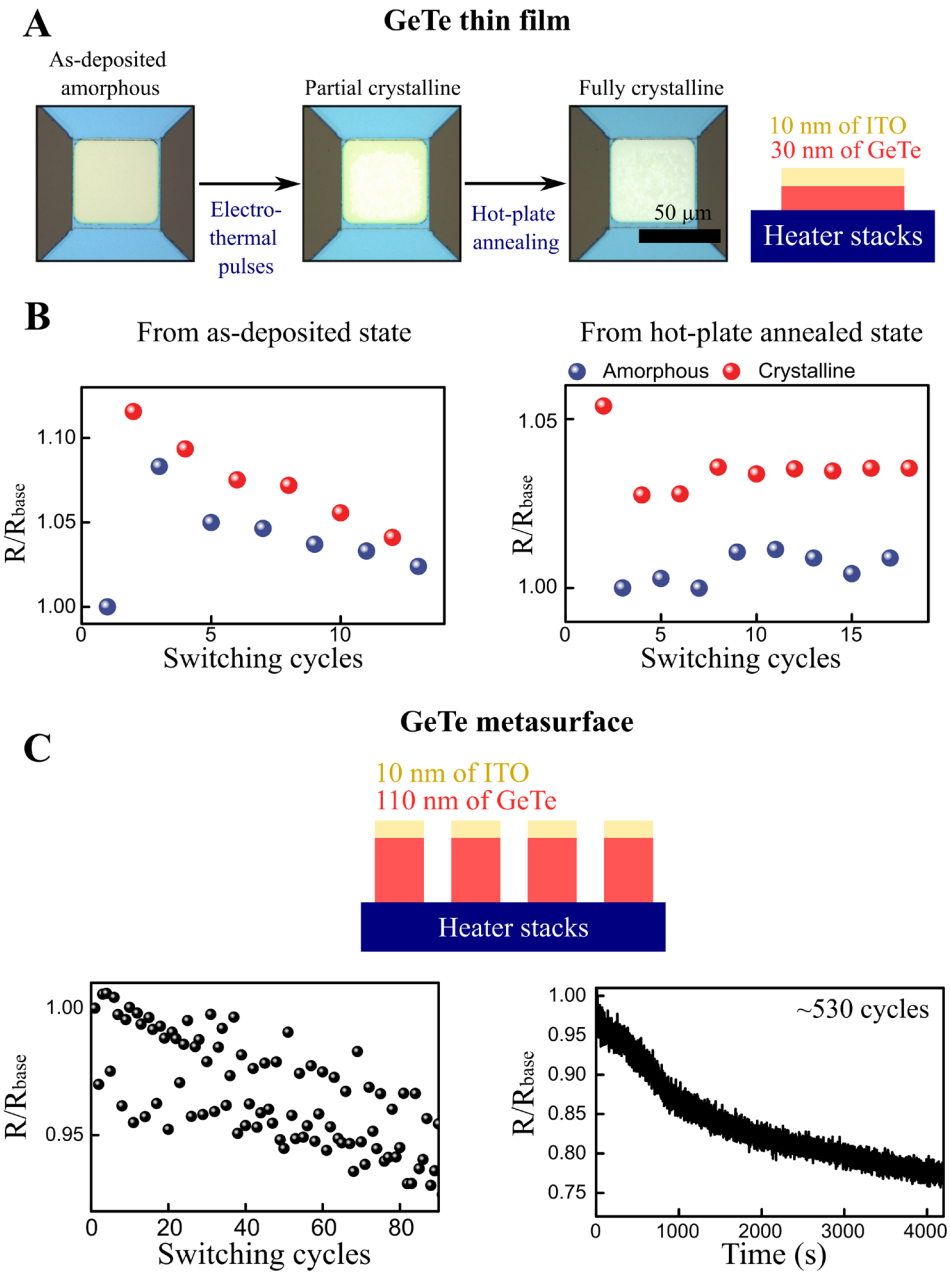


Figure 5.20 Measurement of switching cycles in the GeTe thin film and metasurfaces. (**A**) OM images of GeTe thin film (thickness of 30 nm with 10 nm of ITO capping layer) in as-deposited amorphous, electro-thermally switched and hot-plate annealed states. The pulse has an amplitude of 1.2 V and 2.1 µs. Hot-plate annealing was done at 200°C for 5 minutes. (**B**) Normalized reflection measurement at the wavelength of 532 nm upon a series of *SET* and *RESET* pulses, starting from (*left*) as-deposited states or (*right*) hot-plate annealed states. *RESET* pulses require an amplitude of 4.1V with duration of 500 ns. (**C**) Normalized reflection measurement of reversibly switching GeTe metasurfaces (thickness of 135 nm with 10 nm of ITO capping layer, width of 300 nm and period of 900 nm).

to thermal drift in the stage or microscope focus. Although further improvement in switching contrast (~5%) is needed through fine-tuning of pulse conditions such as pulse shapes, this result demonstrates reversible low-loss large-area (30×30 μm^2) metasurface switching using a micro-heater. The number of switching cycles achieved was comparable to or greater than state-of-the-art PCM metasurfaces with microheaters, which typically showed ~50 cycles using 40×40 μm^2-sized GST[41] or GSST[40] metasurfaces. This underscores the importance of incorporating an indirect heater for the reconfiguration of large-area low-loss PCM metasurfaces, enabling efficient and high-bandwidth wavefront modulation. The substitution of the NiCr heater with transparent conductors such as fluorine-doped tin oxide (FTO) heaters[160] can achieve similar metasurface switching, while operating in a transmissive mode.

GeTe metasurface for potential beam steerer in NIR wavelengths

The ability to switch the large-area metasurface with a single pulse presents interesting opportunities for the development of high-speed active metasurfaces, such as a beam steerer.[162] Figure 5.21 demonstrates a metasurface composed of subwavelength-sized GeTe nanowires. This metasurface exhibits a tunable dielectric constant (Δn ~0.8) within the telecommunication range ($1500 - 1600$ nm), while maintaining low static losses ($k <$ 0.2). This optical contrast enables the activation of switchable dielectric nanowire resonances. For example, in the amorphous state of the GeTe nanowire array, which consists of nanowires with widths of 210 nm, a thickness of 135 nm, and a periodicity of 410 nm, the magnetic field is effectively confined. However, the spectral resonance of the

metasurface shifts towards longer wavelengths when the nanowires undergo crystallization.

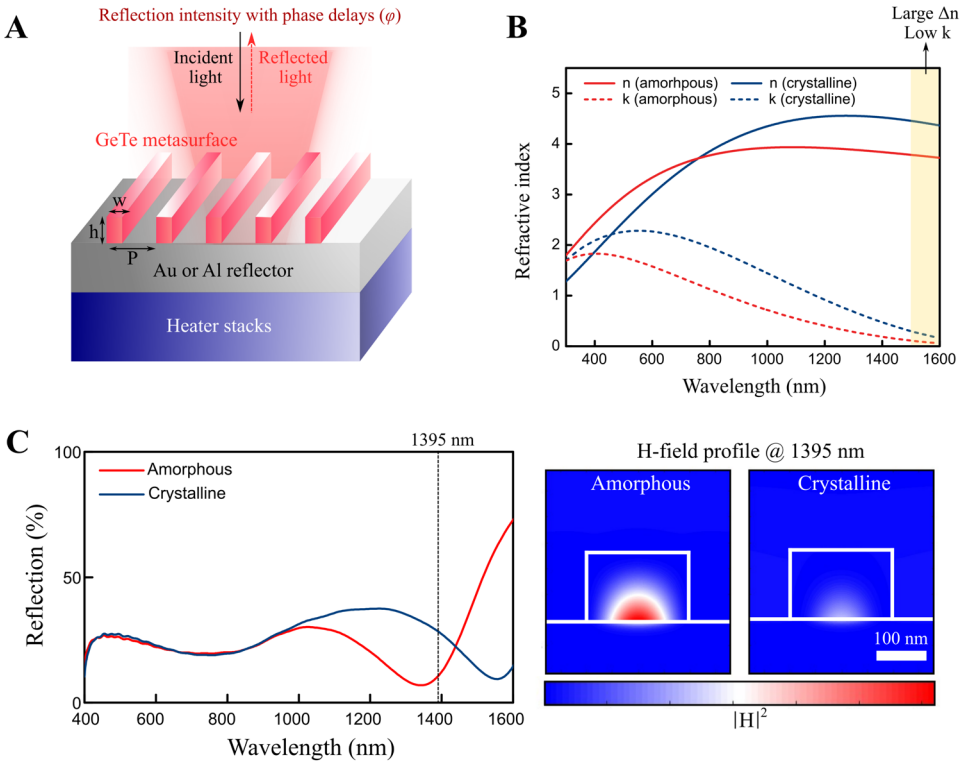


Figure 5.21 GeTe nanowire array. (**A**) Schematic of GeTe metasurface on a metal (Au or Al) substrate. (**B**) Measured refractive indices of GeTe in visible-NIR wavelengths for amorphous and crystalline states (**C**) Reflection response of GeTe metasurface (w = 210 nm, h = 135 nm, P = 410 nm) showing the selective dielectric resonances of amorphous GeTe nanowire at the wavelength of 1395 nm.

By lithographically controlling the nanowire widths from 100 to 400 nm, the reflection response in terms of both amplitude and phases can be modulated in both amorphous and crystalline phases. Similar to Sb_2Se_3 nanopillar in previous chapter, individual GeTe nanowire acts as an optical scatterer that selectively interacts with the phase of incoming light. As shown in Figure 5.22A, the selection of nanowires with appropriate widths can achieve nearly 2π phase shift with relatively high reflection in amorphous states. Conversely, in crystalline states, the nanowires exhibit random phase distribution with

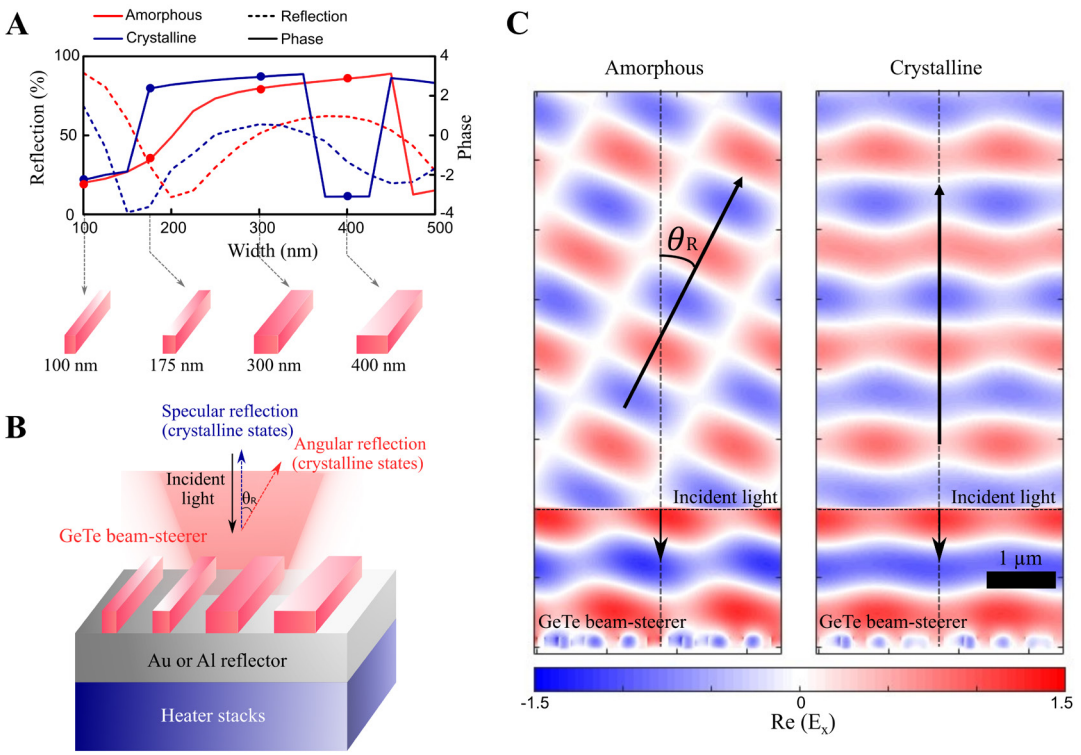


Figure 5.22 Dynamic GeTe meta-deflector. (**A**) Reflection and phase response as a function of GeTe nanowire widths at the incident wavelength of 1395 nm. Four elements of nanowires are selected to selectively cover full 2π phase shifts in amorphous states. (**B**) Schematic diagram and (**C**) simulated electric-field distribution showing that GeTe beam-steerer exhibits anomalous reflection with the deflection angle (θ_R) in amorphous states, but specular reflection in crystalline states.

low transmission. Therefore, tunable phase-gradient metasurface can be realized, turning the device *ON* in amorphous and *OFF* in crystalline states.

The arrangement of these nanowires in a periodic array ($P = w + 200$ nm) with an increasing sequence of the selected nanowire widths allows for anomalous reflection with an outgoing angle of reflection (θ_R), described by following equation of the generalized Snell's law,

$$n \cdot \sin(\theta_R) = \frac{\lambda \cdot \Delta\varphi}{2\pi P} + n \cdot \sin(\theta_I) \qquad (5.\ 5)$$

where $\Delta\varphi$ is the phase increment introduced by the nanowire array, n is the effective refractive index of medium, and θ_I is the angle of incidence (i.e. 90°). In amorphous states, 0.4π phase shift is progressively added per nanowire, resulting in an intensified +1st order deflection at the wavelength of 1395 nm. However, in the crystalline state, the absence of full phase coverage leads to high zero-order reflection. The angle of refraction (θ_R) in amorphous states can be tailored by modulating phase increment ($\Delta\varphi$) or periodicity (P). Therefore, by combining these designs with active electro-thermal switching using micro-heaters, a dynamic meta-deflector can be achieved. This meta-deflector actively tunes its operation from anomalous to specular reflection based on the crystalline states of GeTe nanowires (Figure 5.22C). Such capabilities are particularly useful for applications involving micro-scale solid-state LIDAR sensors,[163] which require compact device integration and fast scanning of an infrared optical beam for 3D image acquisition.

5.4 Further exploitation of low-loss metasurfaces for multi-factor switching

The potential of the low-loss metasurface with the thermal switching method can be further explored to incorporate additional functionalities, particularly for multi-factor switching. An example of this approach has been demonstrated by S. G. Sarwat *et al*., who utilized metal-Ge_2Se_3-metal stacks as multi-factor memristors,[28] where the phase-change material responds to multiple input stimuli, electrical biasing and optical illumination. These two stimuli were combined in such a way that a switching event only occurs when both inputs are simultaneously applied to the system. Similarly, the GeTe layer on a

microheater can be excited by two input sources: electrically-programmed thermal energy and optical power from free-space illumination. Figure 5.23 illustrates the repeatable switching of reflection observed when *RESET* or *SET* pulses were applied to the system, although the modulation contrast is relatively low due to the limited optical contrast in visible wavelengths. The *SET* pulse with an input biasing of 2.1 V was found to successfully trigger the reversible switching of the GeTe layer, while a pulse of 2.0 V was not sufficient to induce the switch. Interestingly, when the *SET* pulse in the microheater was combined with laser illumination of optical power ranging from 45 to 75 mW, multiple levels of switching were induced, indicating that optical energy was effectively

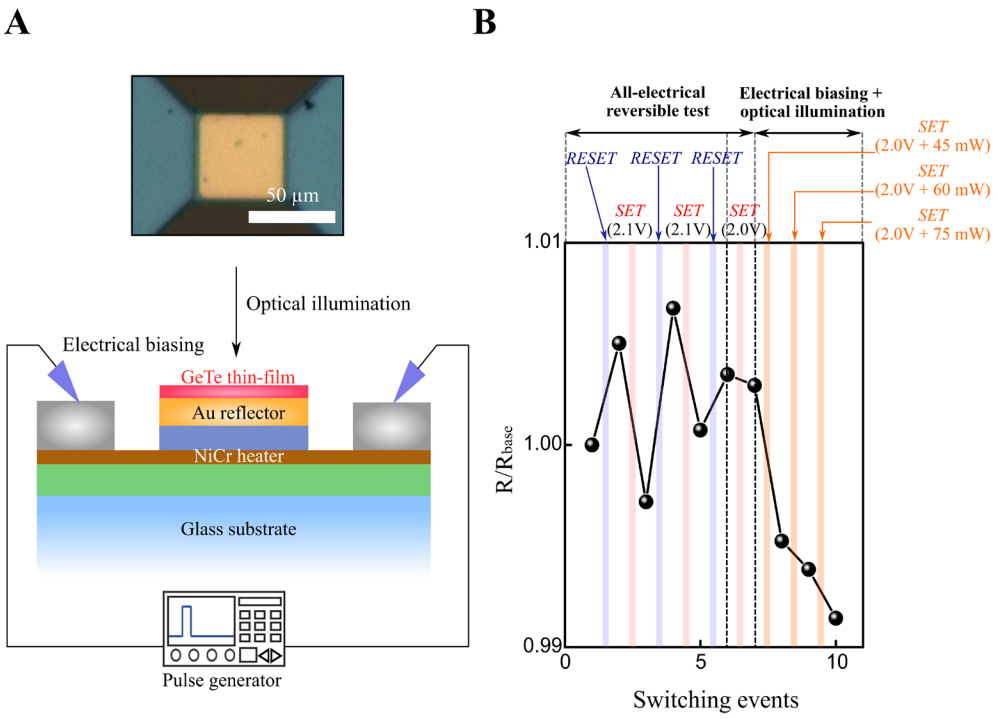


Figure 5.23 Multi-factor switching of low-loss resonators. (**A**) OM image and schematic diagram of GeTe layer on a microheater. (**B**) Multi-factor switching of the GeTe layer using electrically programmed *SET* and *RESET* pulses and optical illumination from 45 to 75 mW. *SET* and *RESET* pulses refer to 2.0 – 2.1V for 1.5 µs and 4.1 V for 500 ns, respectively. Normalized reflection was measured at a wavelength of 550 nm.

utilized to raise the overall temperature above the switching threshold. Consequently, the thermal-optical pulses serve as an accumulative factor for a single switching event.

This intriguing concept raises the possibility of utilizing additional optical properties as multi-factors for accumulative switching. For example, by incorporating such low-loss materials into nanowires, polarization-selectivity can be achieved, similar to the concept

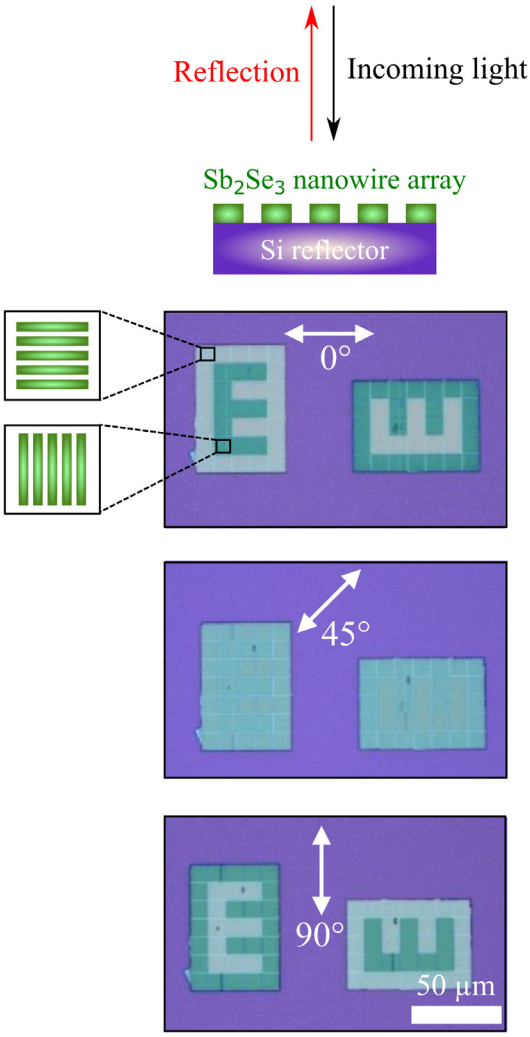


Figure 5.24 Sb_2Se_3 polarization-encrypted nanowire pixels. Schematic diagram and OM images of smart pixels composed of Sb_2Se_3 nanowire arrays in different orientations. The width, period and thickness of Sb_2Se_3 nanowire array are 230, 530 and 60 nm, respectively. 10 nm of SiO_2 is deposited on the top of nanowire as a protection layer. Each OM image was acquired with a varying polarization angle of input illumination from 0° to 90°.

demonstrated in *Chapter 4*. In this case, the low-loss nanowire itself hosts dielectric resonances within its cross-sections. Figure 5.24 provides an example of this concept, where Sb_2Se_3 nanowires on a Si substrate exhibit polarization-selective pixels that exhibit varying scattering colors depending on the polarization angle of incoming light. By placing such polarization-sensitive low-loss nanowires on the microheater shown in Figure 5.23A, more advanced forms of multi-factor switching can be achieved, with the polarization angle as one of the tunable factors. Consequently, polarization-selective switching can be realized on a larger scale (i.e. total area of the metasurface), with the aid of thermal energy provided by the microheaters. Furthermore, the concept of multi-factor switching can be expanded to incorporate other optical properties such as wavelength or orbital angular momentum (OAM). Using these features, as Figure 5.24 shows a glimpse of its potential application as smart pixels, this technique holds great promise in the fields of security encryption or anti-counterfeiting.

5.5 Chapter summary

This chapter presents the use of a low-loss phase-change resonator as an optical-phase selector for active dielectric metasurfaces. Due to the low optical loss but high index contrast, the resonator possesses various forms of multipolar dielectric resonance which can be tuned upon the crystalline states of the material. For instance, by optimizing the geometry of Sb_2Se_3 nanopillars, the mode overlap could be realized between electric and magnetic dipole moments only in specific crystalline phases, resulting in switchable phase shifters with zero absorption loss. By arranging these nanopillars into a phase-gradient metasurface, it became feasible to manipulate waveforms by dynamically reconfiguring

the crystalline phases of the meta-atoms. Consequently, both intensity- and focal-length tunable Sb_2Se_3 meta-lens were demonstrated, marking the first experimental realization of low-loss phase-change metalenses in the telecommunication wavelength range. This provided further evidence of the potential for implementing dynamic holograms using similar approaches.

In addition to this, the second part of this chapter includes a demonstration of actively and reversibly switching low-loss PCMs, addressing a recognized challenge and unmet need within the PCM community. This was accomplished through the utilization of out-of-plane light pulses for dynamic laser annealing and the introduction of a large-sized micro-heater capable of reliably switching GeTe metasurfaces through multiple cycles. By combining these advancements, a multitude of unexplored functionalities could be achieved in dynamic waveform manipulation using a collection of adjustable phase shifters.

The work described in this chapter holds timely significance and substantial impact for the fields of low-loss PCMs and dynamic metasurfaces. Moreover, it showcases the scalability of individual nanoelements and the exploitation of additional optical degrees-of-freedom, such as optical phase, by assembling multiple independent nanoelements within a shared illumination area.

While this achievement introduces new functionality through the scaling up process, yet the switching contrast remains insufficient for meaningful wavefront manipulation. Moreover, this raises fundamental questions about the feasibility of complex integration or cascading between multiple layers. Despite the demonstration of a multi-layered diffractive neural network,[164] the experimental challenges associated with 3D integration

of metasurfaces persist, and reconfiguring them at each layer becomes even more intricate. Therefore, these challenges have led to the exploration of alternative forms of nanophotonic systems that retain similar photonic functionalities, such as integrated photonic circuits, which will be addressed in the next chapter (*Chapter 6*).

5.6 Acknowledgement and contribution

All design, simulation, fabrication, and measurement of metalens were performed by the author and Mengyun Wang. Sb_2Se_3 metasurfaces for dynamic holograms were fabricated by the author with assist of Guoce Yang. The setup of out-of-plane switching was built by the author, and the measurement of different devices were done with the contribution of Nikolaos Farmakidis and Johannes Feldmann. The fabrication of the NiCr micro-heater was done by the collaborators in Bodle Technologies Ltd, while the additional fabrication of the GeTe metasurface on the heater and its switching measurement were conducted by the author. The work of varifocal metalens presented in this chapter has been published in the following article:

- M. Wang, † **J. S. Lee**, † (†, equal contribution) S. Aggarwal, N. Farmakidis, Y. He, T. Cheng, H. Bhaskaran, "Varifocal metalens using tunable and ultralow-loss dielectrics", *Advanced Science,* **10**, 2204899 (2023)

Also, this work has been presented at international conferences including *CLEO 2022*, and *EPCOS 2022*.

The work of low-loss Sb_2Se_3 phase shifter on the integrated photonic circuit has been published as the proceedings of *EPCOS 2021* and was presented at the conference, as below:

- **J. S. Lee**, J. Feldmann, T. Cheng, M. Wang, X. Li, W. Zhou, S. Agarwal, F. Brückerhoff-Plückelmann, C. D. Wright, W. H. P. Pernice, H. Bhaskaran, "Dynamic modulation of low-loss phase change materials on photonic waveguides"*, European Phase-Change And Ovonic Symposium (EPCOS) 2021*, 13–15th Sep 2021, Virtual Conference (**Poster presentation**)

Chapter 6

Spatio-spectral reconfiguration of coherent integrated nanophotonics

This chapter aims to extend the photonic reconfigurability described in *Chapter 4* and *5* from free-space optical system to integrated photonic circuits. In this integrated system, wavelength is used as a tunable factor to control photonic resonances. Specifically, the concept of 'photonic spatio-spectral reconfiguration (PSR)' is demonstrated using the wavelength-tunability of GST nanoantennas on a dielectric waveguide. The theoretical analysis of integrated photonic elements is firstly introduced (*Section 6.2*). Then, *Section 6.3* describes the concept of PSR, followed by simulation and experimental results (*Section 6.4*) of wavelength-selective reconfiguration in a microring resonator. The chapter proceeds with an analytical investigation of scaling up the functionality in *Section 6.5*, along with a discussion of the advantages of PSR in *Section 6.6*. Additionally, the potential of exploiting PSR on other platforms is explored in *Section 6.7*, leading to a summary of the findings in *Section 6.8*.

6.1 Overview: Exploiting spatial degrees of freedom in integrated photonics

Despite the implementation of unique polarization-selective functionalities in a nanowire (*Chapter 4)* and the further enhancement of nanophotonic capabilities in a phase-gradient metasurface (*Chapter 5*), it remains challenging to readily utilize such components as a building block to scale up or cascade their functionalities in free space. Consequently, interconnecting their optical responses often requires 3D integration of multiple chips[165,166] at a cost of fabrication complexity – it is especially more difficult to interconnect them at compact scale. This limitation can be significantly improved by using photonic integrated circuits (PICs) which can easily cascade multiple photonic or electronic functionalities in a single chip (as described in *Chapter 2.5*).

There is a clear distinction between two types of photonic systems in terms of device functionality: free-space photonic systems that utilize out-of-plane optical responses, and PICs that utilize in-plane mode propagation. The former allows for embedding more photonic elements into a single field-of-view, maximizing device functionalities (Figure 6.1A), while the latter increases device density by cascading photonic elements along a propagation axis in waveguides (Figure 6.1B). The ability to access multiple photonic elements of different sizes, shapes, or orientations simultaneously, which is exhibited by free-space photonic systems, is crucial for enhancing device functionalities through the exploitation of multi-faceted properties of light (i.e. polarization, wavelength, or phase). This is enabled by the attainment of spatial degrees-of-freedom within a broad field-of-view illumination, which accordingly demonstrates polarization-selective or phase-gradient system in *Chapter 4 and 5* using a multi-nanoresonator and metasurface,

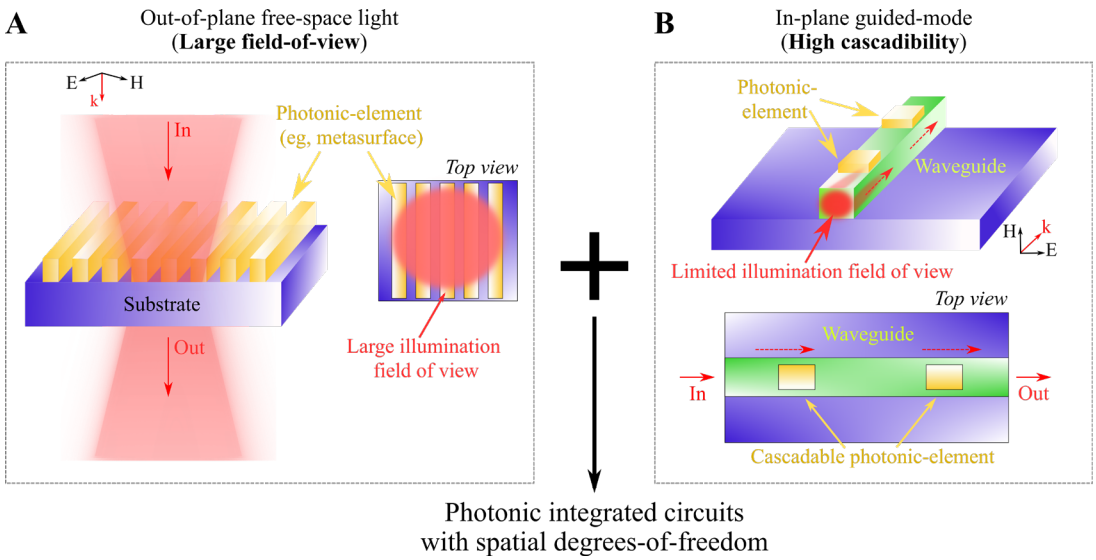


Figure 6.1 Schematic illustrations of two photonic systems, demonstrating (**A**) free-space photonic devices that utilizes out-of-plane illumination and (**B**) photonic integrated circuits that exploit guided-modes. These two systems exhibit contrasting tradeoffs between the size of field of view and cascadability**.**

respectively. However, the employment of out-of-plane optical propagation in this system presents challenges in harnessing a series of these functionalities in a cascaded form (i.e. 3D structure), thereby restricting scalability to larger systems.

In contrast, PICs offer excellent device integration and scalability (as described in *Chapter 2. 5*), where in-plane mode propagation occurs primarily through dielectric waveguides. This guided-mode propagation can be manipulated or cascaded via a compact integration of photonic modulators, resonators, or routers. However, the field-of-view of the in-plane mode is constrained by guided modes in waveguide cross-sections, resulting in a lack of selective spatial degrees-of-freedom.

This raises the question of whether photonic integrated circuits can overcome the limitation of a confined field-of-view, allowing for simultaneous and selective addressing of multiple photonic elements based on the optical properties of light. In doing so, the

PICs can leverage the functionality of multi-faceted light along the waveguide, akin to the case of out-of-plane illumination, but also retain the advantages of efficient device integration and scalability. In this chapter, such a challenge is addressed by utilizing the approach known as 'photonic spatio-spectral reconfiguration (PSR)', thereby enabling the effective enhancement of device functionalities of PICs through the spectral dimension.

6.2 Theoretical wave propagation analysis

The development of the PSR relies on several essential integrated photonic components, including dielectric waveguides that conduit guided-mode light or a microring resonator that couples the light into a closed loop optical path under resonant conditions.[167] Moreover, the standing-wave propagation in a waveguide is crucial to the operation of PSR. Therefore, a theoretical analysis of wave propagation analysis within these fundamental building blocks is described as follows

6.2.1 Dielectric waveguides

The propagation of light in a waveguide is similar to that in optical fiber, relying on total internal reflection occurring at the interface between a core with a higher refractive index (n_2) and a cladding with a lower refractive index (n_1, n_3). To simplify the demonstration, a slab waveguide is first presented in Figure 6.2A, where each medium has the refractive indices arranged as $n_2 > n_1 > n_3$. This waveguide exhibits electric ($\boldsymbol{E}$) and magnetic ($\boldsymbol{H}$) fields in the propagating mode, given by the following:[168]

$$\boldsymbol{E}(x, y, z, t) = \boldsymbol{E}(x, y)e^{i(\omega t - \beta z)} \qquad (6.\ 1)$$

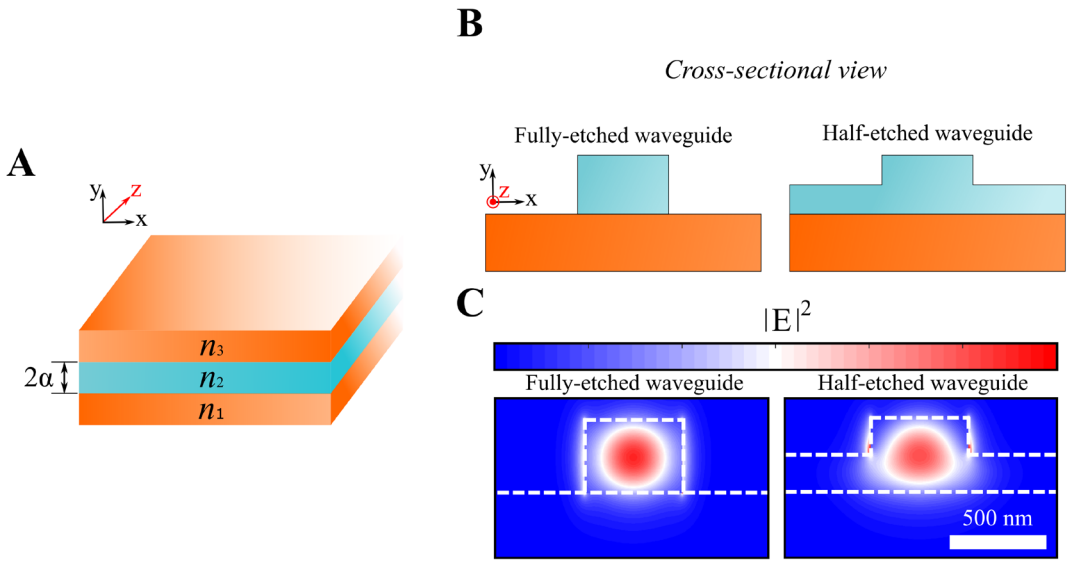


Figure 6.2 Schematic illustration of (**A**) 1D slab waveguides and (**B**) 2D waveguides, and (**C**) cross-sectional TE mode profile in 2D waveguides, calculated by Lumerical. (B-C) show demonstration of both fully-etched waveguides (etching thickness = 220 *nm*) and half-etched waveguides (etching thickness = 110 *nm*).

$$\boldsymbol{H}(x,y,z,t) = \boldsymbol{H}(x,y)e^{i(\omega t-\beta z)} \tag{6. 2}$$

where ω refers to angular frequency and β refers to the propagation constant in z-direction. Assuming that the fields propagate along the $\hat{z}$-direction, the wave-equations ($\mathcal{E}_x, \mathcal{H}_x$) for transverse-electric (TE) and transverse-magnetic (TM) planar modes are calculated as follow, where $k = \omega\sqrt{\epsilon_0\mu_0}$:

$$\nabla^2\mathcal{E}_x + (\beta^2 - k^2n^2)\mathcal{E}_x = 0 \tag{6. 3}$$

$$\nabla^2\mathcal{H}_x + (\beta^2 - k^2n^2)\mathcal{H}_x = 0 \tag{6. 4}$$

When applying this to a different 2D waveguide geometry, such as a fully-etched or half-etched structure (Figure 6.2B), the corresponding wave equation for TE modes can be described as:

$$\nabla^2\mathcal{E}_{x,y} + (\beta^2 - k^2n^2)\mathcal{E}_{x,y} = 0 \tag{6. 5}$$

However, non-symmetrical geometries and effective refractive index of such 2D cross-sections between $\hat{x}$- and $\hat{y}$-directions impose the difficulties in calculating an exact analytical model for the wave equations. Therefore, the effective index method (EIM) approach[169] is employed to provide a good analytical approximation of the corresponding mode profiles (Figure 6.2C), which can be Lumerical Finite Difference Eigenmode (FDE) solver.

6.2.2 Microring resonators

The guided-mode propagation of 2D waveguides can be further manipulated in a circular closed-loop channel, allowing light to circulate within the ring and enabling compact integration of micro resonators. The simplest form of microring resonator consists of a circular ring with input and output coupled waveguides as depicted in Figure 6.3.[170,171] The ratio of input (E_{I_1}, E_{T_1}) and output field (E_{I_2}, E_{T_2}) at the coupling region can be expressed as:

$$\begin{pmatrix} E_{T_1} \\ E_{T_2} \end{pmatrix} = \begin{pmatrix} t & \kappa \\ -\kappa^* & t^* \end{pmatrix} \begin{pmatrix} E_{I_1} \\ E_{I_2} \end{pmatrix} \quad (6.\ 6)$$

where t and κ are the coupling coefficients, and $t*$ and $\kappa*$ refer to their complex conjugates, respectively. Due to the symmetry of the matrix,

$$|\kappa^2| + |t^2| = 1 \quad (6.\ 7)$$

To further simplify this relation, the input field (E_{I_1}) is set to 1, resulting in:

$$E_{I_2} = \alpha \cdot e^{j\phi} E_{T_2} \quad (6.\ 8)$$

where α represents the loss coefficient of the ring (α equals to 1 in lossless system), $\phi = \frac{\omega L}{c}$, with L being the round-trip length. c is the phase velocity of the ring mode ($c =$

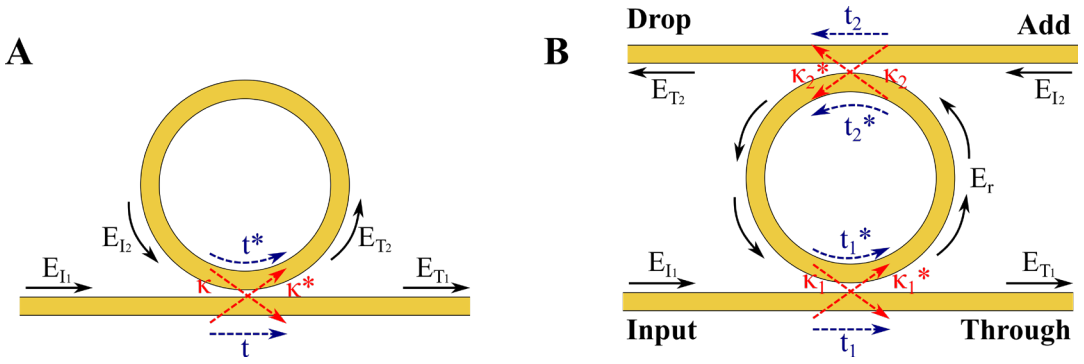


Figure 6.3 Schematic illustrations of all-pass ring resonators with (**A**) including one input waveguide couplers or (**B**) symmetric input and output waveguide couplers.

c_0/n_{eff}) at a fixed angular frequency $\omega = kc_0$ with c_0 representing the speed of light in vacuum and $k = \frac{2\pi}{\lambda}$ denoting the wavenumber in vacuum. Using this relationship, the effective refractive index n_{eff} of the ring can be described within coupling relations as:

$$\phi = \frac{kc_0 \cdot 2\pi r}{c} = n_{eff} \cdot \frac{4\pi^2 r}{\lambda} \qquad (6.\ 9)$$

Also, by combining *(6. 6)* and *(6. 8)*, the following wave-equations are derived:

$$E_{T_1} = \frac{-\alpha + t \cdot e^{-j\phi}}{-\alpha t^* \cdot e^{-j\phi}}, \qquad E_{I_2} = \frac{-\alpha\kappa^*}{-\alpha t^* + e^{-j\phi}}, \qquad E_{T_2} = \frac{\kappa^*}{1 - \alpha t^* \cdot e^{-j\phi}} \qquad (6.\ 10)$$

These lead to the transmission power of out-coupled light P_{T_1}:

$$P_{T_1} = \left|E_{T_1}\right|^2 = \frac{\alpha^2 + |t|^2 - 2\alpha|t| \cos(\phi + \delta)}{1 + \alpha^2|t|^2 - 2\alpha|t| \cos(\phi + \delta)} \qquad (6.\ 11)$$

$$t = |t|e^{j\delta} \qquad (6.\ 12)$$

where δ represents the phase shift in the coupler and $|t|$ denotes the coupling loss. Under resonant conditions, $(\phi + \delta) = 2\pi m$, where m represents an integer index. Consequently, the output transmission is obtained as:

$$P_{T_1} = \frac{(\alpha - |t|)^2}{(1 - \alpha|t|)^2} \qquad (6.\ 13)$$

It is important to note that the critical coupling occurs when $\alpha = |t|$, resulting in P_{T_1} becoming 0.

Introducing both input and output waveguide couplers to the ring allows for the manipulation of two output ports (through and drop ports). In this configuration, the half round trip loss and phase can be represented as $\alpha_{0.5}$ and $\phi_{0.5}$, respectively, where $\alpha = {\alpha^2}_{0.5}$ and $\phi = 2\phi_{0.5}$. As a result, the corresponding mode amplitudes in the through port E_{T_1} and drop port E_{T_2} become the following:

$$E_{T_1} = \frac{t_1 - t_2^* \alpha e^{-j\phi}}{1 - t_1^* t_2^* \cdot \alpha e^{-j\phi}} \quad (6.\ 14)$$

$$E_{T_2} = \frac{-{\kappa_1}^* \kappa_2 \cdot \alpha_{0.5} e^{-j\phi_{0.5}}}{1 - t_1^* t_2^* \cdot \alpha e^{-j\phi_{0.5}}} \quad (6.\ 15)$$

At resonance, the power transmission at the drop port (P_{T_2}) is given by:

$$P_{T_2} = \left|E_{T_2}\right|^2 = \frac{(1 - |t_1|^2) \cdot (1 - |t_2|^2) \cdot \alpha}{(1 - \alpha|t_1 t_2|)^2} \quad (6.\ 16)$$

In a lossless system ($\alpha = 1$), when $t_1 = t_2$, the mode amplitude at the through port (E_{T_1}) becomes 0. For a passive resonator system with a fixed constant α, the maximum transmission at the drop port (P_{T_2}) is determined by the minimum transmission at the through port ($P_{T_1} = 0$). This indicates the relationship between the loss coefficients and coupling parameters:

$$\alpha = \left|\frac{t_1}{t_2}\right| \quad (6.\ 17)$$

The spectral resonance position can be characterized by the free spectral range (*FSR*), which represents the spacing between resonance peaks. By considering the relationship of the propagation constant $\beta = \frac{2\pi}{\lambda} n_{eff}$,

$$\frac{d\beta}{d\lambda} = -\frac{\beta}{\lambda} + k\frac{dn_{eff}}{d\lambda} \approx \frac{k}{\lambda}n_g \qquad (6.\ 18)$$

where n_g is the group refractive index, described as:

$$\mathrm{n_g} = \mathrm{n_{eff}} - \lambda\frac{\mathrm{dn_{eff}}}{\mathrm{d}\lambda} \qquad (6.\ 19)$$

Consequently, the approximated *FSR* can be given by

$$FSR = \Delta\lambda \approx \frac{\lambda^2}{n_g L} \qquad (6.\ 20)$$

Under the assumption of neglecting the wavelength dependence of the effective refractive index, the simplified expression for *FSR* is:

$$FSR = \Delta\lambda \approx \frac{\lambda^2}{n_{eff} L} \qquad (6.\ 21)$$

6.2.3 Coherent perfect absorption with standing-waves

In this work, standing-wave is mainly exploited as a carrier of light, where the optical behavior of standing-wave can be analytically explained by using the concept of coherent perfect absorption (CPA). CPA refers to a phenomenon where incoming radiation is completely absorbed through the coherent illumination of an absorber, representing a time-reversed process of lasing.[172-174] The coherent illumination is achieved by combining two counter-propagating waves with equal strength, resulting in standing-wave interference between transmitted and reflected waves. In a simplified two-port CPA model with a thin absorber (Figure 6.4), the input waves can be described as follows:[175,176]

$$E_k^{(in)} = \mathcal{E}_k^{(in)} e^{j(kz-\omega t)} \qquad (6.\ 22)$$

$$E_{-k}^{(in)} = \mathcal{E}_{k}^{(in)}\, e^{-j(kz+\omega t)} \qquad (6.\ 23)$$

where $\mathcal{E}$ represents complex amplitudes, k is the wave vector, z is the spatial coordinate, t is the time, and ω is the frequency. The output waves can be expressed as:

$$E_{k}^{(out)} = \mathcal{E}_{k}^{(out)}\, e^{j(kz-\omega t)} \qquad (6.\ 24)$$

$$E_{-k}^{(out)} = \mathcal{E}_{k}^{(out)}\, e^{-j(kz+\omega t)} \qquad (6.\ 25)$$

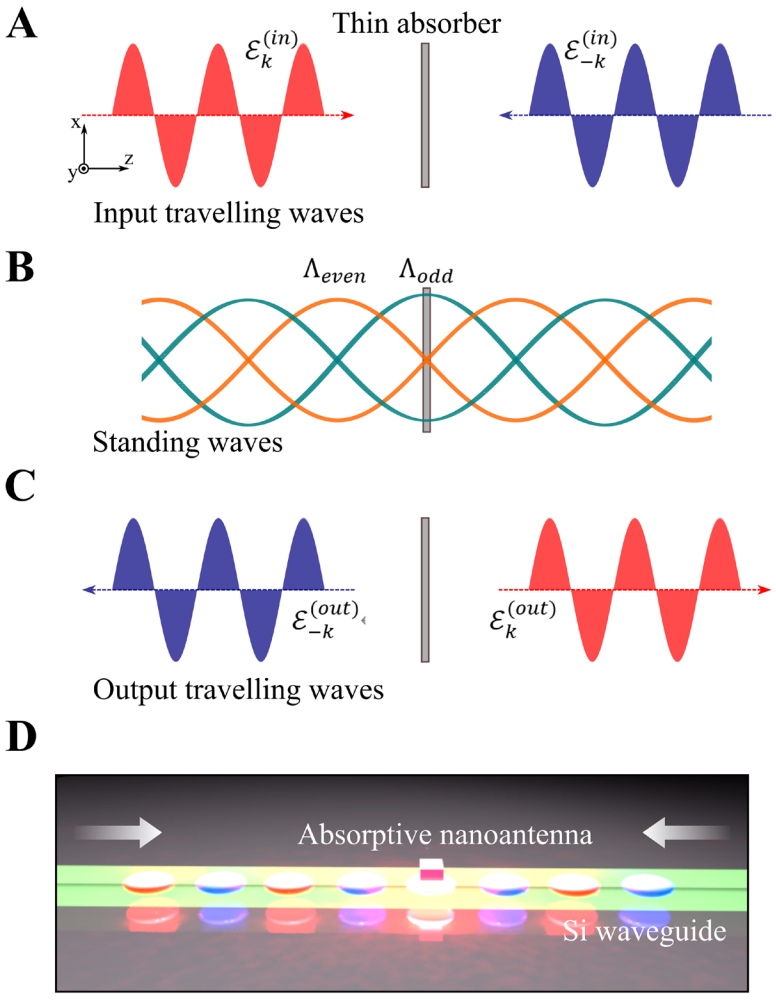


Figure 6.4 Schematic illustrations of (**A**) two counter-propagating travelling waves are decomposed into (**B**) superposition of two standing-waves. One of standing-wave modes is strongly absorbed by the thin absorber and (**C**) the resulted standing-wave is transmitted back to two output travelling waves with selectively modulated intensity. (**D**) Schematic illustration of standing-waves formed in a Si waveguide while an absorptive nanoantenna achieves near-CPA absorption via evanescent coupling.

To satisfy the CPA condition with full absorption, $E_k^{(out)} = E_{-k}^{(out)} = 0$ and the absorption coefficient under each side illumination should be as follow:

$$1 - |t|^2 - |r|^2 = 0.5 \qquad (6.\ 26)$$

where t and r represent the transmission and reflection coefficients, respectively. By applying these, the CPA-transformation can be described with a non-unitary matrix S_{CPA} as follow:

$$\begin{pmatrix} \mathcal{E}_k^{(out)} \\ \mathcal{E}_{-k}^{(out)} \end{pmatrix} = S_{CPA} \begin{pmatrix} \mathcal{E}_k^{(in)} \\ \mathcal{E}_{-k}^{(in)} \end{pmatrix} \qquad (6.\ 27)$$

$$S_{CPA} = 0.5 \begin{pmatrix} 1 & -1 \\ -1 & 1 \end{pmatrix} \qquad (6.\ 28)$$

Also, the input waves with equal coefficient $\mathcal{E}_0$ and their phase difference $\Delta\theta = \theta_k - \theta_{-k}$ can rewrite the equation *(6. 22)* and *(6. 23)* as:

$$E_k^{(in)} = \mathcal{E}_0 \cdot e^{j\theta_k} \qquad (6.\ 29)$$

$$E_{-k}^{(in)} = \mathcal{E}_0 \cdot e^{j\theta_{-k}} \qquad (6.\ 30)$$

Total absorption ($E_k^{(out)} = E_{-k}^{(out)} = 0$) occurs when $\Delta\theta = 2\pi n$ ($n = 0,1,2, \dots$), and total transmission ($E_k^{(in)} = E_k^{(out)}, E_{-k}^{(in)} = E_{-k}^{(out)}$) occurs when $\Delta\theta = \pi(2n+1)$. These features are also explained by the standing-wave analysis, where the total input field $E^{(in)}$is obtained by combining two input waves, thus a superposition of two cosine and sine-standing-waves,

$$E^{(in)} = E_k^{(in)} + E_{-k}^{(in)} = \sqrt{2}(\Lambda_{odd}^{(in)} \cos kz + j\Lambda_{even}^{(in)} \sin kz) \cdot e^{-j\omega t} \qquad (6.\ 31)$$

The amplitudes of input travelling and standing-waves are correlated through a beamsplitter-like transformation as shown below:

$$\begin{pmatrix} \Lambda_{odd}^{(in)} \\ \Lambda_{even}^{(in)} \end{pmatrix} = S_{BS} \begin{pmatrix} \mathcal{E}_{k}^{(in)} \\ \mathcal{E}_{-k}^{(in)} \end{pmatrix} \quad (6.\ 32)$$

$$S_{BS} = \frac{1}{\sqrt{2}} \begin{pmatrix} 1 & 1 \\ 1 & -1 \end{pmatrix} \quad (6.\ 33)$$

By substituting *(6. 31)* into *(6. 32)*,

$$\Lambda_{odd}^{(in)} = \sqrt{2}\,\mathcal{E}_0 \cdot e^{j(\theta_k+\theta_{-k})/2} \cdot \cos\frac{\Delta\theta}{2} \quad (6.\ 34)$$

$$\Lambda_{even}^{(in)} = j\sqrt{2}\,\mathcal{E}_0 \cdot e^{j(\theta_k+\theta_{-k})/2} \cdot \sin\frac{\Delta\theta}{2} \quad (6.\ 35)$$

The formation of different modes of standing-waves, such as odd or even modes, is dependent on the phase differences between travelling waves, where the odd mode is fully absorbed when they are in-phase, while the even mode is unaffected when they are out-of-phase. Similarly, the relation between output field and standing-to-travelling wave is described as following:

$$\begin{pmatrix} \mathcal{E}_{k}^{(out)} \\ \mathcal{E}_{-k}^{(out)} \end{pmatrix} = S_{BS} \begin{pmatrix} \Lambda_{odd}^{(out)} \\ \Lambda_{even}^{(out)} \end{pmatrix} \quad (6.\ 36)$$

Based on these transformation, one can find that one of the standing-waves is fully absorbed while the unaffected mode of standing-waves is split into two output travelling waves. This principle can be applied to guided-mode propagation by placing a subwavelength-sized plasmonic absorber on a dielectric waveguide[177] (Figure 6.4D) or microring resonator.[178] The resulting standing-wave of the photonic mode in a dielectric waveguide with two counter-propagating waves with phase difference of $\Delta\varphi$ and the effective refractive index of a waveguide n_{eff}, is described by

$$E_{tot} = E_0 e^{-j(k_{eff}z+\omega t)} + E_0 e^{j(k_{eff}z-\omega t+\Delta\varphi)} \quad (6.\ 37)$$

$$= 2E_0 \sin\left(\omega t + \frac{\Delta\varphi}{2}\right) \cos\left(k_{eff} z - \frac{\Delta\varphi}{2}\right)$$

Under the assumption of $\Delta\varphi = 0$, it can be observed that the field of standing-wave mode oscillates periodically when $z = \frac{\lambda}{2n_{eff}}$.

Likewise, the standing-wave intensity at resonant wavelengths (λ_{res}) in the micro-ring resonator is expressed as:

$$|E_{tot}(l)|^2 = 2{E_0}^2 \left[1 + \cos\left(\frac{4N\pi l}{L} + \Delta\varphi\right)\right] \qquad (6.\ 38)$$

where l is the position along the ring resonator from the out-coupling region, L is the perimeter of the ring, and N is the resonance index. This equation indicates that odd mode exhibits 0 electric-field, while even-mode exhibits $4{E_0}^2$, when $l = \frac{L}{4}$, and this intensity oscillates as $l = \frac{L}{4} + \frac{\lambda}{2n_{eff}}$.

This indicates the important implication that selective absorption of individual modes can be achieved by manipulating the phase difference ($\Delta\theta$) between two inputs or by adjusting the position (z, l) of absorber along the propagation axis. The correlation between spatial location and spectral position, specifically as ($l = \frac{L}{4} + \frac{\lambda}{2n_{eff}}$), in the standing-wave oscillation further underscores the possibility to control the interaction of electric-field with the absorber by using wavelength. Previously, absorptive nanoantennas were placed on PICs to achieve on-chip CPA,[177,178] but these systems have exhibited static absorptive features, making the realization of active CPA elusive.

Combining these features of dielectric waveguide, microring resonator and CPA, the functional photonic circuits were implemented in this work to demonstrate the concept of PSR, which will be discussed in following sections.

6.3 Photonic spatio-spectral reconfiguration

Conventional PICs, comprising various components as discussed in *Chapter 6.2*, have brought significant advancements to information processing through the utilization of spatial,[179] wavelength,[5,180] and polarization[181] multiplexing. These technologies have facilitated high-bandwidth photonics for efficient and compact photonic cores, broadband photodetection, optical switches, and neuromorphic network arrays. However, despite the passive functionalities demonstrated by photonic accelerators,[182] the reconfiguration of these circuits remains a bottleneck. Active photonic circuits, employing thermo-optic,[97] electro-optic,[95,96] and electro-mechanical[99] mechanisms, have been implemented to address this challenge. Nevertheless, the independent selection of multiple optical signals within a photonic structure, particularly in waveguides where guided modes propagate longitudinally, poses significant challenges (Figure 6.5, *top*). In contrast to out-of-plane photonic systems, in-plane modes lack spatial degrees-of-freedom, limiting the harnessing of photonic bandwidth for parallel modulation of multiple wavelengths within a single carrier (as described in *Chapter 6.1*). Moreover, the integration of active electronic circuitry has relied on relatively weak optical responses induced by thermo-optic and electro-optic mechanisms, resulting in increased device footprint and energy consumption. These devices also require long interaction lengths, which compromise wavelength or phase selectivity. Therefore, there is an urgent need for techniques capable of achieving a strong optical response within a sub-wavelength spatial domain, offering compact and selective modulation capabilities.

One promising approach to overcome these limitations is the utilization of standing-waves (i.e. CPA), whose spatial distribution of the electric field can be controlled by the

interference of two counterpropagating waves. By placing the evanescently-coupled active nanoantennas along the optical propagation axis, the spatial overlap between standing-waves and the nanoantennas can be dynamically reconfigured. In other words, the spatio-spectral relation, described in *Chapter 6.2.3*, can independently address the material states of spatially-separated nanoantennas using the corresponding wavelength channels. Notably, these phase-change materials exhibit a high refractive index contrast

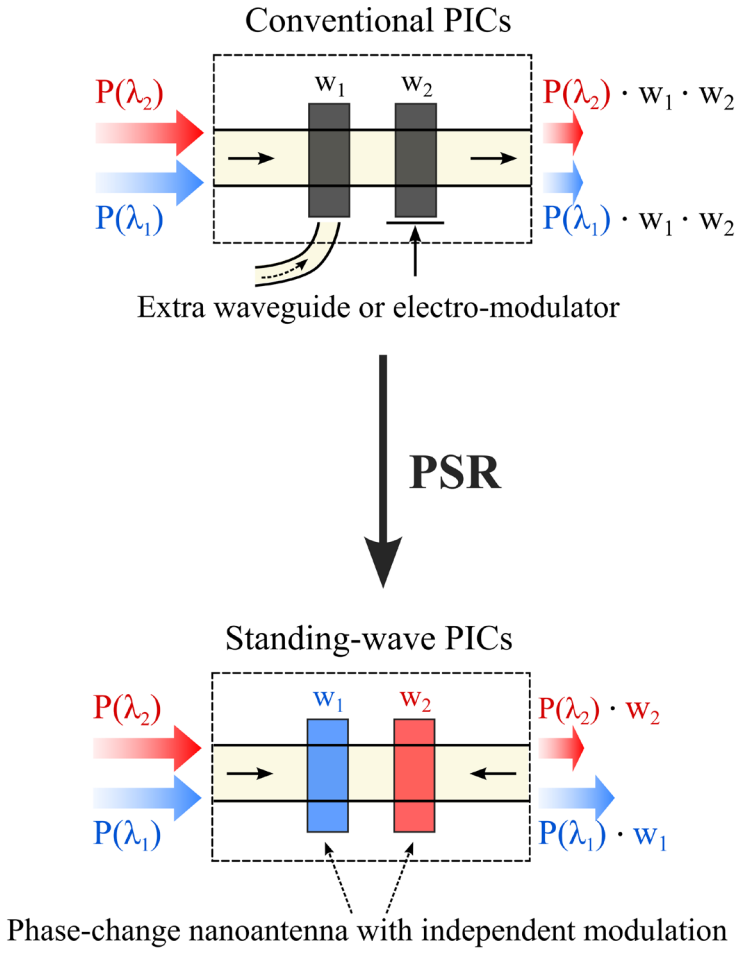


Figure 6.5 Comparison of conventional and standing-wave PICs. Conventional PICs (*top*) allow for the transmission of multiple optical signals within a single waveguide, but lack selective modulation (w_1 and w_2). In contrast, standing-wave PICs (*bottom*) provide the added capability of selectively modulating wavelength-multiplexed signals without the need for additional waveguides or electro-modulators. This is achieved through photonic spatio-spectral reconfiguration (PSR) of phase-change elements within the standing-wave cavities.

during phase transformations, such as in GST with $\Delta n \geq 1.9$ and $\Delta k \geq 0.8$, which enables sub-wavelength interaction volumes of nanoantennas to achieve significant modulation within the guided mode.[10,15] Consequently, non-volatile tunability over a broad optical range can be achieved at a compact spatial scale, allowing for independent modulation of wavelength-multiplexed optical signals travelling within a single waveguide (Figure 6.5, *bottom*). Achieving all-optical, wavelength-selective, and non-volatile tunability within a single photonic element (denoted as, photonic spatio-spectral reconfiguration (PSR)) represents a significant breakthrough for compact and highly functional integrated photonic systems, realizing active CPA.

To more clearly demonstrate the concept of PSR, the simulation results and schematic representations of standing-waves with a plain waveguide, incorporating phase-change nanoantennas, are presented in Figure 6.6. The simulation involved the propagation of light with two distinct wavelengths (λ_1 and λ_2) in opposite directions. The active GST nanoantenna, with dimensions of 100 nm (width), 200 nm (length), and 25 nm (thickness), was positioned on the waveguide, specifically at a location 4 µm away from the central axis of the waveguide along the direction of propagation. The field profile was extracted accordingly from Figure 6.7. A series of multi-wavelength field profiles revealed that the guided mode at each wavelength produced standing-wave patterns with slightly different spatial periodicities. Consequently, this resulted in discrepancies in the positions (x_1 and x_2) of the maxima and minima (i.e., antinodes) along the propagation axis of the standing-waves. This configuration functions as a wavelength-selective system, where the standing-wave at λ_2 is evanescently coupled with the nanoantenna, while the other standing-wave at λ_1 passes through the nanoantenna without perturbation. The wavelength-selectivity is

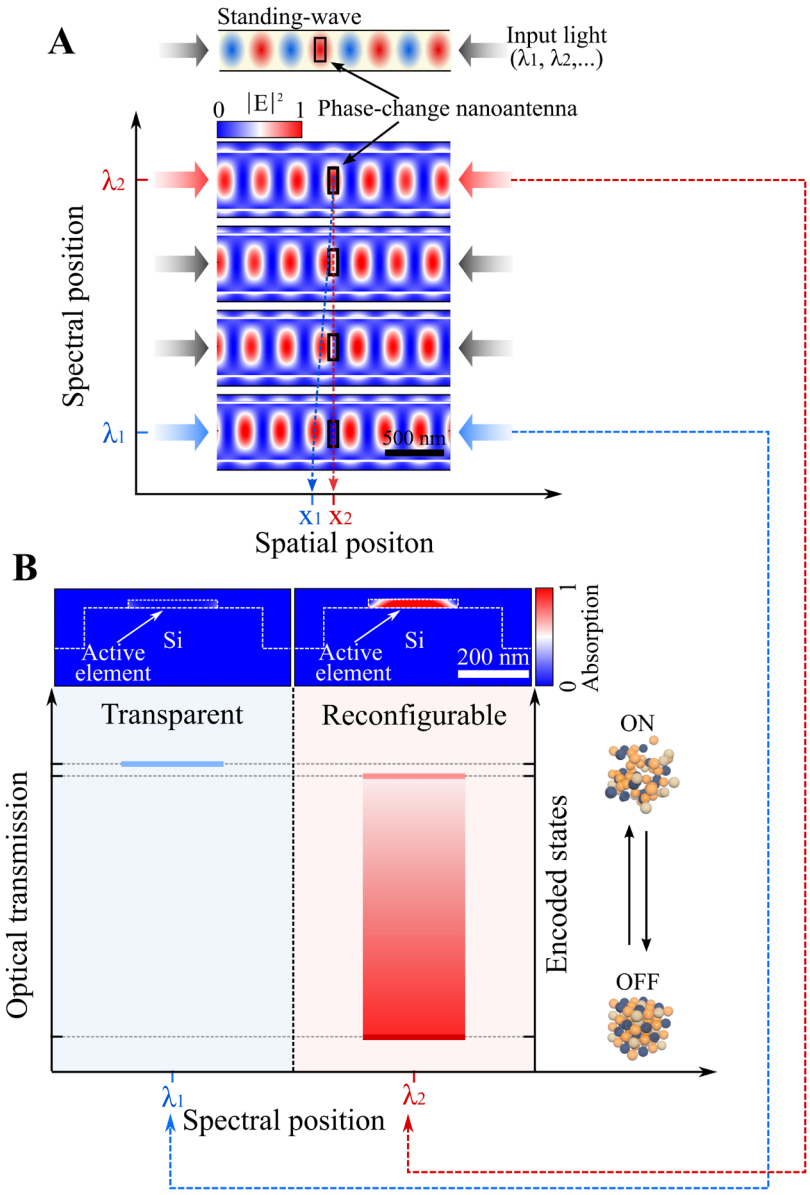


Figure 6.6 Schematic illustrations of PSR. (**A**) Schematic representation and electric-field profile within a single Si waveguide where wavelength-selective standing-waves are formed through the interference of counter-propagating light (λ_1 (1538 nm) - λ_2 (1578 nm)). The amorphous GST nanoantenna, with dimensions of 25 nm thickness, 100 nm width, and 250 nm length, is placed on the waveguide. Spatial positions ($x_1 - x_2$) of the standing-waves exhibit shifts at different spectral positions (λ_1 - λ_2), enabling spatio-spectral control. This allows the light to pass through the nanoantenna undisturbed at one wavelength (λ_1) but interact with it at the other wavelength (λ_2). Please note that the field profile shown is an enlarged view derived from the full-field distribution presented in Figure 6.7. (**B**) Wavelength-selective programmable optical transmission (i.e., absorption) is achieved at λ_2 by switching the nanoantenna between *ON* (*amorphous*) and *OFF* (*crystalline*) states, while the absorption at λ_1 is suppressed. The inset presents a cross-section of the normalized absorption profile for a Si waveguide with the active nanoantenna, demonstrating wavelength-selective absorption via evanescent coupling.

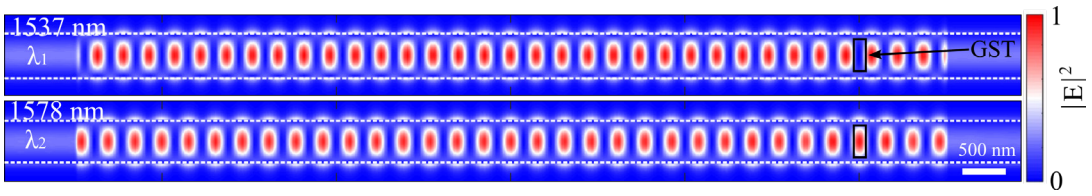


Figure 6.7 Simulated electric-field distribution of standing-waves in a plain waveguide at two wavelengths (1538 and 1578 nm). The guided-mode passes through the GST without disturbance at a wavelength of 1538 nm (λ_1), while interacts with the GST at a wavelength of 1578 *nm* (λ_2).

effectively combined with the non-volatile tunability offered by our phase-change nanoantenna. As depicted in Figure 6.6B, the nanoantenna exhibits full reversibility between its on state (*amorphous*; *low k*) and off state (*crystalline*; *high k*). As a result, the device states can be selectively reconfigured and stored at the desired wavelength of interest (e.g., λ_2). It is important to note that the feasibility of selective modulation is contingent upon either selecting two closely spaced wavelengths (eg, $\Delta\lambda \sim 40$ nm) positioned at a considerable distance (eg, 4 μm) from the central axis of the waveguide along the optical axis or choosing significantly different wavelengths at a spatial position in proximity to the central axis, due to the inherent spatio-spectral relationship of standing-waves. Additionally, it is crucial to ensure that the width of the absorptive nanoantenna (w) is much smaller than half the period of the standing-waves ($w \ll \frac{\lambda}{2n_{eff}}$).

6.4 Spatio-spectral reconfiguration in a microring resonator

6.4.1 Tunable GST nanoantenna on a microring resonator

The concept of PSR in a plain waveguide can be extended to a resonant structure by utilizing the oscillation of standing-waves in a microring resonator to enhance the wavelength-selectivity, which therefore can be experimentally demonstrated, as well.

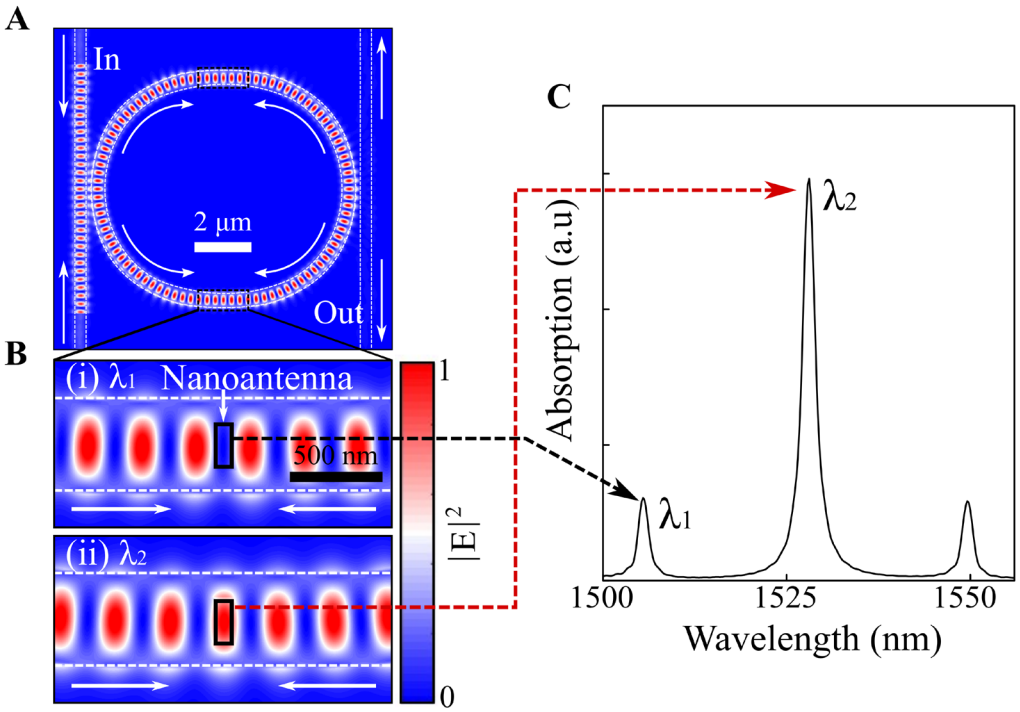


Figure 6.8 PSR in a microring resonator. (**A-B**) Simulated electric-field distribution of a racetrack microring resonator showcasing the standing-waves generated by counter-propagating waves from two input arms of a waveguide. The GST nanoantenna remains invisible to the odd-mode (*top*, 1505 nm (λ_1)), but it is evanescently coupled to the even-mode (*bottom*, 1528 nm (λ_2)). (**C**) Simulated absorption spectrum of the GST nanoantenna displaying wavelength-selective absorption at the even-mode.

Simulated electric-field profiles of standing-waves at resonance modes of the microring resonator were obtained using variational-FDTD (varFDTD, Lumerical), as shown in Figures 6.8A-C. These standing-waves showcase the enhanced optical confinement with periodic position (P) of oscillations from the center of illumination sources as:

$$P = l \cdot \lambda / 2n_{eff} \qquad (6.\ 39)$$

where l is the position index along the microring resonator. l is the integer ranging from 0 to m, where m is the resonance index. The phase difference ($\Delta\varphi$) between two input arms is assumed to be negligible.

Also, two adjacent resonant wavelengths (λ_1 and λ_2) can be represented as follow:

$$\lambda_1 = \frac{L \cdot n_{eff}}{m} \tag{6. 40}$$

$$\lambda_2 = \frac{L \cdot n_{eff}}{m-1} \tag{6. 41}$$

where L is the perimeter of microring resonator.

For two standing-waves with adjacent resonant wavelengths to be nearly out-of-phase with each other, the spatial position discrepancy ($\Delta P_{out-of-phase}$) between two standing waves should be close to $P/2$.

$$\Delta P_{out-of-phase} = (\lambda_2 - \lambda_1) \cdot l/2n_{eff} \approx L \cdot \lambda/4n_{eff} \tag{6. 42}$$

Combining equation (*6. 42*) with (*6. 40*) and (*6. 41*), the corresponding position index $l_{out-of-phase}$ and position $P_{out-of-phase}$ can be described as

$$l_{out-of-phase} = \frac{m}{2} \tag{6. 43}$$

$$P_{out-of-phase} = \frac{L}{4} \tag{6. 44}$$

with the assumption that the microring resonator is large enough so that $\frac{m}{2}$ is close to $\frac{(m-1)}{2}$. This implies that at resonant wavelengths, near the position (L/4), two different modes (odd and even modes) are manifested at resonant wavelengths in alternating order. Because the two modes were out-of-phase with each other, the spatial overlap between the nanoantenna and one of these modes was observed in a wavelength-selective manner, as depicted in Figure 6.8B. As a result, this led to wavelength-specific coupling. In Figure 6.8C, strong absorption was observed at the resonance of the even-mode (λ_2), indicating interaction between the nanoantenna and the even-mode, while the odd-mode (λ_1) propagated through the microring unaffected. This wavelength-selective interaction is a distinctive characteristic of the standing-wave microring resonator, unlike the one with

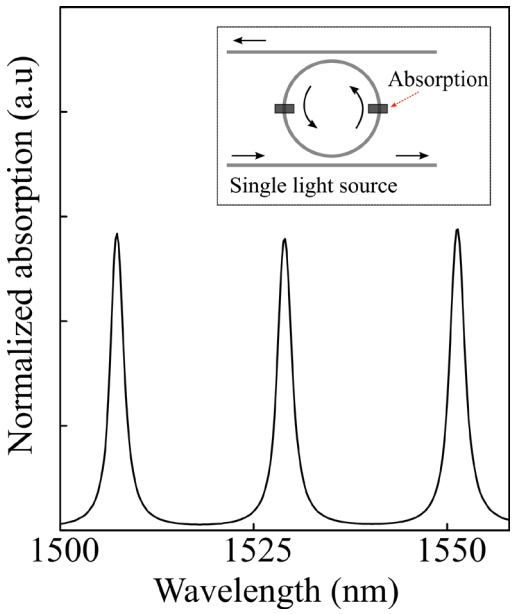


Figure 6.9 Simulated absorption spectrum of GST nanoantennas in a microring resonator when the input light was guided from a single illumination source.

unidirectional travelling waves (Figure 6.9) where this feature is absent.

The concept of PSR was further validated experimentally, as depicted in Figure 6.10. In this setup, the input light was guided through a 1:2 multimode-interference (MMI) splitter and combined into a racetrack microring resonator (30 µm diameter, 2 µm racetrack straight region) from opposite directions. Light propagation occurs in a half-etched Si waveguide, with grating couplers used for coupling in and out. Within the microring resonator, standing-waves were generated by the propagation of two counter-propagating waves and subsequently outcoupled to drop waveguides, where the output transmission was measured. To maximize the absorptive interaction strength with the standing-waves, absorptive GST/SiO_2 nanoantennas were placed at each arm of the microring. These nanoantennas have dimensions of 100 nm width, 250 nm length, and a total thickness of 30 nm (25 nm GST at the bottom with 5 nm SiO_2 on top as a passivation layer). SEM

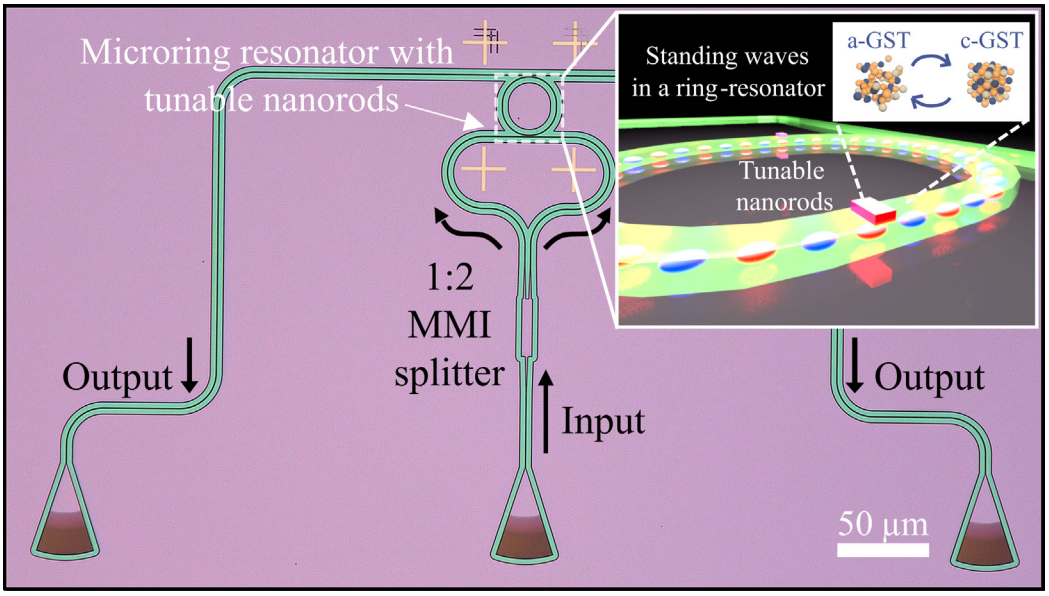


Figure 6.10 Optical microscope image of a microring PSR system. Light is coupled in and out by grating couplers, and a 1:2 MMI splitter is used to induce two counter-propagating waves into a microring resonator. Output transmission is measured at one of the drop ports. Inset shows a schematic illustration of standing-waves in a microring resonator interacting with phase-change nanoantenna.

scans (Figure 6.11) provide an enlarged view of the fabricated devices. The interaction between the oscillating electric field and the subwavelength-sized nanoantennas leads to wavelength-selective attenuation of the propagating light. The absorption loss tunability was achieved through GST crystallization, which enabled modulation of the optical transmission levels of specific modes. Experimental measurements (Figure 6.11) demonstrate a selective reduction in even-mode transmission (λ_2) when GST was switched from the as-deposited amorphous state to the lossy crystalline state after hotplate-annealed at 200 °C for 5 minutes. The even-mode resonance (λ_2) exhibits an attenuation of 49.2%, while the odd-mode (λ_1) remains non-absorptive ($\leq$ 2.1%). These results qualitatively agree with the calculated absorption spectrum in Figure 6.8C, although slight discrepancies in spectral peak positions are observed due to the use of smaller ring sizes

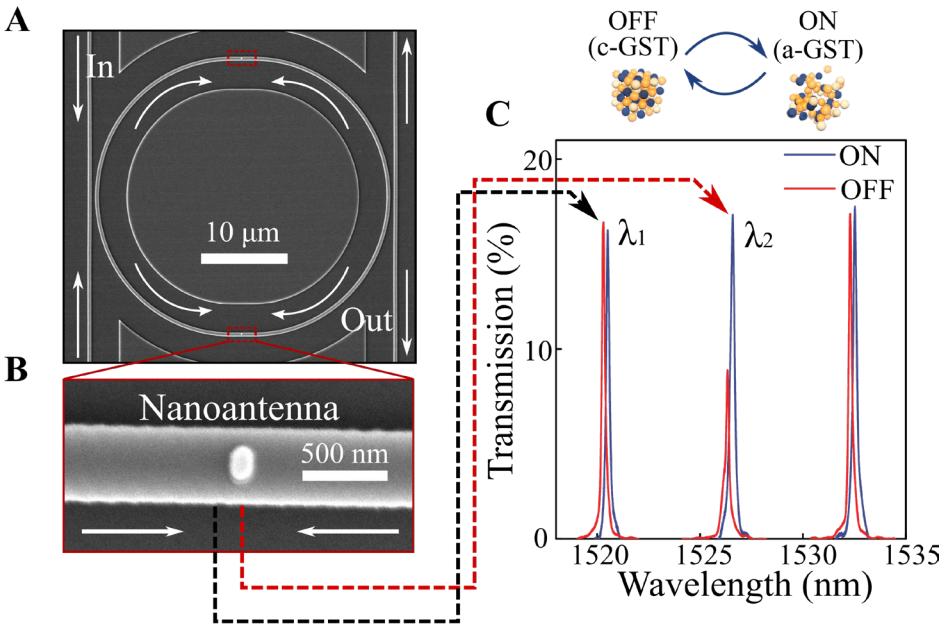


Figure 6.11 Experimental demonstration of selective absorption of GST nanoantennas in a PSR system. (**A-B**) SEM images of a racetrack microring resonator with the active nanoantenna deposited on a waveguide. (**C**) Transmission spectra of a racetrack microring resonator while the GST nanoantenna is hot-plate annealed from s-deposited amorphous (*blue*, *ON*) to crystalline (*red*, *OFF*).

(d = 8 μm) in the calculations. The slight blueshifts of transmission peaks in Figure 6.11C after hot-plate annealing is associated with evaporation of solvent or residue, causing nontrivial reduction in effective refractive index.[183] Such low fabrication tolerance can be overcome by post-processing techniques[184-187] or using additional phase shifters, which will be discussed later. This system showcases high-resolution wavelength-selective tunability in both spatial and spectral scales. The spatial resolution, calculated based on the separation of the two standing-waves ($\lambda/4n_{\text{eff}}$), is approximately 149 nm, and the spectral resolution, determined by the *FSR* of the ring resonators, is around 6.2 nm.

6.4.2 Wavelength-selective reconfigurability

Dynamic wavelength-selective modulator

After the confirmation of the passive tunability of GST using a hot-plate, further investigation was conducted to explore the active reconfiguration of the nanoantennas using optical write pulses. In this approach, the device states were optically addressed by exploiting the wavelength as a tunable factor. To enhance the absorptive coupling, a GST/metal heterostructure consisting of Cr/Au layers with thicknesses of 3 nm and 20 nm, respectively, was added onto the GST/SiO_2 nanoantennas. The nanoantennas were deterministically positioned at the spatial location of even-mode resonances (λ_2). For achieving fully reversible switching, selective illumination of the *SET* pulses (319 pJ for 10 ns followed by 83 pJ for 300 ns with a repetition of 50 times at intervals of 10 µs) and the *RESET* pulse (319 pJ for 10 ns) was performed specifically at the even-mode

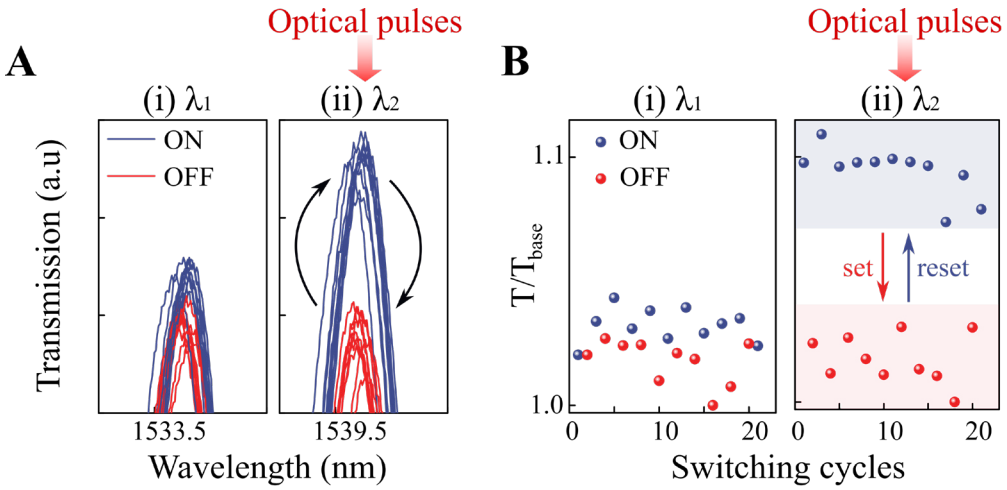


Figure 6.12 Wavelength-selectively reversible system by optical pulses. (**A**) Transmission spectra of the wavelength-selectively reconfigurable system with hybrid active nanoantennas (GST/Au) at the odd-mode (*left*, λ_1) and even-mode (*right*, λ_2) wavelengths. Optical pulses for *SET* (319 pJ for 10 ns + 83 pJ for 300 ns with a repetition of 50 times) and *RESET* (319 pJ for 10 ns) are applied at the even-mode wavelength, enabling reconfigurable transmission levels specifically at the even-mode wavelength. (**B**) Cycling performance of wavelength-selective switching as depicted in **A**.

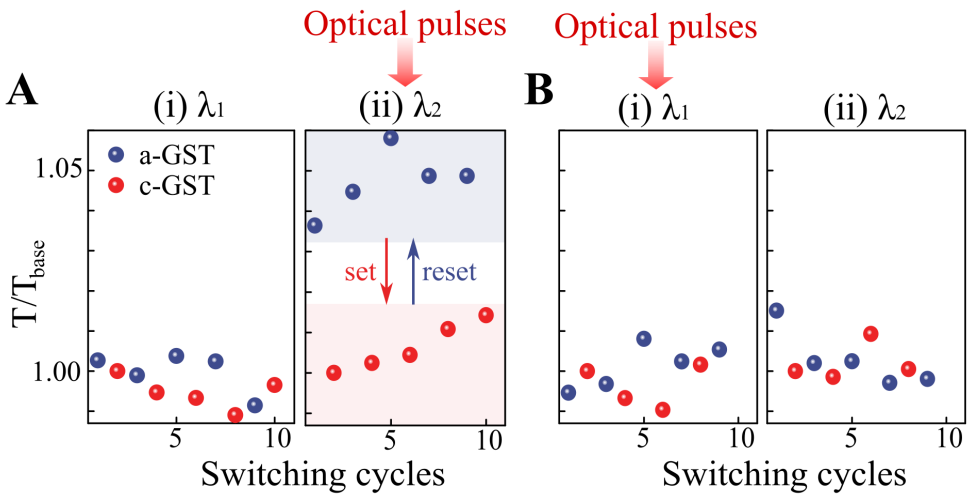


Figure 6.13 Wavelength-selective active switching cycles of GST/Au nanoantennas with optical pulses at different wavelengths. The odd-mode pulse at λ_1 (1533.5 nm) is illuminated for **A** and the even-mode pulse at λ_2 (1539.5 nm) is illuminated for **B**, where no change was observed when the even-mode is illuminated.

wavelength (1533.5 nm). As a result, the even-mode resonance (λ_2, 1539.5 nm) exhibited reversible states, while the odd-mode (λ_1, 1533.5 nm) remained unaffected (Figure 6.12A). The modulation contrast for the even-mode resonance maintained a level above 10%, whereas it was below 1.8% for the odd-mode (Figure 6.12B). To further confirm the selective programmability, negligible transmission contrast ($\leq$ 2%) was observed in both modes when the laser pulses of odd-resonances were applied (Figure 6.13).

Optimization of nanoantennas for enhanced modulation depth

Figure 6.14 displays the full-intensity transmission spectra of the PSR. The normalized transmission intensity, relative to that of the plain waveguide, is observed to be 25±7%. Consequently, considering the equal splitting at two drop ports, the total output transmission was estimated to be approximately 50%. This resulted in an insertion loss of 3.2±1.2 dB. However, this can be further improved by adjusting the stoichiometry ratio of

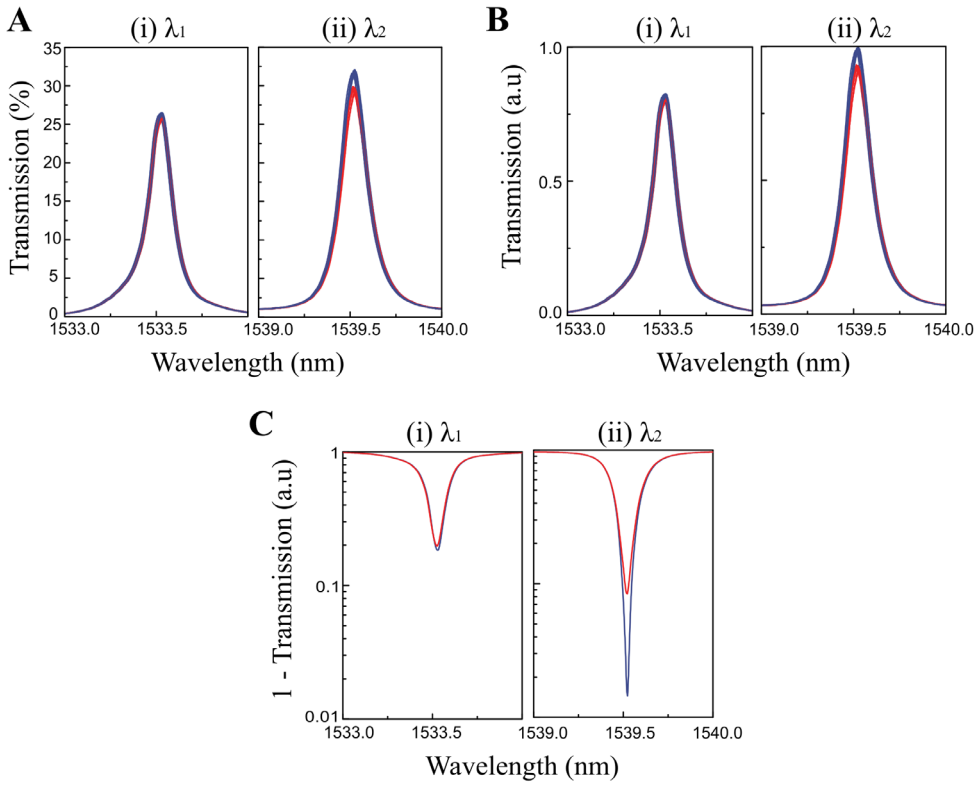


Figure 6.14 Full-intensity spectra of the PSR system. The optical pulses are illuminated at the odd-mode (*left*, λ_1) and even-mode (*right*, λ_2) wavelengths, respectively. (**A**) Normalized transmission spectra (**A**) with respect to the plain waveguide and (**B**) the one scaled to unity. (**C**) Average inverted transmission spectra derived from **A**.

phase-change alloys or replacing them with low-loss phase-change materials.[57] The maximum modulation contrast was observed to be 10±2%, which was slightly smaller compared to micron-sized GST layers on waveguides,[10,92] but comparable to or higher than other optically-switched GST nanostructures.[15] Additionally, the inverted form of the transmission spectra (Figure 6.14C) provides a clearer visualization of the wavelength-selective intensity changes.[188] This finding opens up possibilities for enhancing the modulation depth through the measurement of transmission in a through port of the microring resonator[10] or directly measuring the absorption of nanoantennas. The integration of electrical control with nanoantennas can enable absorption measurements,

where both electrical indirect switching and photocurrent readout are expected to enhance the modulation depth, as described in previous research.[39,189]

Alternatively, optimizing the size and number of nanoantennas can also contribute to tailoring the modulation depth (Figure 6.15). Initially, a single nanoantenna with a width of 100 nm and a length of 250 nm exhibited approximately 53.2% and 14.8% transmission when it reached fully crystalline and partially crystalline states (50% crystalline), respectively (Figure 6.15A). The attenuation became more pronounced when three nanoantennas were placed on the nodes of on-resonance (λ_2) standing-waves, while slight spatial overlaps between the nanoantennas and off-resonance standing-waves resulted in non-trivial changes in the off-resonance peak (λ_1). However, reducing the size of nanoantennas can minimize this undesired absorption at off-resonance (Figure 6.15C-D). Overall, increasing the number of nanoantennas with smaller widths (Figure 6.15D) helps to enhance the modulation contrast (57.0% for fully crystalline, 17.2% for partially crystalline states) without significantly degrading the crosstalk (7.1% for fully crystalline, 1.2% for partially crystalline states). Further improvements can be achieved by fine-tuning their size, thickness, or material choices. In an ultimate scenario, the position of resonances can be shifted in a wavelength-selective manner to attain even higher modulation contrast with low crosstalk.[62,190]

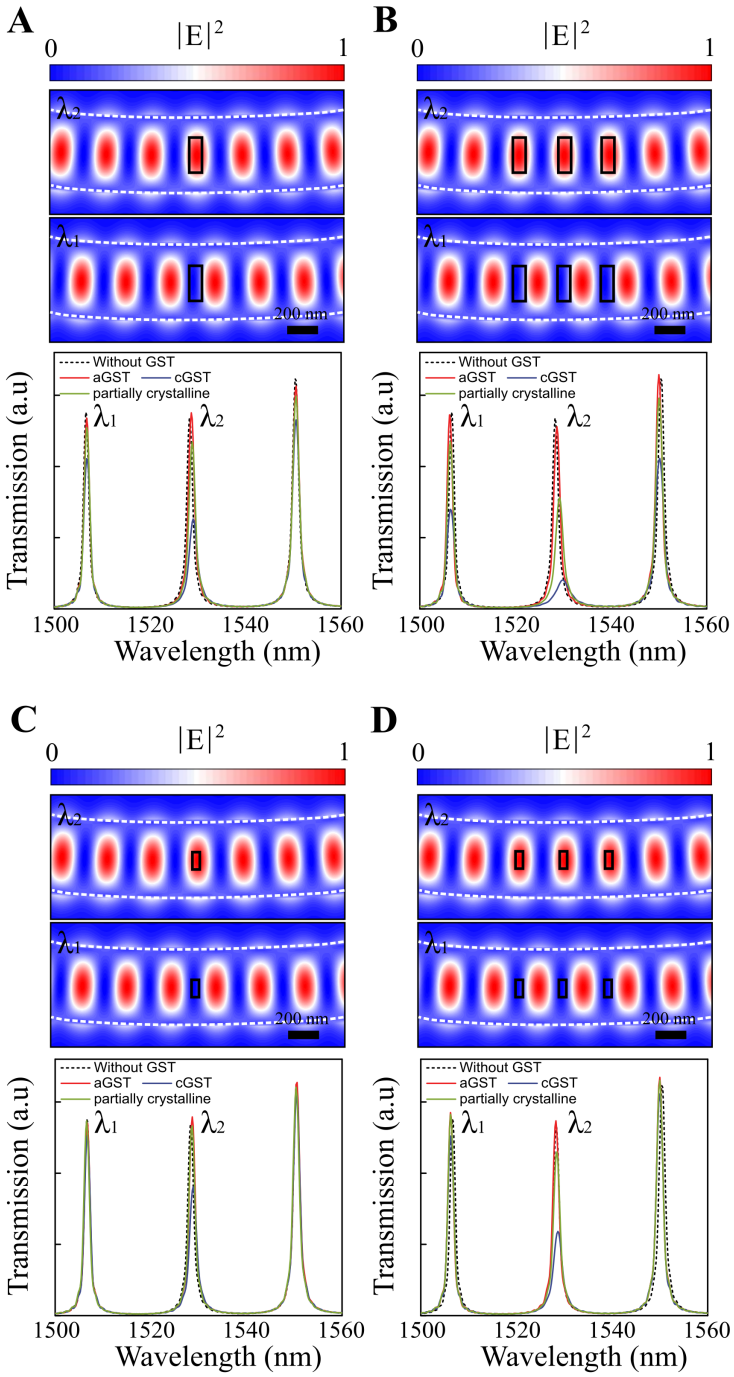


Figure 6.15 Exploring spectral selectivity through varying sizes and quantities of nanoantennas. The enlarged field distributions at on-resonance (*top*, λ_1) and off-resonance (*middle*, λ_2) conditions are demonstrated with nanoantennas positioned at the nodes of the on-resonance electric field. Simulated transmission spectra (*bottom*) of a bare ring resonator and the ones with nanoantennas are demonstrated. The GST nanoantennas exhibit three different material states: amorphous, partially crystalline (50% crystalline), or fully crystalline phases. **A-B** (**C-D**) demonstrate nanoantennas with widths of 100 nm (65 nm) and lengths of 250 nm (130 nm) respectively, while the left column represents devices with a single nanoantenna, and the right column shows configurations with three nanoantennas.

Multilevel wavelength-addressable device states

Controlling the energy of input pulses allows for achieving intermediate transmission levels of multilevel crystallinities in GST nanoantennas,[106] as the optical transmission levels depend on the fractional volume of the switched crystalline domains in the GST.[27,100] The number of set pulses was varied from 10 to 50 to achieve multilevel crystallization (Figure 6.16). Under the excitation of even-mode pulses (λ_2, 1539.5 nm), the device exhibited four distinct multilevels selectively at the even-mode wavelength, while the odd-mode wavelength (λ_1, 1533.5 nm) did not show such levels. The wavelength-selectively programmable multilevel operation could be repeated for multiple cycles, underscoring a significant improvement over a standard microring resonator that lacks selective tunability at every wavelength.

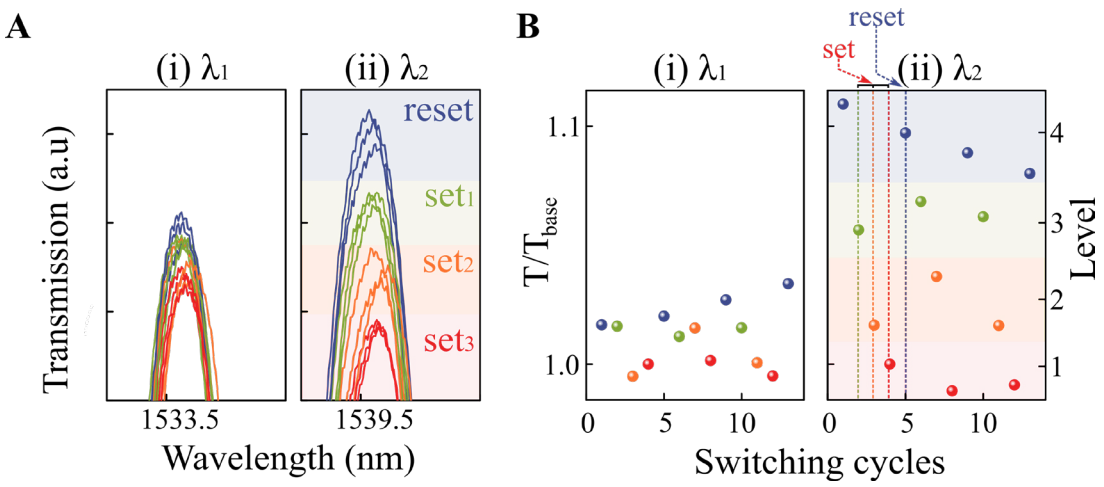


Figure 6.16 Multilevel wavelength-selective operation. (**A**) Enlarged transmission spectra showcasing the implementation of multilevel wavelength-selective operations at the odd-mode (*left*, λ_1) and the even-mode (*right*, λ_2). Optical pulses are applied specifically at the even-mode wavelength, with the number of set pulses ranging from 10 to 50. (**B**) Cycling capability of wavelength-selective multilevel operations, deducted from **A**.

Multi-spectral all-optical modulator

A reconfigurable and multi-spectral all-optical modulator was then achieved by extending the PSR model into multiple nanoantennas. The all-optical modulator enabled independent control of intensity at each wavelength. The precise placement of two sets of GST/Au nanoantennas on a racetrack microring resonator, as illustrated in Figure 6.17A, with a spacing of 460 nm ($3\lambda/4n_{eff}$) at the nodes of odd- and even-modes, allowed for wavelength-selective accessibility to individual nanoantennas through mode-selective coupling. Consequently, the intensities of wavelength-selective inputs ($P_{\lambda 1}$ and $P_{\lambda 2}$) were modulated independently by employing wavelength-selective weighting coefficients (G_{left}

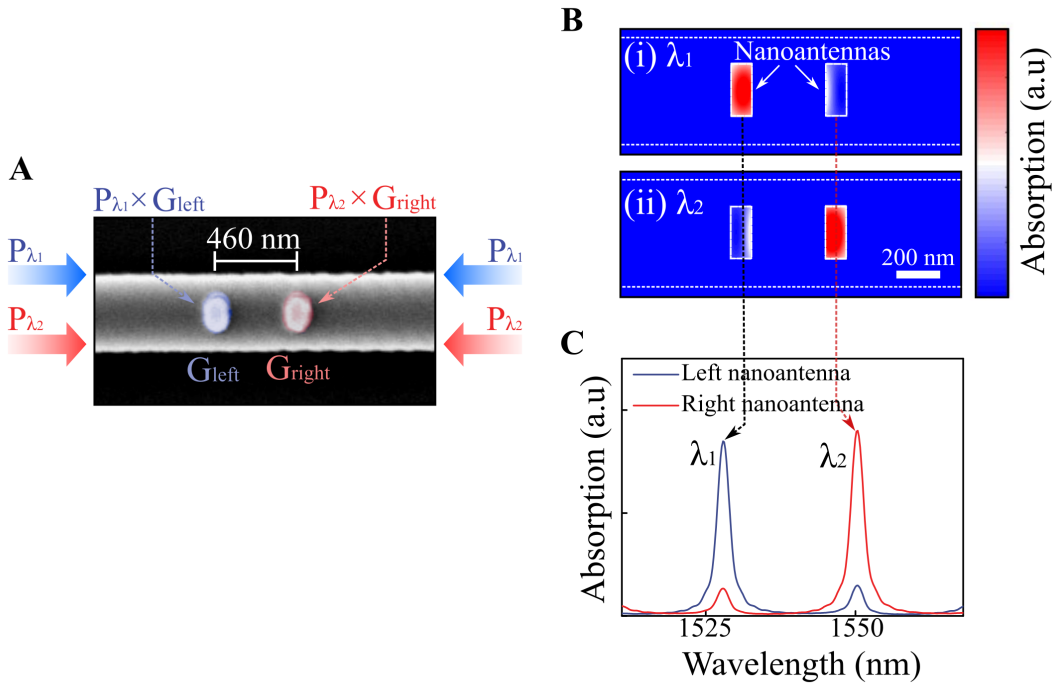


Figure 6.17 Dynamic multi-spectral modulator in a single element. (**A**) A SEM scan displaying the active nanoantennas (GST/Au) on a waveguide of the microring PSR system. The interspacing between the two nanoantennas measures 460 nm. Wavelength-independent optical inputs ($P_{\lambda 1}$ and $P_{\lambda 2}$) are selectively modulated by the weighting coefficients of each nanoantenna (G_{left} and G_{right}). (**B**) Simulated absorption profile of the PSR system featuring double nanoantennas, where the left nanoantenna couples with the odd-mode (1528 nm, λ_1) and the right nanoantenna couples with the even-mode (1550 nm, λ_2), and (**C**) corresponding absorption spectra at each nanoantenna.

and G_{right}). Spatio-spectral absorptive coupling at odd- and even-mode resonances, resulting in absorption contrast at each resonant wavelength, was demonstrated for the left and right nanoantennas, as illustrated in Figure 6.17B-C. This absorption contrast served as the basis for establishing the threshold for selective switching of individual nanoantennas. Accordingly, experimental validation proves the demonstration of wavelength-selective multilevel operation (Figure 6.18) and switching cyclability (Figure 6.19) for each photonic mode. Under illumination with odd-mode (λ_1, 1530.3 nm) light, it was observed that the laser power was sufficiently large to induce the selective switching of the left nanoantenna while leaving the right nanoantenna unaffected. As a result, selective independent multilevel encoding for the left nanoantenna was successfully demonstrated (Figure 6.18A). This selective multilevel operation involved switching from the crystalline state and manipulating the fractional volume of the amorphized GST by

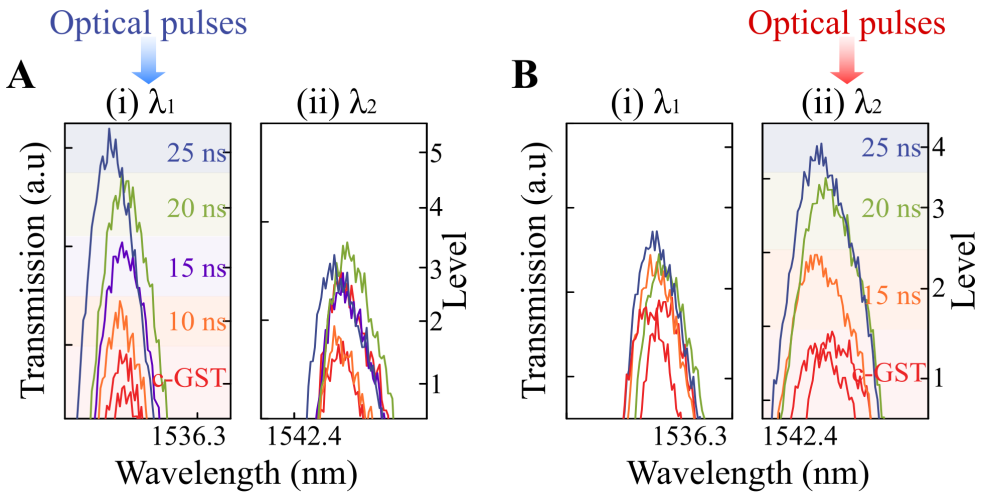


Figure 6.18 Measured spectra of a multi-spectral modulator. (**A-B**) Enlarged transmission spectra demonstrating the reconfigurable multi-spectral modulator at the odd-mode (1536 nm, λ_1) and the even-mode (1542 nm, λ_2) respectively. Multilevels are achieved wavelength-selectively by using *RESET* pulses with different pulse durations (ranging from 10 to 25 ns) under odd-mode (even-mode) illumination in **A** (**B**). Initialization of the transmission level is accomplished using a piecewise *SET* pulse (319 pJ for 10 ns + 83 pJ for 300 ns, repeated 50 times).

controlling the *RESET* pulse duration within the range of 10 ns to 25 ns. In doing so, five wavelength-selective multilevels were encoded in the odd-mode without impacting the even-mode. Importantly, this encoding process was entirely reversible, as the multilevels could be erased back to the initial state using a high-power *SET* pulse. Replication of the wavelength-selectivity was achieved by reversing the mode selections under even-mode illumination (λ_2, 1536.5 *nm*), as demonstrated in Figure 6.18B.

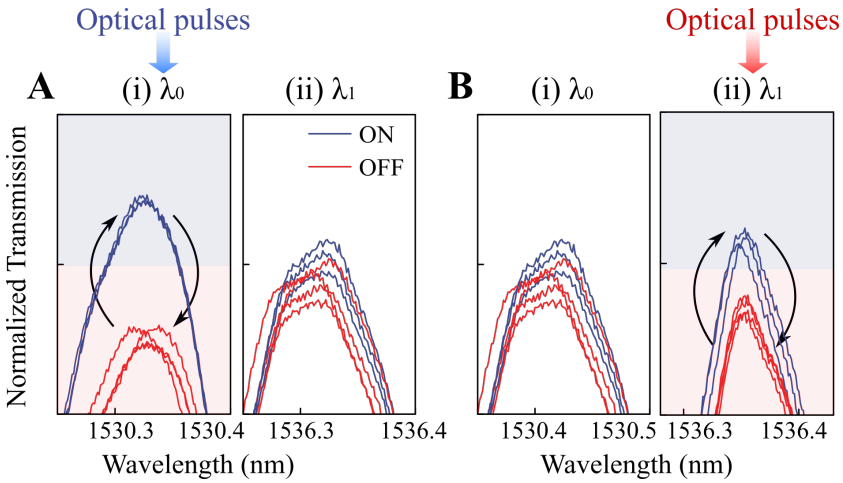


Figure 6.19 Wavelength-selective reversibility in the microring PSR system. (**A**) Even-mode even- (λ_0, 1530. 5 nm) and (**B**) odd-mode (λ_1, 1536.4 nm) optical pulses are illuminated to *SET* (220 pJ for 10 ns + 1.8 nJ for 300 ns with repetition of 50 times) and *RESET* (220 pJ for 10 ns) the device.

As briefly described in *Chapter 4.6*, this wavelength selectivity can be translated into polarization selectivity through a system capable of spatially separating electric field intensity with varying polarizations. The application of a standing-wave approach is also viable in this case, where mode selectivity is determined by polarization rather than wavelength. As demonstrated in many polarization-division multiplexing (PDM) techniques in integrated photonic circuits, a silicon waveguide can support multiple transverse-electric (TE) and transverse-magnetic (TM) modes while these modes exhibit

distinct effective index.[191] This variation in effective index can lead to the decoupled spatial position of standing waves, as described in equation (*6. 39*), between two different polarization states – TE and TM modes. By locating the individual nanoantennas at each optimized position, the polarization-selective modulation can be achieved in a similar manner. This is however beyond the scope of this work, but an interesting and impactful outlook.

6.5 Expanding the number of modulation

While two independent modulations were demonstrated in previous chapter, the number of modulation can be further increased by the extended analysis of standing-waves and the precise positioning of nanoanennas, making the functionality of PSR more powerful, especially in a upscaled system.

Spatio-spectral relation in a plain waveguide

As denoted in equation *(6. 39)*, the spatio-spectral relation is determined by the spatial periodicity (P) of a standing-wave given by the selection of wavelength ($P = m\lambda/2n_{eff}$). This means that the electric-field intensity at the center of the two light sources exhibits minimal wavelength-selectivity, when two counter-propagating waves are introduced into a plain waveguide, as illustrated in Figure 6.20. As the offset distance (ΔL_{offset}) increases, the selectivity becomes more prominent due to the greater spatial mismatch ($\Delta P = P_{\lambda 1} - P_{\lambda 1}$) between standing-waves of different wavelengths. This underscores the feasibility of attaining strong electric-field intensity modulation by modulating either the spatial

separation (ΔL) or the spectral separation ($\Delta\lambda$). Consequently, this concept can be applied to the microring resonator to increase the number of modulation channels beyond two.

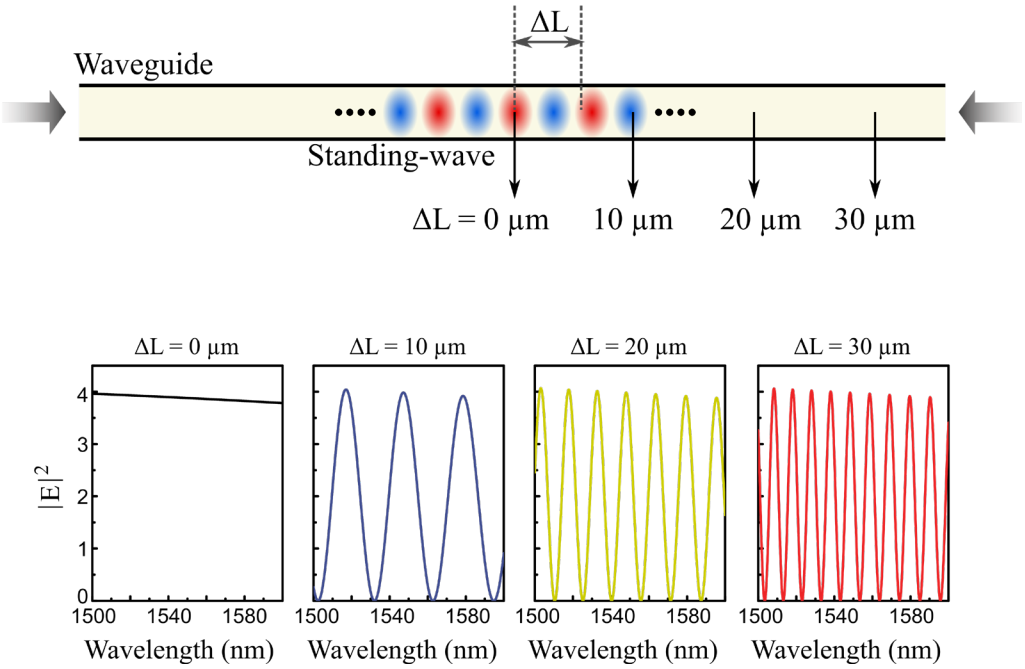


Figure 6.20 Spatio-spectral relation in a plain waveguide with two couter-propagating waves. (*top*) Schematic illustration of a PSR system in a plain waveguide and (*bottom*) simulated electric-field intensity as a function of wavelengths at each position with varying L_{offset} along the waveguide.

Increasing the number of modulation channels in a single PSR microring resonator

The aforementioned observation raises the possibility of increasing the number of independent modulation channels by identifying the optimal spatial location and resonances (λ_{res}) in the given spectral range (1.5 – 1.6 μm) for a microring resonator with a radius (R) of 15 μm. In order to determine the spatial overlap of standing-waves with multiple nanoantennas, the periodicity (P_{res})) of resonant standing-waves was calculated using the simulated electric-field intensity as follows:

$$E_{res}(x) = \cos(P_{res} \cdot x + \Delta\varphi) \qquad (6.\ 45)$$

where x is the position along half the ring perimeter ($R \cdot \pi$) of the propagation axis and $\Delta\varphi$ refers to the constant phase shift.

By applying the equation *(6. 45)* to all wavelengths within the specified spatial and spectral range, it became possible to calculate the optimal combination of three resonant wavelengths (λ_1, λ_2, λ_3) along with their respective spatial positions (x_1, x_2, x_3). This optimization aimed to minimize the crosstalk between the on-resonance and off-resonance standing-waves, as depicted in Figure 6.21 – 6.22. Crosstalk was defined as the ratio of electric-field intensity of the on-resonance standing-wave to the sum of the intensities of the off-resonance waves. It is worth noting that three nanoantennas placed accordingly exhibited wavelength-selective absorption, demonstrating a minimum crosstalk selectivity of <-15 dB. Therefore, wavelength-selective absorption allowed for independent switching of up to three separate channels, and the phase transition of nanoantennas induces wavelength-selective changes in readouts (Figure 6.21D).

The number of modulations could be increased by sacrificing the size of the microring, the spectral range of modulation, or the size of the nanoantennas. In Figure 6.21E, each of these parameters was varied to observe the optimal spatio-spectral positions (x_n, λ_n) that minimize crosstalk while increasing the number of modulations from 2 to 4. Increasing the size of the microring resonator resulted in a longer optical propagation distance ($R \cdot \pi$), allowing for increased spatial overlap between the high-intensity of on-resonance standing-waves and the low-intensity of off-resonance standing-waves (Figure 6.21E, *left*). Moreover, larger ring radii led to a reduced *FSR*, which in turn provided a greater number of resonances (λ_{res}) within a given spectral range. This expanded range of resonances reduces crosstalk in the system by enabling more combinations of various resonances. In

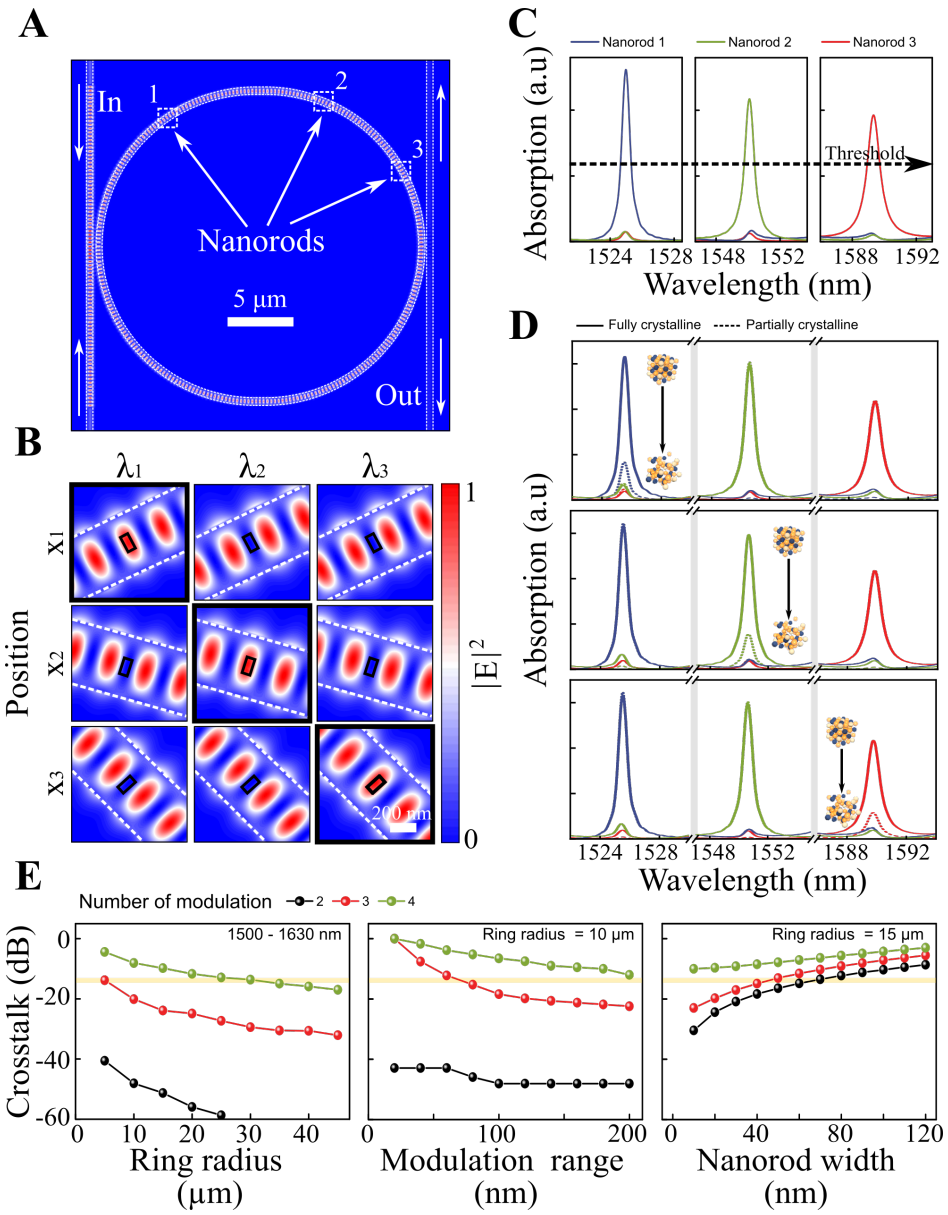


Figure 6.21 Multiple independent modulation in a single PSR system. (**A-B**) Electric-field distribution of a PSR microring resonator, with a ring radius of 15 µm. Three nanoantennas are positioned at different locations (x_1, x_2, x_3) along the optical axis of miroring, each illuminated by a distinct wavelength (λ_1, λ_2, λ_3). The enlarged field profile at each spatio-spectral position reveals that each on-resonant nanoantenna exhibits spatial overlap with the corresponding standing-waves of the respective wavelengths (outlined in ***bold***), while the off-resonant nanoantennas do not interact with the standing-waves. It should be noted that an additional three nanoantennas are placed on the opposite side of the microring to balance the interaction strength. (**C-D**) Simulated absorption spectra of each nanoantenna. As each nanoantenna switches from a fully crystalline state to a 50% crystalline state while the others remain fully crystalline, the absorption intensity varies only in the nanoantenna of interest. (**E**) Quantitative calculation of crosstalk as a function of (*left*) ring radius, (*middle*) modulation range, and (*right*) widths of nanoantennas, with an increase in the number of modulations from 2 to 4. The yellow lines represent a reference crosstalk level of -15 dB.

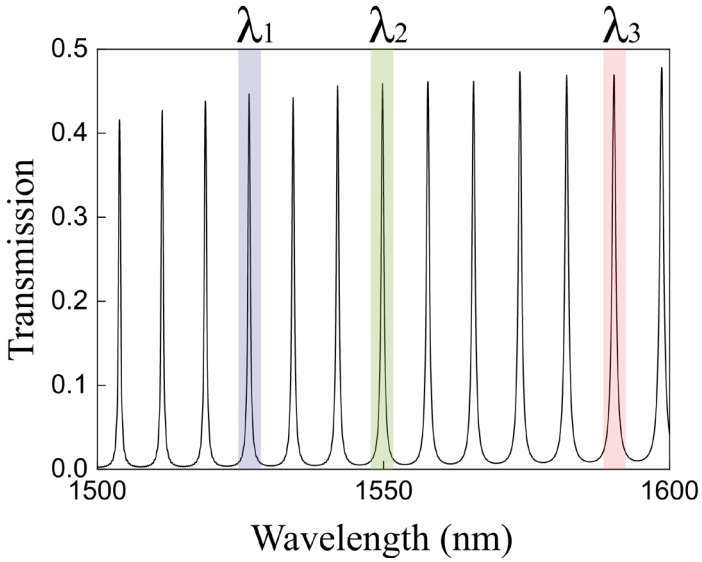


Figure 6.22 Transmission spectra of a PSR microring resonator with a radius of 15 μm, showing three resonant wavelengths (λ_1, λ_2, λ_3) which correspond to the independent modulation channels in Figure 6.21.

some cases, particularly for two-wavelength modulation, a smaller *FSR* contributes to decreased discrepancies in the period (ΔP) of standing-waves, improving their selectivity. On the other hand, for a higher number of modulations, crosstalk could be further minimized by broadening the spectral range of modulation (typically determined by the types of optical couplers[192]). This expansion of the spectral range corresponded to increased spatial offsets between standing-waves, resulting in an increased number of wavelength selections (Figure 6.21E, *middle*). However, larger nanoantenna sizes introduced non-trivial absorption at off-resonances, leading to degradation in overall crosstalk (Figure 6.21E, *right*). This limitation can be mitigated by exploring a wider range of material options, moving from lossy chalcogenide materials to low-loss alternatives.

6.6 Advantages of enhanced functionalities in the PSR system

It is worth emphasizing that the example depicted in Figure 6.21 already demonstrates the

feasibility of controlling three independent wavelengths with a crosstalk ranging from -16-19 dB, with viable device parameters, including a ring radius of 15 μm, a modulation spectral range of 66 nm (1524 – 1590 nm), and a nanoantenna width of 65 nm. The level of selectivity achieved is comparable to that of other state-of-the-art integrated (de)multiplexer designs such as angled multimode interferometers,[193] integrated ring demultiplexers,[194,195] or mode-division multiplexers.[196,197] However, the all-optical PSR approach offers the advantage of a significantly smaller device footprint due to its operation within a single photonic element. Consequently, it achieves a larger modulation density (number of modulations · modulation depth/device footprint) or multiplexing density (number of modulations · crosstalk/device footprint) compared to the aforementioned designs (Table 6.1). Additionally, the non-volatile tunability of our active nanoantennas enables the realization of energy-efficient modulators with zero static energy, surpassing the performance of electro- or thermos-optic switches, while programming energy was observed to be within the range of sub-nJ (~319 pJ). This programming energy can be further reduced by confining the electric field within the volume of the PCM, leveraging techniques such as plasmonic nanogaps or photonic-crystal microcavities (in the upcoming *Chapter 6.7*). While the modulation bandwidth of our system is currently constrained by the crystallization time of the phase-change material, most programming tasks can be accomplished using 10 – 25 ns pulses with bandwidths ranging from 50 to 100 MHz. By exploiting picosecond or femtosecond optical pulses[92,198] or employing phase-change nanoantennas as wavelength-multiplexed in-memory units,[5] modulation bandwidths can be extended to the GHz-THz regime.

	Number of modulation	Tunability	Modulation depth (dB)	Crosstalk selectivity (dB)	Insertion loss (dB)	Device footprint (μm^2)	Selectivity resolution	Modulation density (dB/mm^2)	Multiplexing density (dB/mm^2)
Tilted multimode interferometer[a]	3	N/A	N/A	<-15	-1	~1350	N/A	N/A	-33000
Integrated ring demultiplexer[b]	2	N/A	N/A	<-15	-1.8	~3500	~150 µm	N/A	-8600
Mode-division multiplexer[c]	3 (mode multiplexing only)	Volatile (*electrical integration*)	16.7	<-15	-1	~97000	~100 µm	520	-470
WDM-compatible mode-division multiplexing[d]	3 (mode multiplexing only)	N/A	N/A	-17.3	-1.5	~22000	~90 µm	N/A	-2400
Microring matrix with mode multiplexer[e]	16	Volatile (*electrical integration*)	>20	-20	-3 (coupling loss) -8 (mode-multiplexer)	~$2 \cdot 10^6$	~300 µm	160	-160
Non-volatile phase-change memory in macroring resonators[f]	3	Non-volatile (*all-optical*)	3 (through)	<-20	-10	~27000	~50 µm	330	-2200
This work (experimental, modulation = 2)[g]	2	Non-volatile (*all-optical*)	~0.56 (drop)	-11.5	-3.2	707 ($R = 15$)	460 nm	1600	-33000
This work (theoretical, modulation = 2)[h]	2	Non-volatile (*all-optical*)	~1.3 (drop)	-17.5 (partially-crystalline)	N/A	78.5 ($R = 5$)	146 nm	33000	-450000
This work (theoretical, modulation = 3)[i]	3	Non-volatile (*all-optical*)	~0.78 (drop)	-16.4 (partially-crystalline)	N/A	707 ($R = 15$)	8 – 10 µm	3300	-70000

Table 6.1 Quantitative comparison of multiplexing or modulation densities with the state-of-the-art integrated tunable multiplexer. Some devices do not have integrated modulators with multiplexers but can potentially integrate active tunability within the device. Only active area was considered for device footprints. Device features are deducted from the following references: [a]Ref. [193], [b]Ref. [194], [c]Ref. [195], [d]Ref. [196], [e]Ref. [197], [f]Ref. [10]. The results of this work were extracted from [g]Figure 6.12, [h]Figure 6.15 and [i]Figure 6.21.

Upscaling the PSR system

These advantages of the PSR system become even more beneficial when scaled up, such as by assembling multiple microring resonators in series. Conventional PICs typically require three ring resonators with different ring radii for three independent modulations (Figure 6.23). In this case, the optical storage density can be defined as 2^N and M^N for binary and multilevel modulation, respectively, where N represents the number of microrings and M denotes the number of multilevel operations. On the other hand,

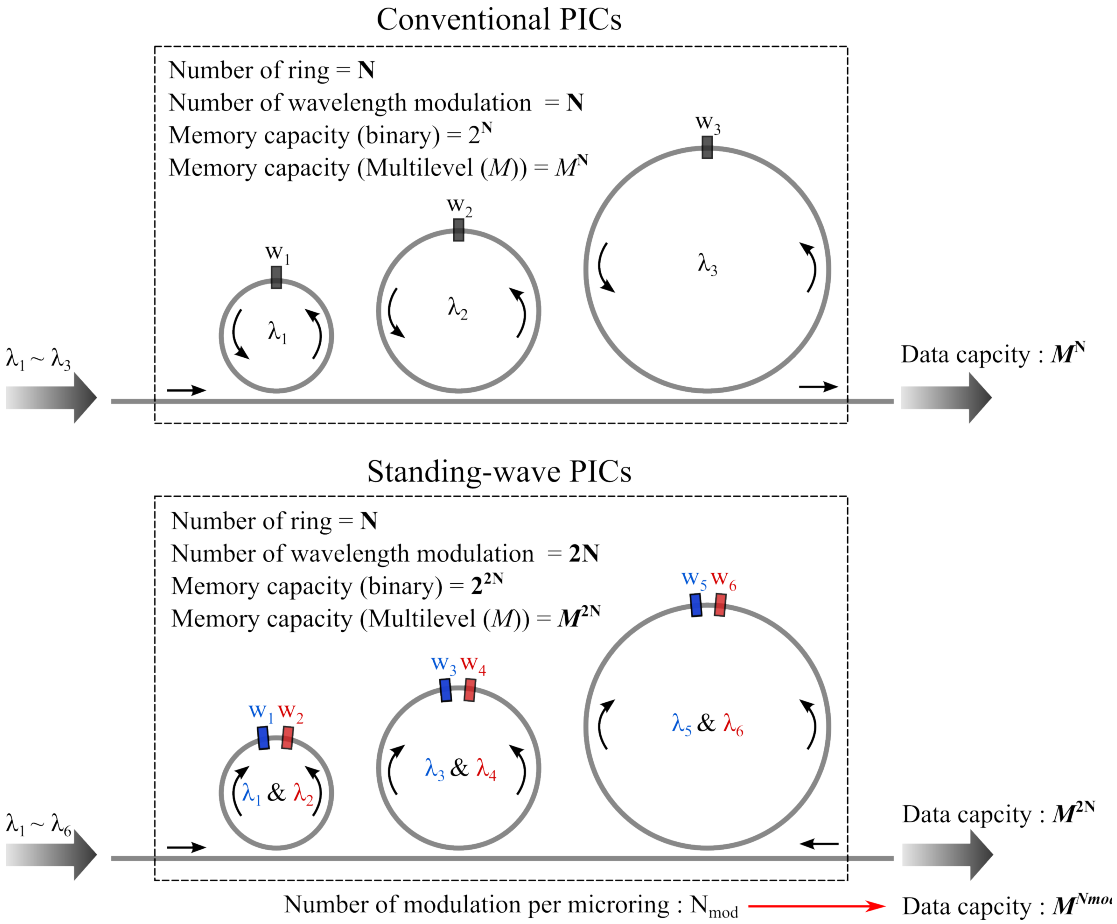


Figure 6.23 Schematic illustration of the enhanced optical storage density based on a permutation scheme from (*top*) conventional PICs using unidirectional optical propagation to (*bottom*) standing-wave PICs using counter-propagating waves. The optical storage density is enhanced from $\boldsymbol{M^N}$ to $\boldsymbol{M^{N_{mod} \cdot N}}$, where $\boldsymbol{N}$ is the number of microring, $\boldsymbol{M}$ is the number of multilevel modulations and $\boldsymbol{N_{mod}}$ is the number of wavelength modulation channels per microring.

standing-wave PICs with two modulations per ring can expand the optical storage limit to 2^{2N} and M^{2N}. By incorporating the concept of multiple modulations per microring (N_{mod}), this enhancement can be further increased to $M^{N_{mod}}$. Overall, in a large-scale PSR system with an increasing number of microrings (N), the confined multiplexing functionality is expected to exponentially enhance the optical storage capacity as the number of multilevels (M) or modulations (N_{mod}) per microring increases.

Utilization of optical phase and wavelength as the tunable factors

Another advantage of the PSR system is the controllability of spatio-spectral responses through the utilization of relative optical phase shifts between two input sources. By using an electro- or thermo-phase shifter (see Figure 6.24), the optical phase of one input arm can be modulated to modify the interference conditions of two counter-propagating light,

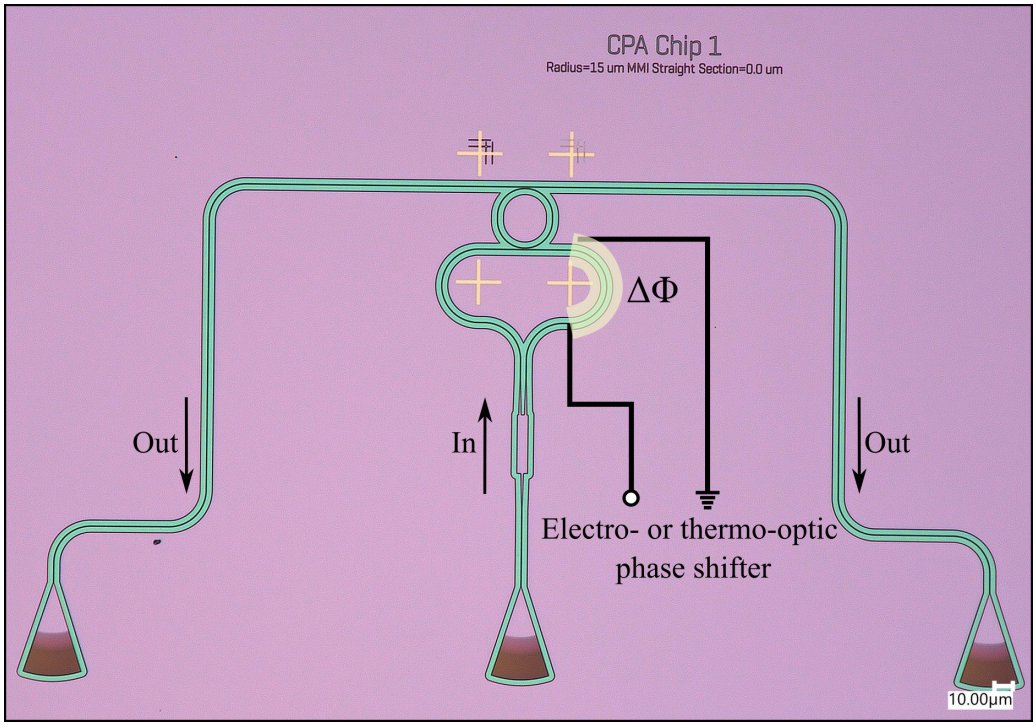


Figure 6.24 Schematic illustration of a PSR microring resonator with varying the optical phases of input arms. ($\Delta\Phi$ from 0° to 180°).

thereby allowing for the tuning of spatial positions of standing-waves within a microring resonator. Consequently, the spatial overlap between standing-waves and nanoantennas is modulated as a function of the phase delay (ΔΦ) of one arm (Figure 6.25). As ΔΦ varies from 0° to 180°, the left nanoantenna transitions from being transparent to fully absorptive, while the right nanoantenna exhibits the opposite behavior. This approach enhances the robustness of our system and introduces additional tunable functionalities in the phase domain, along with the wavelength domain. In particular, the direct control of optical response within a microring resonator from the outside of the microring can provide a wide array of interesting functionalities. For instance, the high-resolution spatial information of naonantenna or other subwavelength-sized absorber on the microring can be obtained by continuously sweeping the optical parameters (i.e. wavelength and phase),

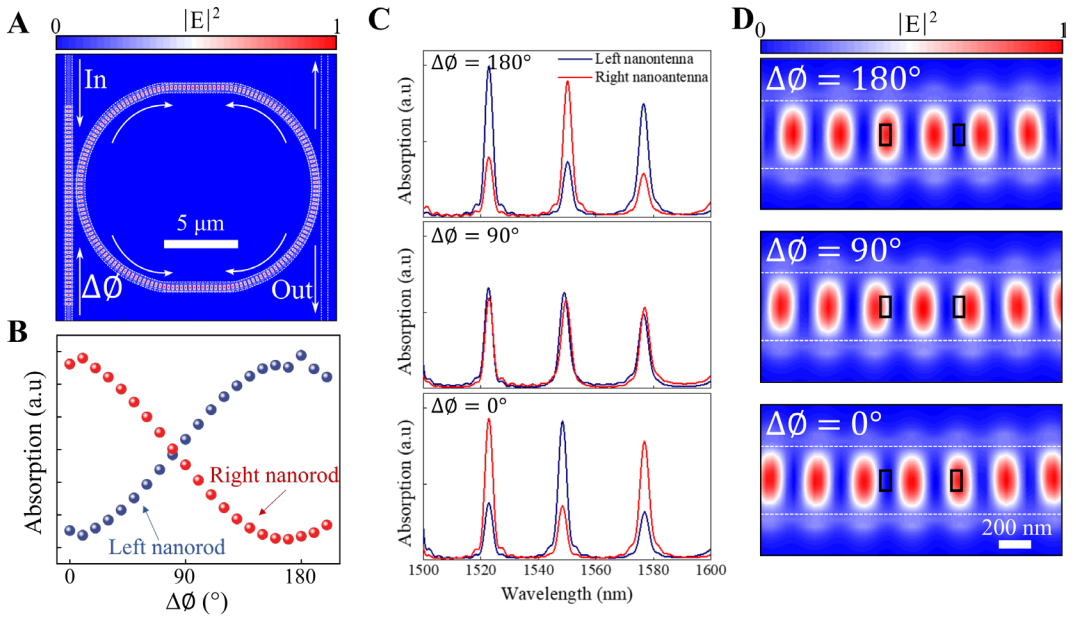


Figure 6.25 Demonstration of a PSR microring resonator with optical phase delays as a tunable factor. (**A**) Simulated electric-field distribution of a PSR microring resonator with one input arm experiencing phase delays (Δ*Φ*) (**B**) Absorption intensities and (**C**) absorption spectra of each nanoantenna as a function of Δ*Φ*. (**D**) Enlarged electric-field profile to show phase-delay-selective coupling with individual nanoantenna.

thereby realizing the application of integrated imaging or sensing. Additionally, the simultaneously-addressable nanoantennas on a single photonic carrier by optical means suggest the use of the PSR system as powerful in-memory computing[55] units for both addition and multiplication processes.

6.7 Further exploitation of spatio-spectral photonics

Compact PSR resonator using photonic crystal microcavities

The density of multiplexing/modulation in a PSR microring resonator can be further increased by confining light to smaller volumes within photonic crystal microcavities. As depicted in Figure 6.26, an array of subwavelength holes (i.e. scattering centers) can induce a photonic bandgap in a single-mode Si waveguide,[199] analogous to the electronic bandgap found in solid-state crystals. The presence of periodic holes with a periodicity (a) restricts the wavevector to π/a, acting as a Bragg reflector that selectively allows the guided mode of wavelengths outside the photonic bandgap. By incorporating two different Bragg reflectors with a specific spacing (or creating defects) between them, the light can be effectively trapped within the volume in which the periodicity is broken, forming a microcavity.[200] Because this confinement occurs along the propagation axis, spatio-spectral coupling can be introduced by implementing multiple cavities with distinct resonant wavelengths. In this system, the input light was guided in one direction due to the individual mode confinement occurring within each microcavity between two Bragg mirrors. Figure 6.26 illustrates the implementation of a Bragg mirror composed of an array of apodised holes on a fully-etched Si waveguide with a thickness of 220 nm. The array

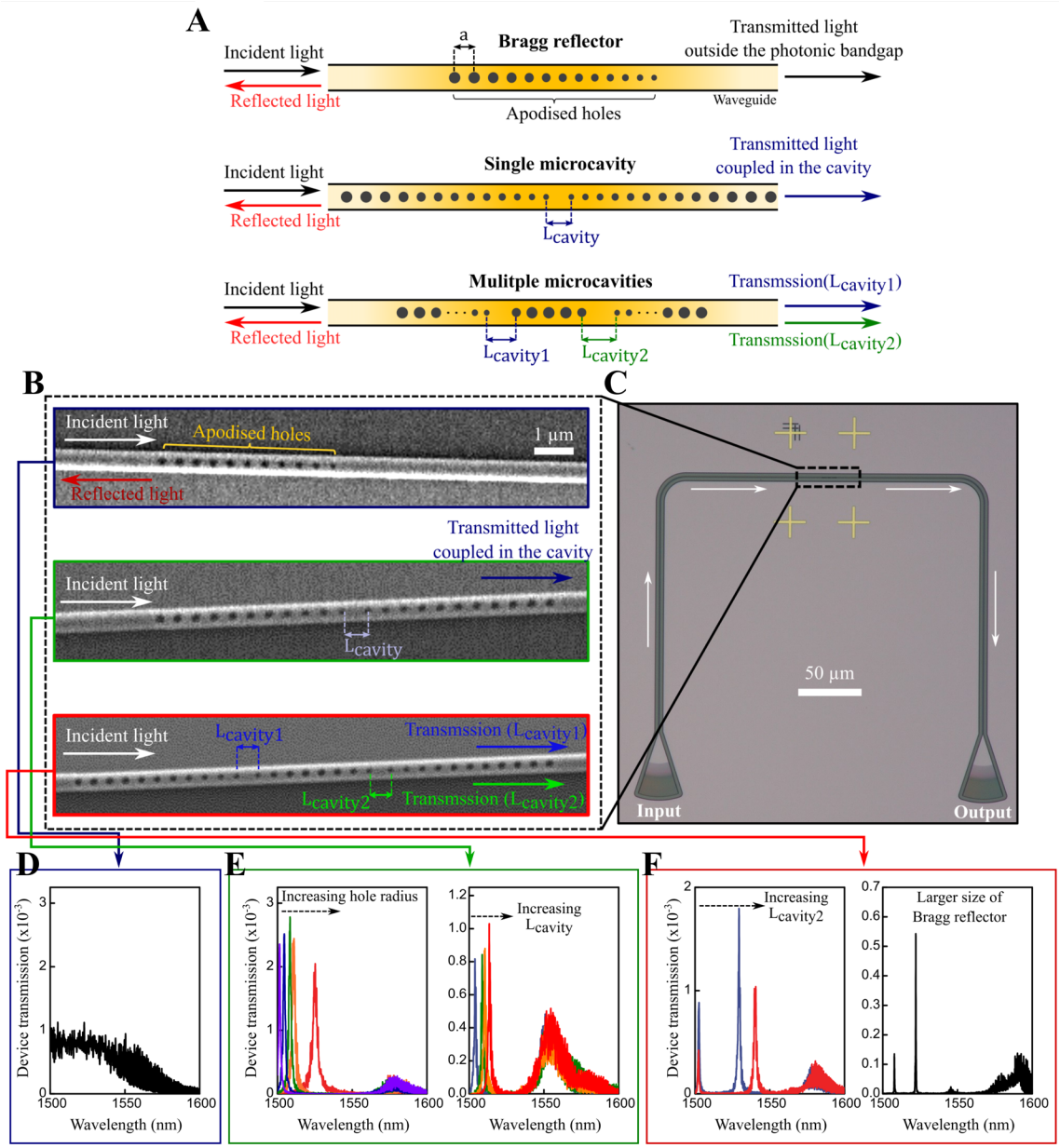


Figure 6.26 Photonic-crystal microcavities for spatio-spectral accessibility. (**A**) Schematic illustration and (**B**) SEM scans of photonic-crystal based (*top*) Braggs reflector and multiple Bragg reflectors with (*middle*) single or (*bottom*) double microcavities. Photonic-crystal Braggs mirror consists of apodised holes (radius varies from 100 to 180 nm) with a periodicity of 350 nm on a fully-etched 220 nm-thick Si waveguide. Cavity length varies from 390 to 430 nm. (**D**) Measured device transmission of (**D**) Braggs reflector, (**E**) a single photonic crystal microcavity with varying hole radius or cavity length (L_{cavity}) or (**F**) double photonic crystal cavities. The base hole radius in **E** (*left*) varies from 90 to 110 nm, and the L_{cavity} in **E** (*right*) varies from 420 to 500 *nm*. **F** (*left*) shows the double microcavities with $L_{cavity2}$ varying from 480 to 540 nm, while $L_{cavity1}$ is fixed with at 450 nm. **F** (*right*) shows the double cavities with the increased number of holes for Braggs mirror.

has a periodicity of 350 nm, and the hole radius varies from approximately 100 to 180 nm. Experimental evidence shows that a single hole array blocked most of the incoming light, while two sets of arrays with a cavity length (L_{cavity}) of 400 nm produced a strong transmission peak. The resonance peak varied depending on the hole radius or cavity length. Moreover, multiple microcavities can be constructed by selectively varying the cavity lengths, where each cavity length corresponds to an individual spectral peak. The quality factor of these resonances was found to be higher than that of microrings discussed in previous chapters, and it increased even further (Q-factor $\gg$ 6,000) as the size of the periodic array increased (Figure 6.26D, *right*). Overall, this photonic crystal system allows for selective and strong field confinement in both spatial and spectral dimensions, making it suitable for ultracompact PSRs. However, one drawback in this case is that multiple cavities fall within the same pass band of the Bragg mirror, resulting in continuous attenuation as the number of cavities increases.

To address this, as shown in Figure 6.27, the light was illuminated from both sides of the waveguide, compensating for the overall loss and enhancing the confinement. This configuration allowed for wavelength-selective modulation with up to five independent channels when combined with a GeTe nanoantenna measuring 80 nm in width, 120 nm in length, and 10 nm in height. Experimental demonstrations have shown a GeTe nanoantenna with a width of 100 nm, length of 200 nm, and height of 15 nm. Using this system, individual nanoantennas were found to exhibit wavelength-selective absorption above the switching threshold from the simulation, suggesting the possibility of exploiting five independent modulation channels. The feasibility of such system was further emphasized through the demonstration of wavelength-selective optical changes (i.e.

absorption) in each nanoantenna, where one nanoantenna underwent crystallization while the others remained in amorphous states. This showcases the potential for achieving more than five independent modulations within a waveguide range of 25 μm, thereby maximizing the density of both multiplexing and modulation. However, further optimization is needed to improve the decoupling between multiple cavities that share the same spectral window of the Bragg mirrors.

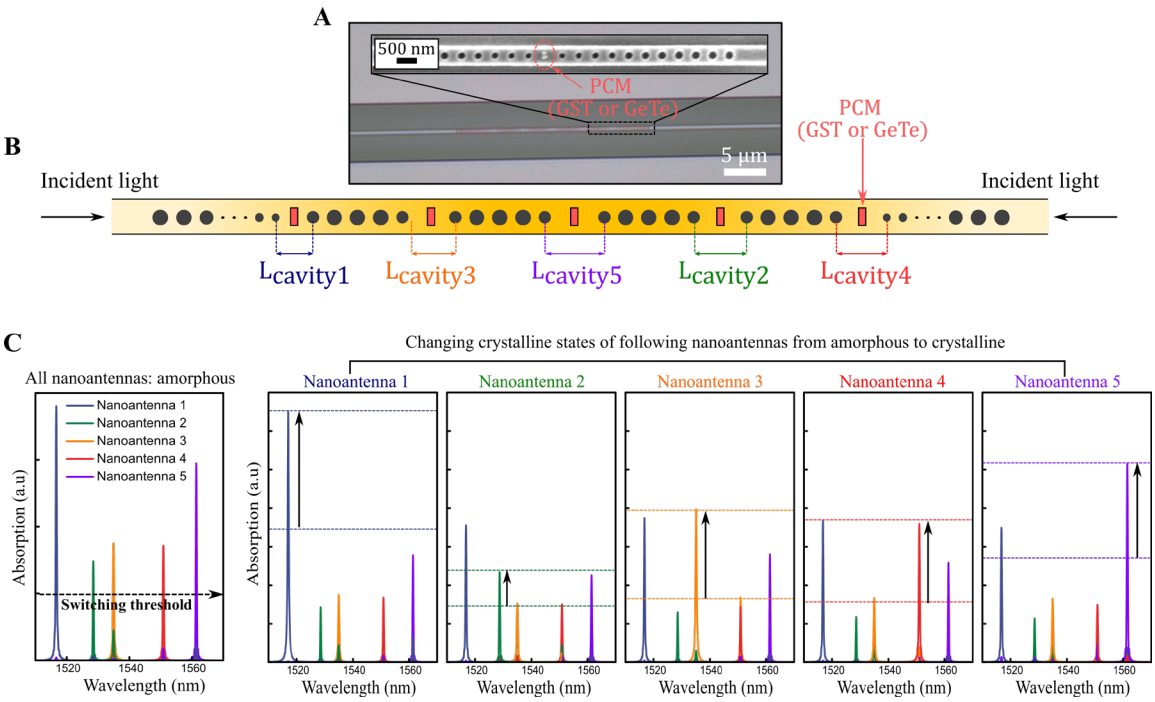


Figure 6.27 Photonic crystal microcavities with two counter-propagating waves. (**A**) OM and SEM images, and (**B**) schematic demonstration of five microcavities with two input light from opposite directions. The GeTe nanoantenna is placed in each microcavity. (**C**) Simulated absorption spectra of individual nanoantennas when all of them are in amorphous phases, showing five distinct resonant absorption from each nanoantenna. (**D**) Simulated absorption spectra demonstrating the wavelength-selective changes of attenuation in individual nanoantenna as they become crystalline while the others remain in amorphous phases. The lengths of each microcavity from $L_{cavity1}$ to $L_{cavity5}$ are as follow: 400, 445, 427, 464, and 380 nm, respectively.

Electrical integration with a PSR microring resonator

In addition to all-optical modulation, the feasibility of electro-optic mixed-mode operation was also investigated by directly integrating electrical components into a PSR microring resonator (Figure 6.28). A lossless waveguide crossing was implemented on each side of the microring, allowing for the integration of submicron-scale Au electrodes. To ensure electrical insulation, a 5 nm layer of SiO_2 was deposited on the waveguide in advance of fabricating electrodes. Two electrodes were positioned with a confined nanogap (~150 nm), and a GST nanoantenna, annealed on a hot-plate, served as the connection between

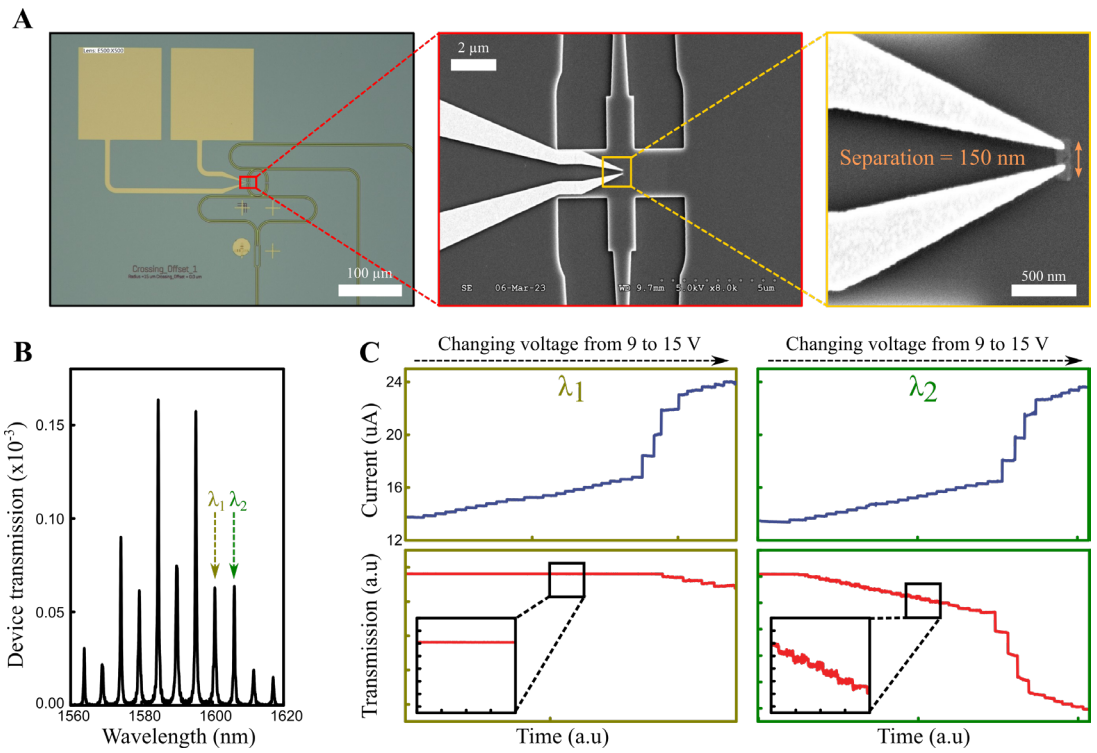


Figure 6.28 Electrically-programmable PSR system. (**A**) OM and SEM scans of confined GST nanoantenna with Au electrodes on a PSR microring resonator. Waveguide crossing is incorporated on each side of ring resonator, enabling access to the electrodes. The interspacing between two electrodes (i.e. length of GST nanoantenna) is around 150 nm. (**B**) Transmission spectrum of the electrically-programmable PSR system with the selected odd ($\boldsymbol{\lambda_1}$) and even ($\boldsymbol{\lambda_2}$) wavelengths. (**C**) Time-traced electrical current and optical transmission as the applied voltage varies from 9 to 15 V, depicting the wavelength-selective reduction of optical transmission at $\boldsymbol{\lambda_2}$, while the one at $\boldsymbol{\lambda_1}$ is unchanged.

them. By placing this GST nanoantenna at the spatial location of an even-mode standing-wave, the electro-optic response of the nanoantenna can be wavelength-selectively monitored at the even-mode wavelengths.

Figure 6.28B-C depict the transmission spectrum and time-traced electrical and optical responses as the applied voltage varied from 9 to 15 V. When current flows through the conductive GST, Joule's heating causes the conductive channel to heat up. The induced heat quickly dissipates to the Au electrode, resulting in a localized temperature profile within the microring resonator. Since the standing-waves inside the microring propagate in a spatio-spectrally selective manner, only the even-mode standing-wave experiences thermo-optic shifts caused by the localized heat. Consequently, the peak transmission at λ_2 decreases with a threshold voltage of 9 V, while the one at λ_1 remains constant until ~13 V is applied across the electrodes. These wavelength-selective optical responses triggered by electrical stimuli demonstrate the potential of a hybrid PSR system, enabling the exploration of a wide range of optoelectronic properties by measuring wavelength-selective photocurrent or implementing electro-optically programmable and wavelength-selective building blocks.

6.8 Chapter summary

This chapter introduces a first prototype that combines the exploitation of spatial degrees-of-freedom in integrated photonics with reconfigurability using active materials, enabling wavelength-selective addressability of device states. Through the exploitation of the standing-waves of an in-plane mode in a waveguide, independent modulation of light intensity was achieved at each wavelength channel of a single photonic element. The

integration of standing-waves within a microring resonator enabled strong electric-field confinement, resulting in high-resolution optical responses in both the spatial and spectral domains. The correlation between spatial position and spectral properties of the incoming light gave rise to spatio-spectral coupling, which is effectively combined with the non-volatile tunability of PCMs, leading to the realization of photonic spatio-spectral reconfiguration (PSR). Through this approach, an all-optical, reconfigurable, multi-spectral modulator was achieved at the individual element level. Furthermore, the capacity for multiplexing and modulation density could be further expanded by accommodating a greater number of wavelength channels within a single microring resonator, and as the system was upscaled, the device densities demonstrated exponential growth.

This is a significant advance in reconfigurable photonics that overturns the generalized concept that single-mode light cannot be separated or modulated in a single waveguide. Additionally, it addresses the longstanding challenges encountered by the PICs community in achieving simultaneous excitation and functionality of multiple photonic elements. The concept of PSR overcomes these limitations by combining the spatio-spectral relationship of standing-waves with the reconfigurability of active materials. This approach not only unlocks unexplored device functionalities but also preserves the advantages of integrated photonic circuits, such as compact device integration or system cascadability.

The experimental demonstration, however, revealed some practical limitation such as modulation contrast, the extent of achievable multilevels or the number of modulation channels exceeding two. Nevertheless, these limitations primarily arose from the specific

focus of this work on exploiting wavelength as the only tunable factor, aimed at establishing the first proof-of-concept for the PSR.

The potential of these functionalities can be further expanded by integrating additional capabilities. For instance, it can be augmented by controlling the standing-waves through the optical phase difference between two inputs, enhancing field confinement with ultracompact photonic crystal microcavities, or integrating electrically-programmable abilities. These results lay the foundation for the realization of functional photonic circuits where input wavelengths or optical phases can be manipulated as variables. Furthermore, this work serves as a fundamental building block for the development of coherent nanophotonic circuits, thereby opening up numerous potential applications in areas such as neuromorphic networks,[12] in-memory computing paradigms,[5] optical communications,[201] and high-resolution sensing[202] and imaging[203] applications.

6.9 Acknowledgement and contribution

All design, simulation, fabrication, and measurement of an all-optical PSR system using a microring resonator were performed by the author and Nikolaos Farmakidis. The work of microring PSR presented in this chapter has been submitted to the journal and is currently under review:

- **J. S. Lee**, † N. Farmakidis, † (†, equal contribution) S. Aggarwal, W. Zhou, W. H. P Pernice, H. Bhaskaran "Spatio-spectral control of coherent nanophotonics", *Under review in Nature Communication* (2023)

Also, this work has been presented at international conferences including *Rank Symposium 2023*, *MRS Spring meeting 2023*, and *2nd Workshop on Neuromorphic Photonics and Applications (2023)*.

Chapter 7

Conclusion and outlook

This thesis demonstrates a range of phase-change nanophotonic devices through analytical simulations and experiments, where the active switching behavior between two crystallographic states of phase-change material induces distinct optical and electrical characteristics. While the specific structures and applications investigated in each chapter differ, the underlying objective of the research remains consistent – to unlock the potential of multi-faceted photonic degrees-of-freedom, such as polarization, phase, or wavelength, within ultracompact phase-change nanophotonic devices. Each of the foundational platforms possesses the unique architecture that bridges the device functionality across photonic, temporal, and spatial dimensions. These densely packed photonic capabilities pave the way for a wide range of active nanophotonic/optoelectronic applications ranging from displays, routing, storage, and optical communication to in-memory neuromorphic computing or information processing.

7.1 Polarization: Hybridized-active-dielectric nanowire

The very first prototype of polarization-selective active nanowire (i.e. hybridized-active-dielectric nanowire) was described. The unique design of Si/GST hybrid nanowire enabled selective absorptive switching of the electrically-readable device states based on the polarization direction of incoming optical pulses. By using this approach, polarization-selective, optically-reconfigurable and electrically-accessible memory devices were experimentally demonstrated. Combining the multiple nanowires into a single device, a novel matrix-vector multiplication unit has been demonstrated that exploits polarization as a tunable factor. This approach represents the first-ever demonstration of utilizing polarization for device reconfigurability, which is especially powerful for enhancing computing and storage densities by processing the information in parallel in polarization space.

7.2 Phase: Active low-loss metasurface

In the second part of the thesis, the concept of the above-mentioned phase-change nanoresonators was extended by arranging them in a periodic array to create dynamic metasurfaces. The approach consisted of low-loss phase-change material, mainly Sb_2Se_3, so that the optical phase change delays of each Sb_2Se_3 nanoresonator were modulated by its geometrical parameters (i.e. diameter or thickness of nanopillars) or material properties (i.e. crystalline phases of Sb_2Se_3). Such a low-loss active metasurface was used to tune the propagation of emerging wavefront, thereby enabling varifocal metalens with adjustable focal lengths or intensity with zero material loss. Furthermore, the demonstration of various approaches to dynamically switching the low-loss phase-change

material has been presented. This comprehensive investigation on the reconfigurability of low-loss dielectrics introduces new functionality to the newly emerging field of high-efficiency, active metasurfaces for displays, holograms, beam steering, or image processing.

7.3 Wavelength: Spatio-spectral reconfiguration in integrated photonics

Finally, the phase-change nanoresonators were interfaced with photonic integrated circuits, leading to the transformation of nanophotonic switching into guided-mode propagation. This integration involved the concept of standing-waves to enhance the spatial degrees-of-freedom of in-plane modes, which, in turn, achieved the independent modulation of a multi-wavelength signal within a single photonic carrier for the first time. The demonstration of modulation analysis in the spatio-spectral relation of standing-waves has been analytically and experimentally presented, suggesting the potential to parallelize both programming and probing multiple signals across the wavelength domain. Moreover, this selective optical accessibility offered remarkable confinement in both spatial and spectral scales, as well as non-volatile tunabilities, leading to energy-efficient and highly dense modulation/multiplexing capabilities. The compact integration of these functionalities effectively addresses an unmet need and a critical challenge in the field of coherent silicon photonics.

7.4 Critical review and outlook

The findings described in this study introduce pioneering proof-of-concepts that signify conceptual advances in enhancing the multi-dimensionality of active nanophotonic devices, which, in turn, require extensive exploration of material, structure and platforms. As a result, the foundational prototypes of such active nanophotonic devices possess functionalities that interface with various fields, including new materials, nanophotonics, optoelectronics, and quantum science. These interdisciplinary intersections hold immense potential for driving future development by enhancing device functionalities and, consequently, enabling practical implementation. At the same time, it is important to acknowledge that despite the manifold prospective applications that can be realized these findings, the current state of these technologies remains in its nascent stage, leaving ample room for improvement. Each chapter exploits different photonic or electro-optic platforms that faces with fundamental limitation and practical challenges.

Practical challenges and limitations

For the hybridized-active-dielectric nanowire in *Chapter 4*, its polarization-selective functionality provides an additional degree-of-freedom for device reconfigurability, yet its scalability remains a crucial challenge. This is primarily attributed to the electro-optic configuration which requires individual free-space illumination pathways for each programming unit-cell. Although this issue can be addressed by fast raster scanning[139] or the use of LED arrays[140], the nontrivial energy consumption associated with programming each unit cell needs to be further optimized.

The assembly of these nanowires into an array, explored in *Chapter 5*, enhances the

scalability of nanowire functionality as a low-loss active metasurface. Nevertheless, the early-stage development of low-loss phase-change material, such as Sb_2Se_3, leads to undesirable scattering losses, particularly when the meta-atom becomes crystalline. This loss poses challenges for cascading free-space optics, in applications such as diffractive neural network[164] or cascaded metalens system. Simultaneously, the lossless nature of material creates a dilemma that its low absorption or conductivity makes it challenging to switch between states. Although the incorporation of low-wavelength pump laser or microheater can be a promising solution, achieving robust dynamic switching for an efficient, cascadable system still remains a challenge.

The use of integrated photonic circuit, discussed in *Chapter 6*, can provide strong cascadability for information storage/processing applications due to its compact on-chip components capable of splitting, combining, routing, or focusing guided light. While the concept of photonic spatio-spectral reconfiguration can realize wavelength-selective addressability in highly-confined integrated photonic circuits, scalability issues persist, such as limited operations into two wavelengths within a microring resonator. Various approaches (outlined in *Chapter 6.5*) can address these challenges, but practical issues like low modulation contrast and fabrication tolerance of microring resonators hinder the scaling up of functionality.

It is important to emphasize that exploiting polarization- (*Chapter 4*) or wavelength-selectivity (*Chapter 6*) to parallelize the switching operation necessitates high-power optical pulses. These pulses are obtained using multiple light sources or optical splitter/combiner configuration, thereby reducing overall energy efficiency. This is particularly evident when considering efficient photonic processors that actively utilize

the optical domain for their inferencing tasks,[204] as opposed to programming or training tasks. Due to these challenges and experimental constraints, in each chapter of this thesis, the practical exploration of tunable factors was confined to a maximum of two polarization states (*Chapter 4*), two attainable crystalline states of metasurfaces (*Chapter 5*), and two distinct wavelength channels (*Chapter 6*).

Despite many practical challenges and technical limitation, particular focus should be given to the development of initial prototypes that offer unexplored functionalities by integrating photonic degrees-of-freedom with phase-change reconfigurabilities. These nanophotonic/optoelectronic architectures can serve as an important cornerstone for maximizing device functionalities in various forms of information processing/storage systems.

The prospective pathway towards further advancing these technologies involves capitalizing on the synergetic potential inherent in the diverse fields with which they interface, ultimately enhancing the design, performance, functionality, and scalability of these devices. Some key aspects to consider for the future outlook of these technologies are outlined below.

Electrical/optical mixed-mode devices

One of the main advantages of phase-change alloys is their unique dual functionality in both the electrical and photonic domains, meaning that the material manifests the coupled tunability of both the electrical conductance and optical constant. Consequently, when such devices undergo switching via electrical, optical, or combined stimuli, their states

can be effectively monitored through electrical or optical means. This capability paves the way for the realization of complete mixed-mode operation, as demonstrated in previous research employing plasmonic nanogaps.[15,39] These nanogaps facilitate the programming and probing of phase-change nanoelements through both electrical and optical methods. Using this, a part of mixed-mode operation was presented in *Chapter 4* of this thesis using optically-reconfigurable and electrically-readable hybrid nanowire; however, the full demonstration of electrical programmability remained incomplete. While electrically-programmable micro/nano-heaters were demonstrated in *Chapter 5 and 6*, respectively, the output response of devices was focused in the optical domain. Considering the advantages that electronics can offer in terms of throughput and programmability efficiency, alongside the current state-of-the-art in optical modulation, which inherently relies on electrical components, it becomes apparent that the potential design of active mixed-mode devices exploiting both electrical and optical domains holds significant promise. It is envisioned that all three platforms described herein have the potential to be integrated in such a manner to achieve this goal.

Interfacing with multiple stimuli for correlation/accumulative effect

The switching of phase-change alloys can be achieved through various types of energy stimuli, such as electrical, optical, or thermal forms, provided that the intensity and duration of these energy pulses meet the requirements of melt-quenching processes, thereby ensuring that the transient temperature rise of the material surpasses the threshold. This leads to the intriguing implication of accumulative effects resulting from a single threshold switching phenomenon driven by multiple input energy stimuli. For example, in

Chapter 5.4, both the optical laser power and electrically-programmed heater were required to exceed a certain threshold in order to switch the states of GeTe metasurfaces, while the device remained unaffected when neither stimulus reached the threshold. Accumulative effects have recently been demonstrated in memristor-type devices, such as metal-semiconductor-metal crossbars[28] or stacks of 2D materials,[205] thus introducing novel possibilities for multi-factor neural network processing. This accumulative effect can similarly be applied to the hybridized-active-dielectric (HAD) nanowire discussed in *Chapter 4* or the phase-change nanoantenna explored in *Chapter 6* by subjecting them simultaneously to both electrical and optical pulses.

The key takeaway from these findings is that various input energy pulses are required to be fed into a single phase-change system through multiple channels. This can be realized solely in the optical plane by guiding the parallel streams of light via spatially- or spectrally-separated channels. Integrated photonics has demonstrated this approach, where multiple waveguides or microring resonators provide individual optical energy for a single switching event, enabling all-optical arithmetic operations[92] or correlation detection computations.[206] Such concepts can be effectively adapted to the multi-dimensional photonic devices described in this thesis. For instance, the polarization-selectivity of the HAD nanowire can combine polarization direction, laser power, and electrical biasing across the nanowire as accumulative factors for inducing a single switching event. Additionally, the wavelength-selectivity of the nanowire (Figure 4.7) can introduce wavelength as an additional tunable factor, enhancing the accumulative or correlation effect. A similar approach can be applied to the phase-change nanoantenna within a standing-wave microring resonator, which can be subjected to multiple

wavelengths of light separated by modes, enabling accumulative effects across different spectral (i.e., modal) scales. Moreover, by incorporating optical-phase-dependent selectivity (Figure 6.25), the active nanoantenna can achieve combined reconfigurability in terms of phase and wavelength. As a result, the concept of accommodating multiple energy stimuli within a single active system holds great promise for a wide range of applications in opto-memristors,[207] modulators,[208] and neural computing.[12] This aligns well with the underlying motivation of this thesis, which delves into the exploration of multiple degrees-of-freedom to synergistically enhance the device functionalities.

Exploration of active material

Although the approach described here involves phase-change materials as active elements, the concept of absorptive switching can be readily generalized to other active materials whose switching mechanism is dependent on optical power. For instance, a variety of alternative tuning methods, such as the electro-optic[95] or thermo-optic[97] effects, can still be employed to achieve the desired selective resonant tunability. By replacing the phase-change nanoantenna with materials possessing electro-optic or thermally-sensitive properties—examples being lithium niobate[96] or silicon nitride[209]—the desired selective resonant tunability can be effectively achieved. The implementation of these methods necessitates the modulation of the spatial degrees-of-freedom of optical illumination through the manipulation of resonance control parameters. Furthermore, the integration of 2D materials[210] like MoS_2,[211] graphene[189] or black phosphorus,[212] or epsilon-near-zero materials[136] such as indium tin oxide,[213] with suitable dielectrics, allows for the formation

of hybridized resonances that can be switched through optical excitation while retaining their polarization, phase, or wavelength selectivity.

Larger scale device integration

The implications of large-scale integration of the prototype devices presented herein could be immense for upscaled photonic storage and neuromorphic computing. The preliminary demonstration of upscaled or cascaded microring resonators in *Chapter 6* hints at the exponential growth of information processing capabilities. This scalable approach can be extended to other active nanophotonic devices, employing multiple photonic bandwidths in a similar manner.

The increasing prevalence of chip-scale photonic neural networks has brought the development of photonic tensor cores[5] closer to commercialization, serving as a viable alternative to CMOS technology. The demonstrated concept of photonic spatio-spectral reconfiguration (*Chapter 6*) holds promise for the application of such upscaled photonic tensor cores. This not only allows for parallel inferencing but also facilitates independent training of multiple matrix elements across the wavelength domain. It should be noted that the all-optical simultaneous programming of multiple elements remains a significant challenge in terms of programming efficiency within these systems.

Moreover, the potential for scaling up polarization-selectivity in HAD nanowires (*Chapter 4*) or active metasurfaces (*Chapter 5*) lies in their integration with suitable platforms and applications. For instance, ongoing developments in the field of light-emitting diode (LED) micro-arrays[140] offer the opportunity to combine polarization or phase-selectivity, enhancing device functionality for tasks such as snapshot imaging,

computing, or image recognition in parallel. This integration holds the potential to provide ultrafast bandwidths and significantly expand the capabilities of these systems on a large-scale.

Exploring additional degrees-of-freedom

Yet, despite the exploration of polarization, phase, and wavelength within appropriate platforms in this thesis, there is still ample room to explore additional degrees-of-freedom. One notable example is the work by K. Melde *et al.* in 2016,[214] which demonstrated the generation of holographic images in the acoustic domain, harnessing the unique functionalities offered by ultrasonic manipulation. This illustrates that different degrees-of-freedom can still be harnessed beyond the optical domain. For instance, the responses can be further harnessed by utilizing resonances in radio-frequency (RF) electronics or micro-/nano-electromechanical systems.[215] Additionally, the concept of acoustic holography raises intriguing possibilities, such as using heat as a light source to create temperature-gradient surfaces in the imaging plane, giving rise to the concept of a thermal hologram. By exploiting the dominant blackbody radiation in the mid-infrared (MIR) wavelength range, heat itself can serve as an illumination source, opening up new avenues for achieving novel functionalities in the MIR-heat coupled regime.[216,217]

Numerous well-known degrees-of-freedom still exist within the optical domain as well. For instance, apart from the linear polarizations used in selectively switching HAD nanowires, the exploration of circular or elliptical polarizations can be pursued, particularly in combination with chirality-sensitive active structures.[218] Furthermore, the concept of angular momentum, encompassing spin angular momentum (SAM)[112] and

orbital angular momentum (OAM),[6,113] presents a powerful multiplexing parameter. OAM, in particular, is highly advantageous for multiplexing data in free-space or optical fibers, enabling high-capacity optical communication. Furthermore, in the field of integrated photonics, various forms of wavelength-, mode-, or polarization-division multiplexing are actively employed by utilizing different types of resonators or multimode interferometers.[181,196,219] These additional degrees-of-freedom can be independently or simultaneously harnessed to enhance the controllability of guided modes.

Combining all of these additional reconfigurabilities in extra physical dimensions with the active materials holds great potential for maximizing the device functionalities at the given scale.

Publications

This thesis is represented by the compilation of publications, patents, conference proceedings presentations and awards listed below.

Publications

[1] **J. S. Lee**, N. Farmakidis, C. D. Wright, H. Bhaskaran, "Polarization-selective reconfigurability in hybridized-active-dielectric nanowires", *Science Advances,* **8 (24)**, eabn9459 (2022)

[2] N. Farmakidis, N. Youngblood, **J. S. Lee**, J. Feldmann, A. Lodi, X. Li, S. Aggarwal, W. Zhou, L. Bogani, W. H. P Pernice, C. D. Wright, H. Bhaskaran, "Electronically reconfigurable photonic switches incorporating plasmonic structures and phase change materials", *Advanced Science,* **9**, 220383 (2022)

[3] M. Wang, † **J. S. Lee**, † (†, equal contribution) S. Aggarwal, N. Farmakidis, Y. He, T. Cheng, H. Bhaskaran, "Varifocal metalens using tunable and ultralow-loss dielectrics", *Advanced Science,* **10**, 2204899 (2023)

[4] N. Farmakidis, H. Yu, **J. S. Lee**, J. Feldmann, M. Wang, Y. He, S. Aggarwal, B. Dong, W. H. P Pernice, H. Bhaskaran "Scalable High-Precision Trimming of Photonic Resonances by Polymer Exposure to Energetic Beams", *Nano Letters,* 10.1021/acs.nanolett.3c00220 (2023)

[5] **J. S. Lee**, † N. Farmakidis, † (†, equal contribution) S. Aggarwal, W. Zhou, W. H. P Pernice, H. Bhaskaran "Spatio-spectral control of coherent nanophotonics", *Under review in Nature Communications* (2023)

[6] B. Dong, S. Aggarwal, W. Zhou, U. E. Ali, N. Farmakidis, **J. S. Lee**, Y. He, X. Li, D. L. Kwong, C. D. Wright, W. H. P, H. Bhaskaran "Higher-dimensional processing using a photonic tensor core with continuous-time data", *Accepted in Nature Photonics* (2023)

[7] B. Dong, F. Brückerhoff-Plückelmann, S. Aggarwal, N. Farmakidis, M. Wang, G. Yang, **J. S. Lee**, Y. He, D. L. Kwong, C. D. Wright, W. H. P, H. Bhaskaran "Partial coherence enhanced parallelized photonic computing", *Under review in Nature* (2023)

Patents

[1] Y. Zhang, N. Farmakidis, **J. S. Lee**, H. Bhaskaran, "Optical device for multi-wavelength control", *Filed* (2023)

Conference Presentations and Proceedings

[1] **J. S. Lee**, J. Feldmann, T. Cheng, M. Wang, X. Li, W. Zhou, S. Agarwal, F. Brückerhoff-Plückelmann, C. D. Wright, W. H. P. Pernice, H. Bhaskaran, "Dynamic modulation of low-loss phase change materials on photonic waveguides", *European Phase-Change And Ovonic Symposium (EPCOS) 2021*, 13–15th Sep 2021, Virtual conference (**Poster presentation**)

[2] **J. S. Lee**, N. Farmakidis, C. D. Wright, H. Bhaskaran, "Polarization-selectively tunable hybrid nanowire", *Oxford Photonics Mini-Symposium,* 4th Feb. 2022, Virtual conference (**Oral presentation**)

[3] M. Wang, **J. S. Lee**, S. Aggarwal, N. Farmakidis, J. Tan, H. Bhaskaran, "Reconfigurable Metasurfaces Based on Low-Loss Phase Change Material Sb2Se3", *Conference on Lasers and Electro-Optics (CLEO) 2022,* 15–20th May 2022, Virtual

conference, /doi.org/10.1364/CLEO_QELS.2022.FTh2D.2

[4] **J. S. Lee**, N. Farmakidis, C. D. Wright, H. Bhaskaran, "Polarization-selective electro-optical tunability in phase-change nanowires", *IEEE International Conference on Nanotechnology (IEEE-Nano),* 4–8th Jul. 2022, Palma de Mallorca, Spain (**Oral presentation**)

[5] **J. S. Lee**, N. Farmakidis, C. D. Wright, H. Bhaskaran, "Polarization-selective tunability in phase-change nanowires", *European Phase-Change And Ovonic Symposium (EPCOS) 2022,* 18–21st Sep. 2022, Oxford, UK (**Oral presentation**)

[6] **J. S. Lee**, N. Farmakidis, C. D. Wright, H. Bhaskaran, "Hybridized-Active-Dielectric (HAD) nanowires for polarization-selective memory", *Oxford Photonics Day 2022,* 28th Sep. 2022, Oxford, UK (**Oral presentation**)

[7] **J. S. Lee**, N. Farmakidis, H. Bhaskaran, "Integrated photonic components for computing and beyond", *SPIE Nanoscience + Engineering,* 3rd Oct. 2022, San Diego, California, SA /doi.org/10.1117/12.2633563

[8] S. Aggarwal, B. Dong, **J. S. Lee**, M. Wang, A. Katumba, P. Bienstmana, H. Bhaskaran, "Design for Robust and Efficient Neuromorphic Photonic Accelerator", *2022 IEEE International Conference on Emerging Electronics (ICEE)*, 11–14 Dec 2022, Bangalore, India /10.1109/ICEE56203.2022.10117902

[9] **J. S. Lee**, N. Farmakidis, C. D. Wright, H. Bhaskaran, "Polarization-Selective Non-Volatile Switching in Hybrid Phase-Change Nanowires", *2022 MRS Fall Meeting & Exhibit,* 27th Nov.–2nd Dec. 2022, Boston, Massachusetts, USA (**Oral presentation**)

[10] **J. S. Lee**, N. Farmakidis, C. D. Wright, H. Bhaskaran, "Exploiting degrees of freedom in active nanophotonic devices", *Rank Symposium Neuromorphic Photonics*, 6–

9th Feb. 2023, Grasmere, Cumbria, UK (**Oral presentation**)

- Awarded as '*Best Student Presentation*'.

[11] M. Wang, **J. S. Lee**, S. Aggarwal, N. Farmakidis, Y. He, T. Cheng, H. Bhaskaran, "Tunable metasurfaces using ultralow-loss phase-change materials"*, SPIE OPTO,* 17th Mar. 2023, San Francisco, California, USA /doi.org/10.1117/12.2650320

[12] **J. S. Lee**, N. Farmakidis, S. Aggarwal, W. Zhou, W. H. P. Pernice, H. Bhaskaran, "On-chip wavelength-selective and non-volatile reconfigurability in a single photonic element", *2023 MRS Spring Meeting & Exhibit,* 10–14th Apr. 2023, San Francisco, California, USA (**Oral presentation**)

[13] M. Wang, S. Aggarwal, **J. S. Lee**, B. Dong, N. Farmakidis, G. Yang, H. Bhaskaran, "Wide-angle optical beam steering using phase-change materials for tunable gratings", *Conference on Lasers and Electro-Optics (CLEO) 2023,* 7–12th May. 2023, San Jose, California, USA /doi.org/10.1364/CLEO_SI.2023.STu3O.3

[14] Y. He, N. Farmakidis, S. Aggarwal, **J. S. Lee**, M. Wang, W. Zhou, H. Bhaskaran, "Ultra-Efficient Plasmonic Phase-Change Devices on SOI Platform", *Conference on Lasers and Electro-Optics (CLEO) 2023,* 7–12th May. 2023, San Jose, California, USA /doi.org/10.1364/CLEO_SI.2023.STh1O.7

[15] **J. S. Lee**, N. Farmakidis, H. Bhaskaran, "'Integrated photonic processor for neuromorphic computing and beyond", *2nd Workshop on Neuromorphic Photonics and Applications*, 13-14th Jul. 2023, Athens, Greece (**Oral presentation**)

[16] G. Yang, M. Wang, **J. S. Lee**, N. Farmakidis, H. Bhaskaran, "Reconfigurable nonlocal metasurface based on phase change materials", *SPIE Optics + Photonics,* 22nd Aug. 2023, San Diego, California, USA.

Awards

[1] **Best Student Presentation** – *Rank Symposium in Neuromorphic Photonics*, Feb. 2023

[2] Nominated in **'Photonics100'** from *Electro Optics – highlighting "100 individuals in academia and industry who have made remarkable strides driving photonics technology forward.",* Nov. 2022

[3] Nominees for **Best PGR Materials Research Student Talk (Hetherington Prize)** at *Department of Materials, University of Oxford,* Dec. 2021

Bibliography

1 Moore, G. E. Cramming more components onto integrated circuits, Reprinted from Electronics, volume 38, number 8, April 19, 1965, pp.114 ff. *IEEE Solid-State Circuits Society Newsletter* **11**, 33-35 (2006).

2 Waldrop, M. M. J. N. N. The chips are down for Moore's law. *Nature* **530**, 144 (2016).

3 Thompson, S. E. & Parthasarathy, S. Moore's law: the future of Si microelectronics. *Materials Today* **9**, 20-25 (2006).

4 Li, J., Hung, Y.-C., Kulce, O., Mengu, D. & Ozcan, A. Polarization multiplexed diffractive computing: all-optical implementation of a group of linear transformations through a polarization-encoded diffractive network. *Light: Science & Applications* **11**, 153 (2022).

5 Feldmann, J. *et al.* Parallel convolutional processing using an integrated photonic tensor core. *Nature* **589**, 52-58 (2021).

6 Miao, P. *et al.* Orbital angular momentum microlaser. *Science* **353**, 464-467 (2016).

7 Kirchain, R. & Kimerling, L. A roadmap for nanophotonics. *Nature Photonics* **1**, 303-305 (2007).

8 Ovshinsky, S. R. Reversible Electrical Switching Phenomena in Disordered Structures. *Physical Review Letters* **21**, 1450-1453 (1968).

9 Wuttig, M. & Yamada, N. Phase-change materials for rewriteable data storage. *Nature Materials* **6**, 824-832 (2007).

10 Ríos, C. *et al.* Integrated all-photonic non-volatile multi-level memory. *Nature Photonics* **9**, 725-732 (2015).

11 Raeis-Hosseini, N. & Rho, J. Metasurfaces Based on Phase-Change Material as a Reconfigurable Platform for Multifunctional Devices. *Materials* **10** (2017).

12 Shastri, B. J. *et al.* Photonics for artificial intelligence and neuromorphic computing. *Nature Photonics* **15**, 102-114 (2021).

13 Hosseini, P., Wright, C. D. & Bhaskaran, H. An optoelectronic framework enabled by low-dimensional phase-change films. *Nature* **511**, 206-211 (2014).

14 Wang, Q. *et al.* Optically reconfigurable metasurfaces and photonic devices based on phase change materials. *Nature Photonics* **10**, 60-65 (2016).

15 Farmakidis, N. *et al.* Plasmonic nanogap enhanced phase-change devices with dual electrical-optical functionality. *Science Advances* **5**, eaaw2687 (2019).

16 Abdollahramezani, S. *et al.* Tunable nanophotonics enabled by chalcogenide phase-change materials. *Nanophotonics* **9**, 1189-1241 (2020).

17 Zhang, M. *et al.* Plasmonic Metasurfaces for Switchable Photonic Spin–Orbit Interactions Based on Phase Change Materials. *Advanced Science* **5**, 1800835 (2018).

18 Waterman, A. T. The Electrical Conductivity of Molybdenite. *Physical Review* **21**, 540-549 (1923).

19 Gravesteijn, D. J. Materials developments for write-once and erasable phase-change optical recording. *Appl Opt.* (1988).

20 Yamada, N. *et al.* Phase-Change Optical Disk Having a Nitride Interface Layer. *Japanese Journal of Applied Physics* **37**, 2104 (1998).

21 Hudgens, S. J. & Johnson, B. Overview of Phase-Change Chalcogenide Nonvolatile Memory Technology. *MRS Bulletin* **29**, 829-832 (2004).

22 Pernice, W. H. & Bhaskaran, H. Photonic non-volatile memories using phase change materials. *J. Applied Physics Letters* **101**, 171101 (2012).

23 Carrillo, S. G.-C. *et al.* A Nonvolatile Phase-Change Metamaterial Color Display. *Advanced Optical Materials* **7**, 1801782 (2019).

24 Choi, C. *et al.* Metasurface with Nanostructured Ge2Sb2Te5 as a Platform for Broadband-Operating Wavefront Switch. *Advanced Optical Materials* **7**, 1900171 (2019).

25 He, J. *et al.* Design of a Multi-Functional Integrated Optical Switch Based on Phase Change Materials. *Photonics* **9** (2022).

26 Li, X., Luo, M., Jiang, X., Luo, S. & Yang, J. Tunable Color-Variable Solar Absorber Based on Phase Change Material Sb(2)Se(3). *Nanomaterials* **12** (2022).

27 Li, X. *et al.* Fast and reliable storage using a 5 bit, nonvolatile photonic memory cell. *Optica* **6**, 1-6 (2019).

28 Sarwat, S. G., Moraitis, T., Wright, C. D. & Bhaskaran, H. Chalcogenide optomemristors for multi-factor neuromorphic computation. *Nature Communications* **13**, 2247 (2022).

29 Wuttig, M., Bhaskaran, H. & Taubner, T. Phase-change materials for non-volatile photonic applications. *Nature Photonics* **11**, 465-476 (2017).

30 Lee, B.-S. *et al.* Nanoscale nuclei in phase change materials: Origin of different crystallization mechanisms of Ge2Sb2Te5 and AgInSbTe. *Journal of Applied Physics* **115**, 063506 (2014).

31 Ríos, C., Hosseini, P., Taylor, R. A. & Bhaskaran, H. Color Depth Modulation and Resolution in Phase-Change Material Nanodisplays. *Advanced Materials* **28**, 4720-4726 (2016).

32 Wuttig, M., Deringer, V. L., Gonze, X., Bichara, C. & Raty, J.-Y. Incipient Metals: Functional Materials with a Unique Bonding Mechanism. *Advanced Materials* **30**, 1803777 (2018).

33 Zhu, M. *et al.* Unique Bond Breaking in Crystalline Phase Change Materials and the Quest for Metavalent Bonding. *Advanced Materials* **30**, 1706735 (2018).

34 Robertson, J. & Huang, B. Bonding and optical contrast in phase change memory materials. *physica status solidi (b)* **249**, 1867-1873 (2012).

35 Shportko, K. *et al.* Resonant bonding in crystalline phase-change materials. *Nature Materials* **7**, 653-658 (2008).

36 Kolobov, A. V., Fons, P. & Tominaga, J. Local structure of amorphous Ge-Sb-Te alloys: Ge umbrella flip vs. DFT simulations. *physica status solidi (b)* **246**, 1826-1830 (2009).

37 Kolobov, A. V. *et al.* Understanding the phase-change mechanism of rewritable optical media. *Nature Materials* **3**, 703-708 (2004).

38 Taghinejad, H. *et al.* ITO-based microheaters for reversible multi-stage switching of phase-change materials: towards miniaturized beyond-binary reconfigurable integrated photonics. *J Optics Express* **29**, 20449-20462 (2021).

39 Farmakidis, N. *et al.* Electronically Reconfigurable Photonic Switches Incorporating Plasmonic Structures and Phase Change Materials. *Advanced Science* **9**, 2200383 (2022).

40 Zhang, Y. *et al.* Electrically reconfigurable non-volatile metasurface using low-loss optical phase-change material. *Nature Nanotechnology* **16**, 661-666 (2021).

41 Abdollahramezani, S. *et al.* Electrically driven reprogrammable phase-change metasurface reaching 80% efficiency. *Nature Communications* **13**, 1696 (2022).

42 Ghazi Sarwat, S. *et al.* Projected Mushroom Type Phase-Change Memory. *Advanced Functional Materials* **31**, 2106547 (2021).

43 Raoux, S., Xiong, F., Wuttig, M. & Pop, E. Phase change materials and phase change memory. *MRS Bulletin* **39**, 703-710 (2014).

44 Graham, B. in *Electromagnetic Fields and Waves* (eds Yeap Kim Ho & Hirasawa Kazuhiro) Ch. 4 (IntechOpen, 2019).

45 Gemo, E. *et al.* Plasmonically-enhanced all-optical integrated phase-change memory. *Opt Express* **27**, 24724-24737 (2019).

46 Tian, J. *et al.* Active control of anapole states by structuring the phase-change alloy Ge2Sb2Te5. *Nature Communications* **10**, 396 (2019).

47 Tittl, A. *et al.* A Switchable Mid-Infrared Plasmonic Perfect Absorber with Multispectral Thermal Imaging Capability. *Advanced Materials* **27**, 4597-4603 (2015).

48 Shalaginov, M. Y. *et al.* Reconfigurable all-dielectric metalens with diffraction-limited performance. *Nature Communications* **12**, 1225 (2021).

49 Wang, Y. *et al.* Electrical tuning of phase-change antennas and metasurfaces. *Nature Nanotechnology* **16**, 667-672 (2021).

50 Lee, S.-Y. *et al.* Holographic image generation with a thin-film resonance caused by chalcogenide phase-change material. *Scientific Reports* **7**, 41152 (2017).

51 Liu, Y., Aziz, M. M., Shalini, A., Wright, C. D. & Hicken, R. J. Crystallization of Ge2Sb2Te5 films by amplified femtosecond optical pulses. *Journal of Applied Physics* **112**, 123526 (2012).

52 Hase, M., Fons, P., Mitrofanov, K., Kolobov, A. V. & Tominaga, J. Femtosecond structural transformation of phase-change materials far from equilibrium monitored by coherent phonons. *Nature Communications* **6**, 8367 (2015).

53 Fons, P. *et al.* Photoassisted amorphization of the phase-change memory alloy Ge2Sb2Te5. *Physical Review B* **82**, 041203 (2010).

54 Sundaram, S. K. & Mazur, E. Inducing and probing non-thermal transitions in semiconductors using femtosecond laser pulses. *Nature Materials* **1**, 217-224 (2002).

55 Ríos, C. *et al.* In-memory computing on a photonic platform. *Science Advances* **5**, eaau5759 (2019).

56 Fang, Z. *et al.* Non-Volatile Reconfigurable Integrated Photonics Enabled by Broadband Low-Loss Phase Change Material. *Advanced Optical Materials* **9**, 2002049 (2021).

57 Delaney, M., Zeimpekis, I., Lawson, D., Hewak, D. W. & Muskens, O. L. A New Family of Ultralow Loss Reversible Phase-Change Materials for Photonic Integrated Circuits: Sb2S3 and Sb2Se3. *Advanced Functional Materials* **30**, 2002447 (2020).

58 Delaney, M. *et al.* Nonvolatile programmable silicon photonics using an ultralow-loss Sb2Se3 phase change material. *Science Advances* **7**, eabg3500 (2021).

59 Gosciniak, J. Ultra-compact nonvolatile plasmonic phase change modulators and switches with dual electrical–optical functionality. *AIP Advances* **12**, 035321 (2022).

60 Hemmatyar, O. *et al.* Enhanced meta-displays using advanced phase-change materials. *arXiv preprint arXiv:.12159* (2021).

61 Zhang, Y. *et al.* Broadband transparent optical phase change materials for high-performance nonvolatile photonics. *Nature Communications* **10**, 4279 (2019).

62 Ríos, C. *et al.* Ultra-compact nonvolatile phase shifter based on electrically reprogrammable transparent phase change materials. *PhotoniX* **3**, 26 (2022).

63 Carletti, L. *et al.* Reconfigurable nonlinear response of dielectric and semiconductor metasurfaces. *Nanophotonics* **10**, 4209-4221 (2021).

64 Williams, C., Hong, N., Julian, M., Borg, S. & Kim, H. J. Tunable mid-wave infrared Fabry-Perot bandpass filters using phase-change GeSbTe. *Optics Express* **28**, 10583-10594 (2020).

65 Chaudhary, K. *et al.* Polariton nanophotonics using phase-change materials. *Nature Communications* **10**, 4487 (2019).

66 Heßler, A. *et al.* In3SbTe2 as a programmable nanophotonics material platform for the infrared. *Nature Communications* **12**, 924 (2021).

67 Ruiz de Galarreta, C. *et al.* Reconfigurable multilevel control of hybrid all-dielectric phase-change metasurfaces. *Optica* **7**, 476-484 (2020).

68 Forouzmand, A. & Mosallaei, H. Dynamic beam control via Mie-resonance based phase-change metasurface: a theoretical investigation. *Optics Express* **26**, 17948-17963 (2018).

69 Savinov, V., Papasimakis, N., Tsai, D. P. & Zheludev, N. I. Optical anapoles. *Communications Physics* **2**, 69 (2019).

70 Craig F. Bohren, D. R. H. in *Absorption and Scattering of Light by Small Particles* 57-81 (1998).

71 Mie, G. Beiträge zur Optik trüber Medien, speziell kolloidaler Metallösungen. *Annalen der Physik* **330**, 377-445 (1908).

72 Turkevich, J., Garton, G. & Stevenson, P. C. The color of colloidal gold. *Journal of Colloid Science* **9**, 26-35 (1954).

73 Kuznetsov, A. I., Miroshnichenko, A. E., Brongersma, M. L., Kivshar, Y. S. & Luk'yanchuk, B. Optically resonant dielectric nanostructures. *Science* **354**, aag2472 (2016).

74 van de Haar, M. A., van de Groep, J., Brenny, B. J. M. & Polman, A. Controlling magnetic and electric dipole modes in hollow silicon nanocylinders. *Optics Express* **24**, 2047-2064 (2016).

75 Baek, K., Kim, Y., Mohd-Noor, S. & Hyun, J. K. Mie Resonant Structural Colors. *ACS Applied Materials & Interfaces* **12**, 5300-5318 (2020).

76 Cao, L., Fan, P., Barnard, E. S., Brown, A. M. & Brongersma, M. L. Tuning the Color of Silicon Nanostructures. *Nano Letters* **10**, 2649-2654 (2010).

77 Tripathi, A. *et al.* Tunable Mie-Resonant Dielectric Metasurfaces Based on VO2 Phase-Transition Materials. *ACS Photonics* **8**, 1206-1213 (2021).

78 Lu, L. *et al.* Reversible Tuning of Mie Resonances in the Visible Spectrum. *ACS Nano* **15**, 19722-19732 (2021).

79 Santos, G., Losurdo, M., Moreno, F. & Gutiérrez, Y. Directional Scattering Switching from an All-Dielectric Phase Change Metasurface. *Nanomaterials* **13** (2023).

80 Bai, Y., Zheng, H., Liu, J., Zhang, Q. & Liu, S. Active tuning of directional forward and backward scattering with metallic core/phase change shell nanoparticles. *Optics Communications* **533**, 129302 (2023).

81 Leitis, A. *et al.* All-Dielectric Programmable Huygens' Metasurfaces. *Advanced Functional Materials* **30**, 1910259 (2020).

82 Kerker, M., Wang, D.-S. & Giles, C. L. Electromagnetic scattering by magnetic spheres. *Journal of the Optical Society of America* **73**, 765-767 (1983).

83 Qu, Y. *et al.* Dynamic Thermal Emission Control Based on Ultrathin Plasmonic Metamaterials Including Phase-Changing Material GST. *Laser & Photonics Reviews* **11**, 1700091 (2017).

84 Carrillo, S. G.-C., Alexeev, A. M., Au, Y.-Y. & Wright, C. D. Reconfigurable phase-change meta-absorbers with on-demand quality factor control. *Optics Express* **26**, 25567-25581 (2018).

85 Cao, T., Wei, C.-w., Simpson, R. E., Zhang, L. & Cryan, M. J. Broadband Polarization-Independent Perfect Absorber Using a Phase-Change Metamaterial at Visible Frequencies. *Scientific Reports* **4**, 3955 (2014).

86 Decker, M. *et al.* High-Efficiency Dielectric Huygens' Surfaces. *Advanced Optical Materials* **3**, 813-820 (2015).

87 Pfeiffer, C. & Grbic, A. Metamaterial Huygens' Surfaces: Tailoring Wave Fronts with Reflectionless Sheets. *Physical Review Letters* **110**, 197401 (2013).

88 Fu, Y. H., Kuznetsov, A. I., Miroshnichenko, A. E., Yu, Y. F. & Luk'yanchuk, B. Directional visible light scattering by silicon nanoparticles. *Nature Communications* **4**, 1527 (2013).

89 Chen, K. *et al.* A Reconfigurable Active Huygens' Metalens. *Advanced Materials* **29**, 1606422 (2017).

90 Nisar, M. S., Yang, X., Lu, L., Chen, J. & Zhou, L. On-Chip Integrated Photonic Devices Based on Phase Change Materials. *Photonics* **8** (2021).

91 Faneca, J., Bucio, T. D., Gardes, F. Y. & Baldycheva, A. O-band N-rich silicon nitride MZI based on GST. *Applied Physics Letters* **116**, 093502 (2020).

92 Feldmann, J. *et al.* Calculating with light using a chip-scale all-optical abacus. *Nature Communications* **8**, 1256 (2017).

93 Feldmann, J., Youngblood, N., Wright, C. D., Bhaskaran, H. & Pernice, W. H. P. All-optical spiking neurosynaptic networks with self-learning capabilities. *Nature* **569**, 208-214 (2019).

94 Zheng, J. *et al.* GST-on-silicon hybrid nanophotonic integrated circuits: a non-volatile quasi-continuously reprogrammable platform. *Optical Materials Express* **8**, 1551-1561 (2018).

95 Powell, K. *et al.* Integrated silicon carbide electro-optic modulator. *Nature Communications* **13**, 1851 (2022).

96 Li, M. *et al.* Lithium niobate photonic-crystal electro-optic modulator. *Nature Communications* **11**, 4123 (2020).

97 Harris, N. C. *et al.* Efficient, compact and low loss thermo-optic phase shifter in silicon. *Optics Express* **22**, 10487-10493 (2014).

98 Sun, X. Y. *et al.* Single-Step Deposition of Cerium-Substituted Yttrium Iron Garnet for Monolithic On-Chip Optical Isolation. *ACS Photonics* **2**, 856-863 (2015).

99 Midolo, L., Schliesser, A. & Fiore, A. Nano-opto-electro-mechanical systems. *Nature Nanotechnology* **13**, 11-18 (2018).

100 Rios, C. *et al.* Controlled switching of phase-change materials by evanescent-field coupling in integrated photonics [Invited]. *Optical Materials Express* **8**, 2455-2470 (2018).

101 Sebastian, A., Le Gallo, M., Khaddam-Aljameh, R. & Eleftheriou, E. Memory devices and applications for in-memory computing. *Nature Nanotechnology* **15**, 529-544 (2020).

102 Le Gallo, M. *et al.* Mixed-precision in-memory computing. *Nature Electronics* **1**, 246-253 (2018).

103 Cheng, Z. *et al.* Device-Level Photonic Memories and Logic Applications Using Phase-Change Materials. *Advanced Materials* **30**, 1802435 (2018).

104 Zhou, W. *et al.* In-memory photonic dot-product engine with electrically programmable weight banks. *Nature Communications* **14**, 2887 (2023).

105 Xia, Q. & Yang, J. J. Memristive crossbar arrays for brain-inspired computing. *Nature Materials* **18**, 309-323 (2019).

106 Cheng, Z., Ríos, C., Pernice, W. H. P., Wright, C. D. & Bhaskaran, H. On-chip photonic synapse. *Science Advances* **3**, e1700160 (2017).

107 Tan, J. Y. S. *et al.* Monadic Pavlovian associative learning in a backpropagation-free photonic network. *Optica* **9**, 792-802 (2022).

108 Li, X. *et al.* in *2020 IEEE International Electron Devices Meeting (IEDM).* 7.5.1-7.5.4.

109 Choi, C. *et al.* Hybrid State Engineering of Phase-Change Metasurface for All-Optical Cryptography. *Advanced Functional Materials* **31**, 2007210 (2021).

110 Evennett, P. Kohler illumination: a simple interpretation. *Proc Royal Microsc Soc* **28**, 189-192 (1983).

111 Ascoli, G. A., Bezhanskaya, J. & Tsytsarev, V. in *Encyclopedia of the Neurological Sciences (Second Edition)* (eds Michael J. Aminoff & Robert B. Daroff) 16-20 (Academic Press, 2014).

112 O'Connor, D., Ginzburg, P., Rodríguez-Fortuño, F. J., Wurtz, G. A. & Zayats, A. V. Spin–orbit coupling in surface plasmon scattering by nanostructures. *Nature Communications* **5**, 5327 (2014).

113 Ji, Z. *et al.* Photocurrent detection of the orbital angular momentum of light. *Science* **368**, 763-767 (2020).

114 Palik, E. D. *Handbook of optical constants of solids*. Vol. 3 (Academic press, 1998).

115 Lee, J. S. *et al.* Ultrahigh resolution and color gamut with scattering-reducing transmissive pixels. *Nature Communications* **10**, 4782 (2019).

116 Hyun, J. K. *et al.* Enhanced Second Harmonic Generation by Coupling to Exciton Ensembles in Ag-coated ZnO Nanorods. *ACS Photonics* **2**, 1314-1319 (2015).

117 Haus, H. A. & Melcher, J. R. *Electromagnetic fields and energy*. (Prentice Hall Englewood Cliffs, New Jersey, 1989).

118 Incropera, F. P., DeWitt, D. P., Bergman, T. L. & Lavine, A. S. *Fundamentals of heat and mass transfer*. Vol. 6 (Wiley New York, 1996).

119 Battaglia, J. L. *et al.* Thermal characterization of the SiO2-Ge2Sb2Te5 interface from room temperature up to 400°C. *Journal of Applied Physics* **107**, 044314 (2010).

120 Khulbe, P. K., Wright, E. M. & Mansuripur, M. Crystallization behavior of as-deposited, melt quenched, and primed amorphous states of Ge2Sb2.3Te5 films. *Journal of Applied Physics* **88**, 3926-3933 (2000).

121 Duong, T.-Q. *et al.* First-principles thermal transport in amorphous $Ge_2Sb_2Te_5$ at the nanoscale. *RSC Adv.* (2021).

122 Ghazi Sarwat, S. *et al.* Strong Opto-Structural Coupling in Low Dimensional GeSe3 Films. *Nano Letters* **19**, 7377-7384 (2019).

123 Kim, J. *et al.* Photon-triggered nanowire transistors. *Nature Nanotechnology* **12**, 963-968 (2017).

124 Deng, L. *et al.* Malus-metasurface-assisted polarization multiplexing. *Light: Science & Applications* **9**, 101 (2020).

125 Wang, Z., Ding, X., Liu, S., Zhang, K. & Wu, Q. Polarization-multiplexed Huygens metasurface holography. *Optics Letters* **45**, 5488-5491 (2020).

126 Wang, Q. *et al.* Polarization and Frequency Multiplexed Terahertz Meta-Holography. *Advanced Optical Materials* **5**, 1700277 (2017).

127 Jouppi, N. P. *et al.* in *Proceedings of the 44th annual international symposium on computer architecture.* 1-12.

128 Hail, C. U., Michel, A.-K. U., Poulikakos, D. & Eghlidi, H. Optical Metasurfaces: Evolving from Passive to Adaptive. *Advanced Optical Materials* **7**, 1801786 (2019).

129 Peng, K. *et al.* Single Nanowire Photoconductive Terahertz Detectors. *Nano Letters* **15**, 206-210 (2015).

130 Roddaro, S. *et al.* Giant Thermovoltage in Single InAs Nanowire Field-Effect Transistors. *Nano Letters* **13**, 3638-3642 (2013).

131 Graham, R., Miller, C., Oh, E. & Yu, D. Electric Field Dependent Photocurrent Decay Length in Single Lead Sulfide Nanowire Field Effect Transistors. *Nano Letters* **11**, 717-722 (2011).

132 Wang, D. *et al.* Bidirectional photocurrent in p–n heterojunction nanowires. *Nature Electronics* **4**, 645-652 (2021).

133 Liu, C. *et al.* Silicon/2D-material photodetectors: from near-infrared to mid-infrared. *Light: Science & Applications* **10**, 123 (2021).

134 Shi, Z. *et al.* Two-dimensional materials toward Terahertz optoelectronic device applications. *Journal of Photochemistry and Photobiology C: Photochemistry Reviews* **51**, 100473 (2022).

135 Franklin, D., Frank, R., Wu, S.-T. & Chanda, D. Actively addressed single pixel full-colour plasmonic display. *Nature Communications* **8**, 15209 (2017).

136 Alù, A., Silveirinha, M. G., Salandrino, A. & Engheta, N. Epsilon-near-zero metamaterials and electromagnetic sources: Tailoring the radiation phase pattern. *Physical Review B* **75**, 155410 (2007).

137 Gopalan, P. & Sensale-Rodriguez, B. 2D Materials for Terahertz Modulation. *Advanced Optical Materials* **8**, 1900550 (2020).

138 Long, X., Tan, H., Sánchez, F., Fina, I. & Fontcuberta, J. Non-volatile optical switch of resistance in photoferroelectric tunnel junctions. *Nature Communications* **12**, 382 (2021).

139 Yoo, H. W., Ito, S. & Schitter, G. High speed laser scanning microscopy by iterative learning control of a galvanometer scanner. *Control Engineering Practice* **50**, 12-21 (2016).

140 Bezshlyakh, D. D. *et al.* Directly addressable GaN-based nano-LED arrays: fabrication and electro-optical characterization. *Microsystems & Nanoengineering* **6**, 88 (2020).

141 Jiang, R., Xu, Y., Dong, Y., Zhang, B. & Ni, Y. Integrated TM-through/TE-converted polarization beam splitter based on z-cut lithium niobate-on-insulator platform. *Optik* **255**, 168690 (2022).

142 Chen, W. T., Zhu, A. Y. & Capasso, F. Flat optics with dispersion-engineered metasurfaces. *Nature Reviews Materials* **5**, 604-620 (2020).

143 Khorasaninejad, M. *et al.* Metalenses at visible wavelengths: Diffraction-limited focusing and subwavelength resolution imaging. *Science* **352**, 1190-1194 (2016).

144 Jiang, X. *et al.* All-dielectric metalens for terahertz wave imaging. *Optics Express* **26**, 14132-14142 (2018).

145 Ou, K. *et al.* Broadband Achromatic Metalens in Mid-Wavelength Infrared. *Laser & Photonics Reviews* **15**, 2100020 (2021).

146 Chen, Y. G. *et al.* Hybrid phase-change plasmonic crystals for active tuning of lattice resonances. *Optics Express* **21**, 13691-13698 (2013).

147 Chu, C. H. *et al.* Active dielectric metasurface based on phase-change medium. *Laser & Photonics Reviews* **10**, 986-994 (2016).

148 Gigli, C. *et al.* Fundamental Limitations of Huygens' Metasurfaces for Optical Beam Shaping. *Laser & Photonics Reviews* **15**, 2000448 (2021).

149 Luk'yanchuk, B. S., Voshchinnikov, N. V., Paniagua-Domínguez, R. & Kuznetsov, A. I. Optimum Forward Light Scattering by Spherical and Spheroidal Dielectric Nanoparticles with High Refractive Index. *ACS Photonics* **2**, 993-999 (2015).

150 Arbabi, E. *et al.* MEMS-tunable dielectric metasurface lens. *Nature Communications* **9**, 812 (2018).

151 Afridi, A. *et al.* Electrically Driven Varifocal Silicon Metalens. *ACS Photonics* **5**, 4497-4503 (2018).

152 Ee, H.-S. & Agarwal, R. Tunable Metasurface and Flat Optical Zoom Lens on a Stretchable Substrate. *Nano Letters* **16**, 2818-2823 (2016).

153 Dolan, J. A. *et al.* Broadband Liquid Crystal Tunable Metasurfaces in the Visible: Liquid Crystal Inhomogeneities Across the Metasurface Parameter Space. *ACS Photonics* **8**, 567-575 (2021).

154 Badloe, T., Kim, I., Kim, Y., Kim, J. & Rho, J. Electrically Tunable Bifocal Metalens with Diffraction-Limited Focusing and Imaging at Visible Wavelengths. *Advanced Science* **8**, 2102646 (2021).

155 Khorasaninejad, M. & Capasso, F. Metalenses: Versatile multifunctional photonic components. *Science* **358**, eaam8100 (2017).

156 Chang, C. *et al.* Speckle-suppressed phase-only holographic three-dimensional display based on double-constraint Gerchberg-Saxton algorithm. *Applied Optics* **54**, 6994-7001 (2015).

157 Choi, Y.-S. *et al.* Optical Metasurface-Based Holographic Stereogram. *Advanced Optical Materials* **8**, 1901970 (2020).

158 Sun, H., Qiao, Q., Guan, Q. & Zhou, G. Silicon Photonic Phase Shifters and Their Applications: A Review. *Micromachines* **13** (2022).

159 Raoux, S., Cheng, H. Y., Caldwell, M. A. & Wong, H. S. P. Crystallization times of Ge–Te phase change materials as a function of composition. *Applied Physics Letters* **95**, 071910 (2009).

160 Youngblood, N. *et al.* Reconfigurable Low-Emissivity Optical Coating Using Ultrathin Phase Change Materials. *ACS Photonics* **9**, 90-100 (2022).

161 Loke, D. K. *et al.* Ultrafast Nanoscale Phase-Change Memory Enabled By Single-Pulse Conditioning. *ACS Applied Materials & Interfaces* **10**, 41855-41860 (2018).

162 Berini, P. Optical Beam Steering Using Tunable Metasurfaces. *ACS Photonics* **9**, 2204-2218 (2022).

163 Juliano Martins, R. *et al.* Metasurface-enhanced light detection and ranging technology. *Nature Communications* **13**, 5724 (2022).

164 Lin, X. *et al.* All-optical machine learning using diffractive deep neural networks. *Science* **361**, 1004-1008 (2018).

165 Zhao, P., Lim, Y. D., Li, H. Y., Luca, G. & Tan, C. S. Advanced 3D Integration Technologies in Various Quantum Computing Devices. *IEEE Open Journal of Nanotechnology* **2**, 101-110 (2021).

166 Grabulosa, A., Moughames, J., Porte, X., Kadic, M. & Brunner, D. Additive 3D photonic integration that is CMOS compatible. *Nanotechnology* **34**, 322002 (2023).

167 Bogaerts, W. *et al.* Silicon microring resonators. *Laser & Photonics Reviews* **6**, 47-73 (2012).

168 Okamoto, K. in *Fundamentals of Optical Waveguides (Second Edition)* (ed Katsunari Okamoto) 13-55 (Academic Press, 2006).

169 Reed, G. T. Silicon photonics: the state of the art. *Wiley-Interscience* (2008).

170 in *Integrated Ring Resonators: The Compendium* (ed Dominik G. Rabus) 3-40 (Springer Berlin Heidelberg, 2007).

171 Ahmed, R. *et al.* Optical microring resonator based corrosion sensing. *RSC Advances* **6**, 56127-56133 (2016).

172 Baranov, D. G., Krasnok, A., Shegai, T., Alù, A. & Chong, Y. Coherent perfect absorbers: linear control of light with light. *Nature Reviews Materials* **2**, 17064 (2017).

173 Wan, W. *et al.* Time-Reversed Lasing and Interferometric Control of Absorption. *Science* **331**, 889-892 (2011).

174 Chong, Y. D., Ge, L., Cao, H. & Stone, A. D. Coherent Perfect Absorbers: Time-Reversed Lasers. *Physical Review Letters* **105**, 053901 (2010).

175 Vetlugin, A. N. Coherent perfect absorption of quantum light. *Physical Review A* **104**, 013716 (2021).

176 Müllers, A. *et al.* Coherent perfect absorption of nonlinear matter waves. *Science Advances* **4**, eaat6539 (2018).

177 Bruck, R. & Muskens, O. L. Plasmonic nanoantennas as integrated coherent perfect absorbers on SOI waveguides for modulators and all-optical switches. *Optics Express* **21**, 27652-27661 (2013).

178 Chen, B. *et al.* Hybrid Photon–Plasmon Coupling and Ultrafast Control of Nanoantennas on a Silicon Photonic Chip. *Nano Letters* **18**, 610-617 (2018).

179 Collins, M. J. *et al.* Integrated spatial multiplexing of heralded single-photon sources. *Nature Communications* **4**, 2582 (2013).

180 Feng, C. *et al.* Wavelength-division-multiplexing (WDM)-based integrated electronic–photonic switching network (EPSN) for high-speed data processing and transportation. *High-speed optical switching network* **9**, 4579-4588 (2020).

181 Han, X. *et al.* Mode and Polarization-Division Multiplexing Based on Silicon Nitride Loaded Lithium Niobate on Insulator Platform. *Laser & Photonics Reviews* **16**, 2100529 (2022).

182 Zhou, H. *et al.* Photonic matrix multiplication lights up photonic accelerator and beyond. *Light: Science & Applications* **11**, 30 (2022).

183 Song, S., Dua, J. & Arnold, C. B. Influence of annealing conditions on the optical and structural properties of spin-coated As2S3 chalcogenide glass thin films. *Optics Express* **18**, 5472-5480 (2010).

184 Jayatilleka, H. *et al.* Post-Fabrication Trimming of Silicon Photonic Ring Resonators at Wafer-Scale. *Journal of Lightwave Technology* **39**, 5083-5088 (2021).

185 Wu, Y., Shang, H., Zheng, X. & Chu, T. Post-Processing Trimming of Silicon Photonic Devices Using Femtosecond Laser. *Nanomaterials* **13** (2023).

186 Biryukova, V., Sharp, G. J., Klitis, C. & Sorel, M. Trimming of silicon-on-insulator ring-resonators via localized laser annealing. *Optics Express* **28**, 11156-11164 (2020).

187 Farmakidis, N. *et al.* Scalable High-Precision Trimming of Photonic Resonances by Polymer Exposure to Energetic Beams. *Nano Letters* **23**, 4800-4806 (2023).

188 Lin, G.-R., Baiad, M. D., Gagne, M., Liu, W.-F. & Kashyap, R. Harnessing the fiber fuse for sensing applications. *Optics Express* **22**, 8962-8969 (2014).

189 Schuler, S. *et al.* High-responsivity graphene photodetectors integrated on silicon microring resonators. *Nature Communications* **12**, 3733 (2021).

190 Chakraborty, I., Saha, G., Sengupta, A. & Roy, K. Toward Fast Neural Computing using All-Photonic Phase Change Spiking Neurons. *Scientific Reports* **8**, 12980 (2018).

191 Jiang, W., Miao, J. & Li, T. Compact silicon 10-mode multi/demultiplexer for hybrid mode- and polarisation-division multiplexing system. *Scientific Reports* **9**, 13223 (2019).

192 Fan, D.-H. *et al.* High-efficiency broadband fiber-to-chip coupler using a 3D nanoprinting microfiber. *Applied Optics* **62**, 4203-4212 (2023).

193 Chen, J., Liu, P. & Shi, Y. An on-chip silicon compact triplexer based on cascaded tilted multimode interference couplers. *Optics Communications* **410**, 483-487 (2018).

194 Jayatilleka, H. *et al.* Crosstalk in SOI Microring Resonator-Based Filters. *Journal of Lightwave Technology* **34**, 2886-2896 (2016).

195 Xu, H., Liu, C., Dai, D. & Shi, Y. Direct-access mode-division multiplexing switch for scalable on-chip multi-mode networks. *Nanophotonics* **10**, 4551-4566 (2021).

196 Luo, L.-W. *et al.* WDM-compatible mode-division multiplexing on a silicon chip. *Nature Communications* **5**, 3069 (2014).

197 Jia, H. *et al.* Microring modulator matrix integrated with mode multiplexer and de-multiplexer for on-chip optical interconnect. *Optics Express* **25**, 422-430 (2017).

198 Loke, D. *et al.* Breaking the Speed Limits of Phase-Change Memory. *Science* **336**, 1566-1569 (2012).

199 Saldutti, M. *et al.* Modal Properties of Photonic Crystal Cavities and Applications to Lasers. *Nanomaterials* **11** (2021).

200 Foresi, J. S. *et al.* Photonic-bandgap microcavities in optical waveguides. *Nature* **390**, 143-145 (1997).

201 Dong, P. Silicon Photonic Integrated Circuits for Wavelength-Division Multiplexing Applications. *IEEE Journal of Selected Topics in Quantum Electronics* **22**, 370-378 (2016).

202 Passaro, V. M. N. *et al.* Recent Advances in Integrated Photonic Sensors. *Sensors* **12**, 15558-15598 (2012).

203 Wang, R. *et al.* III–V-on-Silicon Photonic Integrated Circuits for Spectroscopic Sensing in the 2–4 μm Wavelength Range. *Sensors* **17** (2017).

204 McMahon, P. L. The physics of optical computing. *Nature Reviews Physics* (2023).

205 Syed, G. S., Zhou, Y., Warner, J. & Bhaskaran, H. Atomically thin optomemristive feedback neurons. *Nature Nanotechnology* (2023).

206 Ghazi Sarwat, S. *et al.* An integrated photonics engine for unsupervised correlation detection. *Science Advances* **8**, eabn3243 (2022).

207 Youngblood, N., Ríos Ocampo, C. A., Pernice, W. H. P. & Bhaskaran, H. Integrated optical memristors. *Nature Photonics* **17**, 561-572 (2023).

208 Sinatkas, G., Christopoulos, T., Tsilipakos, O. & Kriezis, E. E. Electro-optic modulation in integrated photonics. *Journal of Applied Physics* **130**, 010901 (2021).

209 Yong, Z. *et al.* Power-efficient silicon nitride thermo-optic phase shifters for visible light. *Optics Express* **30**, 7225-7237 (2022).

210 Wu, J. *et al.* Two-Dimensional Materials for Integrated Photonics: Recent Advances and Future Challenges. *Small Science* **1**, 2000053 (2021).

211 Gonzalez Marin, J. F., Unuchek, D., Watanabe, K., Taniguchi, T. & Kis, A. MoS2 photodetectors integrated with photonic circuits. *npj 2D Materials and Applications* **3**, 14 (2019).

212 Huang, L. *et al.* Waveguide-Integrated Black Phosphorus Photodetector for Mid-Infrared Applications. *ACS Nano* **13**, 913-921 (2019).

213 Wang, Y. *et al.* Tunability of indium tin oxide materials for mid-infrared plasmonics applications. *Optical Materials Express* **7**, 2727-2739 (2017).

214 Melde, K., Mark, A. G., Qiu, T. & Fischer, P. Holograms for acoustics. *Nature* **537**, 518-522 (2016).

215 Ali, U. E., Modi, G., Agarwal, R. & Bhaskaran, H. Real-time nanomechanical property modulation as a framework for tunable NEMS. *Nature Communications* **13**, 1464 (2022).

216 Utadiya, S. *et al.* Digital holographic imaging of thermal signatures and its use in inhomogeneity identification. *Optics and Lasers in Engineering* **160**, 107227 (2023).

217 Ravaro, M. *et al.* Mid-infrared digital holography and holographic interferometry with a tunable quantum cascade laser. *Optics Letters* **39**, 4843-4846 (2014).

218 Lee, H.-E. *et al.* Amino-acid- and peptide-directed synthesis of chiral plasmonic gold nanoparticles. *Nature* **556**, 360-365 (2018).

219 Xu, H., Dai, D. & Shi, Y. Silicon Integrated Nanophotonic Devices for On-Chip Multi-Mode Interconnects. *Applied Sciences* **10** (2020).